# Visualization Studies of Evaporation and Combustion of Alternative Liquid Fuels and Aviation Liquid Droplets in Controllable Environments

by

Vignesh Venkatasubramanian

A dissertation submitted to the Graduate Faculty of
Auburn University
in partial fulfillment of the
requirements for the Degree of
Doctor of Philosophy

Auburn, Alabama
May 5, 2018

Keywords: Alternative Liquid Fuels, Aviation Fluids, Microdroplet Generation, Droplet Vaporization, Microexplosion, High Magnification Imaging

Approved by

Steve R. Duke, Associate Professor, Chemical Engineering
Mario R. Eden, Professor, Chemical Engineering
Yoon Y. Lee, Professor, Chemical Engineering
Sushil Adhikari, Associate Professor, Biosystems Engineering

# Abstract

This dissertation describes visualization studies of alternative fuel and aviation liquid droplet behavior in controlled environments. Three experimental setups using free-falling and suspended droplet techniques were designed, constructed, and shown to be effective methods for studying individual droplet behavior. Systematic suspended droplet studies involving ethanol and glycerol mixtures were performed in rapid heating environments inside an infra-red (IR) heater. Aviation liquid (BP Oil) was used as a representative multicomponent liquid mixture. Quantitative data obtained from low and high magnification visualizations along with the internal droplet temperature were obtained. Experimental techniques and results from the IR heater demonstrate a novel method of studying suspended droplet behavior. This research supplements existing literature on the behavior of similar fluids in high temperature environments.

Studying the behavior of alternative fuels and aviation liquids in variable temperature environments was our objective. Generally, applications involve sprays or mist of droplets. A simple approach to understand the spray or mist behavior of a liquid is to consider them as a conglomeration of individual droplet behaviors. We have employed two widely used techniques, namely, the free-falling droplet technique (moving droplet) and suspended droplet technique (stationary droplet) to study individual droplet behavior. Experimental setups using a laboratory scale drop tube furnace and an infra-red heater system with visualization capabilities were constructed for this purpose. A piezoelectric droplet generator was built to perform moving droplet studies in the drop tube furnace. Stationary droplet studies were performed by either

generating the droplet at the tip of a graphite fiber (drop tube furnace) or by suspending a droplet on a fine gauge thermocouple wire (IR heater). Proof of method experiments with visualization images were presented for aqueous glycerol solution, hexadecane, and BP Oil to demonstrate the feasibility of the setup to study individual droplet behavior.

Systematic studies were performed in the IR heater for ethanol – glycerol (E-G) blends. Two blends, namely E30G70 and E70G30 were prepared and studied alongside pure ethanol (E100) and pure glycerol (G100), together the four liquids represent the E-G system. The E-G system was studied at different gas flowrate conditions (5-25 SCFM), different gas environment types (air and nitrogen), and alongside other liquid types such as pure methanol (M100), pure butanol (B100), standard fuel (hexadecane) and multicomponent aviation liquid (BP Oil). Low magnification visualizations were used to obtain quantitative data (quiescent, behavior, and residence times) and to exhibit various droplet behavior phenomenon such as microexplosion, microdroplet escape behavior, puffing, etc. High magnification visualizations of the E-G system suspended droplet behavior were shown; and the quantitative data obtained was used to determine the $d^2$-law parameter and calculate the evaporation rate constant ($k$). Characteristic evaporation phases (transient heating phase, fluctuation evaporation phase, and equilibrium evaporation phase) were shown using temporal droplet diameter data plots ($d^2$ vs $t$) for the four E-G system liquid types. Internal droplet temperature ($T$) and temperature period classifications (period-1, -2, and -3) that include heating rate (°C/s), time duration ($\Delta t$) and temperature change ($\Delta T$) were presented for suspended droplet experiments in the IR heater.

Proof of method experiments demonstrate the ability of our experimental setup to visualize and study the behavior of moving or stationary droplet behavior undergoing vaporization and combustion. Low and high magnification visualizations from the IR heater allowed observation of

significant behavior events for droplets in different heating environments. The capability to determine droplet temperature, temporal droplet diameter change, and evaporation rate constant for a rapid radiant-heating environment such as the IR heater is a unique contribution to study suspended droplet behavior. The results demonstrate successful methods for further experimental studies with liquid types such as crude glycerol, waste oil, bio oils, and other commercially available engine oils that have real world applications.

# Acknowledgments

Thank God! I would like to thank my advisor Dr. Steve R. Duke for providing me with the opportunity to join his research group at Auburn University. His continued support and guidance throughout my graduate program has been invaluable. I would like to thank my committee members Dr. Mario Eden, Dr. Yoon Lee, and Dr. Sushil Adhikari for their guidance, suggestions and time to oversee my Ph. D research. I would also like to thank Dr. Tony Overfelt for research support and for serving as the outside reader and for my dissertation. I would like to thank Brian Schwieker and Michael Crumpler for their excellent assistance in the development of my research setups. I would like to thank the past members of the Duke research group Dr. Rajeshwar Chinnawar, Jingran Duan, and Dr. Bangping Wang. Their support, motivation, and company during the challenging times have been vitally important for my development as a researcher here in Auburn University. I would also like to thank Ms. Karen Cochran and Ms. Elaine Manning of the Chemical Engineering department for all their help during my graduate program in Auburn. Also, during my time at Auburn I had the company of some wonderful friends in Robin, Shantanu, Achin, Pranav, Shaima, Ravi, Nakul, Sam, Vishnu, Vikas, and John. They made my life in this beautiful university town as fun as possible.

Last but not the least, I would especially like to thank my amma, appa, anna Dr. Rajesh Venkatasubramanian and manni Sadhana Radhakrishnan for being a beacon of support and continued belief in my abilities to succeed. I would like to thank my family members and friends Nandha Kumar, Sushanth, and Kalidasan back home in Chennai, India for their moral support and

faith in my ambition to pursue my goals. The values they have imparted in me throughout my life have made me who I am today and I will be eternally grateful.

## Table of Contents

# List of Tables

## List of Figures

# List of Symbols and Abbreviations

| | |
|---|---|
| ℃ | Degree Celsius |
| ℃/min | Degree Celsius per minute |
| ℃/s | Degree Celsius per second |
| µm | micrometre |
| A | Ampere |
| APU | Auxiliary Power Units |
| aq. | Aqueous |
| BT | Behavior Time |
| $CO_2$ | Carbon dioxide |
| $d$ | Droplet diameter |
| $d_0$ | Initial droplet diameter |
| DOE | Department of Energy |
| DrDrTGA | Double Differential TGA |
| DrTGA | Differential TGA |
| EEP | Equilibrium Evaporation Phase |
| FAA | Federal Aviation Association |
| FEP | Fluctuation Evaporation Phase |
| fps | frames per second |
| GC/MS | Gas Chromatography Mass Spectroscopy |
| GJ/tonne | Gigajoule per tonne |
| hz | Hertz |

| | |
|---|---|
| IR | infra-red |
| kWh/tonne | Kilowatthour per tonne |
| $k$ | Evaporation rate constant |
| $k_{avg}$ | Average evaporation rate constant |
| lbs | pounds |
| ml | milliliter |
| mN/m | millinewton per metre |
| mPas | millipascal second |
| ms | milliseconds |
| PAH | Poly Aromatic Hydrocarbon |
| PCA | Portland Cement Association |
| ppb | Parts per billion |
| ppm | Parts per million |
| QT | Quiescent Time |
| RA | RUN ADJUST |
| ROI | Region of Interest |
| RT | Residence Time |
| $t$ | Elapsed time |
| $T$ | Temperature |
| $t'$ | IR heater starting lag |
| TA | TIME ADJUST |
| TCP | tricresyl phosphate |
| Tg | terragram |

| | |
|---|---|
| TGA | Thermogravimetric Analysis |
| THP | Transient Heating Phase |
| TMPP | trimethyl propane phosphate |
| V | Voltage |

# 1. Introduction

This research work involves the investigation of liquid droplets at variable temperature environments to understand their behavior. Specifically, this work is concerned with phenomena of selective alternative fuels and aviation liquids in such form under evaporation and combustion environments. Spray (alternative fuels) or mist (aviation liquids) forms are of concern to us because of their energy applications in cement plants and potential contamination conditions in aircraft environments. In this research, we study the liquids as individual droplets in either free-falling or suspended states under different temperature conditions. The goal is to contribute to the understanding of the fundamental evaporation and combustion processes of these liquids. This is of importance for the researchers working on developing numerical and analytical models to predict the response of the liquid sprays to different temperature environments. Also, the experimental and visualization techniques used in this research contribute to the methods in literature for studying the behavior of certain fuels and liquid types.

## 1.1. Motivation for this Research

Fossil fuel which includes coal, oil, petroleum and natural gas comprises 84 % of total energy consumption in the United States as of 2012 (Trading Economics, 2014). Among these fossil fuels, reducing the consumption of coal in cement industry is of importance for the Department of Energy (DOE) that has funded portions of our work presented in this dissertation. Glycerol and waste oils are alternative liquid fuel options that were evaluated in large scale trials in a cement manufacturing plant along with solid alternative fuels such as waste tires, railroad ties, and biomass as a part of cement plant research (Folta, 2010).

A parallel section of this research involves the study of aviation liquid using the same experimental setup. In the recent years, there has been a growing concern in the Federal Aviation

Association (FAA) regarding the potential contamination of cabin air in flights due to synthetic turbine engine oils, hydraulic fluids or deicing fluids. Hence the need to understand the behavior of these liquid types in potential leak environment conditions. This research work is restricted to the study of engine oils alone with the aim to understand the thermal degradation behavior of the liquid when exposed to bleed air conditions in the event of a leakage.

## 1.2. Why Glycerol as an Alternative Fuel Option?

The DOE estimates suggest that if the United States were to produce enough biodiesel to displace only 2% of current petroleum diesel usage, more than 800 million pounds of glycerol would be produced. As of 2006, the U.S. market for glycerol is about 600 million lbs/year. To biodiesel producers, the crude glycerol generated is a potential financial and environmental liability. Conventional uses of glycerol at present cannot accommodate this excess production, creating a significant glut in the glycerol market (Johnson and Taconi, 2007).

## 1.3. Available Literature on Glycerol

Generally, glycerol is not a favorite option when it comes to its use as an alternative fuel owing to its high viscosity and auto-ignition temperature. In addition, it has comparatively low energy content among the available alternative fuel options. However, a few research attempts have been made to study the effect of glycerol as an alternative option. Patzer (2007) utilized crude glycerol blended with yellow grease as a viable industrial boiler fuel option with little success. Bohon et al. (2011) developed laboratory scale prototype burners for crude glycerol and showed that a properly designed refractory burner could provide the thermal environment to effectively combust glycerol but high particulate emissions are a concern.

Recently, Folta (2010) in his dissertation work that involves the collaboration of Auburn University and the Lafarge Corporation Calera AL cement plant has shown the results of trial runs using liquid glycerol in a cement plant. Results show little impact on the emission levels and cement performance when it was used as a co-firing fuel option. His research work was concentrated on emissions from glycerol combustion and its ability to replace existing fuels, rather than the fundamental aspects controlling the combustion of the liquid. Dee and Shaw (2004), conducted an experimental and analytical study using a suspended droplet technique on propanol-glycerol mixtures under reduced gravity conditions, showing the onset time of flame contractions, and burning rates data, which enabled the estimation of effective liquid species diffusivities. Wardana (2010) conducted experiments involving jatropha oil droplets of varying diameter that were suspended on a thermocouple junction to investigate combustion characteristics. Jatropha oil with its high viscosity and chemical structure containing glycerol in its backbone is very closely related to liquid glycerol. Results from his work revealed the two-step combustion taking place in jatropha oil with fatty acid burning in the first step followed by the glycerol.

## 1.4. Why We are Concerned with Aviation Liquids?

The bleed air system, being very beneficial to the aircraft system for its energy efficient operations, is also seriously questioned for its potential contamination of bleed air from multiple sources. Experimental works in literature clearly portray numerous health risks associated with the exposure of aircraft bleed air contaminants to airline workers (Harrison et al., 2009). On the ground, the compressors on the aircraft tail called the Auxiliary Power Units (APU) have the potential to get contaminated by pyrolyzed engine oil and hydraulic fluids due to maintenance irregularities, mechanical failures, and faulty designs (ASHRAE, 2007; van Netten, 2000; BAe Systems, 2000). There have been several incidents reported in literature regarding noxious gas leaks in the cabin air with tricresylphosphate isomers being the most common along with triphenylphosphates and tributylphosphates (Muir, 2008; Fox, 2000; PCA, 2007; SHK, 2001; van Netten, 2005).

## 1.5. Available Literature on Aviation Liquids

Literary works (Winder and Balouet, 2002; Mackerer et al., 1999) corresponding to aviation fuels and cabin air contamination focus primarily on the specific components present in the aviation fluids that are potentially harmful to crew and the passengers. Van Netten et al. (1998, 1999, 2002) in their work have made attempts to study the pyrolytic breakdown products of jet engine lubricating oils and hydraulic fluids in bleed air conditions. Results showed that the important source of carbon monoxide were engine oils with half the number of tricresyl phosphate isomers present in the bulk oils being detected in the atmosphere at ambient temperatures after pyrolysis. In other studies by van Netten and Leung (2000, 2001), two jet engine oils along with their volatile pyrolytic degradation products are compared using GC- Mass spectroscopy to detect the presence or formation of tricresylphosphates (TCPs) and trimethyl propane phosphate (TMPP). TCP's presence in both the bulk oils and volatiles were confirmed while no TMPP was found in any of the products.

Other notable work regarding aviation liquids include the chemical characterization study of polyester aviation lubricant residues by Bartl et al. (2008) and the investigation of gas phase decomposition and thermal degradation of different commercial industrial lubricants based on triaryl phosphates composition and fatty acid methyl-ethyl esters under pyrolytic and oxidative pyrolytic conditions by Mascolo et al. (2004, 2006). NETZCH instruments on request provided with TGA measurements of four different commercially available aviation oil samples with evolved gas analysis by FTIR and MS adding to the available literature on aviation fluids.

Works related to the potential contamination of aviation liquids in aircrafts include the studies from Dr. Overfelt's group. The goal of their research was to develop continuous monitoring sensors for detecting and recording potential contamination events in the aircraft cabin. Their research work includes the study of steady state and transient response characteristics of commercial catalytic bead sensors (Brooks, 2015), non-dispersive infrared carbon dioxide sensors (Roberts, 2014), and carbon monoxide sensors (Buck, 2014).

## 1.6. Why We Need to Study Liquid Sprays?

Liquids in general are used often in the form of a spray of fine droplets rather than in bulk to generate more liquid surface area and to distribute material over a wide cross section. Atomization of liquids is common in industry and more so when it comes to hydrocarbon liquids due to their widespread use as fuels in diesel engines, gas turbines, etc. Over the years, developing an optimum spray nozzle by considering the spray characteristics such as spray cone angle, spray pattern, spray dispersion, spray penetration, mean drop size, radial and circumferential liquid distribution, etc., have significantly improved. An equivalent amount of work has also been done with respect to understanding the behavior of these fine droplets of liquid as it comes out as a spray.

Some of the notable spray characterization studies in literature with respect to fuels include the investigation on the structure and shape of the diesel fuel spray, spatial and temporal distribution of droplet size of the diesel spray by Kuniyoshi et al. (1980), studies on the penetration of fuel spray in a diesel engine by Wakuri et al. (1960), internal diesel spray structure investigation by laser diffraction and sheet illumination by Gulder et al. (1992) and studies on atomization and burning of liquid fuel sprays by Chigier (1979). In addition to the general spray characteristic studies, the evaporation and combustion phenomenon of droplets in sprays have been studied extensively because of their numerous important applications, including spark ignition engines, diesel engines, aircraft propulsion systems, liquid rocket engines, liquid-fueled furnaces, and liquid-waste incinerators, among others (Faeth, 1996). Combustion of liquid fuels in these systems is dependent on effective atomization to increase the specific surface area of the fuel and thereby achieve high rates of mixing and evaporation (Lefebvre, 1983). Commonly two experimental approaches are widely employed to analyze the spray evaporation and combustion. One way is to analyze them from a global view point and treat the burning fuel spray as a continuum. In another method, individual liquid droplets in the spray are followed in their process and analyzed either as fixed droplets or free falling individual droplets. Both methods have merits and limitations. The selection depends on whether one emphasizes the easiness of measurement and analysis or better approximation to the real combustion phenomena (Chung and Kawaguchi, 1990). The objective of our work is to develop one such experimental process that provides the capability to study liquids as individual droplets and as a spray. Liquids in this research mainly include fuels and oils with respective applications in cement manufacturing and aviation industry. Incorporating the visualization aspect in our experiments adds a new contribution to the study of behavior of these liquids because visualization is not possible in most real-world applications.

## 1.7. Goal of this Research Work

The primary goal of this research is to study liquid sprays as individual droplets with the help of visualization techniques. A drop tube furnace and infra-red (IR) heater chamber were used to create the environment for droplet studies. The individual droplets were studied either by suspending them as pendant droplets or as free-falling droplets under the influence of gravity. A visualization setup was designed and constructed to obtain valuable information of the droplet such as droplet diameter, droplet velocity, ignition delay, onset of droplet microexplosion, droplet flame characteristics, and to observe in general the thermal behavior of the droplets at conditions that would be observed in their respective applications. A detailed understanding of the liquid fundamental physical and chemical processes, such as vaporization, transport, and chemical kinetics thus obtained are useful for reliable modeling. In addition to visualizations, the furnace and IR heater were modified by design to transport the exhaust gases evolved to a gas chromatograph that is equipped with TCD, FID and FPD detectors or to be collected in gas sample bags. This was particularly built to study the aviation liquids, where the degradation products from the liquids are of interest.

Extensive droplet behavior characterization studies have been performed with respect to ethanol-glycerol blends in infra-red heater. The different experimental methods and results of this research will provide an insight to study, understand and characterize the behavior of liquid droplets and subsequently contribute to the existing literature available for these liquids types.

# 2. Background

This chapter provides a brief overview of the cement and aviation industry, potential challenges faced the industry with respective to our work, and the importance for studying the behavior of the liquids at different temperatures.

## 2.1. Cement Production

In a cement industry, limestone makes up most of the raw material ingredient for making portland cement with smaller amounts of clay or shale. Figure 2-1 shows a schematic overview of the cement manufacturing process. Comminution and blending of raw materials involves the energy efficient dry process which yields a dry and intimately mixed substance called the raw meal. This raw meal passes through a series of preheaters and precalciner involving a counter current heat transfer with the hot gas from kiln at a temperature of 900°C. Following the preheaters, the materials enter the rotary kiln, a long cylindrical tube that is sloping at 3-4% from the horizontal and rotating at a speed of 1-4 rev/min. Inside the kiln the material in the upper end flows counter to hot gases produced by a flame in the other end, reaching a maximum temperature of about 1450°C that results in clinker production. This clinker is then mixed with a few percent of calcium sulfate and finely ground to make the cement (Taylor, 1997).

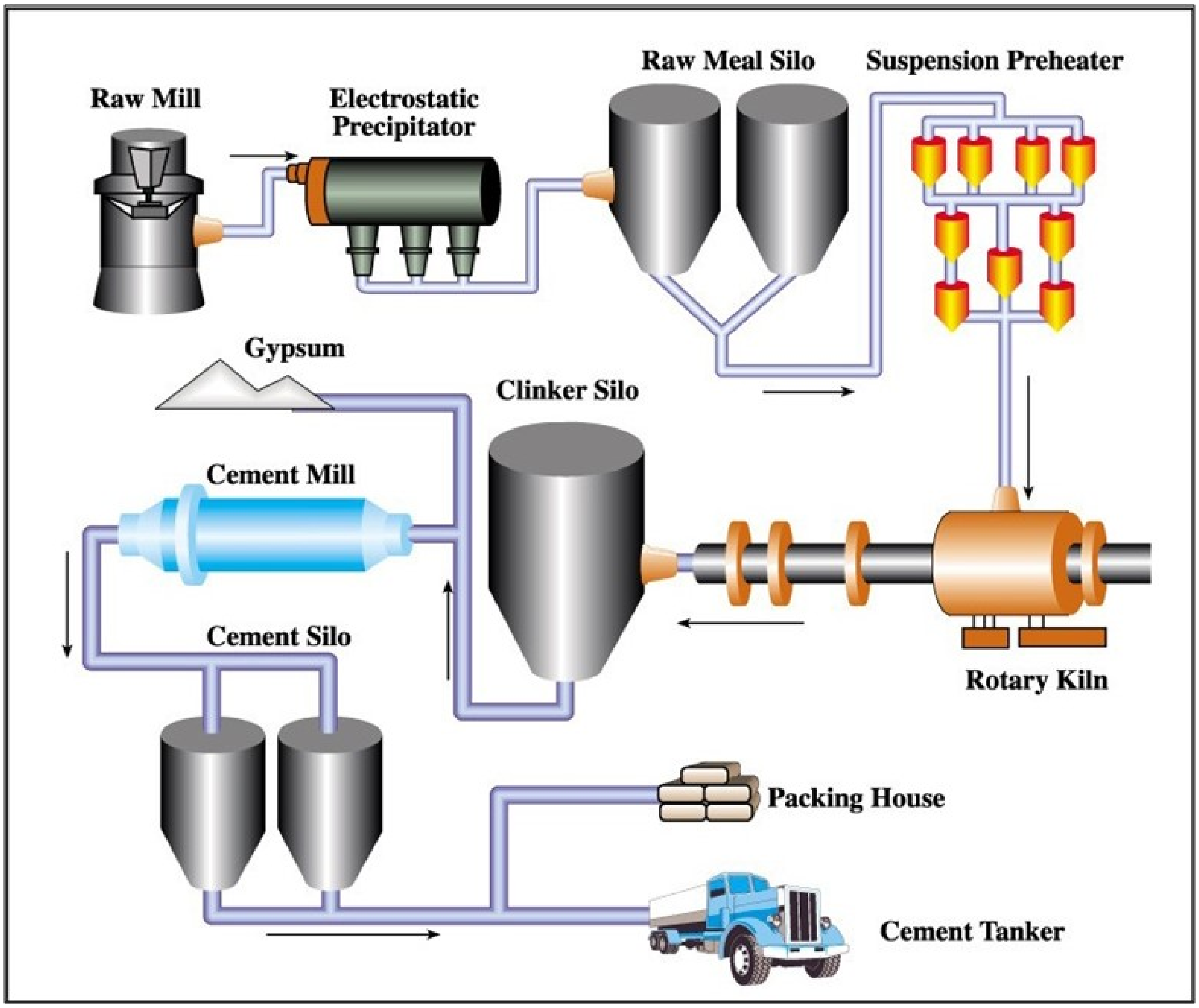

Figure 2-1: Schematic of cement manufacturing process (Source: Lootah group).

## 2.2. Cement Industry - Energy Consumption

The cement industry contributes significantly to the economy of the United States with 39 companies operating 113 cement plants spreading across 36 states with annual shipments valued at approximately $10 billion in 2008 (Portland Cement Association, 2009). Global cement production is much larger, with U.S. production capacity ranked behind China and India contributing to 4.3% of the global capacity (NRMCA, 2012). Cement manufacturing in general is a very energy-intensive operation consuming thermal energy of the order of 3.3 GJ/tonne of clinker produced (Chinyama, 2011) and electrical energy of about 90 – 120 kWh/tonne of cement

(Giddings et al, 2000; Prevention, I. P., 2001). Energy consumption by the cement industry alone contributes 5% of the total global industrial energy consumption (Worrell, 2001). Also, $CO_2$ emission from the cement industry makes up to 7% of global $CO_2$ emissions (average 0.79 tonne of $CO_2$/tonne of clinker) (IPCC, 2005) while combustion related emissions from the U.S cement industry alone were estimated at approximately 36Tg$CO_2$ in 2001 (Hanle, 2004).

Coal has been the primary source of fuel for the cement industry for a long time and continues to do so. Global environmental agencies pressure to reduce carbon dioxide, nitrogen oxide emissions and rising costs of depleting fossil fuels have led cement manufacturers to turn their attention towards partially replacing coal with alternate fuels. The use of alternative fuels in cement manufacturing not only offers ecological benefits of conserving non-renewable resources and potential reduction of emissions, but also provides significant energy costs reduction (Chinyama, 2011).

## 2.3. Alternative Fuel Options

Alternative fuels specific to cement plants include solids such as waste wood, used tires, switch grass, railway ties, etc. and liquids such as glycerol and waste oils. Waste wood and used tires have been extensively used to replace coal or oil, as sources of thermal energy in the cement manufacturing process (PCA, 2007). Lafarge Cement’s Roberta Plant in collaboration with Auburn University and the Department of Energy (DOE), conducted a series of experimental production runs utilizing several different alternative fuels. The key objectives of these studies were to determine the effect of alternative fuels on maintaining a productive operation in the cement plant; detect changes in chemical composition; analyze physical properties of portland cement and the property of concrete made from the portland cement; and monitor the overall emissions released by the cement plant (Folta, 2010; Akkapeddi, 2008).

As a part of this DOE project, solid alternative fuel options examined include scrap and whole tires, waste plastics, broiler litter, wood chips and switchgrass. For an alternative liquid fuel choice, crude glycerol, a very common by-product from biodiesel production was selected as an option for a sustainable approach. Pure glycerol (or glycerin) is a colorless, odorless, viscous liquid with a sweet taste. It is commonly found found in several products such as foods, beverages, pharmaceuticals, cosmetics, and detergents (Rahmat et al. 2010). Crude glycerol however, is an impure form of pure glycerol that is primarily formed as a byproduct of biodiesel production. In general, biodiesel results from a reaction between animal or vegetable oils and alcohol in a process known as transesterification, resulting in a combustion product closely related to petroleum diesel fuel (Astbury, 2008; Gerpen, 2005). Figure 2-2 shows a detailed process flow schematic of biodiesel production. During this process, the glycerol leaving the separator is of low value, and treated usually as a hazardous waste due to its excessive methanol content. It is for this reason acid is added to remove the free fatty acids and methanol, resulting in a crude glycerol that is approximately 85% refined. This crude glycerol is typically sold to a refiner, who brings up the purity to about 99.7% using a vacuum distillation or ion exchange process (Gerpen 2005).

A liquid fuel such as glycerol requires an external source of heat to reduce its viscosity and facilitate pumping, so it is typically stored in cylindrical steel tanks with thermal insulation on their external surface. During injection, these liquid fuels undergo a process called nebulization, which converts a constant stream of liquid into a cloud of individual droplets (Greco et al. 2004). On whether the glycerol, a viable alternative fuel among different options to produce portland cement depends also on local availability, associated costs, and compatibility with the local facility’s production operations.

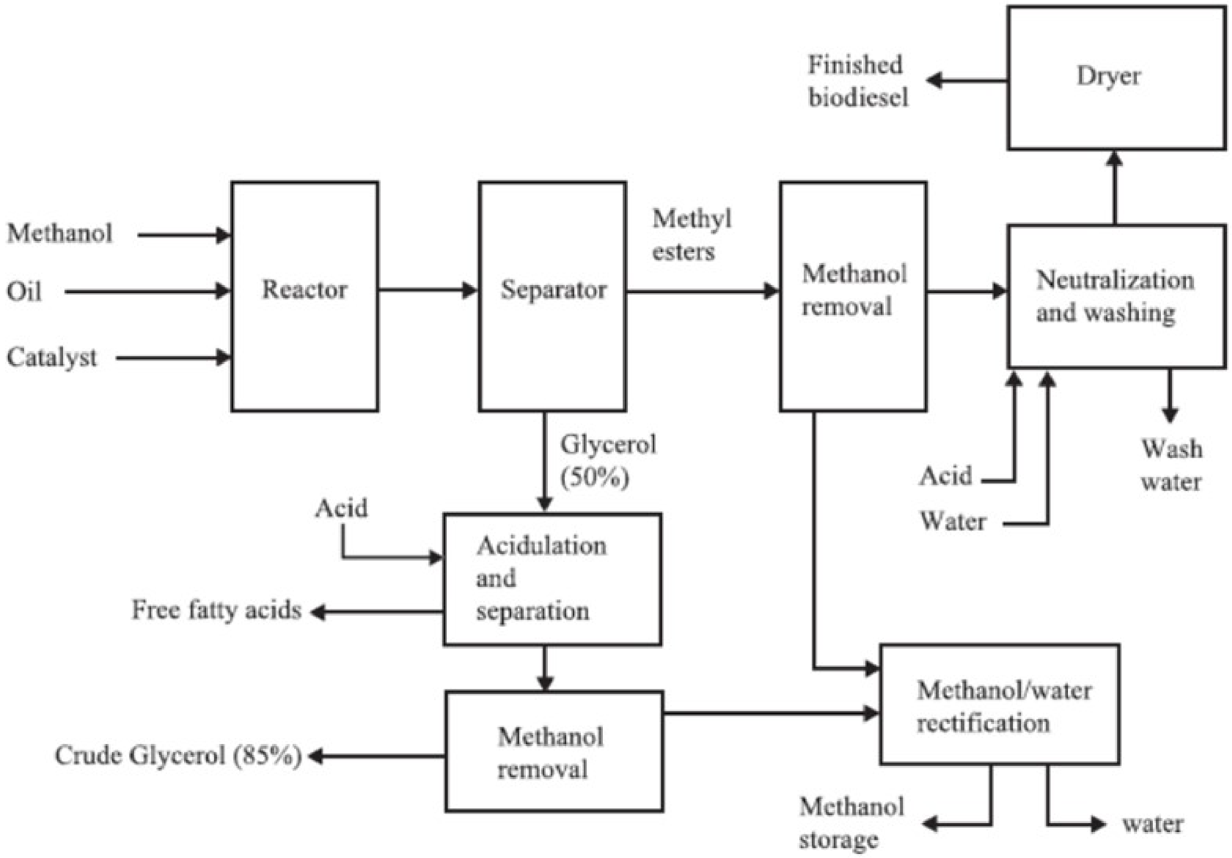

Figure 2-2: Process flow schematic of biodiesel production (Gerpen 2005).

The studies with Lafarge showed that the alternative fuels used to produce portland cement were of considerably high consistency and quality while maintaining targeted production rates. Since, a substantial amount of waste was diverted from landfills, it helped to reduce the production of harmful greenhouse gases caused by incineration (Folta, 2010). At present, no single alternative fuel is capable of completely replacing coal in energy production but they could be utilized in co-firing with traditional fossil fuels (Huang, 2010).

## 2.4. Aviation Industry

The aviation industry, less than 100 years since powered flight has undergone rapid growth and become an integral part of the modern society (Vedantham, 1999). It plays an important role in the global economy supporting commerce, military activity and private travel. In the long-term, the Federal Aviation Administration (FAA) has projected that close to one billion passengers will be flying per year in 2023 and that the number of passengers will only continue to grow (FAA, 2010). Expecting this potential increase in passenger traffic, airline carriers have already shifted their attention on ways to reduce operational costs and maintain profitability. Increase in the commuter travel also raises questions about the passenger safety. The term safety includes preventing terrorists and other anti-social elements using airlines as global weapons and the outbreak of deadly diseases such as severe acute respiratory syndrome (SARS) and HINI flu through domestic and international aircrafts (Haney, 2011). While the above mentioned has been recognized by media there is another safety concern that has only recently started to gain a lot of attention among aircraft travelers and employees. This is about the potential contamination of the cabin air though the aircraft's bleed air system.

## 2.5. Aircraft - Bleed Air System

A schematic representation of bleed air supply to the aircraft system is shown in Figure 2.2 (Hunt, 1995). Bleed air is the compressed air taken from jet engine just before the fuel is injected into the burners. This bleed air owing to its high temperature and pressure is used for several energy efficient operations inside the aircraft such as engine start, deicing the wings, air conditioning, pressurizing the cabin, etc. Since the bleed air is partially used in the cabin environment and has the potential to allow contaminants from the environment, the issue of air quality within the aircraft cabin is receiving increasing attention from both pilot and flight attendant unions (FAA, 2010).

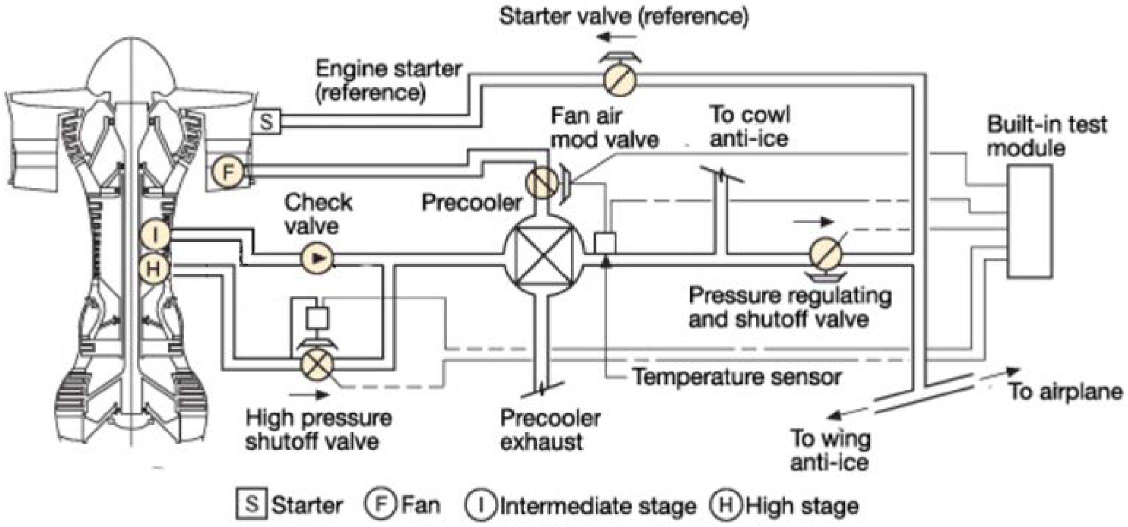

Figure 2-3: Schematic representation of bleed air supply to the aircraft system (Hunt, 1995).

## **2.6.** Cabin Air Quality

Passengers and cabin crew have long complained about the air quality in commercial aircraft. They have expressed concerns regarding exposure to various chemical contaminants in the aircraft cabin and have linked adverse health effects to specific potential exposures. The complaints generally include fatigue, dizziness, headaches, sinus and ear problems, dry eyes, sore throat, and occasionally more serious effects, such as nervous system disorders and incapacitation. Potential leakage of oil, fuel, hydraulic fluids, or deicing fluids from the engines or Auxiliary Processing Unit (APU) is an important suspect for these complaints. At present, limited data is available on contaminants present in bleed air (or cabin air) during an air-quality incident such as a leakage of engine lubricating oil or hydraulic fluid into the cabin air-supply system (Lippmann, 2002).

# 3. Fundamental Equipment of Droplet Behavior Studies: Drop Tube Furnace, IR Heater

Experimental setups used in this research mainly include two fundamental pieces of equipment, the drop tube furnace and the infra-red (IR) heater. The drop tube furnace and its components used in this research were originally constructed to study the combustion behavior of alternative solid fuels at high temperatures. Similarly, the IR heater was used previously for rapid heating applications involving small size tube, cable, or wire. As it will be described later, the auxiliary components of both the drop tube furnace and IR heater used in the development of our experimental setup(s) had to be redesigned to study liquid droplet behavior. This chapter briefly discusses the operation of the two pieces of equipment (drop tube furnace and IR heater) along with their basic support components. Construction, design, and working of all other experimental setup components will be discussed in detail in the proof of method chapters 4, 5, and 6.

## 3.1. Technique and Integral Components

Research investigating the spray combustion behavior using experimental studies involving individual droplets either in suspended or free-falling form is common. In this research, we use the free-falling technique (drop tube furnace) and suspended droplet technique (drop tube furnace and IR heater) to study individual droplet behavior.

Behavior of small sized droplets with a range of volatilities can be studied with the free-falling droplet technique with the benefit of non-interference of the suspending medium. For free-falling droplet studies, a droplet ejector of some kind is used to produce microdroplets. In our experiment, free-falling droplets are suddenly introduced to a high temperature environment with a laminar gas flow, and the droplets fall due to gravity while their behavior is studied using visualization techniques. Suspended droplet techniques usually involve a suspending medium of some kind. They are relatively easy to setup and perform while they restrict the study to low volatile liquids, large droplet sizes and non-spherical shapes due to the interference of the suspending fiber. In our experiments, the two different methods used to suspend droplets involve, a graphite fiber and a fine gauge thermocouple wire.

Figure 3-1 schematics shows the integral components of all three different experimental setups used in this research. As you can see from the figure, the drop tube furnace and IR heater form the centerpiece of experiments to study droplet behavior. Gas control systems help to control the gaseous environment surrounding the droplets. It provides the ability to perform droplet experiments ranging between inert to 99% oxygen content atmospheric composition inside the furnace and IR heater. Test fluid is either a free falling droplet (drop tube furnace) or a droplet suspended over a support (fiber – drop tube furnace, thermocouple – IR heater) depending on the experimental technique used. The visualization setup includes a high-speed camera and high-magnification lens arrangement. Gas analysis refers to the system of collection and testing of exhaust gases from the droplet experiments. The gas analysis equipment includes a gas chromatograph, but the experimental setup also has provisions to collect exhaust gas using gas collection bags for analytical equipment available elsewhere.

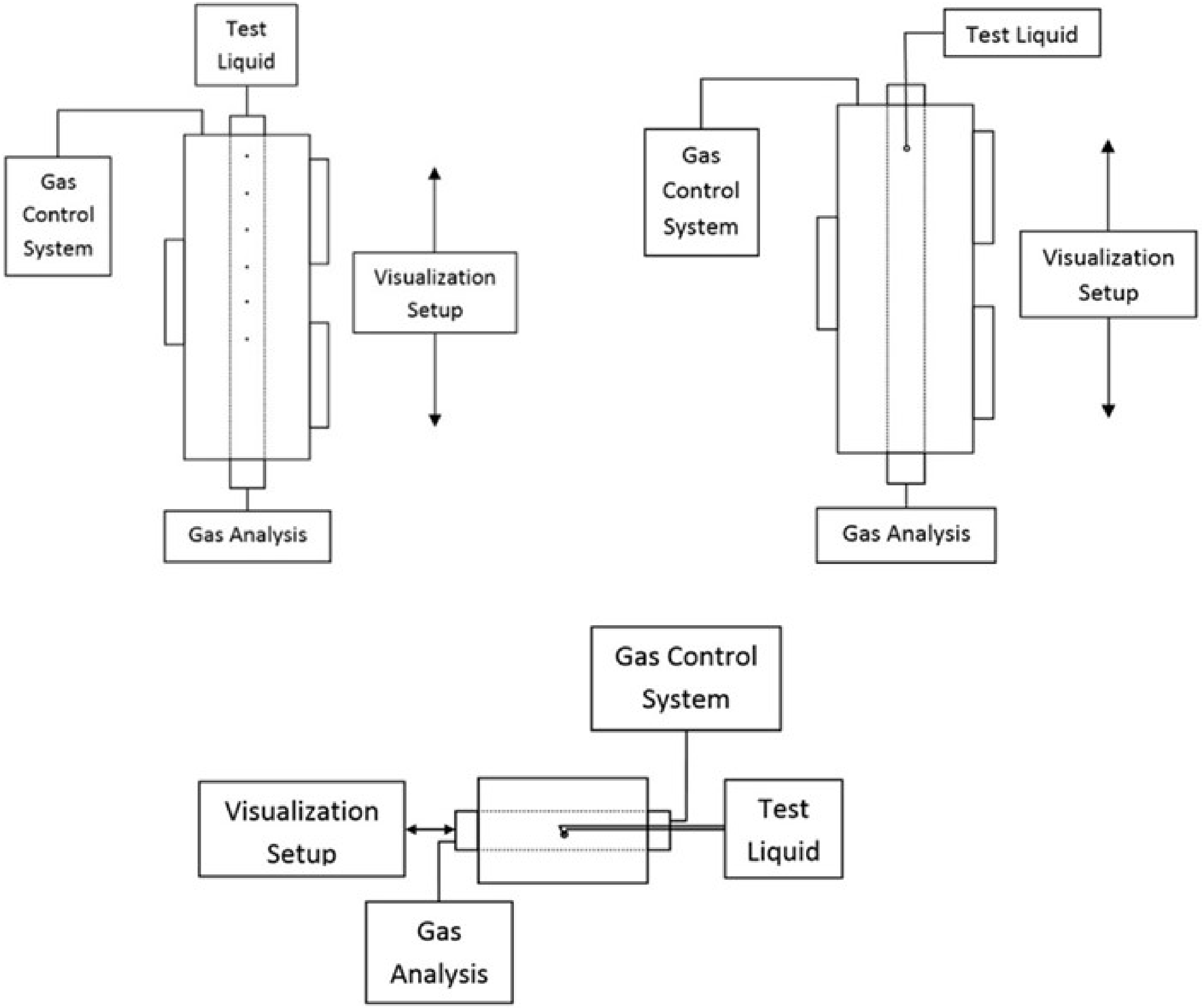

Figure 3-1: Schematic of the three experimental setups used to study droplet behavior. Free-falling droplet studies with the drop tube furnace (top left), suspended droplet studies with the drop tube furnace (top right), and suspended droplet studies with the IR heater.

## 3.2. Drop Tube Furnace

A photograph of the burn simulator used for this research is shown in Figure 3-2. The burn simulator setup used for studying the thermal behavior of solids and liquids was primarily developed by Huang (2010) for his visualization based studies on combustion of solid fuels. Detailed explanation on the developmental criteria and specifications of the tube furnace are explained in the thesis works of Huang (2010) and Livingston (2010).

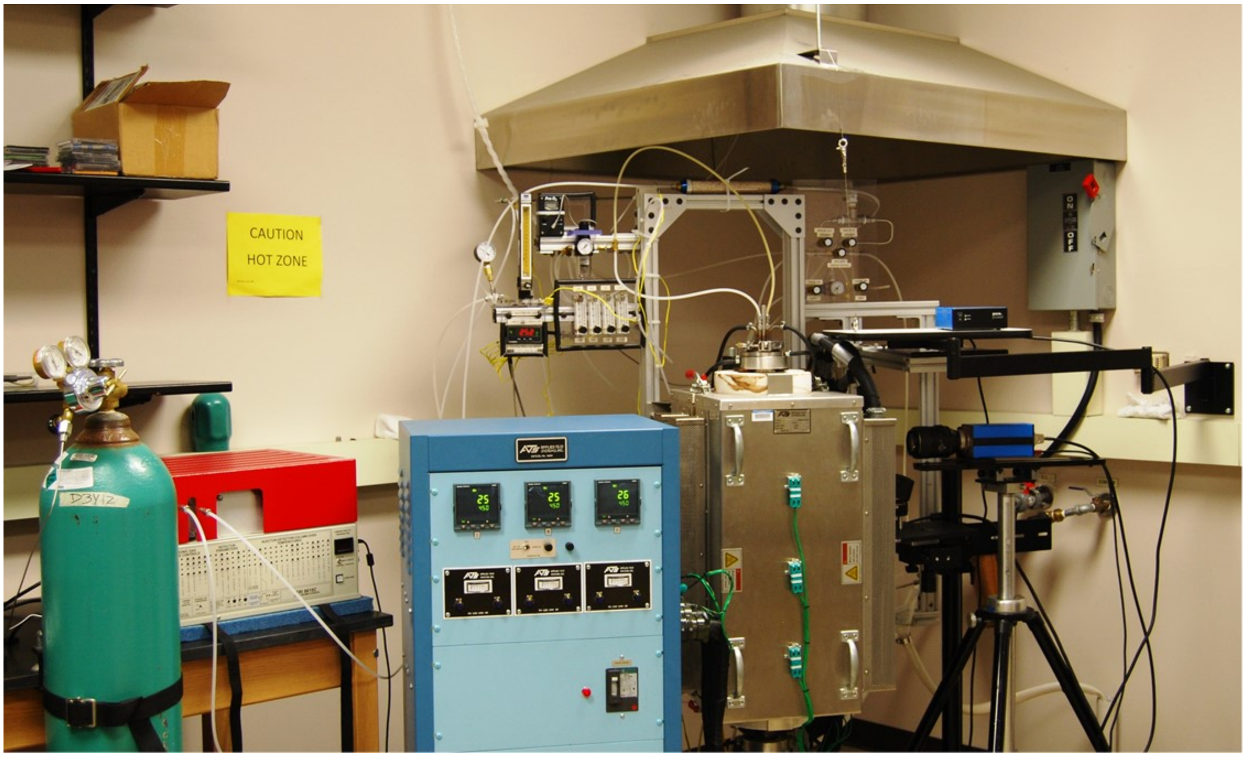

Figure 3-2: Photograph of the laboratory scale burn simulator (drop tube furnace).

The drop tube furnace manufactured by Applied Test Systems, Inc. is an ATS Series 3420 split tube furnace. A photograph of the drop tube furnace with controller is shown in Figure 3-3. The dimensions of the furnace are 32.5 cm in width, 75 cm in height and 35 cm in depth. It has three separately controllable heating zones that can uniformly heat the furnace to a maximum of 1450 °C. Three quartz view windows of 22.5 cm long and 2.5 cm wide on furnace side walls provide visualization capability for the length of the drop tube. A quartz glass retort (drop tube) fabricated in the Auburn University glass shop using Ace Glass tubes, with an outer diameter of 6.25 cm and 90 cm in length, is mounted to the center of the furnace.

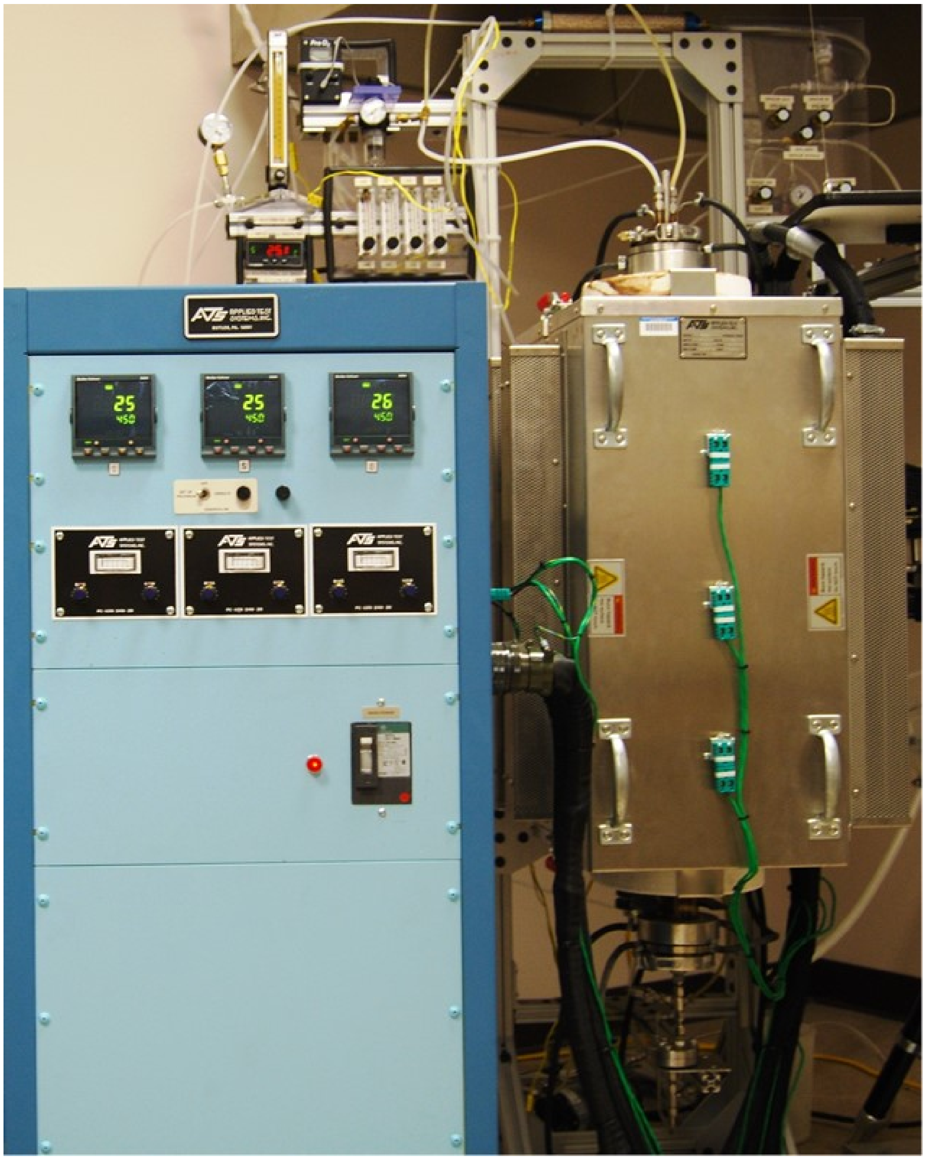

Figure 3-3: Photograph of the drop tube furnace and furnace controller.

### 3.3. Temperature and Gas Control

Series 2404 Barber Colman Programmable controllers from Eurotherm Temperature are used for the controlling the temperature inside the furnace drop tube. Each of three furnace heating zones are individually controlled, and uniform heating rate is achieved by adjusting the controller gain (Livingston, 2010). The gas control system of the furnace is designed to perform combustion studies in varying gas compositions. Process and instrument schematics of the gas control system are shown in Figure 3-4. Air along with $CO_2$, $N_2$, and $O_2$ gas cylinders supplied by Airgas Inc. are coupled to the furnace setup. Gas flow from each cylinder is controlled individually, using needle control valves and rotameters. With a manifold in place, the gas compositions could be altered before it flows into the retort. A Pro $O_2$ Remote TM Oxygen analyzer from Nuvair is connected downstream of the furnace to measure oxygen levels inside the retort. The gas control system overall, can control retort gas compositions between 0 to 99% oxygen compositions with either $CO_2$ or $N_2$ as a balance gas. Downstream of the retort past the filter assembly, is the GAST MOA-P122-AA diaphragm pump from GAST Manufacturing Inc. It operates at 115 V, 2.5 A and 60 hz forming the vacuum system of the furnace. At higher temperatures, the gases tend to rise due to buoyancy driven updraft. The vacuum setup helps counter this effect, and maintain a downward gas flow in the furnace retort. Provided with a bypass line, it provides an option to conduct studies either at atmospheric pressure or pressures below it.

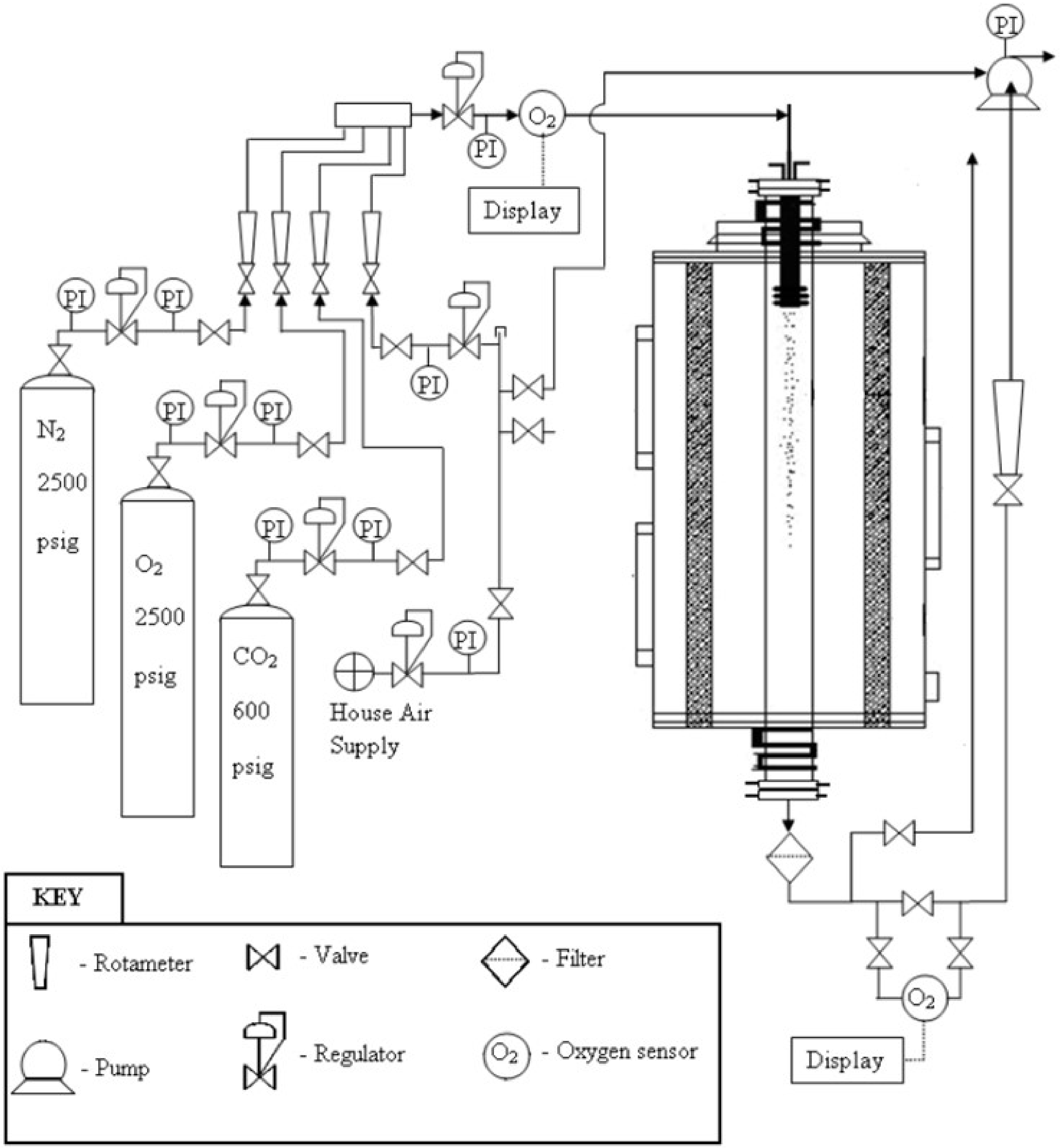

Figure 3-4: Schematic of the gas control system alongside the drop tube furnace (Livingston, 2010).

## 3.4. Cooling System and Char Recovery

Injection nozzles and flanges are water cooled, to prevent the combustion material from getting heated before entering the retort, and to control the combustion within the viewing regions of the glass retort (Huang, 2010). Filtered water supply is controlled through valves and a manifold as shown in Figure 3-5. At the bottom of the glass retort is the particle char recovery setup. It consists of a stainless-steel filter holder housing a 1-micron fiberglass filter manufactured by Millipore Corporation. Photograph of the filter system assembly is shown in Figure 3-6. The primarily design purpose of the filter assembly is to capture the particle char along with uncombusted solid fuel particles, but it could also be used to collect combustion residues of the test liquid if present.

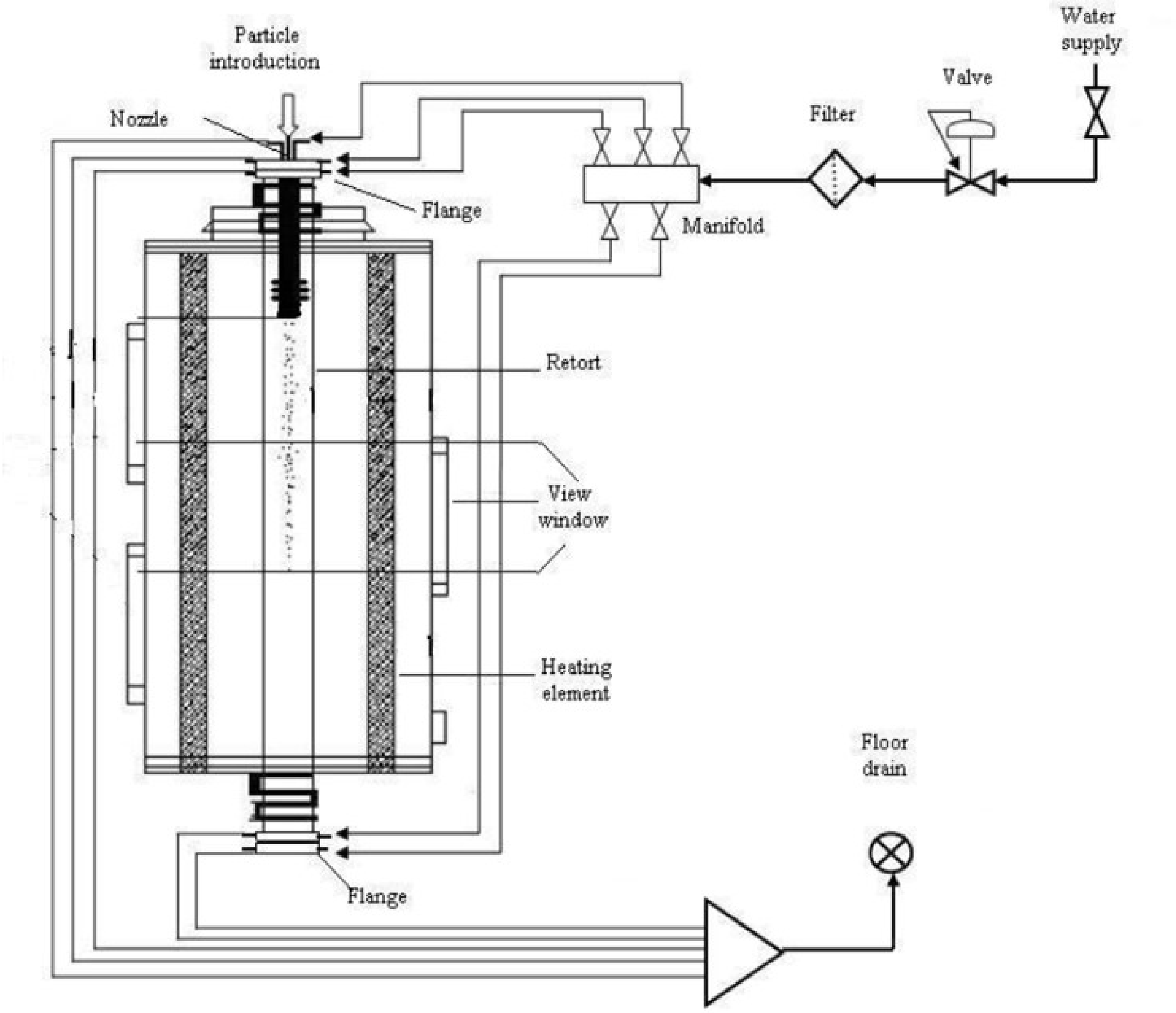

Figure 3-5: Schematic of the drop tube furnace cooling water system (Huang, 2010).

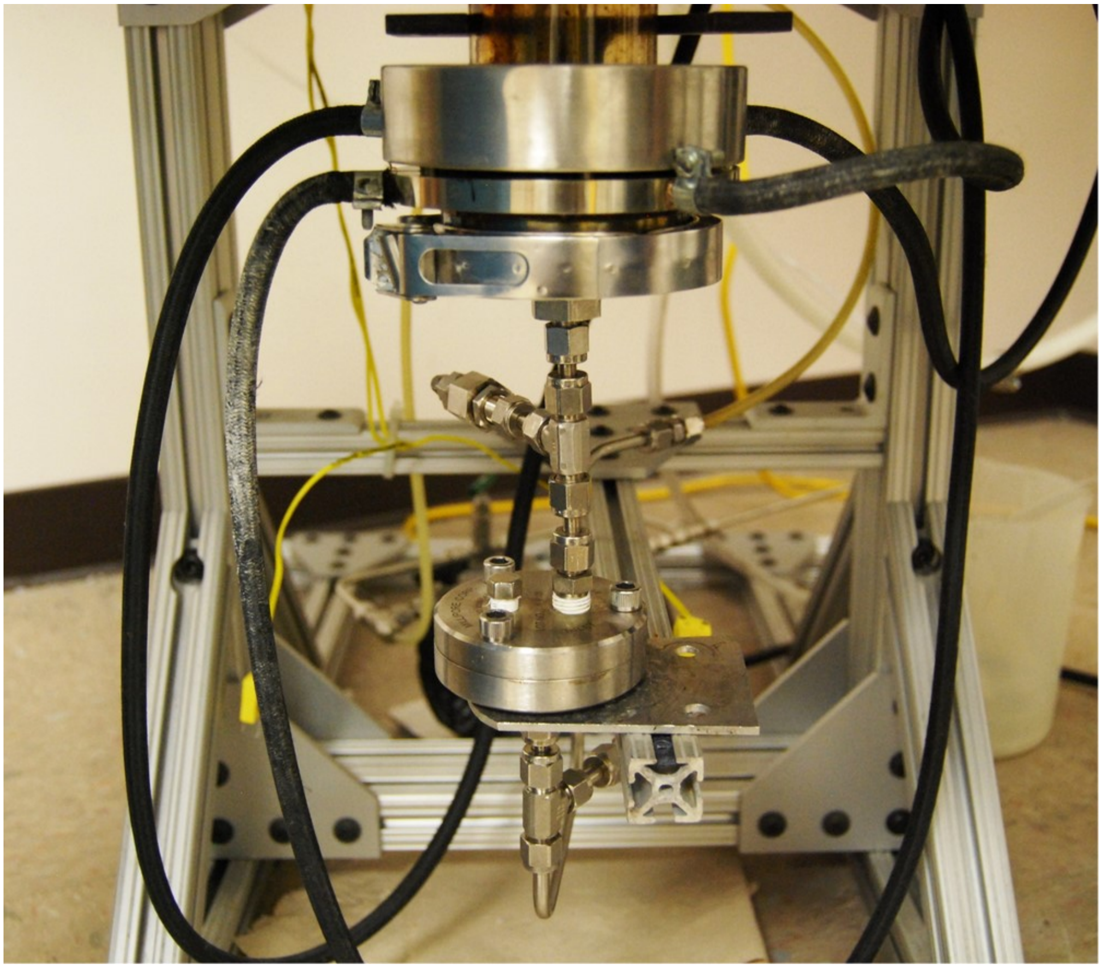

Figure 3-6: Photograph of the filter system assembly at the bottom of the drop tube furnace.

## 3.5. Furnace Operating Procedure

The controller temperature of the drop tube furnace is set according to the condition in which the experimental study is to be performed. The drop tube furnace takes one to two hours to heat up to the required temperature (500 – 900°C). Before furnace startup, the cooling water systems are inspected for leaks. Each of the three controllers are set for the required temperature, and the heating rate is set by adjusting the controller gain. The required gas flow rate and composition inside the retort are maintained through the gas control system. Depending on the viewing window used, the visualization equipment is arranged on a tripod or an optical base that is attached to the furnace frame. Once the experiments are complete, the controller is placed to setup mode and the furnace can cool down before switching off. Until the furnace has been cooled close to room temperature, continuous flow of cooling water is maintained in the injection nozzle and the flanges.

### 3.6. IR heater: Setup and Control

Suspended droplet studies involving fine gauge thermocouple wire are conducted in the ChamberIR infra-red heater (IR Heater) supplied by Research Inc. (now Precision Control Systems, Inc.) as shown in Figure 3-7. This IR heater was obtained from Dr. Overfelt's research group in materials engineering at Auburn University. Previously the IR heater was used by Bakhtiyarov et al. (2004) from their research group, for fraction solid measurements in molten metals.

Heating in the IR heater is accomplished by four T3-style halogen lamps capable of emitting high density infrared energy. This infrared energy from the lamp is focused onto a cylindrically shaped target area with aluminum polished elliptical reflector surfaces. The cylindrical heating region in the center is about 6.35 mm in diameter and 25 cm in length. The IR heater reaches 90% of its full operating temperature within three seconds from a cold start while its radiant energy is dissipated to 10 percent within five seconds after the power is removed. This facilitates a rapid heating region inside the IR heater, capable of instantly heating the suspended test liquid. The halogen lamps of the IR heater are controlled using ControlIR Model 5620 Power Controller. It is used for manually setting the voltage into resistive load. It has provisions for different run power settings (to control lamp voltage) and timer mode settings (to control the illumination duration of lamps). The IR heater also has a constant flow of cooling water around the lamps and reflectors when in operation to prevent excessive heat conditions.

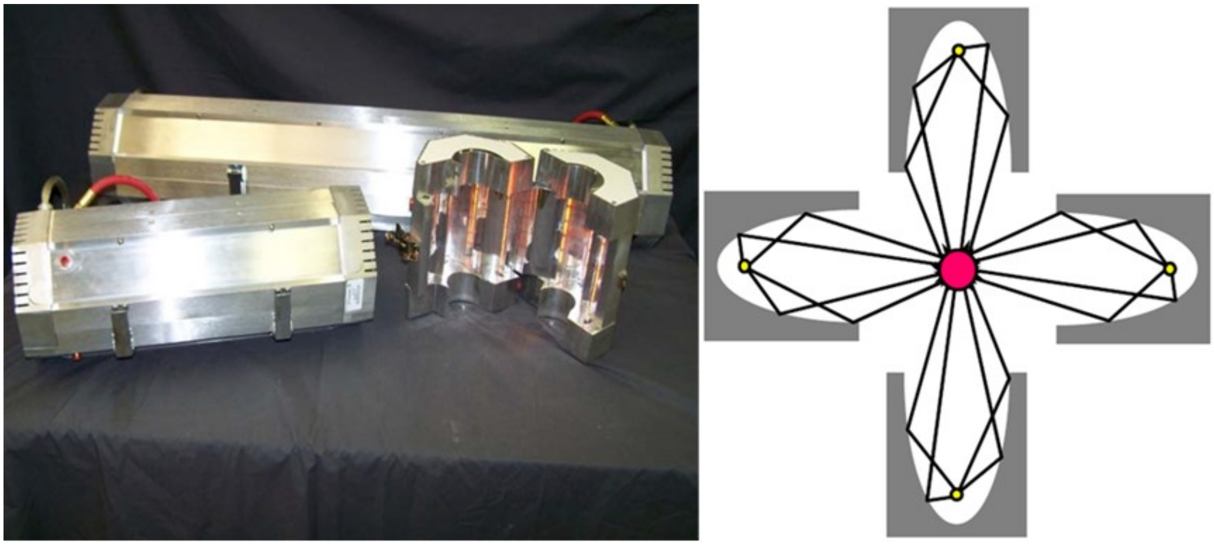

Figure 3-7: Photograph of ChamberIR infra-red heater (left) and the schematic of its mode of operation (right) (Precision Control Sytems, Inc.).

# 4. Proof of Method Experiments to Study Droplet Behavior Using the Free-Falling Technique in a Drop Tube Furnace

## 4.1. Literature Review

Burning of individual fuel droplet in a furnace has been studied since the 1950's. Work of Bolt and Saad (1955) were among the earliest experimental setup and visualization technique developed to investigate the free-falling fuel droplets of n-heptane in a hot atmosphere. Since, several works have been published that seek to understand the fundamental mechanisms controlling spray combustion. Wang et al. (1984), studied the combustion and microexplosion of free-falling multicomponent droplets generated using an ink-jet pulse generator. Results from their study explained the occurrence of a three-staged combustion behavior with the diffusion being the dominant liquid phase transport mechanism. Wornat et al. (1994) investigated the combustion behavior in biomass derived liquids in Sandia's biomass fuel combustion system using an aerodynamic device for droplet generation. Visualization capabilities of their study were useful in distinguishing the distinctive stages of combustion in biomass oils.

Work of Perez et al. (2006) involved the study of evaporation and combustion characteristics of biomass pyrolysis oils using a laminar entrained flow reactor and piezo-electric droplet generator. In this study, they developed correlations between droplet combustion behaviors with respect to the different sized droplets produced from the droplet generator. The free-falling droplet experiments in the literatures mentioned above offers advantages such as small droplet sizes, non-interference from a suspension fiber, and the capability to study volatile fuels. Potential limitations to study droplet behavior using these techniques arise from the difficulty in designing a robust setup to generate free-falling droplets. A dependable droplet generator is of utmost importance for the consistency and reproducibility of the results. Also, the droplet in motion under the influence of gravity in a laminar or turbulent gas flow is challenging to visualize and record thermal behavior.

## 4.2. Technique and Integral Components

The free-falling drop technique is one of the two techniques used in this research to study the thermal behavior of liquids. In this technique, free-falling droplets are suddenly introduced into a high temperature environment with laminar gas flow. As the droplets fall due to gravity in controlled environment, thermal behavior of the droplet is recorded using a combination high-magnification and high-speed visualization system. Figure 4-1 shows the concept of the free-falling technique and the integral components of the experimental setup.

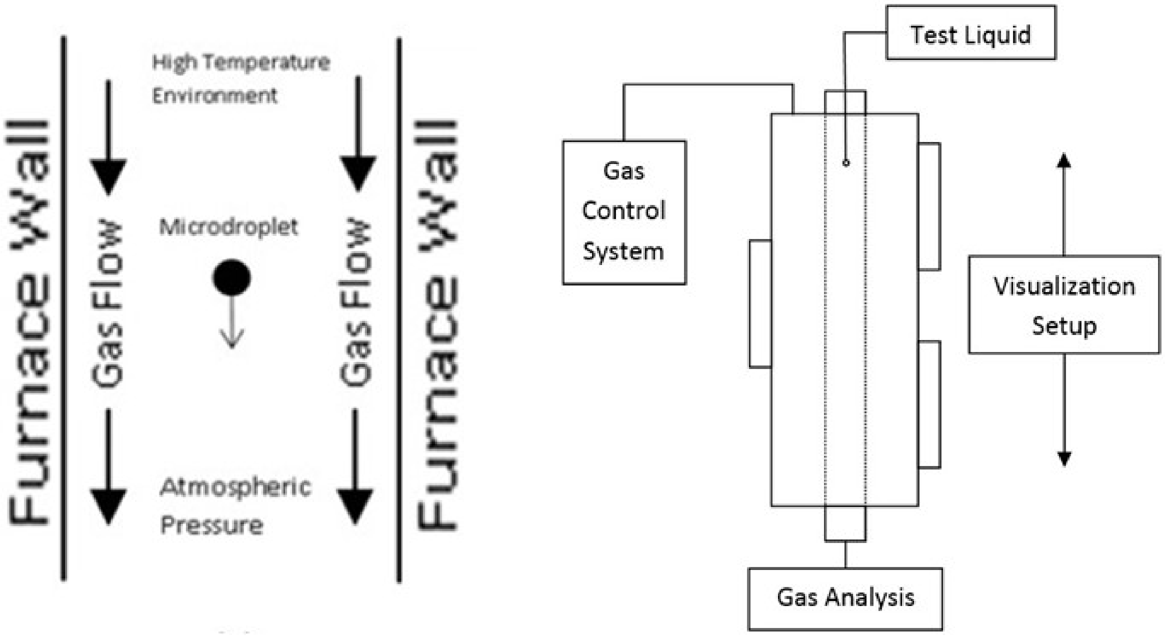

Figure 4-1: Schematic of the free-falling drop technique (left), and the integral components of the experimental setup for the drop tube furnace (right).

A modified drop tube furnace is the centerpiece of the free-falling technique experimental setup, alongside the other integral components in the visualization system and the gas control system. The visualization system consists of a combination of a high-speed camera and a high-magnification lens. A gas control system provides the ability to perform droplet experiments under various oxygen environments (0-100% oxygen) and flow conditions (laminar/turbulent). Test liquids in the free-falling experiment include standard fuels 2.2.4 trimethylpentane (isooctane) and hexadecane (cetane), and aviation liquid (BP Oil). Gas analysis in Figure 4-1 represents the provisions in the experimental setup to collect and analyze the exhaust gases from the furnace; these were not used in the present studies.

## 4.3. Experimental Setup

The experimental setup built for the free-falling liquid droplet study uses many components that were originally designed for solid fuels research in our lab (Huang, 2010; Livingston, 2010; Norris, 2011; Duan, 2011). Components which needed to be redesigned include the injection nozzle and downstream components used for gas collection. In addition, a droplet generator was designed and constructed in-house to generate uniformly sized microdroplets of our test liquids. The following sections describe the design, construction, and function of only the components that were added to the experimental setup to perform the free-falling technique. Information on the other components not included here can be found in the work of Huang (2010).

### 4.3.1. Injection Nozzle

The water-cooled injection nozzle in the drop tube furnace from the solid fuels research was redesigned with the help of Auburn University Chemical Engineering machine shop to allow study of the combustion and vaporization behavior of liquids. Schematic comparison of the solid particle injection nozzle (Huang, 2010) and the newly designed water-cooled liquid injection nozzle are shown in Figure 4-2.

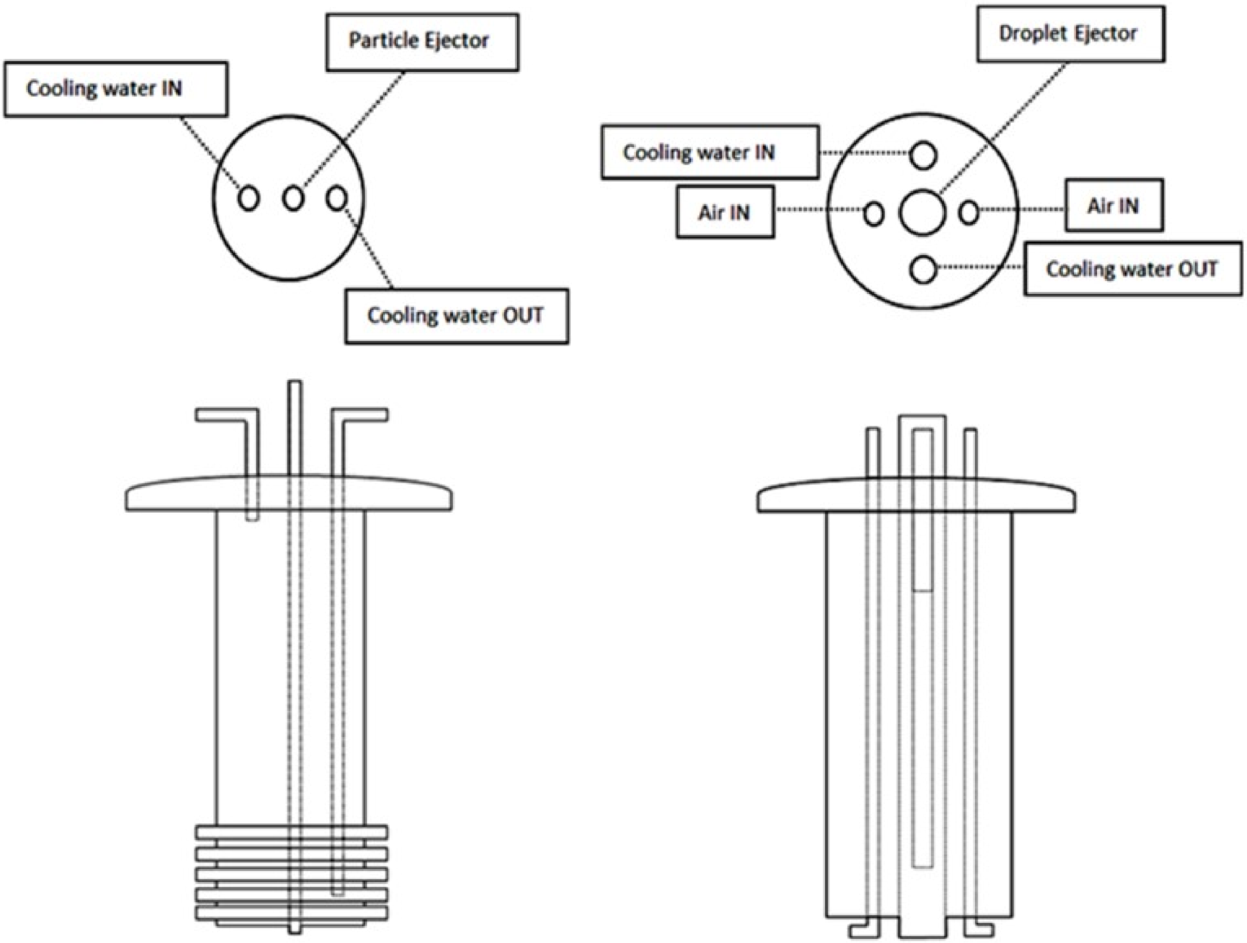

Figure 4-2: Schematics of water-cooled injection nozzle used in solid particles study (left) and liquids study (right).

The injection nozzle used for the solid fuels research had a ¼ inch opening that accommodated both the transport of solid particles and gases into the furnace. This design had to be modified since the droplets have the tendency to drift with the incoming flow of gases. A pair of ¼ inch stainless steel tubes were inserted through bores in the injection nozzle, in addition to the tubes carrying the coolant (water), to transport air and other gases into the furnace. The central opening bored through the axis of the injection nozzle had to be widened from the earlier ¼ inch external diameter to ½ inch diameter to prevent the microdroplets from contacting the walls of the tube before they enter the furnace. The openings of the gas inlet tubes at the bottom of the injection nozzle were also designed to curve towards the retort wall such that the flow of gases would pose minimum disturbance to the path of incoming liquid droplets. Sufficient testing with prototype glass models (not shown here) were performed before construction of the stainless-steel construction of the redesigned water-cooled injection nozzles to ensure successful working of our design.

### 4.3.2. Piezo-Electric Droplet Generator

The purpose of the constructing a droplet generator was to develop a technique that would produce micron sized free falling liquid droplets on demand (Giles, 2013). The piezo-electric droplet generation method used in this research was adapted from the works of Fan (2008) originally intended as a technique for filling liquid crystal displays. The droplet generation method has been suitably modified for the purposes of this study based on the droplet generator prototypes mentioned in Microdroplet Generation by Eric R. Lee (2003). A schematic of the droplet generator and the photograph of the constructed device is shown in Figure 4-3.

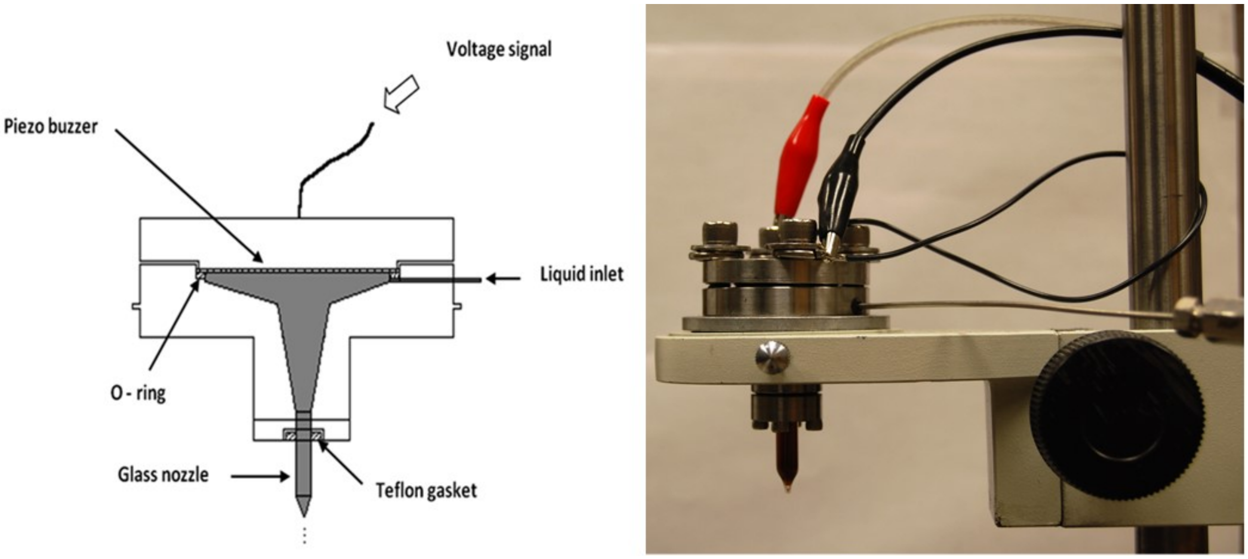

Figure 4-3: Schematic (left) and photograph (right) of the droplet generator.

On the top of the droplet generator is a FT-27T-3.9A1 unimorph piezo disc bender manufactured by American Piezo Ceramics International, Ltd. It is 27 mm in diameter and 0.45 mm in thickness with a resonance frequency of 3.9 kHz. The piezo disc cushioned with an O-ring is placed inside a stainless steel main body with an internal cavity which acts as a liquid reservoir. The liquid inlet positioned below the O-ring is used for maintaining constant liquid level in the reservoir. The bottom portion of the main body is connected to a glass nozzle by means of a Teflon gasket. The nozzle is 31 mm long with an outside diameter of 6.35 mm on one end while the other end tapers to a 350 µm opening. The glass nozzle was delicately fabricated such that it has a tapered cross section, a short cylindrical hole, and smooth edges around the tip. The entire setup of this droplet generator was made in-house with assistance from Auburn University glass (Sandlin, W. and Montgomery, M.) and machine (Schwieker, B.) shops.

### 4.3.3. Droplet Generator – Mode of Operation

The droplet generator operates on the principle of reverse piezoelectric effect which causes the piezoelectric disc to mechanically vibrate on application of an electric voltage. As the piezoelectric disc vibrates, it produces pressure pulses inside the liquid reservoir that results in breaking the surface tension of the liquid meniscus near the tip of the glass nozzle to generate micron sized droplets. A 4011A BK Precision 5 MHz function generator supplies the frequency and voltage for the piezo disc. It can generate frequency levels from 0.5 Hz to 5 MHz with sine, square, and other waveforms. Digital display and provisions for coarse to fine tuning enables us to set the desired frequency conditions for the piezo disc. The maximum supply voltage of this function generator is 12 V. For voltages higher than 12 V, a Model 2340 TEGAM single channel high voltage amplifier was coupled with the function generator. It has a gain of 50 and can amplify any standard function, pulse or waveform from the function generator to a maximum of up to 400 Vp-p. The voltage and waveform type were monitored using a Model 2120B BK Precision 20 MHz oscilloscope to prevent the voltage supply to the piezo disc from exceeding its maximum threshold level. The electronics and the piezo disc were connected using BNC connectors and alligator clips. For the free-falling drop study, the droplet generator was mounted using a modified Edmund Optics optical stand. Liquid to the droplet generator was supplied through a 25 ml disposable Monoject plastic syringe which connects to the inlet tube by 1/16 inch silicone tubing.

### 4.3.4. Visualization System

The term visualization equipment in our research studies represents a combination of a high-speed camera and a high-magnification lens. For the free-falling droplet research work, three different high-speed cameras were used in combination with multiple high-magnification lenses. The combination of camera and lens were selected depending on the objective (liquid droplet) and optical limitations of our experimental setups. The PCO 1200hs manufactured by PCO-TECH Inc. was the primary high-speed camera used in our research. Figure 4-4 shows the photograph of PCO camera attached with a Nikon 105 mm lens.

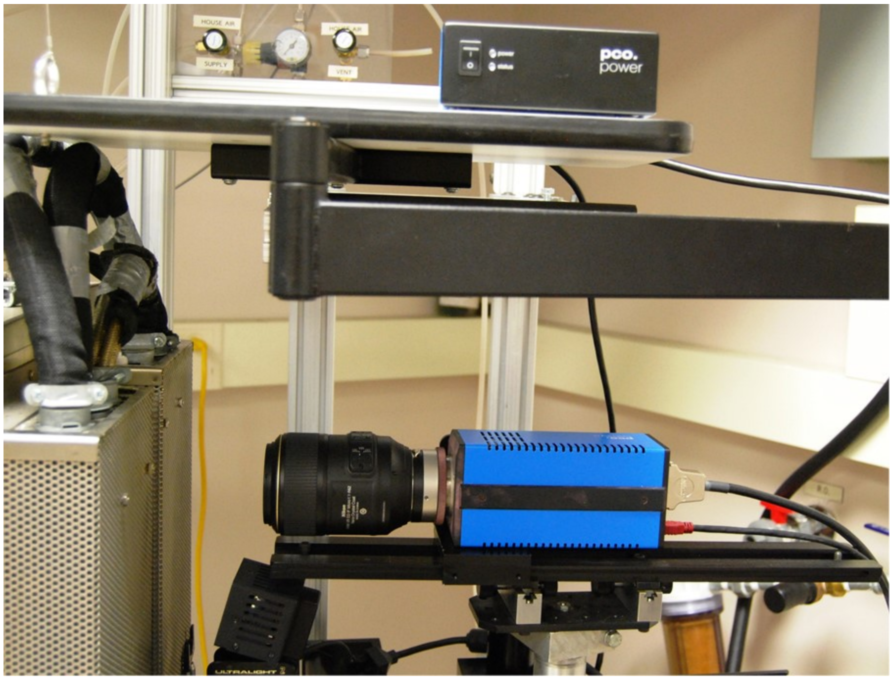

Figure 4-4: Photograph of the visualization system of PCO high-speed camera and Nikon 105 mm macro lens.

PCO1200hs is a 10-bit CMOS color camera system with a maximum resolution of 1280x1024 pixels. It can capture a maximum of 636 frames per second (fps) at full resolution and

1357 fps at VGA resolution. This camera has an IEEE1394 (firewire) interface and operates through the manufacturer's control application software Camware. Other high-speed cameras used in our research include a Guppy FO33 color camera by Allied Vision Technologies and a Cohu 2122 CCD monochrome camera. The Guppy camera can operate at a maximum of 60 fps in 656x494 pixel resolution, while the Cohu camera can operate at a maximum rate of 30 fps in 768x494 pixel resolution. Figure 4-5 and Figure 4-6 shows the photographs of the other camera-lens equipment combination used for our studies.

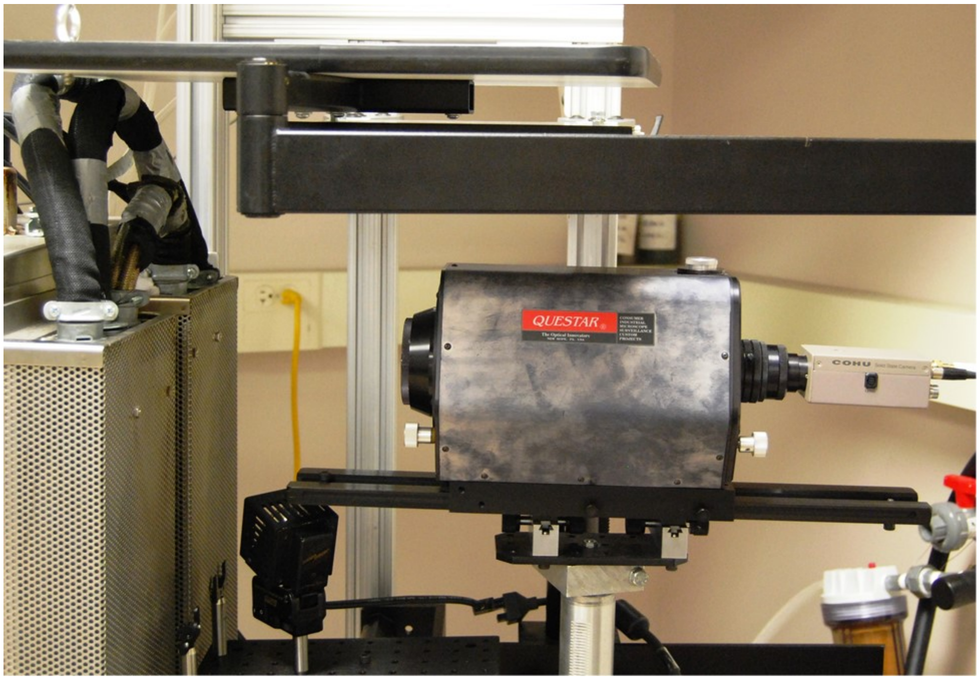

Figure 4-5: Photograph of the visualization system of Cohu camera and Questar long distance microscope lens.

The AF-S VR Micro-Nikkor 105 mm f/2.8G IF-ED (macro lens) manufactured by Nikon Inc. is the high-magnification lens used commonly in the free-falling droplet studies. This f-mount 105 mm lens has a minimum working distance of 31 cm which makes it convenient for visualizations in the drop tube furnace. A photograph of this lens along with the PCO camera is shown in Figure 4-4. The other lenses used include the 60 mm F/2.8D AF micro-Nikkor lens from

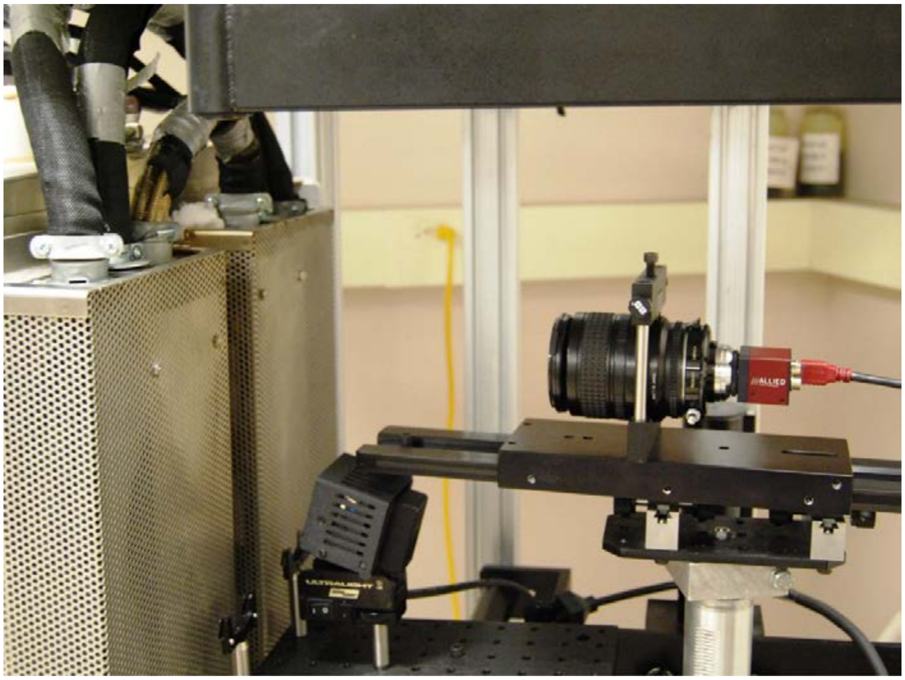

Figure 4-6: Photograph of the visualization system of Guppy camera and Nikon 60 mm lens.

Nikon Inc. and the QM 100 MK III long distance microscope lens from Questar Corporation. Photographs of the Nikon and Questar lenses are shown in Figure 4-5 and Figure 4-6. Among the lenses used, Questar has the maximum magnification of 0.90 µm/pixel followed by Nikon 105 mm, and the Nikon 60 mm lens.

In majority of the visualizations involving free-falling droplets, an external light source was required to illuminate the object. Much like the camera-lens combination, the light source also varies with respect to the objective of the study and optical limitations of the setup. Photograph of the lighting equipment (strobe and halogen bulb) and diffuser are shown in Figure 4-7. Nova Strobe DA Plus by Monarch Instrument with an average light power of 15 W and Ultralight 2 tungsten-halogen bulbs from Anton Bauer with 75 W light power are the two primary external light sources for this research. The lights were used as both front-lit and back-lit illumination options as per our requirements. A 20 x 20 cm semi-transparent ground glass was used for the experiments as a light diffuser.

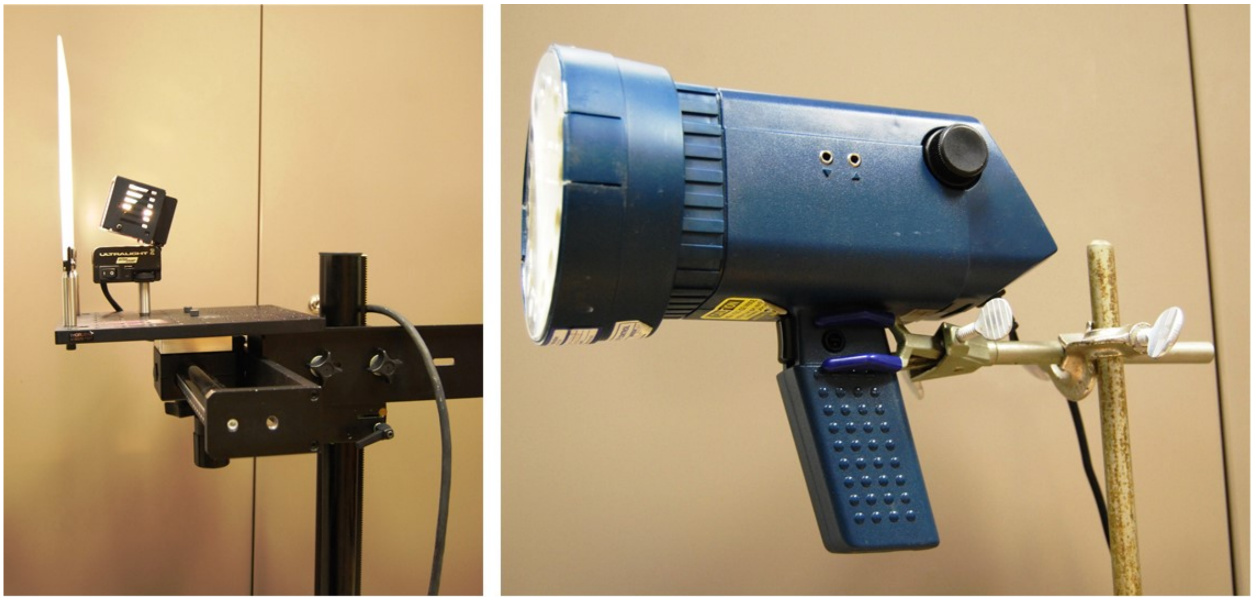

Figure 4-7: Photograph of the external lighting sources used for illumination, Tungsten-Halogen lamp coupled with a light diffuser (left) and strobe light (right).

### 4.3.5. Image Capture and Processing

The visualization images captured for the research studies in the drop tube furnace mainly used the high-speed Guppy and PCO cameras. The Guppy FO33 color camera is operated through AVT SmartView software interface. The destination folder and the image capture rate were predefined for each visualization. The images were recorded in the default .bmp format. The PCO1200hs camera as mentioned before operates through the PCO Camware. Unlike the Guppy, the PCO camera captures the objective as image sequences in .tif format. These video recordings can then be saved either for the entire period of recording or only for a specified timeframe. The Camware software also provides an option to export the recording sequence into image sequences in various image formats such as *.bmp*, *.jpg*, *.avi*, *.wmv*, etc. We generally exported the video recordings to *.bmp* format image sequences that can be used later for qualitative and quantitative image analysis. Before recording with the PCO camera, the horizontal and vertical fields of view were manually adjusted with respect to our objective to obtain the desired frame rate and a reduced image size. ImageJ, Microsoft Visual Studio 6.0, GIMP, and Quicktime were the image processing tools used in our research work. ImageJ is useful for calculation of droplet area, droplet velocity, and droplet trajectory. Visual Studio is useful if droplet diameter calculations were to be performed in series of images. For using the visual studio tool, the images obtained should have a high contrast difference with the background permitting automatic droplet boundary detection. Quicktime/GIMP was useful in recreating the video recordings from the image sequences in *.mov*, *.mpeg*, or *.gif* formats for display purposes.

## 4.4. Droplet Generation Studies

A reliable and robust droplet generator capable of producing on-demand microdroplets is of paramount importance to successfully perform the free-falling droplet studies inside the drop tube furnace. Consequently, the custom made piezoelectric droplet generator was studied systematically to determine the optimum control parameters for consistent microdroplet generation.

### 4.4.1. Choice of Liquid

Results from a systematic study of droplet generation for several liquids were presented in detail in the work of Giles (2013). Studies with the droplet generator includes tests on liquid types of varying physical properties for successful microdroplet generation. Distilled water and 91% isopropyl alcohol were chosen initially as they were commonly available laboratory liquids. Distilled water has a low viscosity and high surface tension value whereas isopropyl alcohol has both low viscosity and surface tension. Subsequently, the droplet generator was tested with liquid types that are of interest to our research study which includes various aqueous glycerin solutions (50, 60, 70, and 98% aqueous glycerin), standard fuels (2.2.4 trimethyl pentane and hexadecane), and aviation liquid (BP Turbo oil 274). All the liquid types that were tested along with their respective physical properties are listed in Table 4-1.

Motivation for testing different liquid types is to a) examine the versatility of the droplet generator, b) troubleshoot the piezoelectric setup before mounting for furnace operation, and c) determine the optimum parameters for controlling the microdroplet generation. Throughout the microdroplet generation studies section, the term ‘operating condition’ involving the droplet generator refers to the collective of voltage supplied to the piezoelectric disc, the drive frequency through function generator, and the liquid flowrate set using syringe pump. Similarly, the term ‘imaging setup’ refers to the collective of camera-lens combination, operating frames per second (fps), and the external light source used for capturing droplet images.

Table 4-1: Viscosity and surface tension properties of test liquids used in droplet generation.

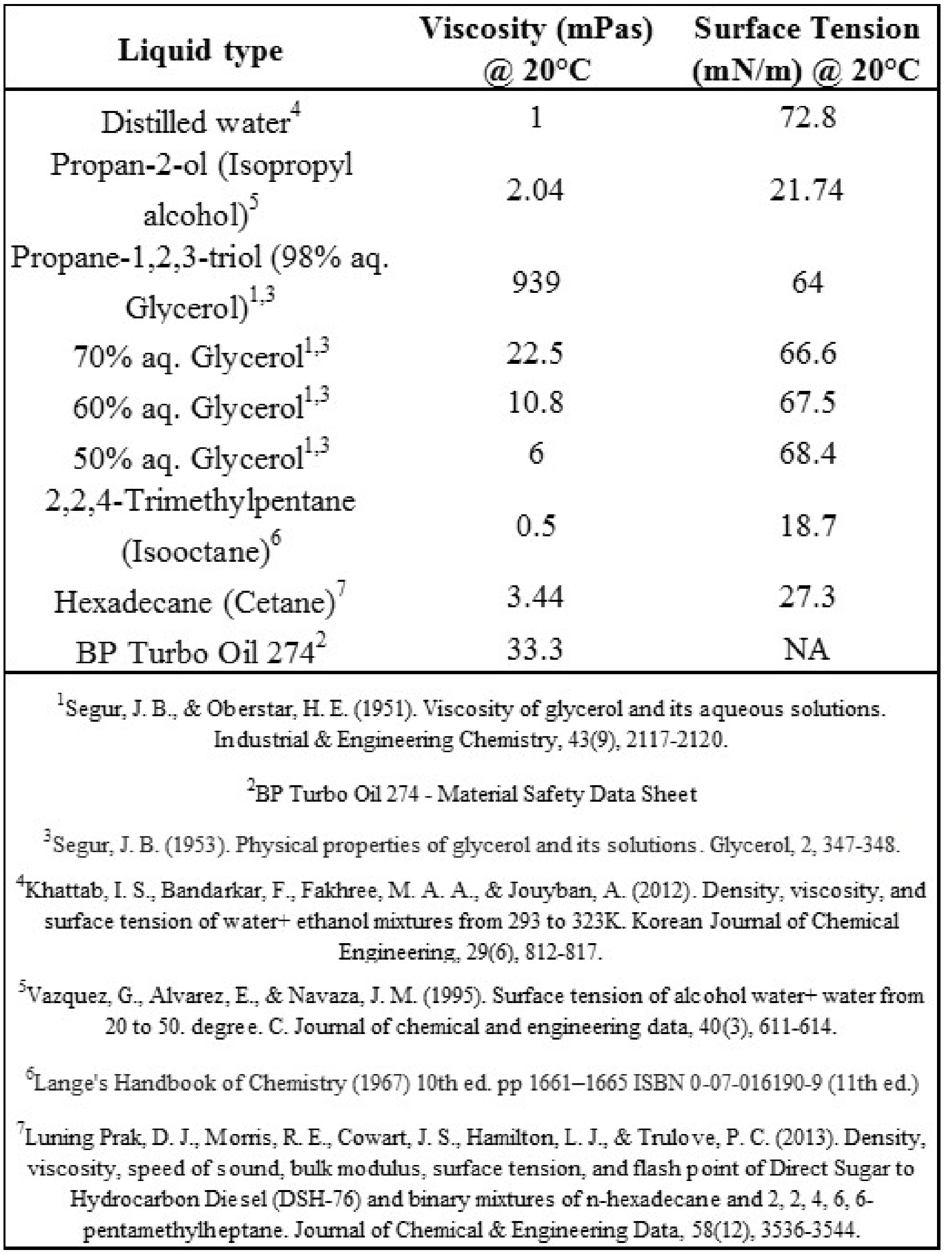

| Liquid type | Viscosity (mPas) @ 20°C | Surface Tension (mN/m) @ 20°C |
|---|---|---|
| Distilled water[4] | 1 | 72.8 |
| Propan-2-ol (Isopropyl alcohol)[5] | 2.04 | 21.74 |
| Propane-1,2,3-triol (98% aq. Glycerol)[1,3] | 939 | 64 |
| 70% aq. Glycerol[1,3] | 22.5 | 66.6 |
| 60% aq. Glycerol[1,3] | 10.8 | 67.5 |
| 50% aq. Glycerol[1,3] | 6 | 68.4 |
| 2,2,4-Trimethylpentane (Isooctane)[6] | 0.5 | 18.7 |
| Hexadecane (Cetane)[7] | 3.44 | 27.3 |
| BP Turbo Oil 274[2] | 33.3 | NA |

[1] Segur, J. B., & Oberstar, H. E. (1951). Viscosity of glycerol and its aqueous solutions. Industrial & Engineering Chemistry, 43(9), 2117-2120.

[2] BP Turbo Oil 274 - Material Safety Data Sheet

[3] Segur, J. B. (1953). Physical properties of glycerol and its solutions. Glycerol, 2, 347-348.

[4] Khattab, I. S., Bandarkar, F., Fakhree, M. A. A., & Jouyban, A. (2012). Density, viscosity, and surface tension of water+ ethanol mixtures from 293 to 323K. Korean Journal of Chemical Engineering, 29(6), 812-817.

[5] Vazquez, G., Alvarez, E., & Navaza, J. M. (1995). Surface tension of alcohol water+ water from 20 to 50. degree. C. Journal of chemical and engineering data, 40(3), 611-614.

[6] Lange's Handbook of Chemistry (1967) 10th ed. pp 1661–1665 ISBN 0-07-016190-9 (11th ed.)

[7] Luning Prak, D. J., Morris, R. E., Cowart, J. S., Hamilton, L. J., & Trulove, P. C. (2013). Density, viscosity, speed of sound, bulk modulus, surface tension, and flash point of Direct Sugar to Hydrocarbon Diesel (DSH-76) and binary mixtures of n-hexadecane and 2, 2, 4, 6, 6-pentamethylheptane. Journal of Chemical & Engineering Data, 58(12), 3536-3544.

### 4.4.2. Droplet Experiments

The operating conditions and imaging setup were optimized through a series of experiments with the droplet generator. Figure 4-8 demonstrates an example of improvement in imaging and droplet generation shown with the different droplet images of water and isopropyl alcohol. As can be seen in the figure, the droplet sizes early on were on the order of few thousand microns like those of pendant droplets (first image from left). Insufficient voltage applied to the piezoelectric disc caused liquid accumulation at the nozzle tip. Eventually the accumulated liquid portion overcomes the surface tension with the tip due to gravity resulting in pendant droplets.

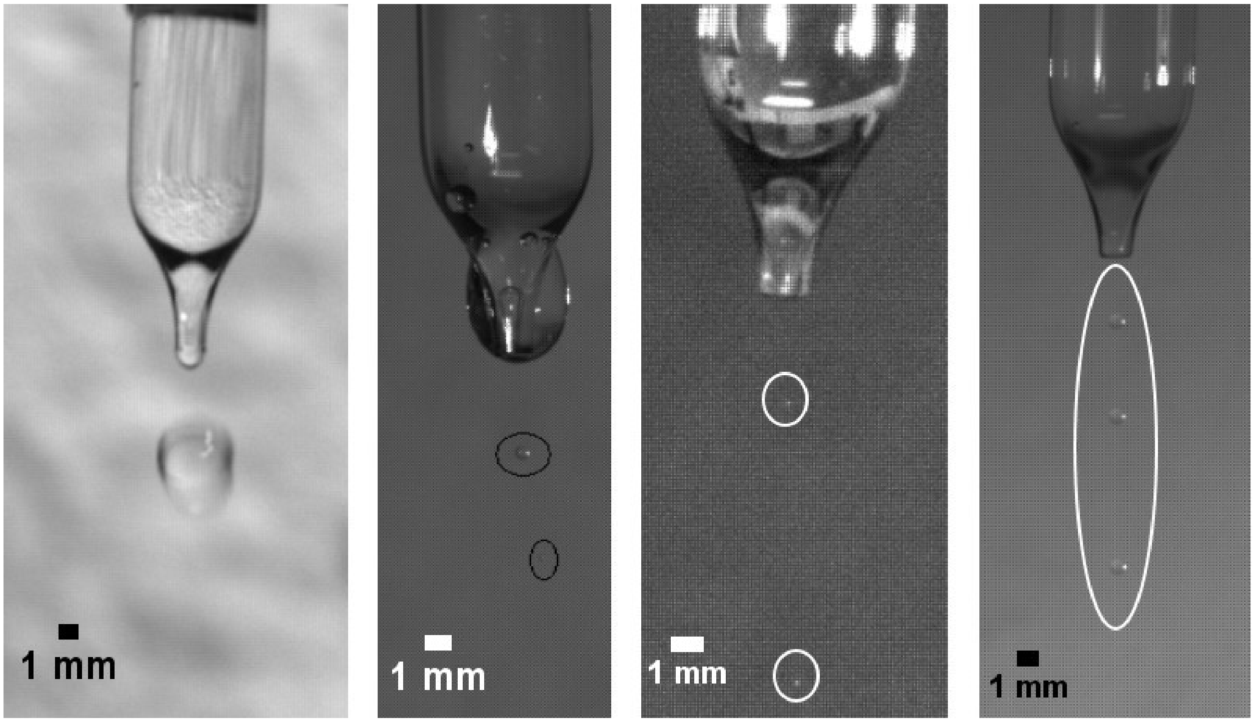

Figure 4-8: Piezo-electric droplet generation using distilled water (first, second, third from left) and isopropyl alcohol (fourth from left) liquid types.

The second image from left in Figure 4-8 shows a large pendant droplet attaching to the outer edge of the nozzle tip and the droplets generated being irregular in size with a non-vertical trajectory. This problem was first encountered when the operating condition (mainly drive voltage) was varied. Droplets could be generated with higher frequency; however, droplets also attach to the outer walls of the nozzle tip. This was found to be due to the positioning of the droplet generator using a clamp stand and due to nozzle imperfections as shown in Figure 4-9. Replacing the clamp stand holding the droplet generator with an optical base with E-arm, the frequency of pendant droplet growth on the nozzle tip was reduced considerably. The optimization of control parameters and imaging setup were evident in the other two droplet images (third from left and fourth from left) of Figure 4-8. The droplets generated were much more consistent in size and they had a vertical trajectory. Also in the two images, we could see the generated droplets being controlled in terms of spherical shape and diameter. For both water and isopropyl alcohol, the droplet sizes and spacing were found to be tunable to an extent by varying the voltage and frequency supplied to the piezo disc along with the liquid flowrate.

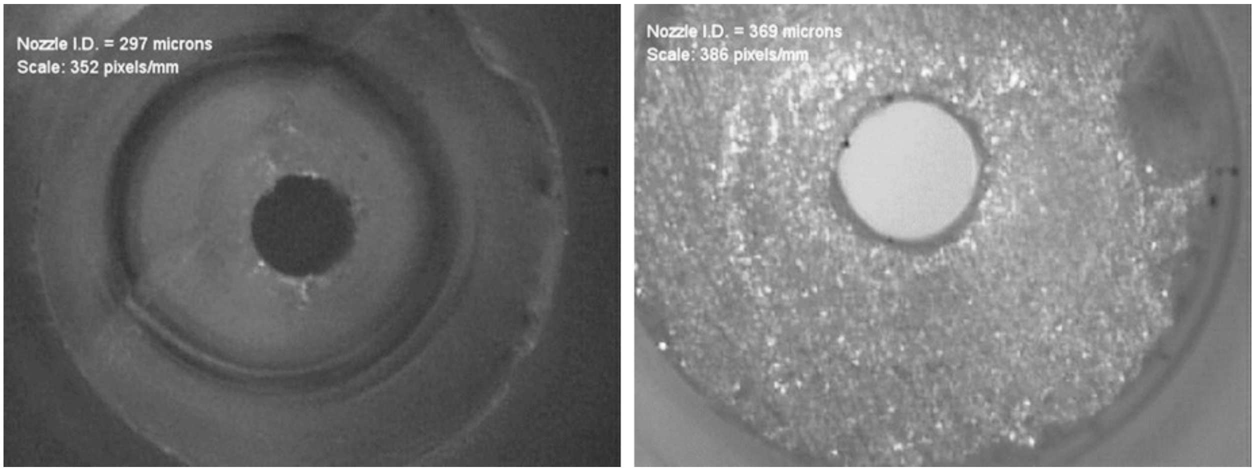

Figure 4-9: High magnification images showing nozzle imperfections.

A schematic diagram of the droplet generator setup with the imaging system is shown in Figure 4-10. Following experimental trials with various cameras and lens, the Nikon 105 mm lens with the PCO high speed camera was found to be the best combination for capturing droplet images. Both front-lit and back-lit imaging techniques were used. Backlit imaging using a pulsed light and light diffuser worked best among the two since it provided a contrast between the droplets and a smooth background. During the changeover from one type of liquid to another, the entire system of droplet generator from liquid inlet to nozzle tip was completely flushed with laboratory grade acetone. The volume of liquid in the droplet generator that includes the liquid reservoir and associated tubing connections is approximately 5 ml. While flushing, more than twice the amount of 5 ml was pumped through the setup to ensure complete removal of the existing liquid. Followed by acetone, the ¼ inch silicone tubing and droplet generator were flushed again with the test liquid.

The droplet generator was disassembled each time the test liquid was changed to inspect for damages in the piezoelectric disc, O-ring and the Teflon gasket. For successful droplet generation, the nozzle tip was wiped free of moisture using KimWipes before supplying the drive voltage.

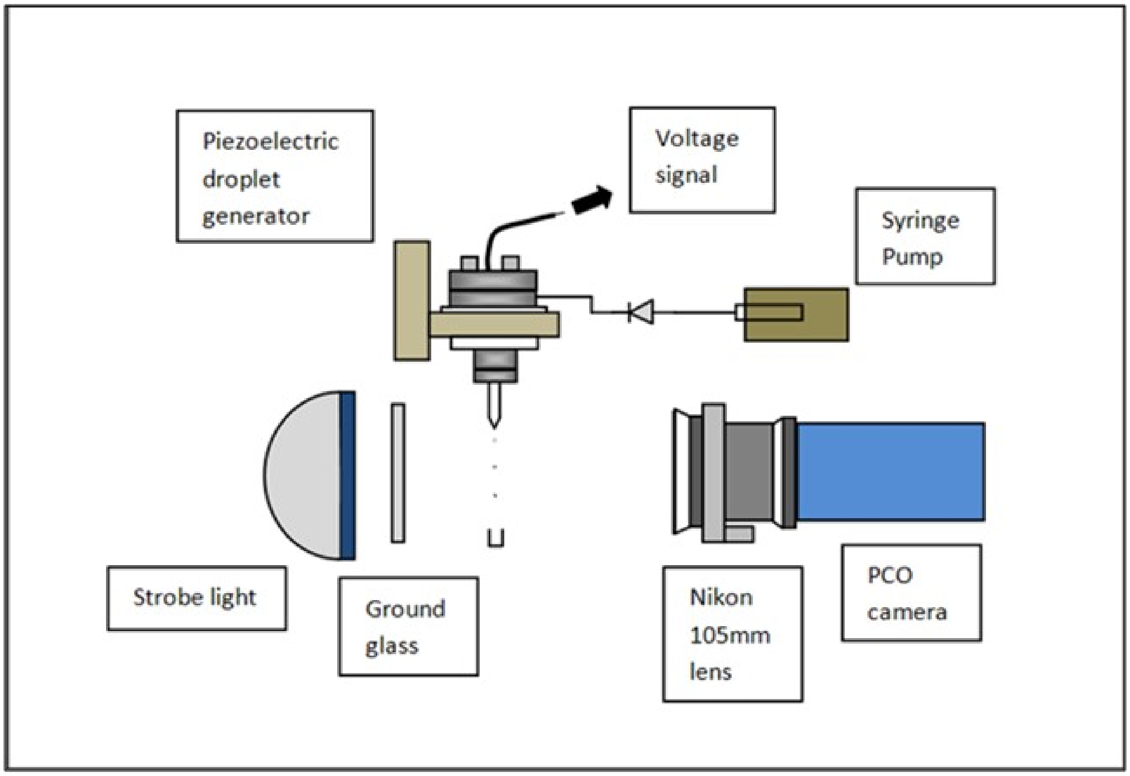

Figure 4-10: Schematic diagram of droplet generation with imaging setup.

#### 4.4.2.1. Aqueous Glycerol Solutions

Concentrated glycerol (98% aq.) was used in piezoelectric droplet generator as part of our alternative fuels study to test the capability of the droplet generator. Images of 98% glycerol droplets are shown in Figure 4-11. Evident from the images, the high viscosity of concentrated glycerol prevented effective generation of micron-sized droplets with this droplet generator. While operating below the piezoelectric disc's threshold voltage (maximum voltage limit for disc vibration without damage to the disc), the droplet generator produces pendant droplets close to 1000 µm as shown in Figure 4-11. To reduce the viscosity of conc. 98% aq. glycerol, we diluted with distilled water to prepare 50, 60 and 70% aqueous glycerol solutions. Droplet images of the aqueous solutions are shown in Figure 4-12. All three aqueous solutions behave in a similar manner with respect to mode of droplet generation and droplet diameters. As the water content in the glycerol was increased, the viscosity of the solution reduced considerably. Consequently, successful droplet generation was relatively easier by changing the operating conditions. The operating conditions includes drive voltage (25 - 50 V), drive frequency (3.5 hz) and liquid flow rate (10 µl/min). Among these, piezoelectric drive voltage was found to be the vital factor affecting the droplet size. Effect of drive voltage on droplet sizes are shown for 60% aq. glycerol, and 70% aq. glycerol in Figure 4-13, and Figure 4-14 respectively.

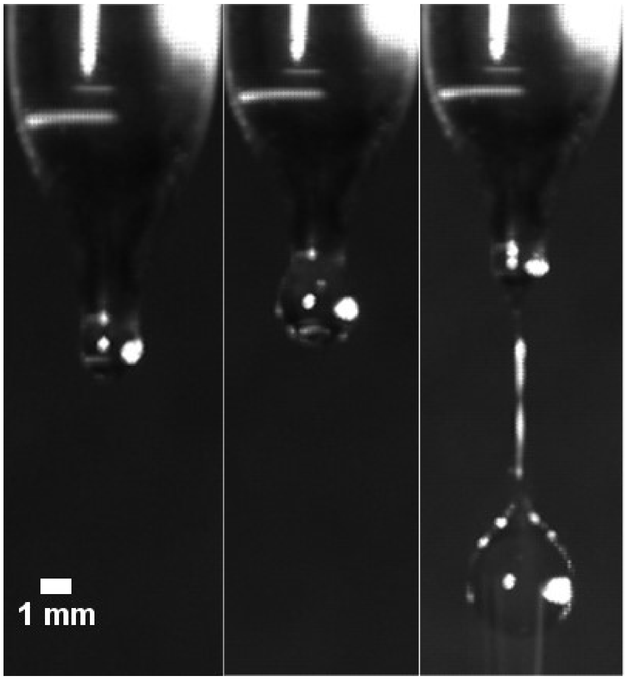

Figure 4-11: Image sequence (left to right) of 98% aqueous glycerol droplet generation.

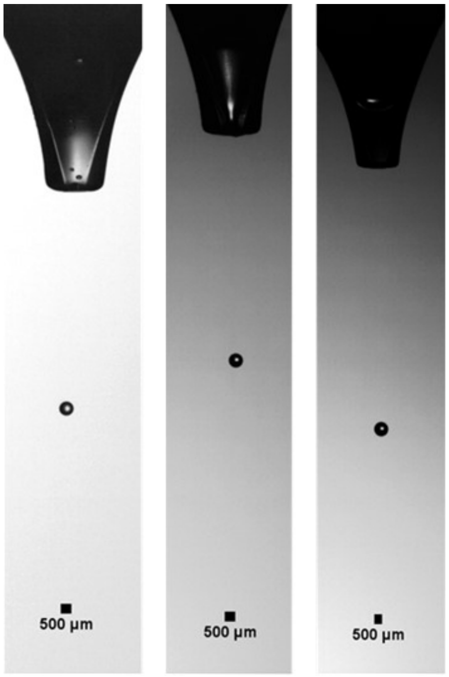

Figure 4-12: Droplet generation images of 50% aq. glycerol, 60% aq. glycerol, and 70% aq. glycerol liquids.

Figure 4-13: Effect of voltage on 60% aq. glycerol. Drive voltage and droplet sizes are (from left to right), 25 V, 260 µm; 37.5 V, 340 µm; 50 V, 400 µm; and 62.5 V, 345 µm.

Figure 4-14: Effect of voltage on 70% aq. glycerol. Piezo voltage and droplet sizes are (from left to right), 25V; 258µm, 37.5V; 346µm, 50V, 467 µm.

#### 4.4.2.2. Standard Fuels

Standard fuels 2,2,4 trimethylpentane (isooctane) and hexadecane (cetane) are liquid types selected as a reference for comparing the behavior of alternative fuels and aviation liquids. These two hydrocarbons form the basic component of gasoline and diesel products. Hexadecane has a cetane number of 100 while 2, 2, 4 trimethylpentane has an octane rating of 100. Figure 4-15 shows an image of hexadecane and 2,2,4-trimethylpentane droplets generated using the piezoelectric droplet generator. As we can see from Table 4-1, viscosity and surface tension properties of the standard fuels are lower than other test liquids. Consequently, lower drive voltages when compared to aqueous glycerol solutions, on the order of 10-12 V, were found to be sufficient for successful droplet generation.

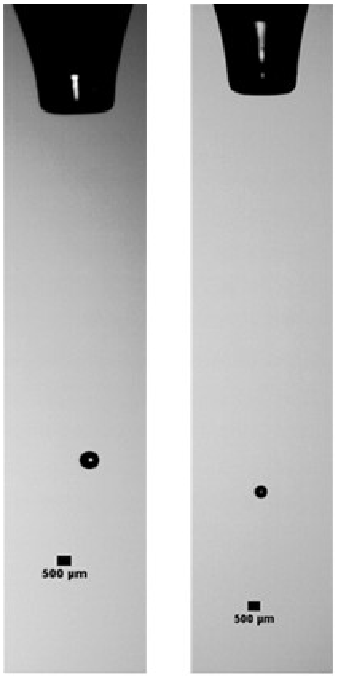

Figure 4-15: Hexadecane (left) and 2,2,4-trimethypentane (right) droplets generated using the droplet generator.

#### 4.4.2.3. BP Turbo Oil 274

BP Oil was selected as part of our degradation behavior studies of aviation liquids. As with other test liquids, the first part involves the feasibility to generate droplets of the liquid type with the piezoelectric droplet generator, and the second part involves the determination of operating conditions for consistent droplet generation. Figure 4-16 shows microdroplet generation of BP Turbo Oil 274 by the piezoelectric droplet generator.

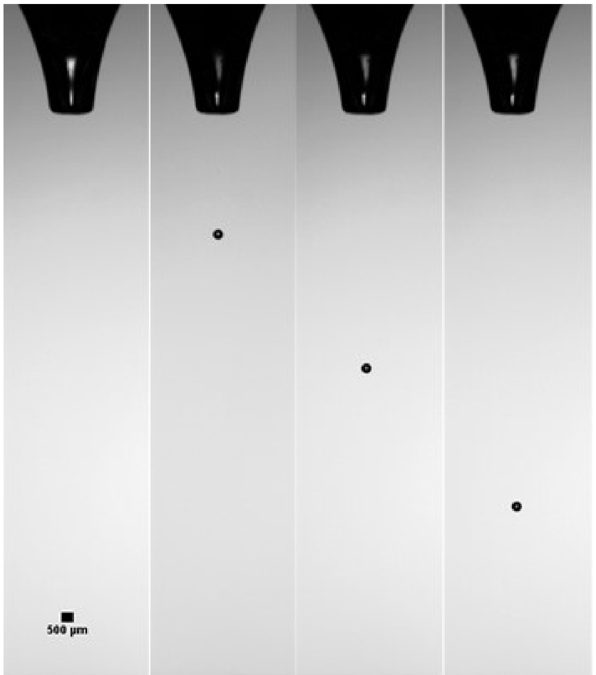

Figure 4-16: Image sequence of BP Turbo oil 274 droplet generation.

### 4.4.3. Influence of Drive Voltage

Influence of drive voltage on the size (droplet diameter) of the generated droplets was studied for 50, 60, and 70% aqueous glycerol solutions. High speed images were recorded for each test liquid under identical drive conditions by varying only the drive voltage. From the images, approximately 60 droplets were selected for calculating droplet diameter for each condition. Plot of average droplet diameter against drive the voltage is shown in Figure 4-17. From the plot, we see that the drive voltage can significantly influence the size of droplets generated. Droplets of consistent size, shape and spacing can be achieved for all test liquids through trial and error procedure, provided the droplet generation is feasible for the selected liquid type.

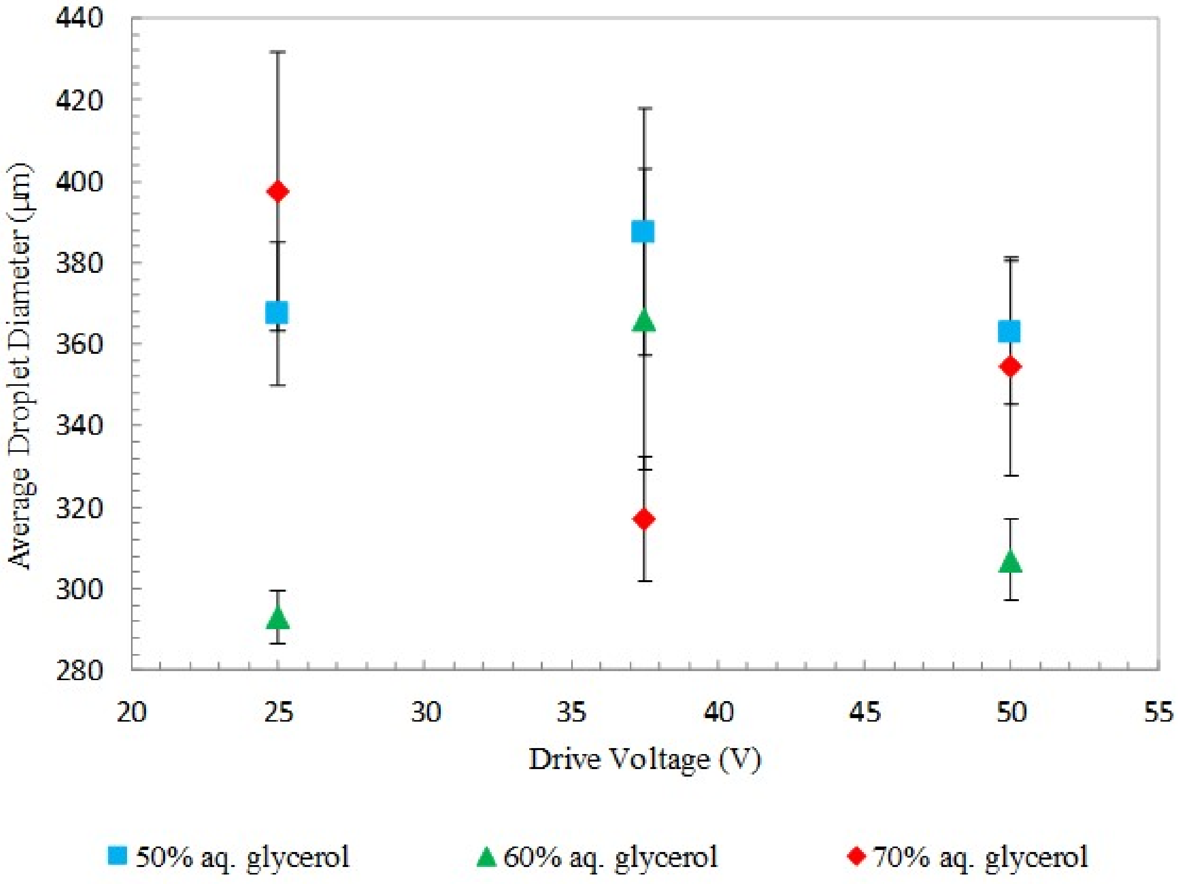

Figure 4-17: Influence of drive voltage on different aqueous glycerol solutions.

### 4.4.4. Summary

The piezoelectric droplet ejector described here was successfully constructed for stable droplet generation. From the visualization images of droplets shown thus far, it is evident that the droplet generator can produce near-spherical droplets for the liquid types of interest. The droplet diameters (350-750 µm) produced from the droplet generator are close to our desired droplet diameters around the 500 µm range. Also, the center-to-center droplet spacing was found to be large enough to avoid interactions between subsequently generated droplets. The droplet generator was cost-effective for our intended free-falling drop technique studies when compared to the commercially available droplet generators.

## 4.5. Observation and Results

Free-falling drop studies were performed by mounting the piezoelectric droplet generator on top of the drop tube furnace. Droplets are generated, pass through a water-cooled injection nozzle, and enter the glass retort of the heated furnace. The test liquids included, 2,2,4-trimethylpentane (isooctane), hexadecane (cetane), and aviation liquid BP turbo oil 274 (BP Oil). The temperature inside the furnace was varied from 500°C to 900°C, and was preset before the droplet of the test liquid entered the furnace. All our free-falling droplet visualizations were restricted to only the top observation window of the furnace. Figure 4-18 shows the two commonly used visualizing position schematics for this study. In the visualization position P1, we image the droplets using a front-lit illumination technique. In such illumination, the light from the lamp hits the surface of the droplet facing the camera, and the reflected light from the droplet was captured in the image as a bright spot against a dark background. In the visualization position P2, a back-lit illumination technique was used. Here, a beam of light projects from the lamp placed directly behind the droplet to provide a good contrast against a bright background. Both the visualization positions P1 and P2 are capable of imaging droplets between 0 to 23 cm from the bottom portion of the water-cooled injection nozzle.

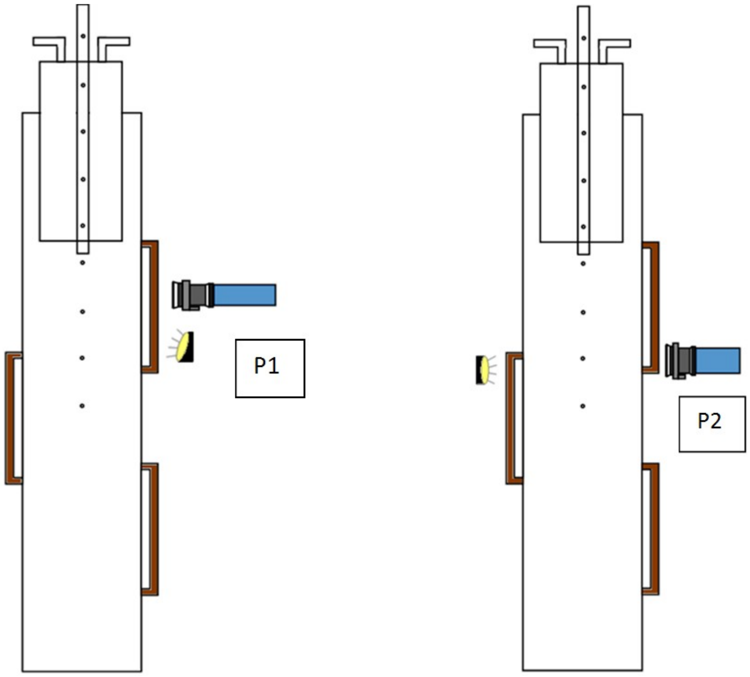

Figure 4-18: Schematic of the visualization positions P1 (left) and P2 (right) used in the free-falling droplet study.

### 4.5.1. Standard Fuel

Free falling droplet studies with 2,2,4-Trimethylpentane (isooctane) were performed at 500, 550, 600, 650 and 700°C furnace temperatures. Visualization image sequences in position P1 at 650°C and 700°C are shown in Figure 4-19 and Figure 4-20. To best describe the droplet behavior inside the drop tube furnace, visualization image sequences shown here contain representative images that are selected and displayed at a different frame per second (fps) rate than the original recording.

Visualization images from Figure 4-19 suggests that the 2,2,4-Trimethylpentane droplets fall through the 650°C, 20.9% oxygen rich atmosphere without any appreciable change in the droplet diameter. In our experiments, the droplets were not always spherical, and hence the term droplet diameter refers to the diameter of a sphere of equivalent area. The images also show no flames around the droplet surface. For a droplet such as isooctane, operating conditions of the experiment suggests a combustion behavior but the results are not as expected. We believe this is due to the inability of the droplet to heat to its auto ignition temperature before it departs the visualization region. In the visualizations of Figure 4-20, we observed the isooctane droplets disappearing within the elapsed time. Our understanding is that the droplet undergoes vaporization at the furnace condition of 700°C.

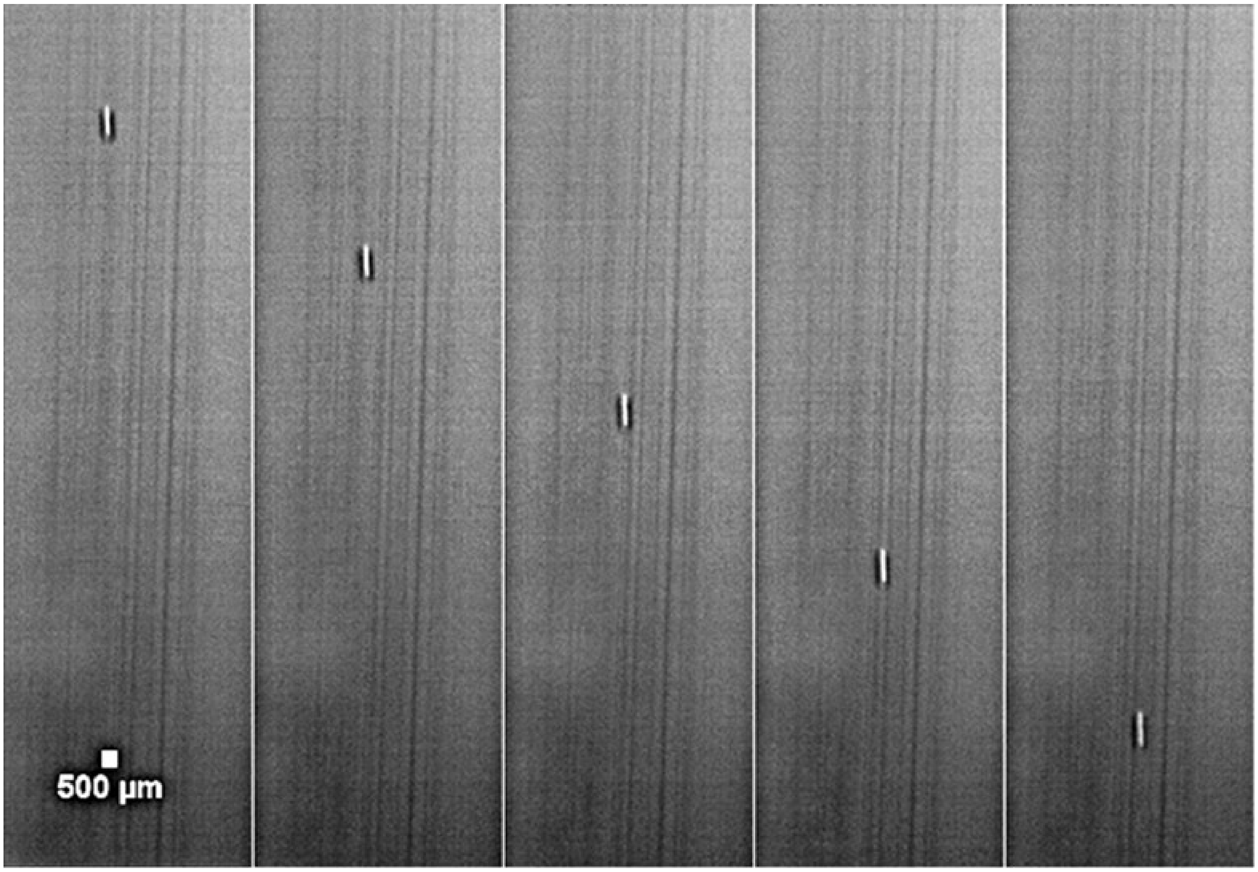

Figure 4-19: Free falling droplet behavior of 2,2,4-trimethylpentane at 650°C captured at 500 fps and displayed at 100 fps (left to right).

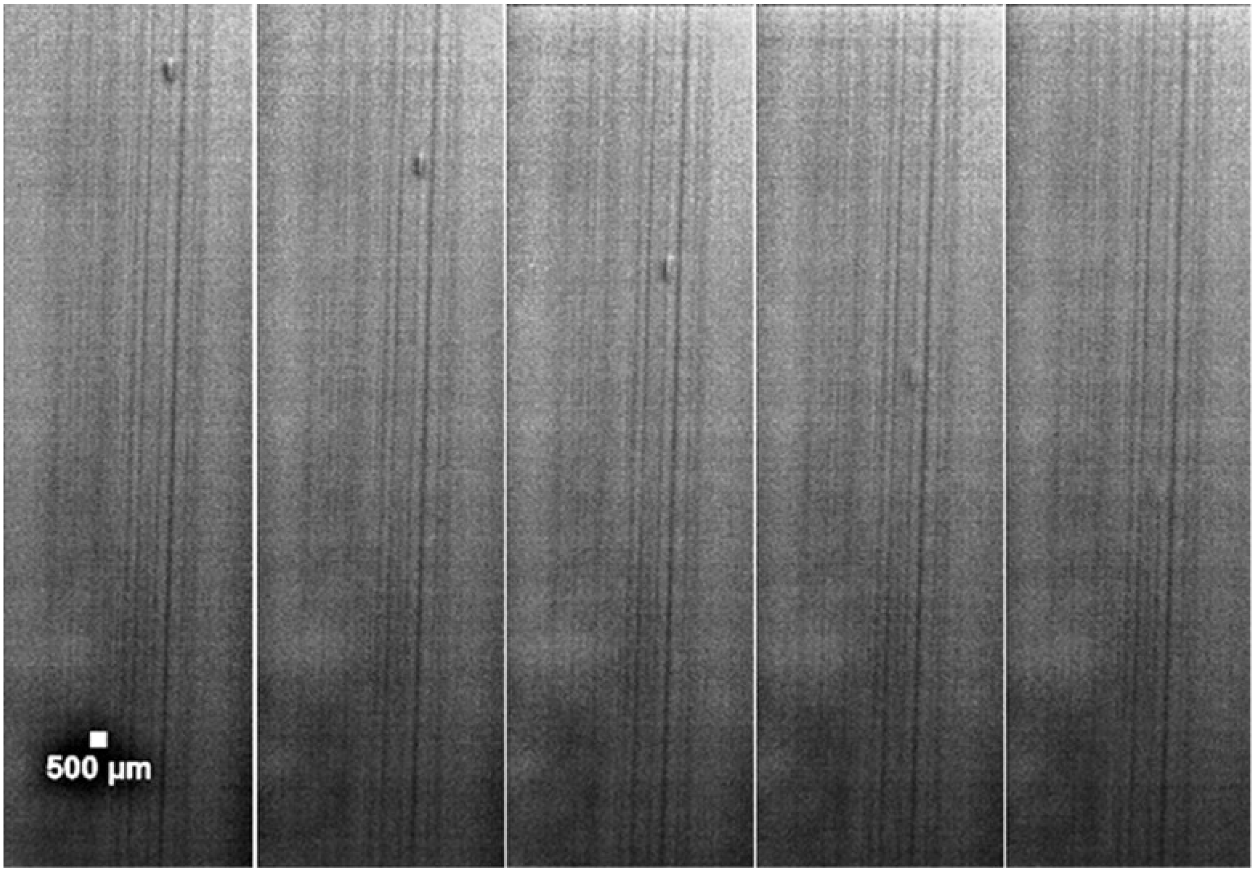

Figure 4-20: Free falling droplet behavior of 2,2,4-trimethypentane at 700°C captured at 500 fps and displayed at 100 fps (left to right).

Free-falling droplet studies of hexadecane are like that of 2,2,4-Trimethylpentane in terms of experimental procedure. Furnace temperatures of 500, 600, 700, 750 and 800°C were selected for the droplet experiments. Figure 4-21 and Figure 4-22 shows the free-falling hexadecane droplet at 750°C with two different conditions of incoming air flowrate. Visualization image sequences for conditions not discussed in this section are shown in appendix B. From Figure 4-21, we observe the hexadecane droplet to be falling without an appreciable change of its shape or size. This droplet behavior is reminiscent of the 2,2,4-trimethyl pentane shown earlier in this section. However, when the incoming flowrate of air inside the furnace was decreased, the free-falling droplets were observed undergoing combustion, evident by flames seen in the image sequence of Figure 4-22. We understand this change in droplet behavior from vaporization to combustion could be a function of the incoming air flowrate. Decreasing the air flowrate results in a local change in atmospheric temperature and oxygen concentrations surrounding the droplet surface. This could have enabled the droplet to reach its auto-ignition temperature (447°C) at a faster rate, and subsequently undergo combustion in our region of interest (ROI). The visualization in Figure 4-22 were captured using the light emitted due to combustion, unlike those of Figure 4-21, where an external illumination source was used. The illumination source potentially masking the combustion flames in Figure 4-21 cannot be completely ruled out.

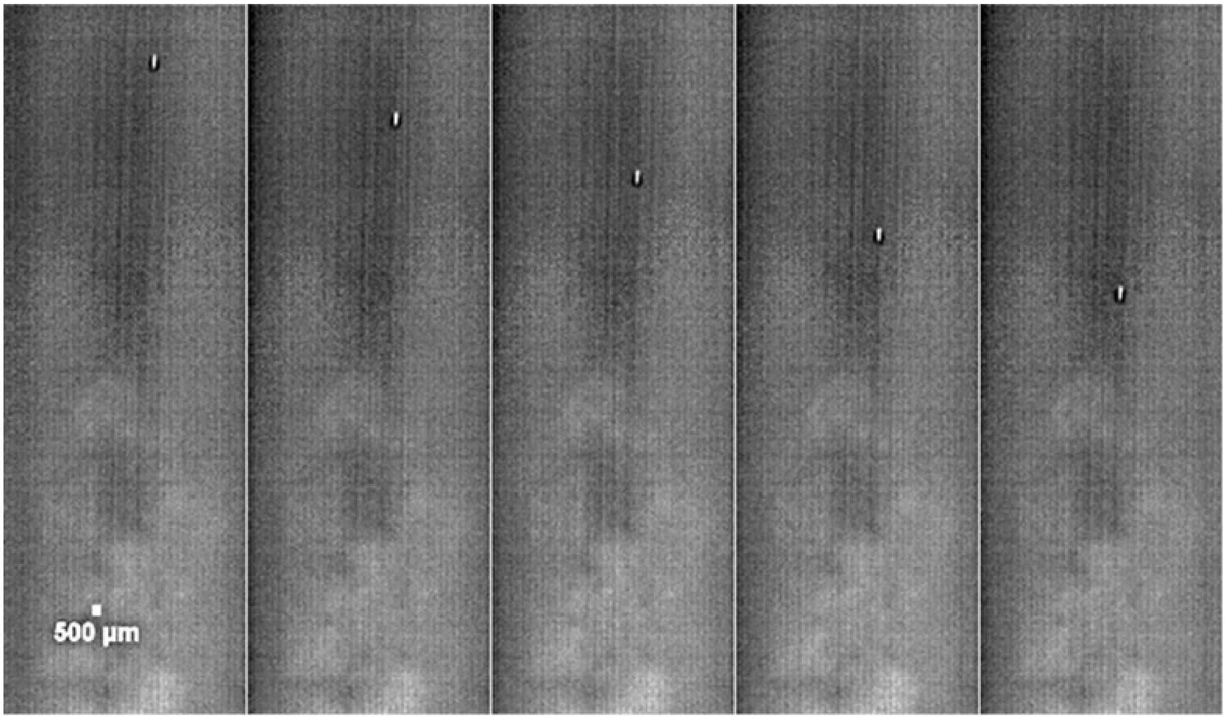

Figure 4-21: Free falling droplets of hexadecane at 750°C (left to right) captured at 1950 fps and displayed at 390 fps.

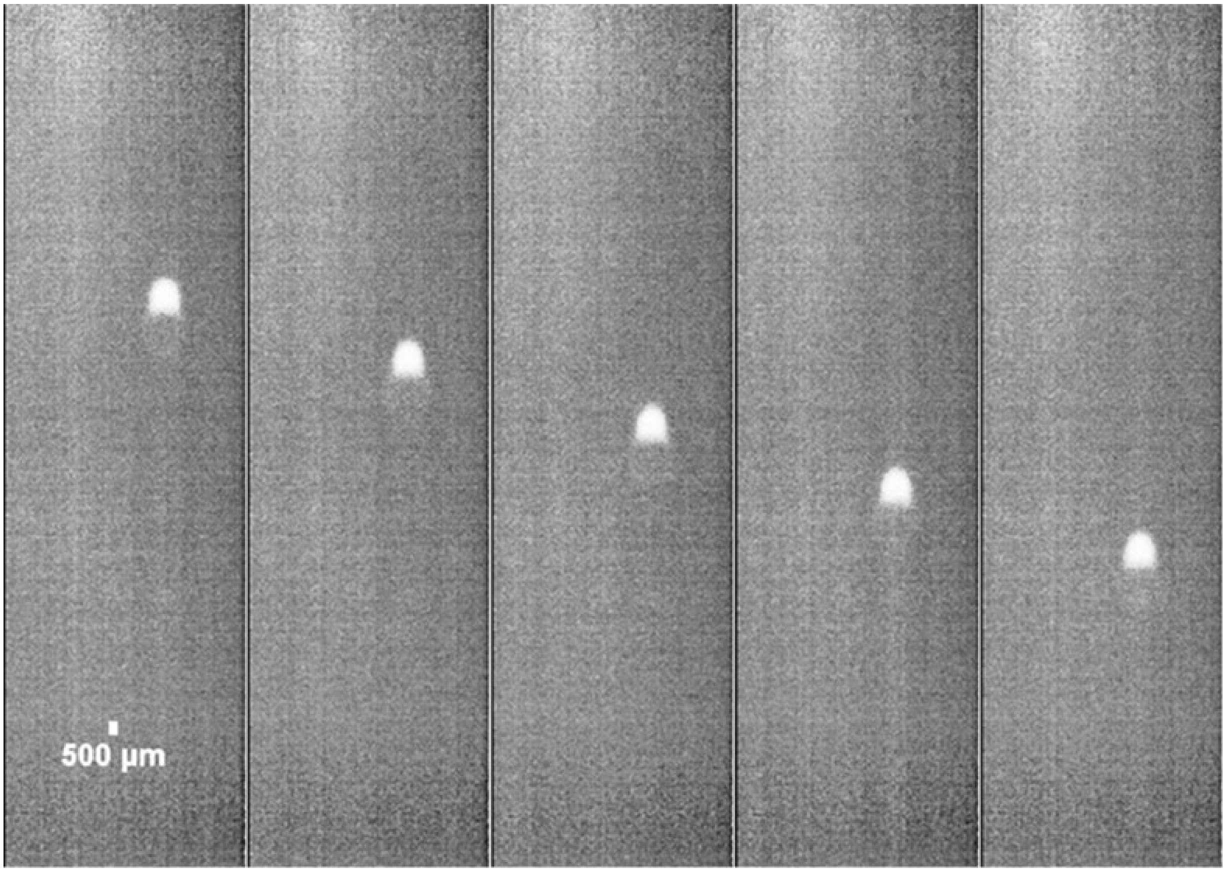

Figure 4-22: Free falling droplets of hexadecane at 750°C captured at 1950 fps and displayed at 390 fps (left to right).

### 4.5.2. Aviation Liquid

Free falling droplet studies of BP turbo oil 274 (BP Oil) were conducted in 500, 600, 700, 800 and 900°C temperature conditions. Figure 4-23 and Figure 4-24 shows the thermal degradation behavior of the oil droplet at 800 and 900°C respectively. For both the visualizations, the backlit illumination technique and visualization position P2 was used to acquire a higher frame rate. Free-falling droplet behavior observed in both the image sequences appear to be identical. As the droplet falls through the hot atmosphere, it gets heated and breaks into multiple fragments. Subsequently, these droplet fragments disappear from the field of view suggesting either a vaporization or combustion behavior. Evidence from flames surrounding the droplets as shown in the image sequence of Figure 4-24 suggests that the droplet undergoes combustion.

## 4.6. Discussion

### 4.6.1. Development of Microdroplet Generator

A piezoelectric droplet generator was constructed for generating micron sized droplets of the liquids of interest. The droplet generator was shown to successfully produce microdroplets of 300-700 µm for test liquids of varying viscosities and surface tensions. Optimum control parameters of drive frequency, pulse width, and drive voltage for consistent microdroplet generation were determined by trial and error procedure for the test liquids. Visualizations show the generation of droplets of consistent size, trajectory, and droplet spacing (center-to-center droplet spacing between two subsequent droplets) for the test liquids. The droplet generator was also tested for its suitability to be mounted with the existing drop tube furnace setup. A glass model of the injection nozzle port was used to determine the percentage of droplets that pass through the nozzle with a vertical trajectory without contacting the wall. We found over 90% of the droplet generated to make it through the glass model without contact, suggesting a good vertical trajectory for the generated droplets.

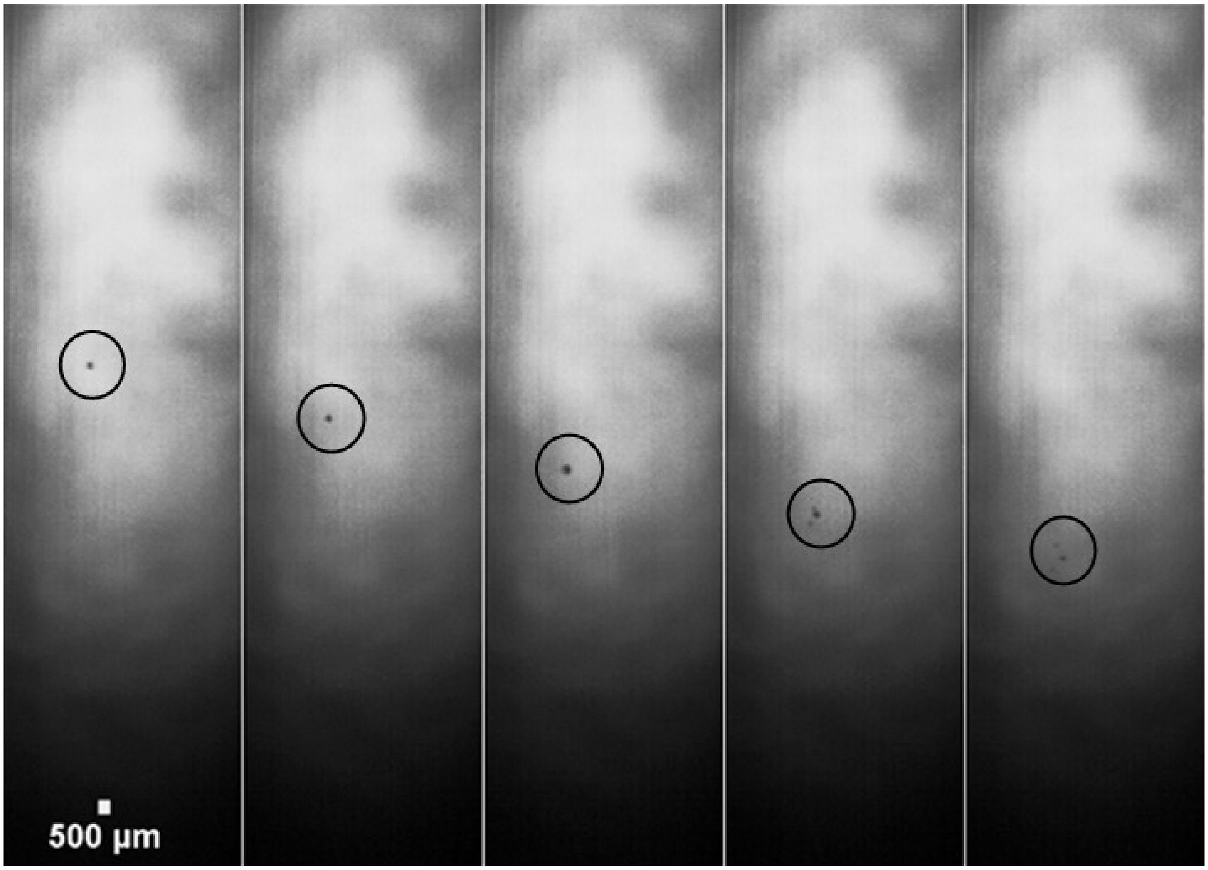

Figure 4-23: Free-falling droplets of BP Oil at 800°C captured at 2620 fps and displayed at 262 fps (left to right).

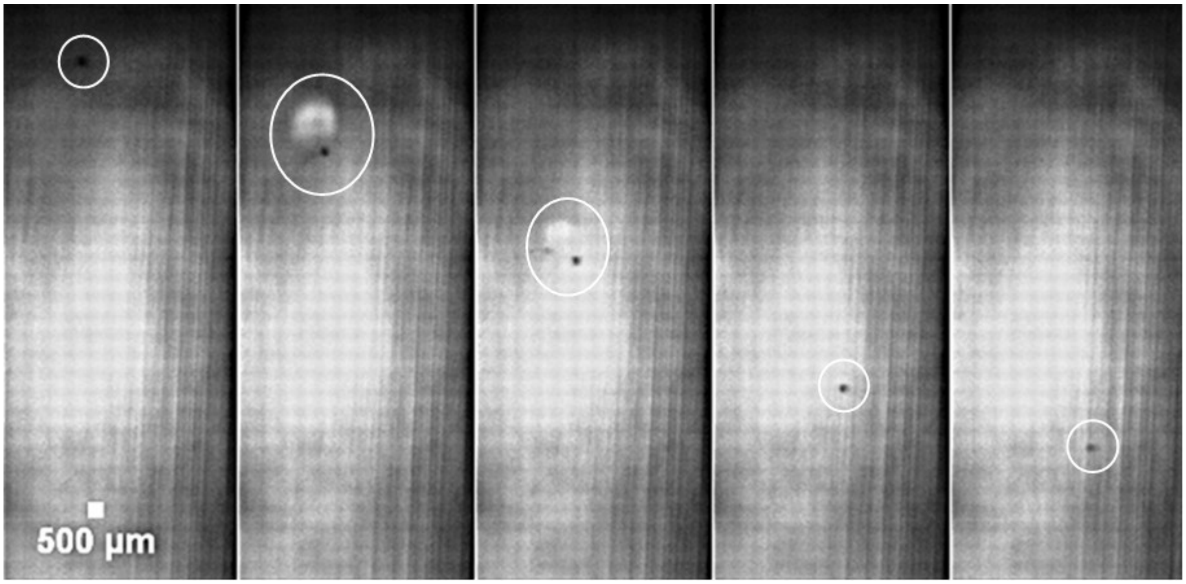

Figure 4-24: Free-falling droplets of BP Oil at 900°C captured at 2620 fps and displayed at 262 fps (left to right).

### 4.6.2. Redesigned Injection Nozzle and Visualization Technique

The existing drop tube furnace injection nozzle from solid fuels research was successfully replaced with a newly designed nozzle suitable for testing liquids. The new nozzle design consisted of a wider injection port to accommodate minor variations in the vertical trajectory of the droplets. The redesigned nozzle was equipped with separate gas flow ports in addition to the injection port, for preventing the contact of gas flow with the droplets before entering the furnace. The ends of the gas flow ports were designed such that the gas flow irrespective of the flowrate did not directly interfere with the trajectory of free-falling droplets. The design of the new nozzle maintains the external dimensions as before such that it fits into the existing drop tube flanges that attaches the nozzle to the furnace.

The PCO high-speed camera was assessed for its visualization capability along with Nikon 105 mm lens, and Questar high magnification lens. Several trial and error experiments were performed with respect to mounting, lighting, magnification, and working distances to achieve the best possible visualization of the objective (free-falling droplets). Overall, we found the back-lit illumination technique using strobe and diffuser (etched glass) worked well, as it provided a better contrast of the droplet and the background. The high-magnification Questar lens was found to require excessive external light to permit high fps recordings. Halogen lamps provided sufficient light to support these recordings albeit at the cost of a reduced field of view. Software such as ImageJ, Visual Studio, and Matlab have all been explored as post processing image options and found ImageJ to be the best suited for our studies.

### 4.6.3. Free-Falling Droplet Study in the Drop Tube Furnace

The primary objective of this study has been to construct a drop tube furnace setup to study the droplet behavior using the free-falling droplet technique. Until now, feasibility studies have been performed for this technique, and the results obtained are shown in the previous section. Visualizations showing the thermal behavior of multiple test liquids successfully demonstrate our ability to obtain results with this experimental setup. Results have shown some of the test fluids at selective operating conditions which included furnace temperature, gas composition, and incoming air flowrate. The experimental setup built for this study can control the droplet surrounding temperature and composition from 100 - 900°C and 0 – 21% oxygen content, respectively. The incoming air flowrate is adjustable to provide laminar or turbulent flow environments and to control the droplet visualizations between the three observation windows.

The quality of the images obtained thus far has the capability for performing quantitative image analysis to obtain temporal change in the droplet diameter and droplet velocity. This data can be used further to calculate droplet lifetime (Wornat et al., 1994), establish $d^2$-law, and determine the burning or evaporation rate constant of the test liquid at the selected operating condition (Wang et al., 1984). We have also shown observations of vaporization, ignition delay, combustion and microexplosion in the droplet visualizations of the standard fuels (isooctane and cetane) and aviation liquid (BP Oil). If systematic studies were to be performed, visualization images are of the quality and resolution such that qualitative analysis of the significant behavior events could be extended for other liquid types and operating conditions. The capability of the experimental setup to obtain visualization at various distances (visualization positions P1and P2) will also be useful in studying the free-falling droplets at multiple residence times after exposure to the furnace environment. Overall, the experimental results shown serves as a proof of method to study the behavior of the droplets with a drop tube furnace experimental setup.

# 5. Proof of Method Experiments to Study Suspended Droplet Behavior Using Graphite Fiber in Drop Tube Furnace

## 5.1. Literature Review

Given the complexities in performing the free-falling droplet experiments, droplet behavior was widely studied by suspending the droplets. The technique of suspending a single droplet using quartz fiber or from a fine thermocouple wire support is a common approach to investigate the evaporation characteristics in emulsified fuel droplets and biomass oils. Kimura et al. (1986) investigated combustion behaviors of emulsified fuel droplets suspended from a copper wire to reveal the effect of gravity on secondary atomization. Calabria et al. (2007) observed the swelling and microexplosion phenomenon in suspended emulsion droplets of pyrolysis oil based fuels which helped understand the fundamentals of combustion in these fuels. Segawa et al. (2000), investigated combustion processes and microexplosions of oil-in-water emulsified fuel droplets suspended from a quartz fiber under micro-gravity, and measured droplet temperature using a Pt-13%Rh/Pt wire. Watanabe et al. (2009) investigated the characteristics of carbonated emulsified fuel droplets suspended from a wire.

Regarding studies with biomass oils, D'Alessio et al. (1998) used suspended droplet technique for thermo-optic investigation of evaporation and combustion in biomass pyrolysis oils derived from multiple feedstock such as hardwood, pine and poplar. Ikegami et al. (2003) studied heavy and light fuel oils under microgravity and normal gravity conditions to show distinctive burning stages between droplet ignition and extinction, suggesting a distillation like mechanism dominating the burning process. Hallett and Clark (2006) devised a numerical model of the evaporation of a single droplet of pyrolysis oil derived from biomass, and verified the thermodynamics with experimental results obtained using the suspended droplet method. Harada et al. (2011) conducted numerical simulation studies on n-dodecane using this technique to establish the relation between the thermocouple used for suspension and evaporation characteristics of the liquid. Recent literary works of Ma et al. (2015) on the evaporation characteristics of acetone-butanol-ethanol and diesel blends at high ambient temperature; and Setyawan et al. (2016) on the comparative studies involving crude glycerol, traditional, and alternative fuels shows that the experimental technique continues to evolve. Results from these literary works in the last few years on the evaporation and combustion characteristics using visualization techniques for several alternative fuels shows the continues importance for understanding individual droplet behavior.

The suspended droplet experimental techniques are comparatively easy to set up and perform. Ignition is usually achieved by a single pulse of a continuous spark discharge. Furthermore, since the droplet is stationary under normal gravity and in some cases under microgravity conditions, detailed visualizations can be obtained of its burning sequence. Limitations of this technique are due to the thickness of the suspension fiber which makes it difficult to suspend a droplet much smaller than 1mm in diameter. This results in studies of droplets much larger than typical droplet sizes within sprays. In addition, the suspension fiber also distorts the droplet shape from spherical, with the distortion especially severe towards the end of droplet lifetime where the droplet size becomes comparable to the suspension fiber. Also, the heat conduction between the droplet and the suspending fiber plays an integral role in fiber diameters higher than 100μm since the heat transfer through the fiber is more efficient than through the gas medium between the flame and the droplet surface. Finally, the suspension technique is limited to fuels that are relatively nonvolatile due to vaporization effects during the suspension of the droplet, preparation of the chamber and applying ignition stimuli.

## 5.2. Technique and Integral Components

The suspended droplet technique experimental setup used in this research includes the graphite fiber in drop tube furnace and the fine wire thermocouple in the IR heater (discussed in Chapter 6). Both techniques involve a suspending medium for the droplets to be studied in a stationary fashion. Graphite capillary tubing serves as that suspending medium for our studies in the drop tube furnace. In our setup, we generate the droplet at the tip of the capillary tube by pumping the fluid through the tube. Figure 5-1 shows the schematic the suspended droplet technique and the integral components of the experimental setup. Suspended droplet studies (drop tube furnace and IR heater) when compared to free-falling technique were relatively easy to setup and perform, while it restricts the study to low volatile liquids, large droplet sizes, and non-spherical shapes due to the interference of suspending fiber.

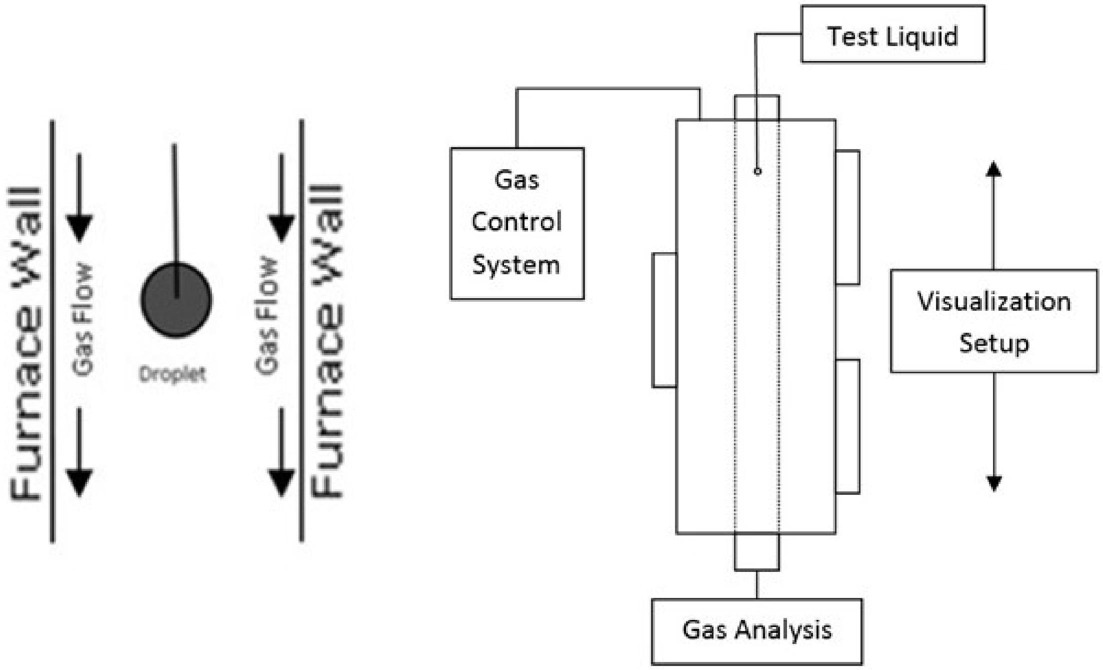

Figure 5-1: Schematic of suspended droplet technique (left) and the integral components of the experimental setup (right) alongside the drop tube furnace.

Suspended droplet studies using the drop tube furnace share many of the experimental components that were discussed in the free-falling droplet section (Chapter 4) The major difference between the two setups is in the method of introducing the test liquids. Photographs of the graphite capillary tube used to suspend the droplet is shown in Figure 5-2. For suspending the droplet, a Hamilton syringe fitted with a 1/16 inch dispensing needle is filled with the test liquid. The syringe then connects to a check valve to prevent liquid backflow, and through to a 100 µm O.D graphite capillary tube using a union and a graphite ferrule. Controlled amount of liquid was pumped at a steady flow rate using a syringe pump. The droplet suspended at the tip was controlled through the liquid flowrate through the tube. Once the droplet was formed at the tip, the graphite capillary tube was lowered such that the droplet moved from a region inside the water-cooled injection nozzle to the heating zone maintained in preset condition. This way, the droplet preheating was minimized before the visualizations were recorded.

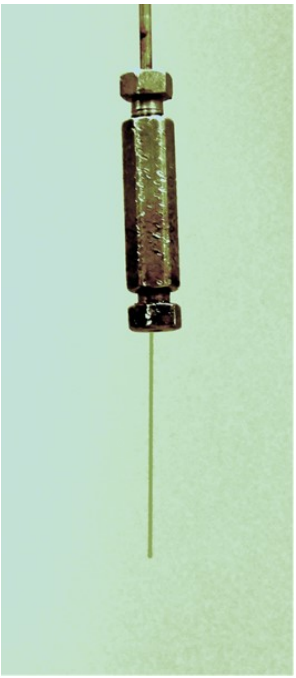

Figure 5-2: Photograph of the graphite capillary tube (O.D 100 µm) used to suspend the droplet inside the drop tube furnace.

## 5.3. Observation and Results

### 5.3.1. Standard Fuel

Suspended droplet experiments of 2,2,4-trimethylpentane (isooctane) and hexadecane (cetane) were performed at a temperature of 500°C, oxygen concentration of 20.9%, and atmospheric pressure. Figure 5-3 and Figure 5-4 shows the thermal behavior of the suspended isooctane and cetane droplets respectively. Evident from the images, we observed the liquid flashing and combusting, producing flames as soon as it enters the furnace conditions. The droplet behavior event last for only 2ms for isooctane whereas for hexadecane it lasts about 8ms. The auto ignition temperatures for isooctane and cetane are 447°C and 202°C, respectively, are much lower than the furnace conditions of 500°C used for these experiments. In combination with the oxygen rich conditions surrounding the droplet, chemical reaction between the droplet and the oxidant takes place that we observe as combustion in these two figures.

Figure 5-3: Image sequence of 2,2,4-trimethylpentane suspended droplet behavior at 500°C. Images captured and displayed at 636 fps (left to right). Lapse time between displayed images is 2ms.

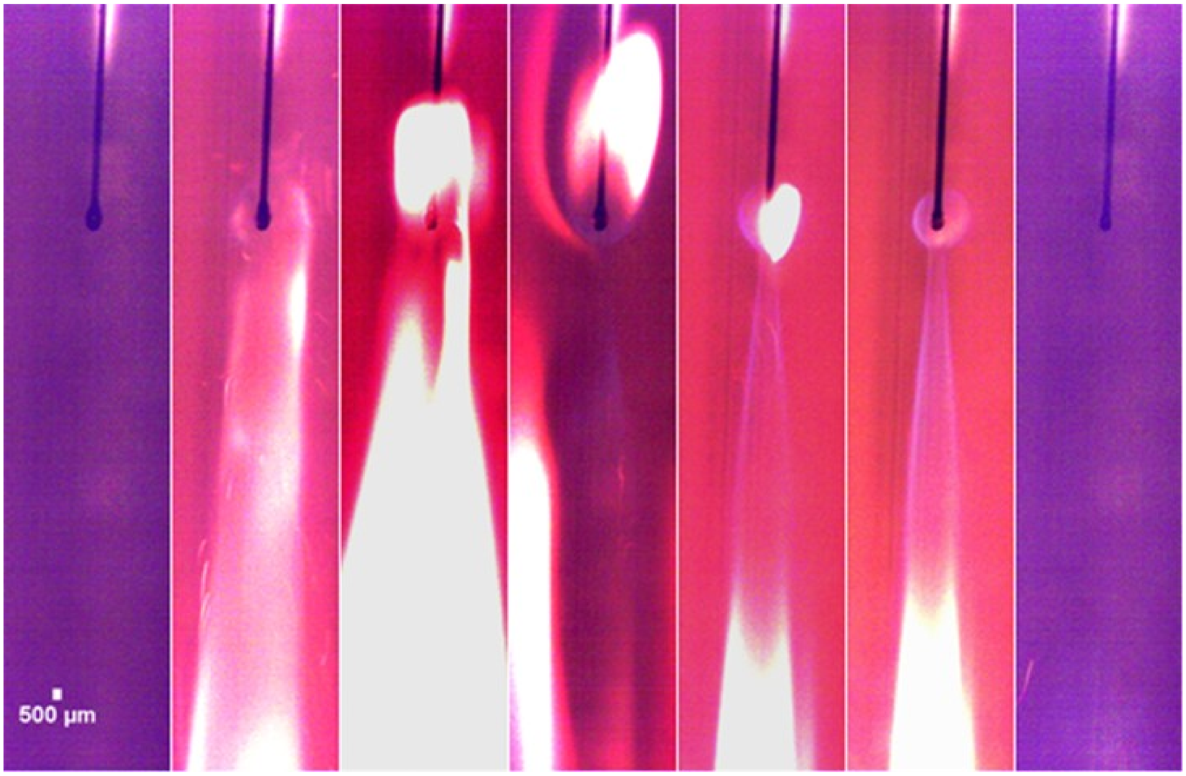

Figure 5-4: Image sequence of hexadecane suspended droplet behavior at 500°C. Images captured at 636 fps and displayed at 127 fps (left to right). Lapse time between displayed images is 8ms.

### 5.3.2. Aqueous Glycerol Solutions

Image sequence of 98% aq. glycerol suspended droplet behavior is shown in Figure 5-5. From the image sequence, we observe the droplet grow on the capillary tip until the surface tension forces can no longer hold the droplet. The glycerol droplet stays on the tip of the capillary tube for considerably longer time (1s) when compared with the standard fuels discussed above. The glycerol droplet shows no thermal degradation in terms of droplet size for the furnace condition of 500°C despite its auto ignition temperature being 370°C. For the selected experimental condition, our understanding is that the glycerol droplet heating time is considerably higher than its residence time on the capillary tip. In other words, before the temperature of the glycerol droplet could reach a threshold value for exhibiting vaporization or combustion behavior, the rate of liquid accumulation causes the droplet formed at the tip to detach and fall.

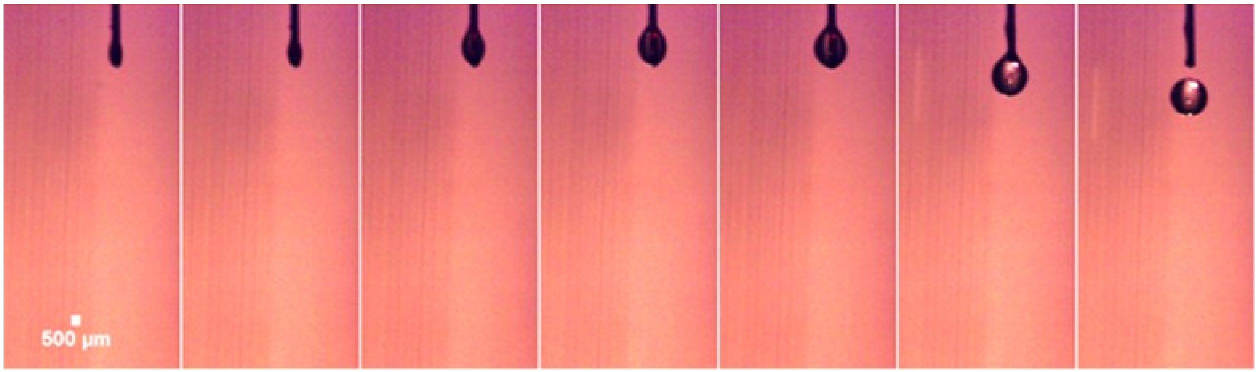

Figure 5-5: Image sequence of 98% aqueous glycerol suspended droplet behavior at 500°C. Images captured at 1000 fps and displayed at 1 fps (left to right). Lapse time between displayed images is 1s.

### 5.3.3. Aviation Liquid

Suspended droplet behavior of aviation liquid BP Turbo oil 274 (BP Oil) at 500 and 450°C are shown in Figures 5-6 and 5-7 respectively. From the image sequence of Figure 5-6 we can observe the suspended droplet grow at the capillary tip analogous to glycerol droplet early on (first two images from left). However, between the third and fourth image (from left) we observe the droplet size decrease and increase eventually resulting in flames as seen in the final image. Our understanding of this behavior is that the droplet undergoes partially vaporization initially (between second and third image from left) that results in the droplet size reduction. But the continuous pumping of the liquid through the tube along with the capillary effect at the tip results in the droplet formation again (fourth image from left). However, the droplet thus formed is at a higher temperature than before due to the continuous exposure to the furnace condition of about 500°C. Between fourth and fifth image in the sequence, we believe the droplet reached its auto-ignition temperature to undergo combustion evident from the flames, and absence of liquid at the tip. This whole suspended droplet behavior event of BP Oil lasts for about 50ms.

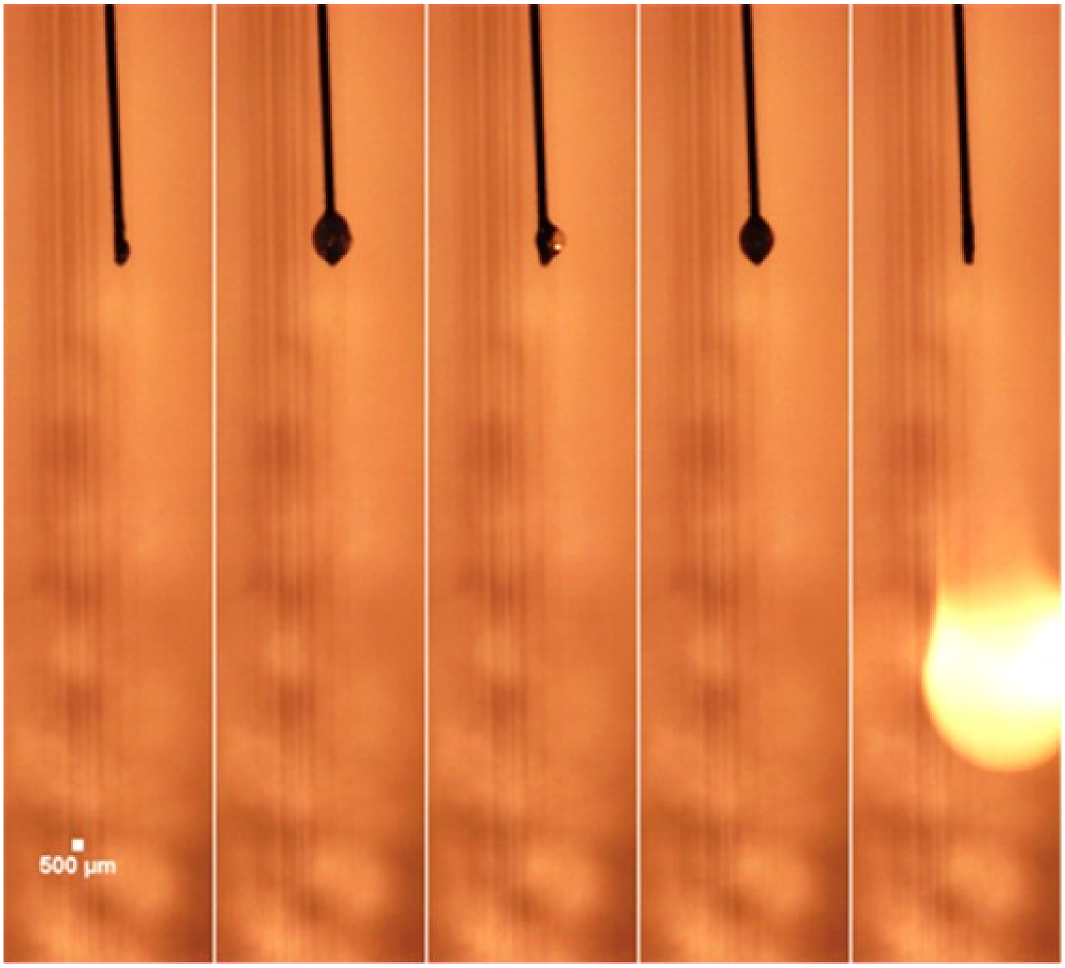

Figure 5-6: Image sequence of BP Oil suspended droplet behavior at 500°C. Images captured at 200 fps and displayed at 20 fps (left to right). Lapse time between displayed images is 50ms.

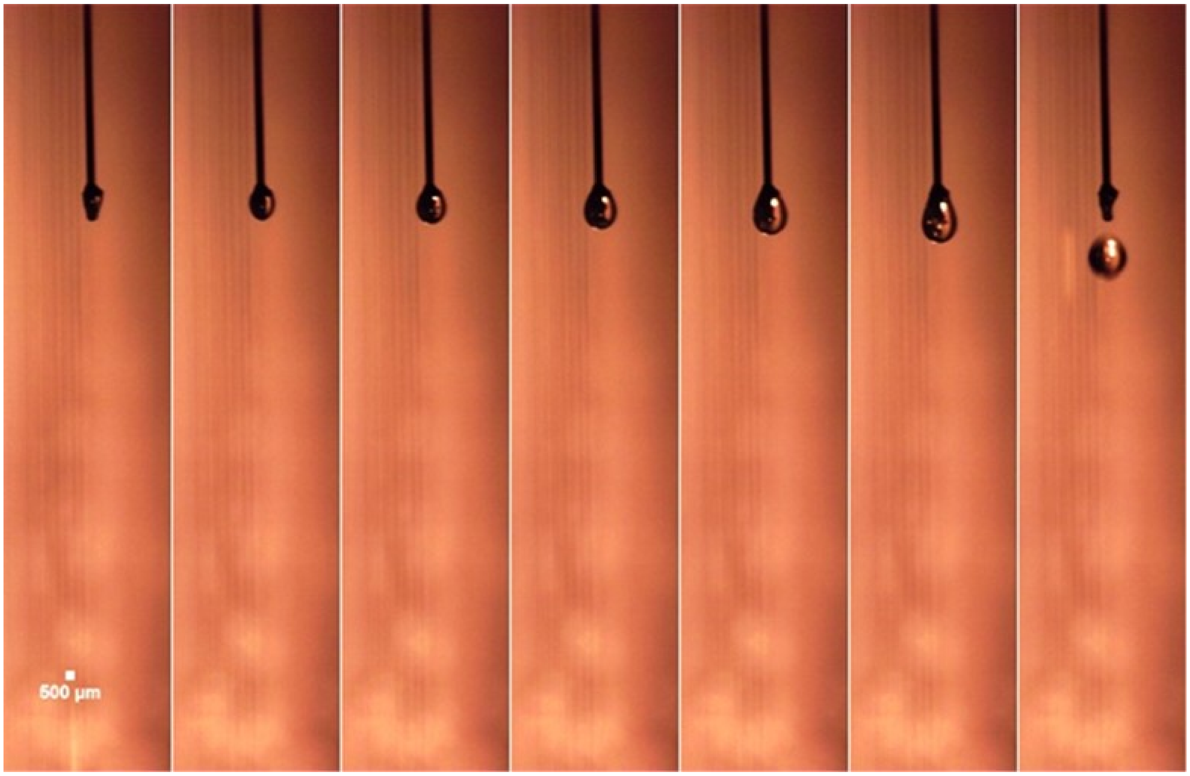

Figure 5-7: Image sequence of BP Oil suspended droplet behavior at 450°C. Images are captured at 200 fps and displayed at 4 fps (left to right). Lapse time between displayed images is 250ms.

Image sequence of Figure 5-7 shows the suspended droplet behavior of BP Oil at 450°C. Form the figure, we can observe the suspended droplet behavior of the aviation liquid to be similar to that of the glycerol suspended droplet shown in Figure 5-5. The droplet does not show significant degradation under the selected furnace condition. Notable observation from the image sequence of Figure 5-7 is the residue formation at the tip of the capillary tube. When the suspended droplet experiment of BP Oil was repeated, over time we observed a brownish-black residue accumulate near the tip. If not removed regularly, the accumulated residue affected the droplet formation and caused capillary blockage.

## 5.4. Discussion

The primary objective of testing the feasibility to perform suspended droplet experiments and to visualize the thermal behavior of the droplet in the drop tube furnace has been successful. Image sequences obtained show the droplet behavior at the tip of a graphite capillary tube in oxygen rich atmosphere (20.9% $O_2$, air) and varying furnace temperature. The preliminary results serve as a proof of method to study droplet behavior by suspension on the tip of a graphite fiber in drop tube furnace. The method described has the potential to obtain quantitative visualization data such as change of the droplet diameter as a function of time that can be used to calculate burning rates. As shown in the literature review earlier, the method described here can also be used for the identification of ignition point, flame color, flame size, extinction point, bubbling, microexplosion, and sooting behavior for several liquid types. However, the drawback of this technique in drop tube furnace is inability to avoid the premature droplet heating.

# 6. Proof of Method Experiments to Study Suspended Droplet Behavior Using a Fine Gauge Thermocouple in an IR heater

## 6.1. Technique and Integral Components

Literature studies and the attributes of suspended droplet techniques for studying droplet behavior were discussed in Chapter 5. The graphite capillary tube was replaced with a fine gauge bare thermocouple wire to suspend the droplets. The thermocouple bead at the junction of +ve and -ve wires was used as the location to suspend the droplet. Figure 6-1 shows the schematic of the technique used in the IR heater along with the key components of the experimental setup. The integral components (gas control system, visualization setup, gas analysis) were the same as with the other two methods, with the main change in the experimental procedure being the introduction of test liquids.

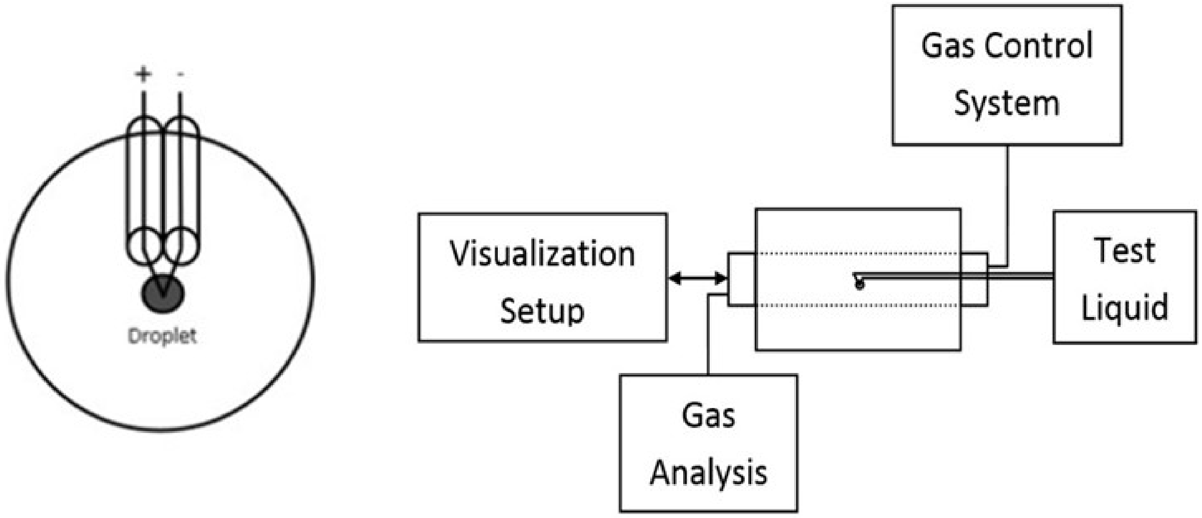

Figure 6-1: Schematic of suspended droplet technique (left) and the integral components of the experimental setup (right) in IR heater.

## 6.2. Experimental Setup

### 6.2.1. IR heater Modification for Droplet Behavior Studies

The IR heater discussed in Chapter 3 was modified for performing suspended droplet studies. A quartz glass tube of 6.35 cm in diameter and 50.8 cm in length was mounted inside the infrared heater to protect the halogen lamps from the volatilized vapors of suspended liquids and to allow control of the gas environment. Ends of this quartz tube were fitted with water cooled flanges like those described earlier with the drop tube furnace experiments. End caps to seal the quartz chamber were constructed in house with the Auburn University Chemical Engineering machine shop. Figure 6-2 shows the IR heater mounted on a support, and the internal view of the heater with halogen lamps and elliptical reflector surfaces.

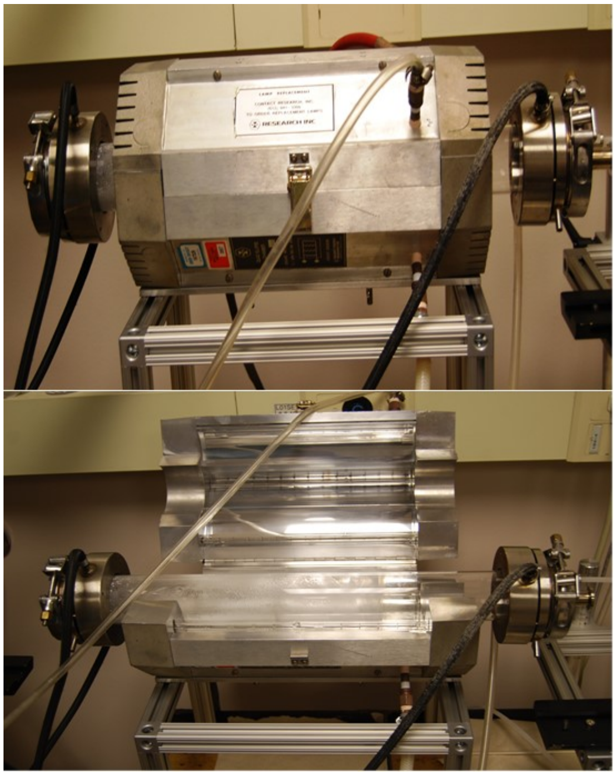

Figure 6-2: Photograph showing IR heater with end caps (top) and an internal view showing the halogen lamps and elliptical reflector surfaces (bottom).

To perform visualization studies and an option to collect exhaust gas simultaneously were important criteria in the design of these end caps. One of the end caps has a ½ inch circular opening with provision to insert the thermocouple and seal. It also has a port for gas flow. A bigger opening of ½ inch was chosen specifically for this end cap such that the droplet does not contact the walls as it is suspended on the thermocouple and slid into the chamber. On the other end, two different end caps can be mounted depending on the purpose of the experiment. Photographs showing the different end caps can be seen in Figure 6-3.

Figure 6-3: Photograph of different end cap configurations used in the IR heater. End caps with thermocouple inlet (left), view window (middle), and septum port (right).

For visualization studies, an end cap housing a 3.81 cm diameter and 0.32 cm thick fused quartz optical window from ESCO Optics was used. For studies involving volatile gas analysis, the optical window end cap was replaced with an end cap containing a gas flow valve, and a septum opening that permits collection of volatile gases from the quartz chamber using a gas collection syringe. The experimental setup for the visualization studies of the suspended droplet using the infrared heater is shown in Figure 6-4. An unsheathed 125 µm thermocouple of type R (Pt/13%Rh-Pt) from Omega was used for suspending the droplet. A disposable syringe fitted with a gauge 30 precision needle was used to place a droplet of approximately 1 mm diameter on the thermocouple junction bead. Temperature at the thermocouple junction bead was recorded using a custom developed temperature data logger at a frequency of 0.1s.

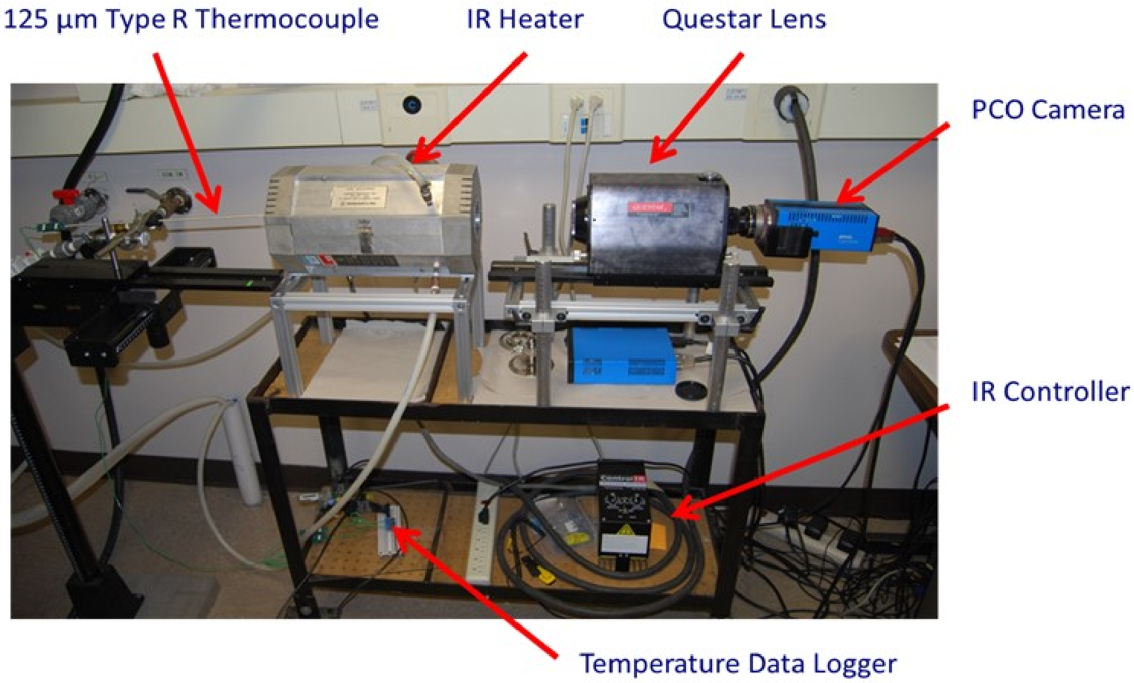

Figure 6-4: Photograph showing the experimental setup including visualization components for studies with the IR heater.

### 6.2.2. IR Heater - Operating Procedure

To perform suspended droplet studies in the infrared heater, a droplet was suspended on the thermocouple using a syringe needle. The thermocouple was then slid on a moving rail to enter the quartz chamber inside the heater. The chamber was filled with the atmosphere in which the test liquid is to be volatilized and sealed. When the infrared heater is switched ON, the suspended droplet undergoes volatilization or combustion. For visualization studies, the video recording through PCO Camware and the temperature data logger were started simultaneously with infrared ON/OFF switch. The visualization studies with IR heater were captured using the PCO camera with three lenses (Nikon 105 mm lens, Nikon 200 mm telephoto lens, and the Questar lens) for varying magnifications.

### 6.2.3. Experimental Setup Modification - Gimbal Mount

The components of the IR heater experimental setup were modified over the period of research to develop a precise, repeatable, and reliable setup to study suspended droplets. The retort stand setup previously used to hold the thermocouple was replaced with a GM100 – Ø1’ Gimbal Mirror Mount from THORlabs as shown in Figure 6-5. The gimbal mount was modified with the help of AU machine shop to hold the thermocouple in a horizontal position and slide in and out of the IR heater on an optical rail. The two knobs (labeled H and V) on the gimbal mounts permitted for controlled and finer rotational movements of the thermocouple bead inside the IR heater.

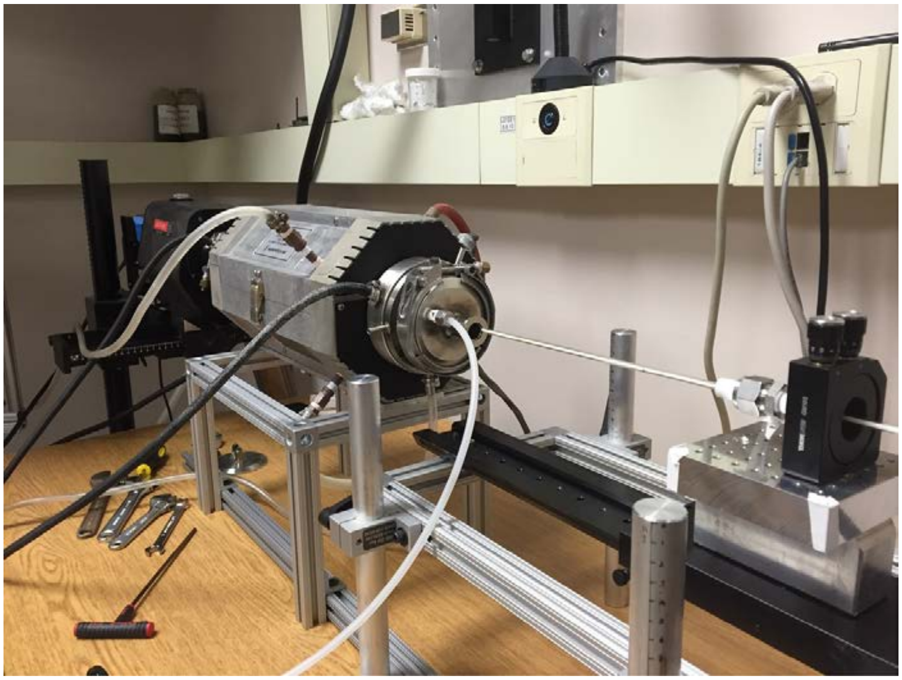

Figure 6-5: Photograph of the modified experimental setup using a gimbal mount for positioning the thermocouple.

### 6.2.4. Visualization Setup Modification – Nikon 200 mm Telephoto Lens

Low magnification visualizations in the IR heater were also performed using an AF-S NIKKOR 200mm f/2G ED VR II telephoto lens obtained from Dr. Brian Thurow’s group (Aerospace Engineering, Auburn University). The lens was mounted to the PCO high speed camera using extension tubes (with a total length of 98 mm) to reduce the working distance and increase the magnification of the lens. The wide opening of the telephoto lens allowed for better light control and improved image clarity over the Nikon 105 mm macro lens previously used for other low magnification studies in this research. Figure 6-6 shows the visualization setup with the PCO camera and Nikon 200 mm lens.

Figure 6-6: Photograph of the PCO camera attached to the Nikon 200mm telephoto lens using multiple extension rings.

## 6.3. Observation and Results

### 6.3.1. Standard Fuel

Suspended droplet experiments were conducted with the standard fuel hexadecane in the IR heater. Studies were not performed with 2,2,4-Trimethylpentane (isooctane) due to the high volatile nature of the liquid. Visualization image sequences showing the behavior of hexadecane droplets in the rapidly increasing temperature environment are shown in Figure 6-7 and Figure 6-8. The low and high magnification images shown for proof of method studies in IR heater were obtained using the Nikon 105 mm or the Questar lens. Maximum heating rate (RA – 10) inside the

IR heater was maintained throughout. Time duration (excluding the time taken by the IR lamps to reach maximum intensity, *t'*) for which the hexadecane droplet was suspended on the thermocouple was about 1.7 to 2.0s. In the Figure 6-7 we observe vapors and microdroplets of hexadecane as a mist that falls below the droplet. In the high magnification images of Figure 6-8 we observe a volatilizing behavior where the droplet reduces in size suggesting vaporization.

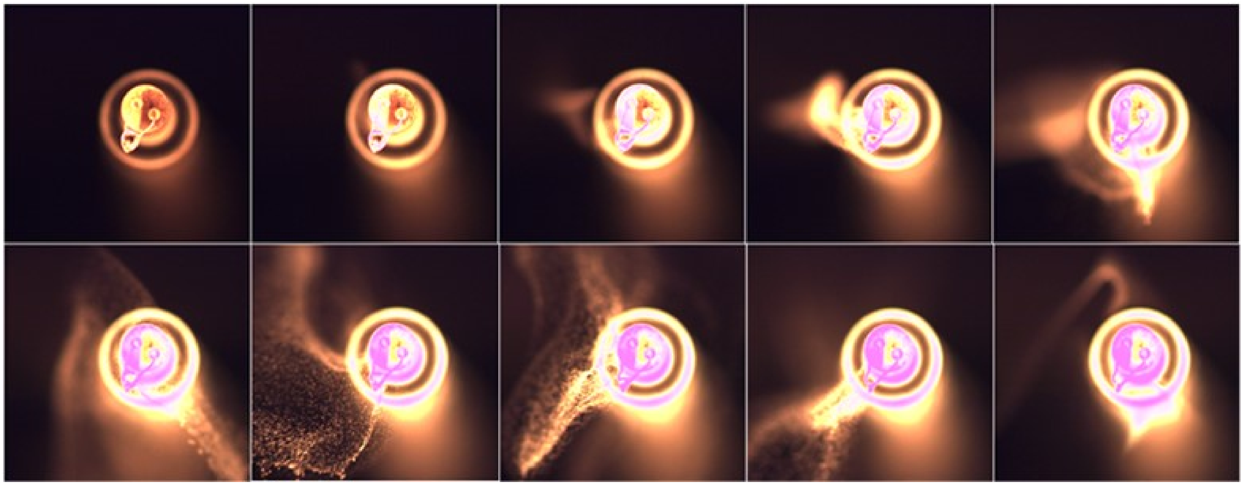

Figure 6-7: Low magnification images of the suspended droplet behavior of hexadecane captured at 1000 fps and displayed at 5 fps between the time interval 2.0 to 3.8s (arranged row wise starting from top left).

Temperature measured at the thermocouple junction for the elapsed time of the experiment is shown in the Figure 6-9. From the figure, we can clearly see the differences in temperature profile of the thermocouple depending on the presence (red) or absence (blue) of a droplet. The temperature profile after the elapsed time of 4s (includes *t'*) are nearly identical since, the total residence time of the hexadecane droplet at the junction is lower than 4s. Hence, temperature recorded after 4s is that of the thermocouple material only.

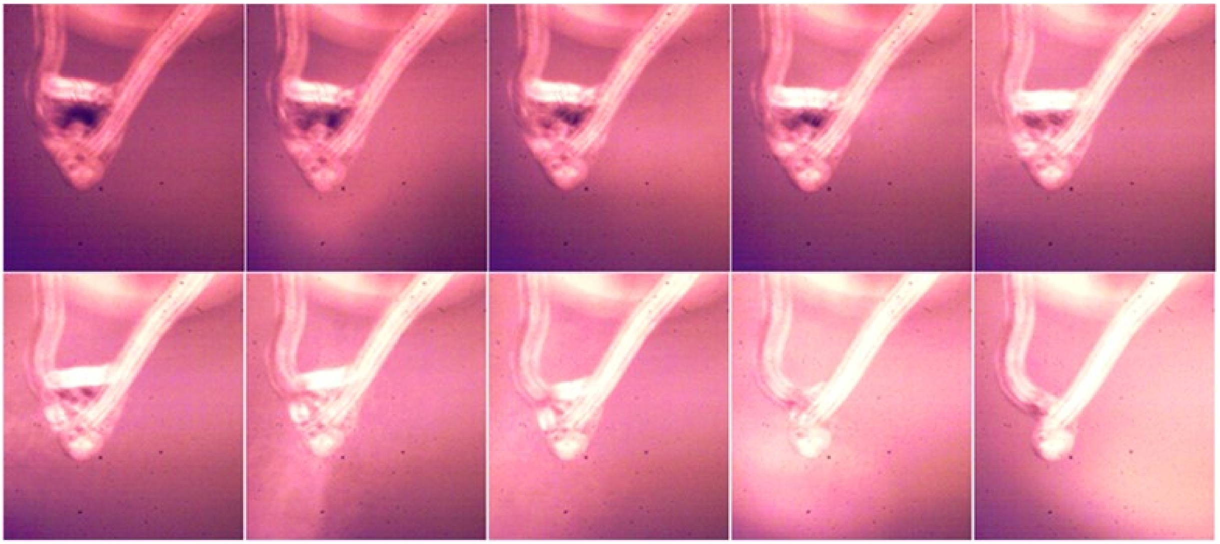

Figure 6-8: High magnification images of the suspended droplet behavior of hexadecane captured at 1000 fps using and displayed at 10 fps between the time interval 2.0 to 2.9s (arranged row wise from top left).

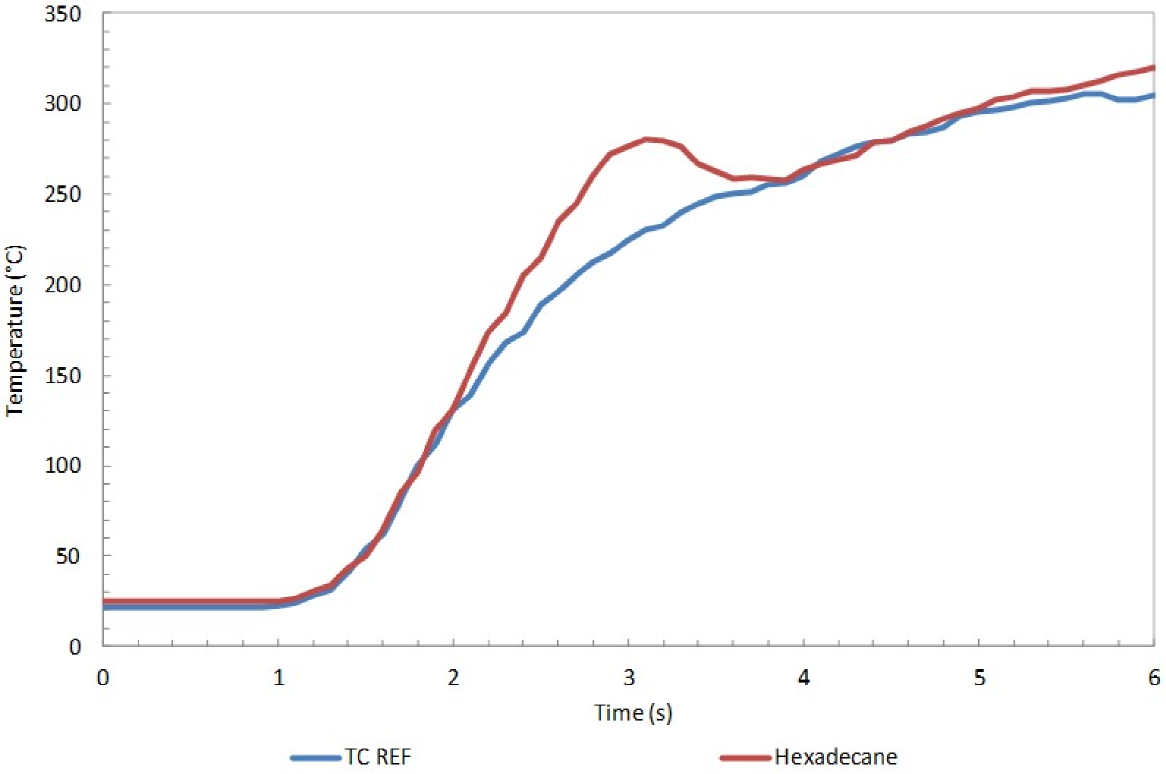

Figure 6-9: Thermocouple temperature profile with a hexadecane droplet compared to the reference thermocouple profile.

The IR lamps take about 1.4s to heat up and reach maximum intensity. During the time interval of 1.4 to 4.0s, the temperature profile of hexadecane (red) represents the internal droplet temperature of the droplet only, and the slope of the temperature profile represents the heating rate of the droplet (Figure 6-9).

### 6.3.2. Pure Glycerol

Visualization image sequences of the thermal behavior of 98% aqueous glycerol are shown in Figure 6-10 and Figure 6-11. The time duration of the droplet on the thermocouple junction is relatively longer when compared to hexadecane around 1.7 to 2.7s. Longer durations observed for a few glycerol droplets were due to their larger initial droplet diameters ($d_0$). In the high magnification visualization of Figure 6-11, we observe the droplet maintaining a spherical shape even during thermal degradation.

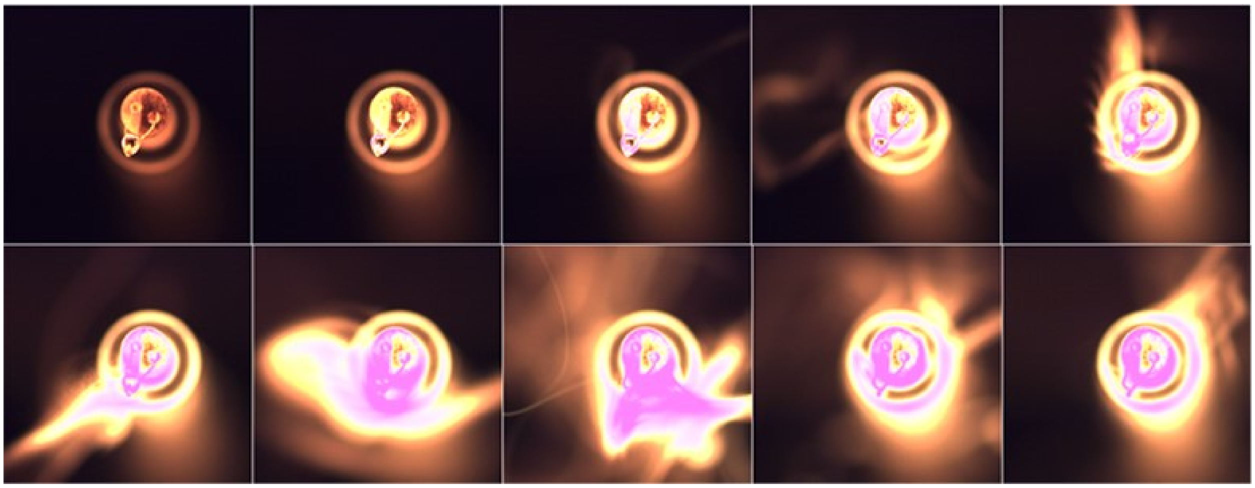

Figure 6-10: Low magnification images of the suspended droplets behavior of 98% aq. glycerol captured at 1000 fps and displayed at 5 fps between the time interval 1.8 to 3.6s (arranged row wise from top left).

The temperature profile for a 98% aq. glycerol droplet suspended on thermocouple junction is shown in Figure 6-12. As stated previously, presence of the droplet at the junction does not affect the temperature profile during the initial period of 0 to 1.4s (IR starting lag, *t'*), and during the elapsed time following the residence time of the droplet. For the time interval of 1.4 to 3.5s, we observe a difference in the temperature profile in terms of heating rate for the thermocouple with the droplet. Around 3.5 to 4.0s when the droplet nears the end of its residence time, the temperature drops and the profile thereafter closely follows the reference profile of the temperature inside IR heater.

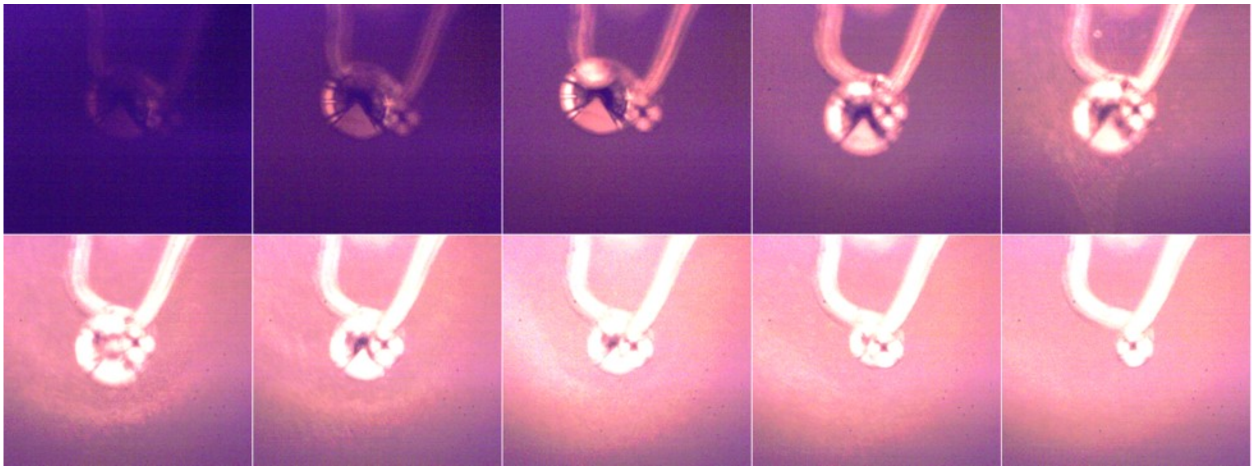

Figure 6-11: High magnification images of the suspended droplet behavior of 98% aq. glycerol captured at 1000 fps and displayed at 3 fps between the time interval 1.5 to 4.2s (arranged row wise from top left).

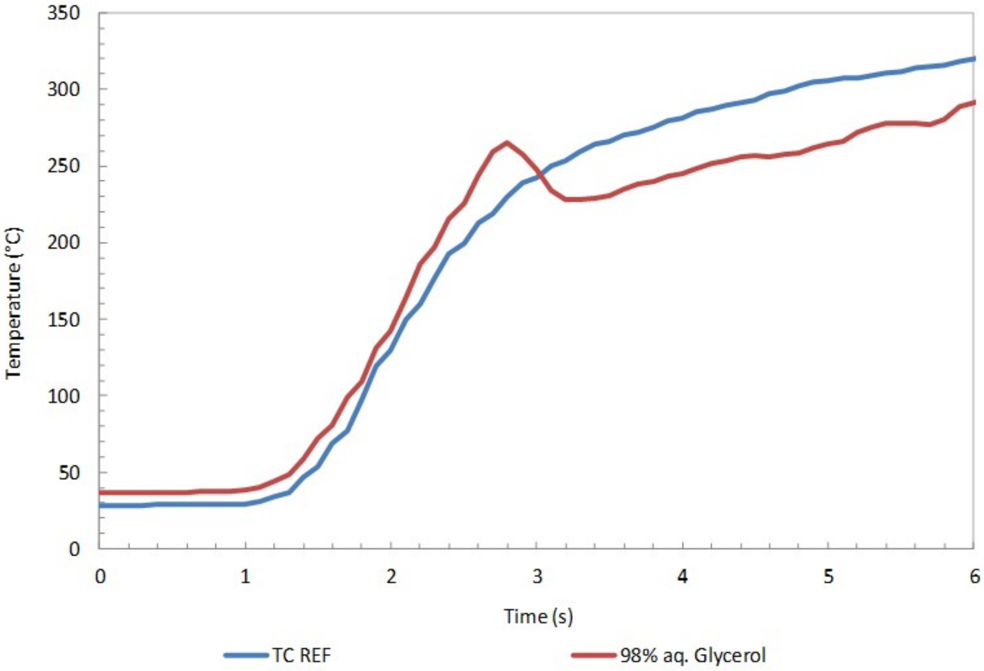

Figure 6-12: Temperature profile of a 98% aq. glycerol droplet suspended inside the IR heater.

### 6.3.3. Aviation Liquid

Visualization image sequences for aviation liquid BP Turbo Oil 274 (BP Oil) droplet suspended inside the IR heater are shown in Figure 6-13 and Figure 6-14. The average duration of the droplet on the thermocouple junction was found to be between 2.2 to 2.8s.

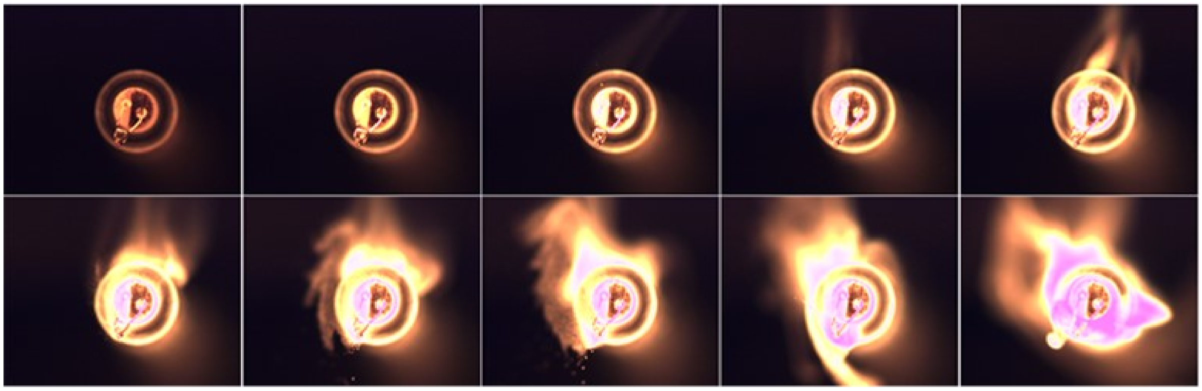

Figure 6-13: Low magnification images of the suspended droplets of BP Oil captured at 1000 fps and displayed at 3 fps between the time interval 1.5 to 4.2s (arranged row wise from top left).

The temperature profile plot for a droplet of BP Oil on the thermocouple junction is shown in Figure 6-15. Presence of the aviation liquid at the thermocouple junction clearly results in a different temperature profile as shown in the figure. The temperature profile plot of the BP Oil droplet shown here has a larger time duration of 3.0 to 3.5s. Between the elapsed time of 3 to 4.5s, the droplet seems to have reached its maximum temperature.

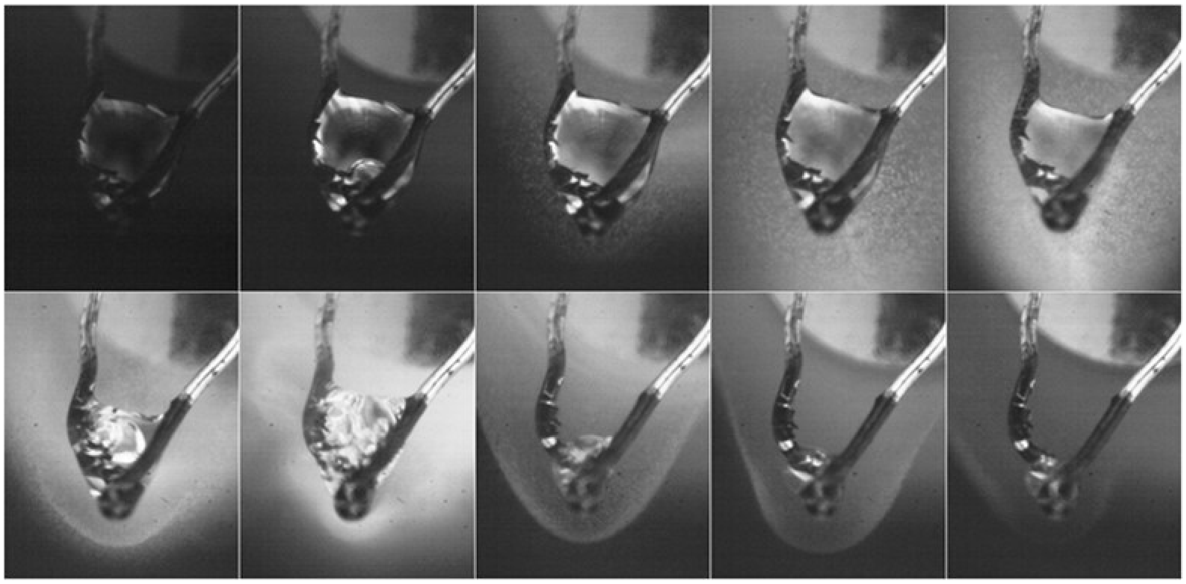

Figure 6-14: High magnification images of the suspended droplet behavior of BP Oil captured at 1000 fps and displayed at 2 fps between the time interval 2.2 to 8.5s (arranged row wise from top left).

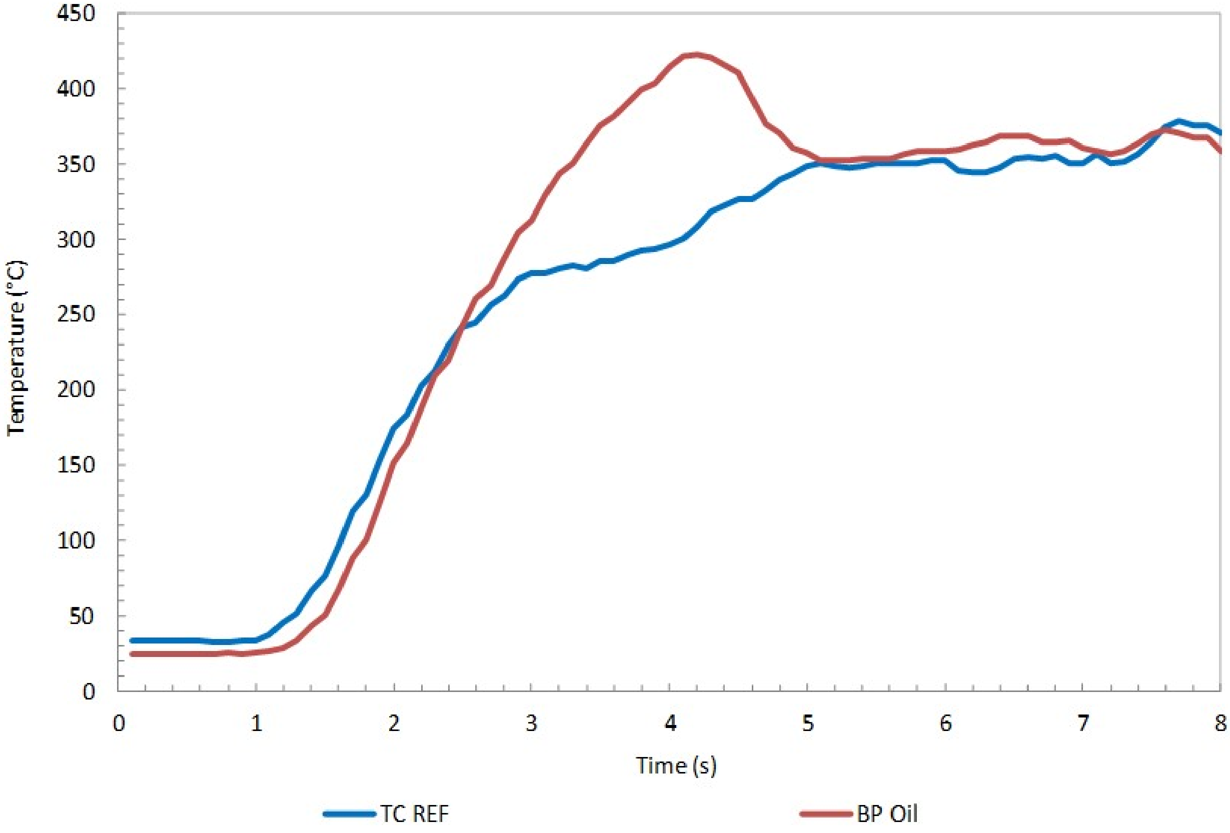

Figure 6-15: Temperature profile of a BP Oil 274 droplet suspended inside the IR heater.

### 6.4. Discussion

The objective of the studies involving the IR heater were to design and construct an experimental setup that will enable study of suspended droplet behavior. The IR heater was shown to be successfully redesigned from its previous application to allow study of droplet behavior using visualization techniques. The thermocouple data logger used in this setup was exclusively built for collecting temperature data from type-R thermocouples inside IR heater. The data logger is controlled using a Raspberry Pi device attached to a custom-built circuit board that can collect, display, and store the obtained temperature information. It can collect temperature readings at a maximum frequency of 10 readings per second. Also, the use of fine gauge thermocouple wire to suspend the droplet was useful in obtaining the droplet temperature. From the temperature plots shown earlier, we can see that the temperature data obtained at the thermocouple bead is a reasonable representation of the internal droplet temperature.

The setup using the IR heater was also able to avoid the liquid preheating problems mentioned with the suspended droplet technique studies in drop tube furnace. We have shown visualization images of standard fuel (hexadecane), pure single component liquid (pure glycerol), and multicomponent liquid (BP Oil). The images demonstrate our capability to suspend and study the droplet behavior of liquids of varying physical properties. Over the course of our experiments, the thermocouple type and the respective thickness were varied for increased temperature sensitivity and reduced droplet size respectively.

Overall, suspended droplets inside the IR heater facilitate better visualization capabilities compared to that of suspended liquid on the capillary tip inside drop tube furnace. As will be shown later, droplet size measurements were feasible with the high magnification visualization. They were helpful to understand the $d^2$ law relation that relates the change in droplet size to temperature.

Also, the internal temperature measurements of the droplet were useful in understanding the heating rate of test liquids is varying operating conditions. Our primary objective from these preliminary visualizations in the IR heater was to demonstrate the proof of method for studying droplet behavior using thermocouple wire as the suspending medium.

# 7. Suspended Droplet Studies Involving E-G System

## 7.1. E-G System - Introduction

Systematic droplet visualization studies were performed with the ethanol-glycerol (E-G) mixtures in the IR heater suspended droplet setup. The objective of the E-G system study was to obtain a fundamental understanding of the droplet behavior of blends of ethanol-glycerol liquid types. Two blends, namely E30G70 (30% Pure Ethanol - 70% Pure Glycerol) and E70G30 (70% Pure Ethanol - 30% Pure Glycerol), were prepared. These blends were compared with the corresponding pure liquid types, E100 (pure Ethanol) and G100 (pure Glycerol). These 4 liquid types collectively represent the E-G system.

The suspended droplet studies of E-G system inside the IR heater include studying the droplet behavior at the following conditions:

- E-G system droplet behavior study (low magnification) under air or pure nitrogen types of gas
- E-G system droplet behavior study (low magnification) under multiple gas flowrates – variable gas flow rate ranging from 5 to 25 SCFM controlled through the rotameter setting
- E-G system droplet behavior study (low magnification) under multiple IR heating rates – controlled variable heating rates through the RUN ADJUST setting of IR heater (RA setting of 4, 6, 8 and 10)
- E-G system droplet behavior study (low magnification) for multiple liquid types – liquid types include pure Methanol (M100), pure Butanol (B100), pure Hexadecane and commercial BP Turbo Oil 274 (multicomponent BP Oil)
- E-G system droplet behavior study using high magnification PCO camera - Questar lens visualization setup

The suspended droplet studies for the E-G system were performed using the procedure described previously for test droplet visualizations inside the IR heater. For the E30G70 and E70G30 blends, 20 ml liquid solutions were prepared from which the suspending droplet samples were taken for experiments. The source for liquid samples of G100, Hexadecane and BP Oil were same as mentioned before in the 'Test fluids' section. B100 represents 99.9% Anhydrous 1-Butanol from Alfa Aesar, E100 represents 200 Proof Anhydrous USP grade Ethyl Alcohol from Pharmco-Aaper, and M100 represents HPLC grade Methanol from Millipore Sigma.

The E-G system analysis includes data collected from the temperature data logger and the data collected from the PCO-Nikon 200 mm telephoto lens visualization videos. The low magnification visualization videos include initial droplet diameter information ($d_0$) and elapsed time information of multiple significant droplet behavior events namely DE-1, DE-2, DE-3 and, DE-4 as will be described later. High magnification visualization videos in addition to the determination of significant droplet behavior events (DE-1, 2, 3, 4) were also used to calculate the temporal variations of the droplet diameter ($d$).

For all the E-G system studies, the temperature data logger, PCO camware software, and the IR heater were manually triggered at the same time. The schematic explaining the timeline of the IR heater, visualization system recording, and the temperature data collection is shown in Figure 7-1. Data from the temperature data logger were in the form of *.dat* files and the temperature information from the *.dat* files are selectively imported to an excel file. The fps (frames per second) at which the visualizations were recorded and the frequency of logging the temperature data were known for each experiment. The elapsed time ($t$) data represents the calculated timeline for each suspended droplet obtained through the timestamp info available on both the temperature data logger output and PCO visualization videos. All droplet diameter calculations were made

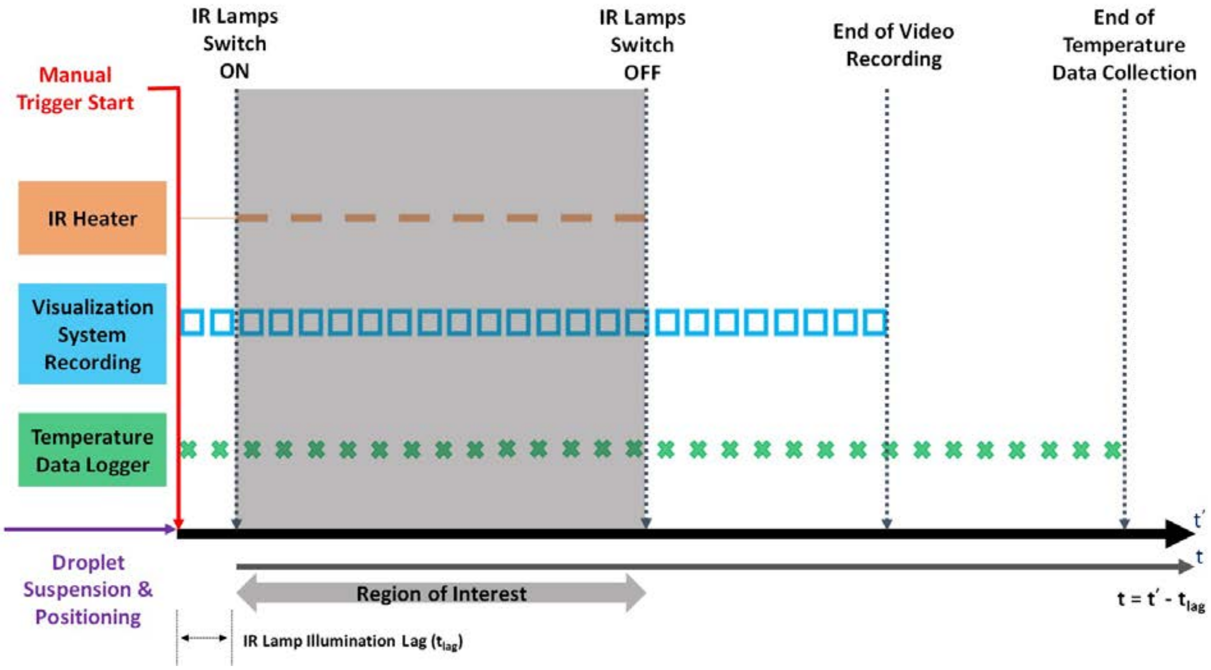

Figure 7-1: Schematic explaining the manual triggering and the timeline of IR heater, visualization system recording, and the temperature data collection events.

using the ImageJ software either by using the known outer diameter of the thermocouple wire (for high magnification videos) or by using the outer diameter of alumina ceramic tube housing the thermocouple (for low magnification videos) as the length scale for the image.

The IR ON and IR OFF events represent the start and end of the illumination of the IR lamps. This is controlled by the RUN ADJUST setting on the IR heater controller. The IR heater has a lag of more than one second (1.4s). This delay is considered and the elapsed time ($t$) is appropriately adjusted such that the IR ON event starts at $t = 0s$. The significant droplet behavior events (DE) are marked at their respective image numbers from reviewing the visualizations which are later converted to elapsed time ($t$) events corresponding to the fps at which the videos were recorded.

The DE-1 event refers to the elapsed time ($t$) at which the first significant droplet behavior change is observed in the low magnification visualization videos after the IR heater is switched

ON. The DE-1 events include the first time the droplet vapors could be spotted in the visualizations; and initial movements in the liquid droplet which include minor changes on droplet surface, droplet swing behavior, or the emergence of the first bubble inside the droplet. The DE-2 and DE-3 events refers to the elapsed time (*t*) at which the second and third significant droplet behavior events are observed respectively. The DE-2 event include the first droplet microexplosion event whereas the DE-3 event refers to the final microexplosion event in the droplet usually after which the remaining suspended droplet exhibits a consistent droplet diameter reduction. In the absence of microexplosion in a droplet, DE-2 refers to either the microdroplet escape or microdroplet attrition events. The DE-4 event represents the elapsed time (*t*) at which the droplet does not exist on the thermocouple bead due to complete vaporization or combustion.

The significant events used for marking DE-1 generally differ depending on the type of the liquid droplet since multiple events can result in the end of quiescent period as it will be explained later. In all droplets experiments, irrespective of the type of significant droplet behavior event, quiescent time (QT) represents the elapsed time (*t*) between IR ON and DE-1 event, and the behavior time (BT) represents the elapsed time (*t*) between DE-1 and DE-4 event respectively. The residence time (RT) on the thermocouple bead is calculated as the elapsed time (*t*) between the IR ON and DE-4 event. Figure 7-2, Figure 7-3, Figure 7-4, and Figure 7-5 show some of the images used in the calculation of DE-1, DE-2, and DE-4 events from the low magnification visualizations. Either the first or the last image number of the image sequence were used to calculate the elapsed time (*t*) depending on the type of the event.

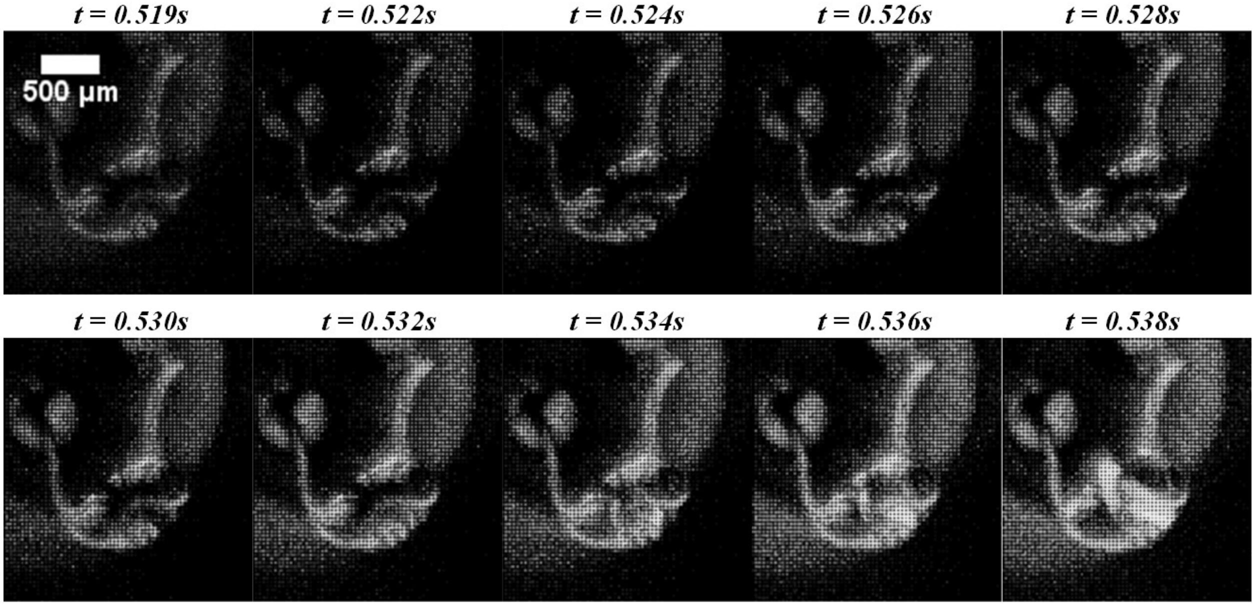

Figure 7-2: Low magnification images of bubbling behavior (DE-1 event) in a E100 droplet ($d_0$ = 0.96 mm; $t_{res}$ = 1.45s) suspended in low flowrate (5 SCFM) air environment.

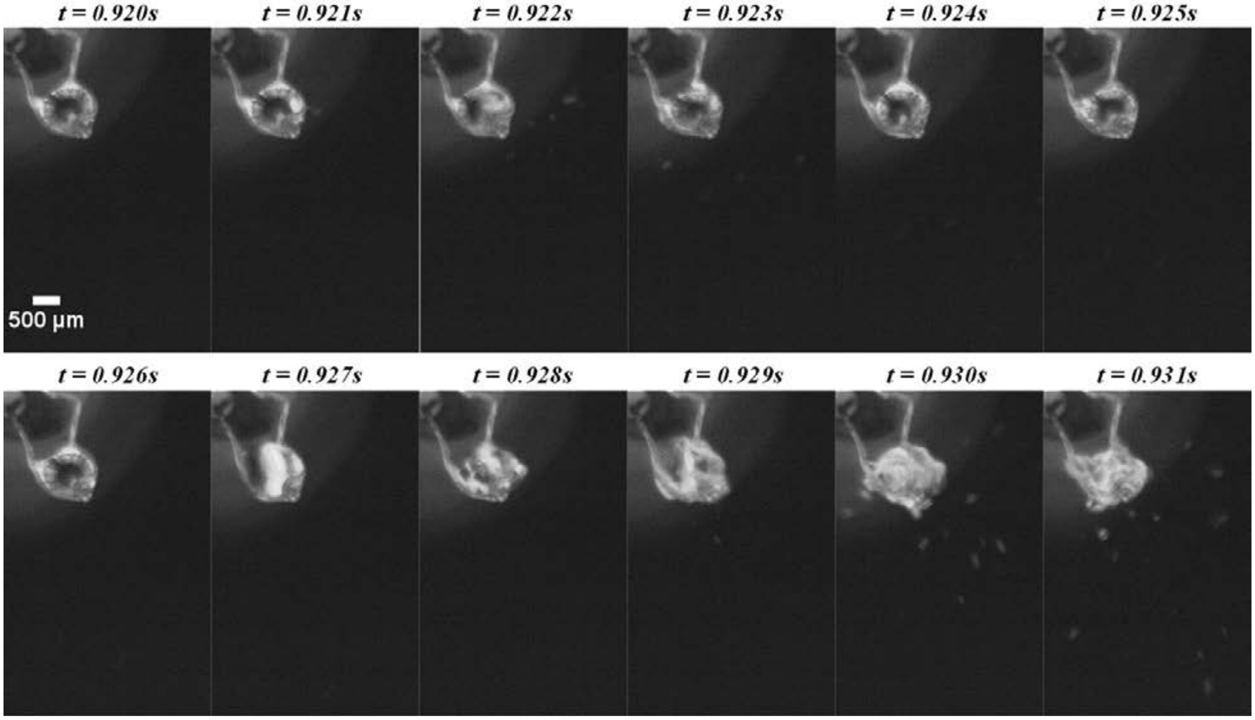

Figure 7-3: Low magnification images of the first microexplosion event (DE-2 event) in a E70G30 droplet ($d_0$ = 1.04 mm; $t_{res}$ = 2.19s) suspended in intermediate flowrate (10 SCFM) air environment.

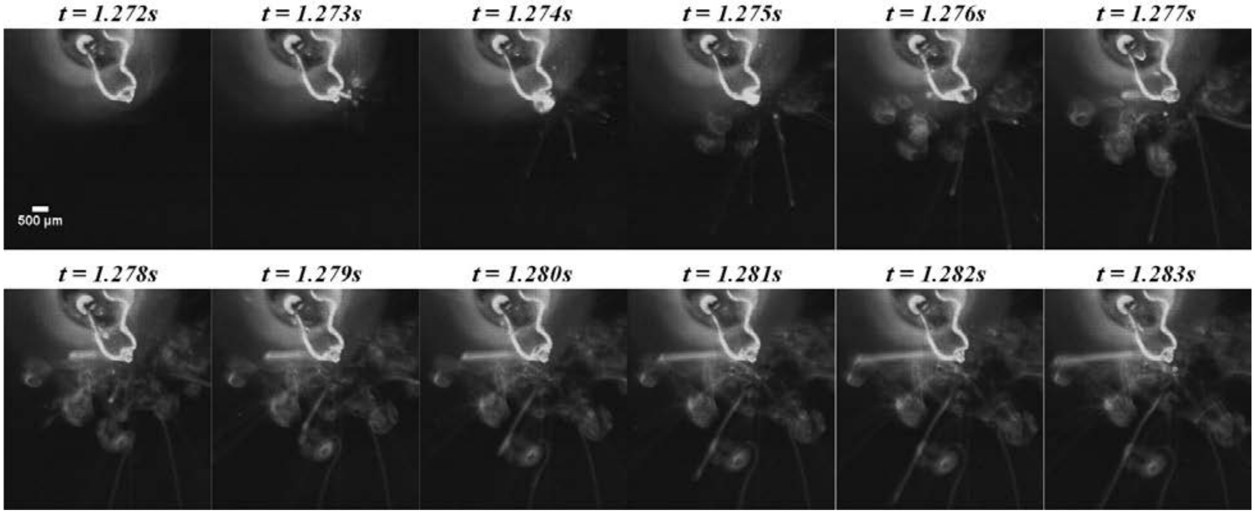

Figure 7-4: Low magnification images of the final microexplosion event (DE-3 event) in a E70G30 droplet ($d_0$ = 1.07 mm; $t_{res}$ = 1.95s) suspended in low flowrate (5 SCFM) nitrogen environment.

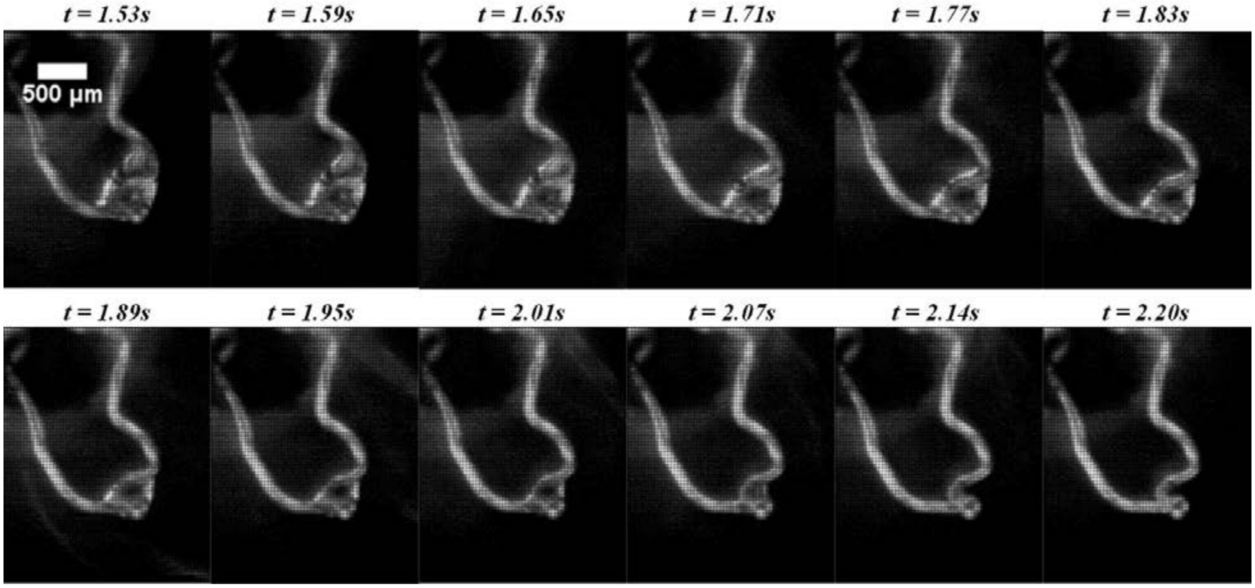

Figure 7-5: Low magnification images of the residual droplet evaporation behavior (DE-4 event) in a E70G30 droplet ($d_0$ = 1.04 mm; $t_{res}$ = 2.19s) suspended in intermediate flowrate (10 SCFM) air environment.

## 7.2. E-G System – Droplet Behavior

The E-G (ethanol-glycerol) system was studied to obtain an understanding of the droplet behavior at elevated temperatures. As previously mentioned, E100 refers to pure ethanol, E30G70 to 30 vol.% ethanol - 70 vol.% glycerol, E70G30 to 70 vol.% ethanol - 30 vol.% glycerol, and G100 to pure glycerol. For comparison purposes, other liquids were studied which include pure single component liquids Methanol (M100) and Butanol (B100), reference fuel Cetane (Hexadecane), and multi-component commercial aviation engine oil BP274 (BP Oil). Observations on the droplet behavior obtained from the PCO-Nikon 200mm Telephoto lens visualizations for the liquids are presented here. The term 'multiple experimental conditions' mentioned in the following refers to the suspended droplet experiments in air and nitrogen environments at different gas flowrates classified as low (5 SCFM), intermediate (10,15,20 SCFM) and high (25 SCFM) flowrate.

As will now be described, droplets of each liquid are suspended on the thermocouple bead and visualized as they experience the rapid heating in the IR heater. The droplets undergo a quiescent period, where they exhibit minimal movement in terms of changes in shape or size. This quiescent period is followed by different droplet behavior events which we label as DE-1, DE-2, DE-3, and DE-4 events. These droplet behaviors events will be described and illustrated in this section. A lapse time *t* associated with behavior signifies the start or onset of the observed behavior. Figure 7-6 explains the schematic of the manual trigger start, elapsed time of the various DE events in relation to the IR heater, visualization system and the temperature data logger.

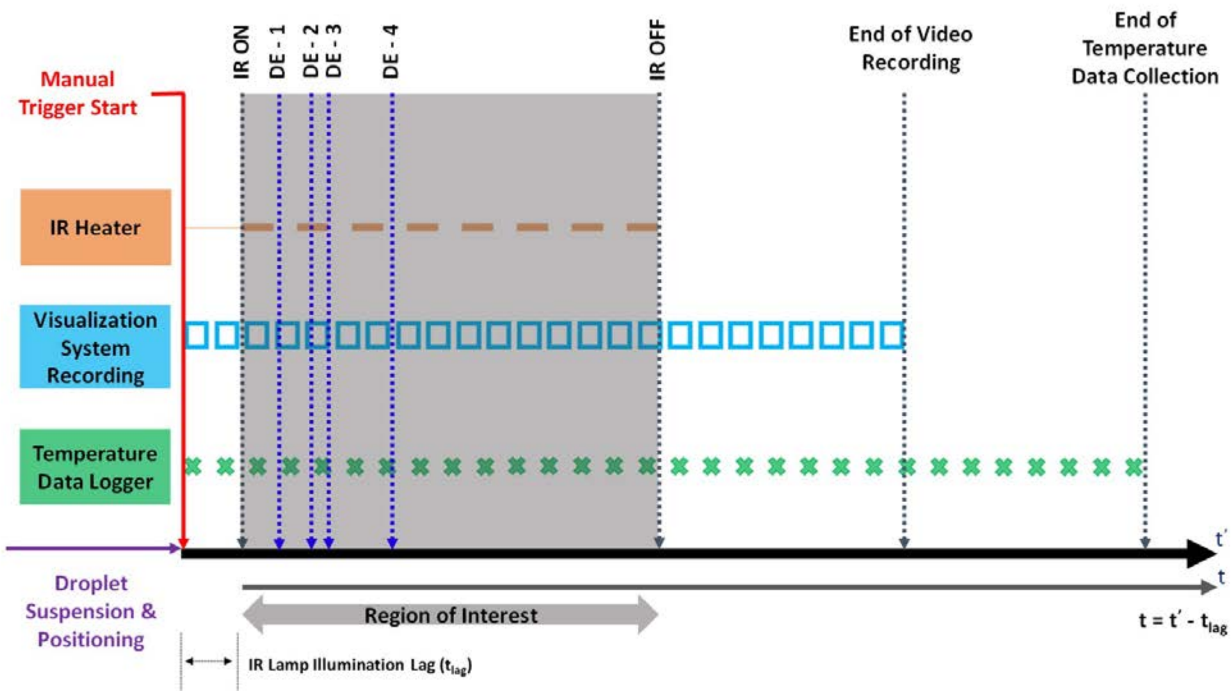

Figure 7-6: Schematic of droplet behavior events (DE-1, 2, 3, 4) in relation to the IR heater, visualization system, and the temperature data logger.

### 7.2.1. E100 – Pure Ethanol

For E100 droplets suspended on the thermocouple bead in low flowrate air and nitrogen environments, we observed ‘single-bubble formation behavior’ inside the droplet as it heats up. The onset of this behavior as shown in the Figure 7-2 earlier characterizes the DE-1 (droplet-behavior event type 1) event. In the visualizations, we observed the bubble formation within the droplet and the bubble seemed to originate from the surface of the bead. As the time elapsed, we observed the bubble grow large enough to cause the droplet surface boundary to expand. This entire process of bubble formation and expansion occurs quickly over a period of about 0.5 seconds. The DE-1 is followed by the ‘micro-droplet escape behavior’ during which several micro-droplets, each small compared to the initial droplet size ($d_0$), eject from the droplet. Figure 7-7 shows an image sequence of the micro-droplet escape behavior (representative behavior shown with a different liquid type) observed in the low magnification visualizations. This event was accompanied by a water-blob type behavior where the droplet constantly changes in shape and wobbles while remaining suspended from the thermocouple bead. We labeled this phenomenon as the 'blob behavior'. Figure 7-8 shows an image sequence of a blob behavior (representative behavior shown with a different liquid type) event in low magnification. The micro-droplet ejection and blob behavior often occur in tandem with the latter behavior generally preceding the former. Following these behaviors, the droplet consistently reduces in size (refers to the droplet diameter) until no more of the droplet is present on the thermocouple bead. When there is no evidence of liquid on the bead in our visualization image, we mark the corresponding elapsed time associated with that image as the DE-4 (no droplet) event. When the suspended droplet is relatively large, instead of the single bubble formation behavior we observed the 'droplet surface ripple behavior' end the quiescent period and characterizes the DE-1 event. In such visualizations, the image frame at which the first ripple action started was considered for marking the DE-1 event. Ripple behavior is not shown here since the behavior event is better observed in a recording video over an image sequence.

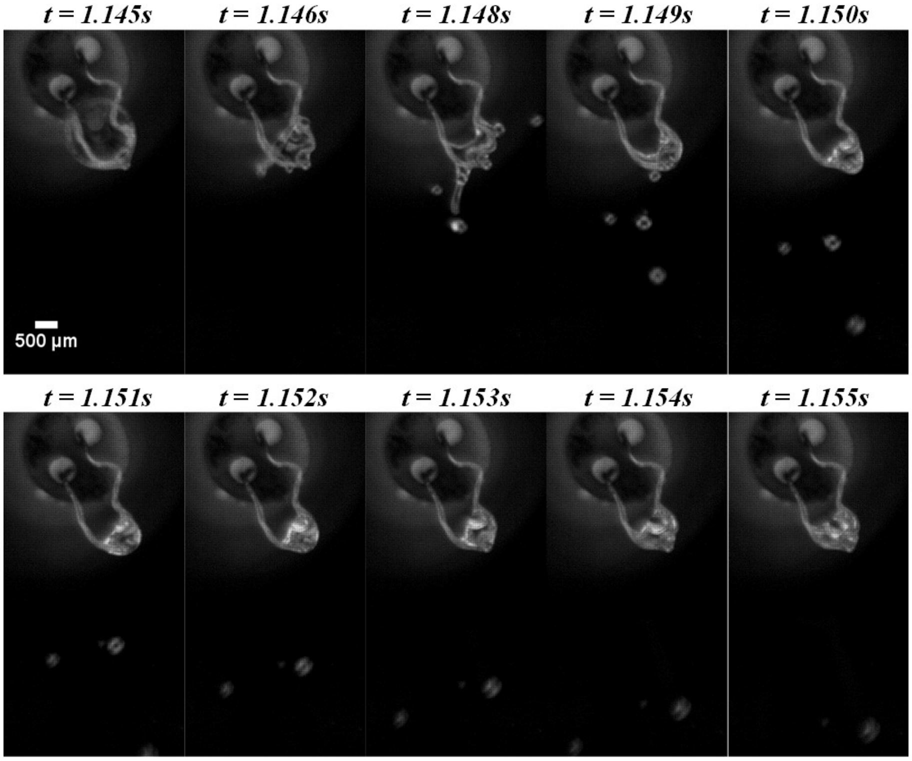

Figure 7-7: Low magnification images of the microdroplet escape behavior in a E70G30 droplet ($d_0$ = 1.04 mm; $t_{res}$ = 2.19s) suspended in intermediate flowrate (10 SCFM) air environment.

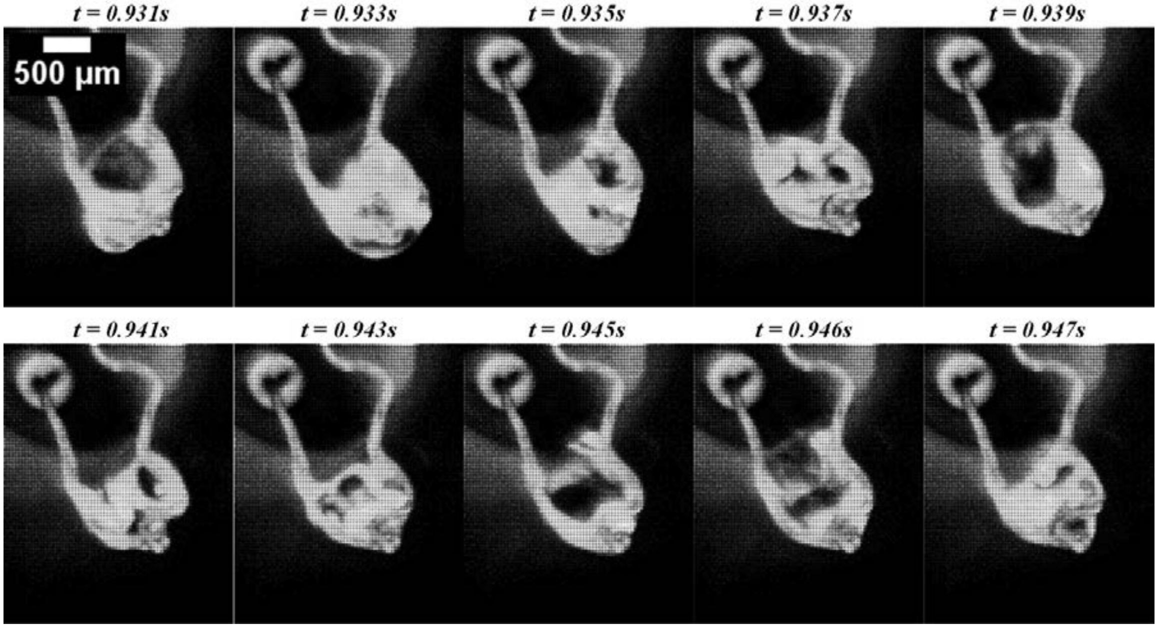

Figure 7-8: Low magnification images of blob behavior in a E70G30 droplet ($d_0$ = 1.07 mm; $t_{res}$ = 1.95s) suspended in low flowrate (5 SCFM) nitrogen environment.

From our observations, the E100 droplets suspended in high flowrate air and nitrogen environments did not exhibit either the single bubble formation or blob behaviors. Instead, the droplets maintained a near spherical shape, and consistently reduced in size in a volatilizing fashion analogous to an evaporating liquid on a hot surface until no liquid was present on the bead (like the behavior observed in B100 and M100 droplets represented in Figure 7-11 and Figure 7-13). For all our experimental conditions, we did not observe a strong evidence to suggest a combustion behavior. Lack of a clear flame visualization combined with the absence of steep temperature rises in the droplet temperature profile that are usually associated with a combusting droplet led us to believe a vaporization scenario in our droplet experiments. The elapsed time ($t$) of DE-1 and DE-4 events varied considerably with the gas environment, gas flowrate, and the initial droplet dimeters ($d_0$) irrespective of vaporization or combustion behaviors. Further understanding of the variations with respect to operating conditions are discussed in the following sections.

### 7.2.2. E30G70 - 30% Ethanol-70% Glycerol Blend

We observed E30G70 suspended droplets exhibit multiple-bubble formation behavior to mark the end of the quiescent period and subsequently the DE-1 event. Micro-bubbles (much smaller than the bubbles observed during the single bubble formation in E100 shown in Figure 7-2) emerged within the suspended droplet. As in the E100 droplet, we observed the bubble grow and expand in size. This was followed by the micro-droplet escape behavior as shown in Figure 7-7 (representative behavior shown with a different liquid type) during which the several micro-bubbles formed within the droplet were ejected from the droplet surface for a brief period. We call these ejected micro volumes of the droplet ‘satellite droplets’; Following this period, we observed multiple bubble formation behavior to continue but without the ejection of satellite droplets that we refer to as the ‘puffing’ behavior (high magnification images of puffing are shown later in this chapter). In many instances, we also observed the puffing behavior to happen during the bubble growth and expansion that precedes the microdroplet escape behavior. Following the puffing and microdroplet escape behaviors, we observed pockets of vapor emerge from the droplet surface in a violent manner that lasts for a relatively shorten interval of time compared to a microdroplet escape event. We labeled this behavior as ‘primary microexplosion or ‘first microexplosion event’ as shown in Figure 7-3 (representative behavior shown with a different liquid type). In some droplets of E30G70, we observed the occurrence of more than one microexplosion event with a brief pause in-between vapor emission. We identified such behaviors as ‘secondary microexplosion event’ as shown in Figure 7-4 (representative behavior shown with a different liquid type). The visualization images that mark the start of primary microexplosion behavior were marked as DE-2, and the start of the final secondary microexplosion was marked as DE-3. After the microexplosion event(s), frequently we observed a reduced volume of the E30G70 suspended droplet to remain on the droplet bead. This liquid portion continued to vaporize and reduce in droplet diameter (*d*) without any appreciable fluctuations in *d* until no more liquid was present on the bead. We labeled this behavior as ‘residual droplet evaporation’ as shown in Figure 7-5 (representative behavior shown with a different liquid type), and the visualizations of such an event closely resemble that of the volatilizing behavior mentioned earlier for the E100 droplets.

For our experiments with the E30G70 liquid type in different operating conditions (air-low, air-high, nitrogen-low, nitrogen-high), the overall sequence of droplet behavior events followed the same pattern as described above. However, the elapsed time (*t*) of the events varied to an extent for each condition. Unlike the E100 droplets, vapor emissions were seen in all the visualizations either before or after the start of the micro-droplet escape behavior. However, its insufficient in the absence of a steep temperature rise in droplet temperature profile to conclude the behavior as combustion.

### 7.2.3. E70G30 - 70% Ethanol-30% Glycerol Blend

DE-1 events of E70G30 droplets were characterized either by the appearance of vapors around the droplet surface or by the observation of ripple movements across the droplet surface. Unlike the E30G70 blend, we did not observe single or multiple bubble formations within the droplet following the quiescent period for low flowrate air and nitrogen environments. Instead, the DE-1 event was followed by either the microdroplet escape behavior (Figure 7-7) or the primary microexplosion behavior (Figure 7-3). Also in such environments, we observed the primary microexplosion event to be followed by one or many secondary microexplosion events. Figure 7-4 shows an image sequence of secondary microexplosion behavior in a E70G30 droplet. In high flowrate air and nitrogen environments, we observed the micro-droplet escape behavior during the early stages of E70G30 droplet evaporation. For some droplet experiments of E70G30, this behavior event was followed by a delayed first microexplosion event. Continued microdroplet escape behavior or the primary microexplosion event was then followed by the residual evaporation behavior (Figure 7-5) for the remainder of droplet presence on the bead.

### 7.2.4. G100 - Pure Glycerol

G100 is the most viscous of all the liquids studied. The G100 droplets attach to the bead with minimum contact due to its high surface tension properties. As the viscosity and surface tension properties of the liquid change with temperature, the droplets wobble on the bead which marks the end of the quiescent period. We labeled this wobbling event as the ‘droplet swing behavior’ as seen in Figure 7-9. This event is either associated or closely followed with the observation of vapors around the droplet surface. Either the swing behavior or the appearance of vapor, depending on which was observed first is used as the elapsed time marker for the DE-1 event. From qualitative analysis of the G100 visualizations, we observed a brief period during the initial phase of evaporation where the appearance of vapors did not accompany a significant change in the droplet size. We referred to this brief period as the ‘surface evaporation phase’. Surface evaporation behavior is not shown here since the behavior event is better observed in a recording video over an image sequence. This behavior event generally occurs during the transient heating phase of G100 droplet evaporation as will be described in the section of high magnification experiments.  Following the surface evaporation phase, rapid droplet size reduction was observed until no more droplet volume was present on the thermocouple bead. The behavior of this final period of evaporation is comparable to the residual evaporation behavior described previously in blend liquids (E30G70 and E70G30) as seen in Figure 7-5. However, unlike the blend liquids, this behavior type constitutes a significantly longer period of the total droplet lifetime of G100 droplets. The droplet behavior G100 does not vary much with varying operating conditions. In isolated cases, we observed bubble formations happen within the droplet following the quiescent period. These bubbles however do not disturb the droplet surface as seen in the micro-droplet escape behavior of blends but instead breaks as it reaches to the surface boundary. We believe this bubble behavior is not a typical characteristic of the pure glycerol liquid type.

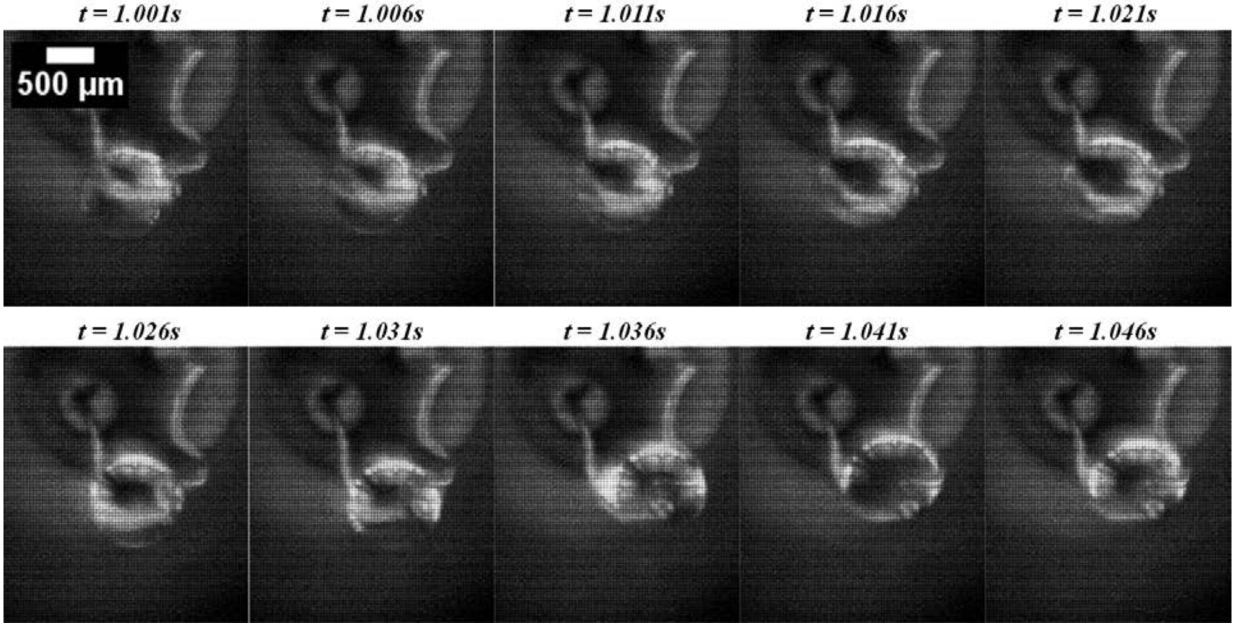

Figure 7-9: Low magnification images of swing behavior in a G100 droplet ($d_0$ = 1.06 mm; $t_{res}$ = 2.82s) suspended in low flowrate (5 SCFM) air environment.

### 7.2.5. Pure Hexadecane

Hexadecane was selected for its properties as a reference fuel in our studies with the E-G system. Hexadecane droplets suspended on the thermocouple did not exhibit microexplosion behavior. Following the quiescent period, we observed a behavior in which vigorous micro-bubbles emerge within the droplet and tiny fragments of the droplet emerge from the droplet surface in a regular fashion that appear as a mist of droplets in the visualizations. We labeled this behavior as ‘micro-droplet attrition’. Unlike the micro-droplet escape behavior, here the bubbles formed and the fragments that leave the droplet surface are extremely small and the droplet fragments follow a downward projection initially as they leave the droplet surface boundary. This micro-droplet attrition behavior was followed by a rapid droplet size reduction until no more liquid was present on the thermocouple bead. Figure 7-10 shows an image sequence of a typical micro-droplet attrition event for a hexadecane droplet. This type of attrition behavior was observed only in the high flowrate air and nitrogen environments. For the low flowrate environments, we observed a surface vaporization phase synonymous with our observations in G100 droplets with an associated *d* reduction.

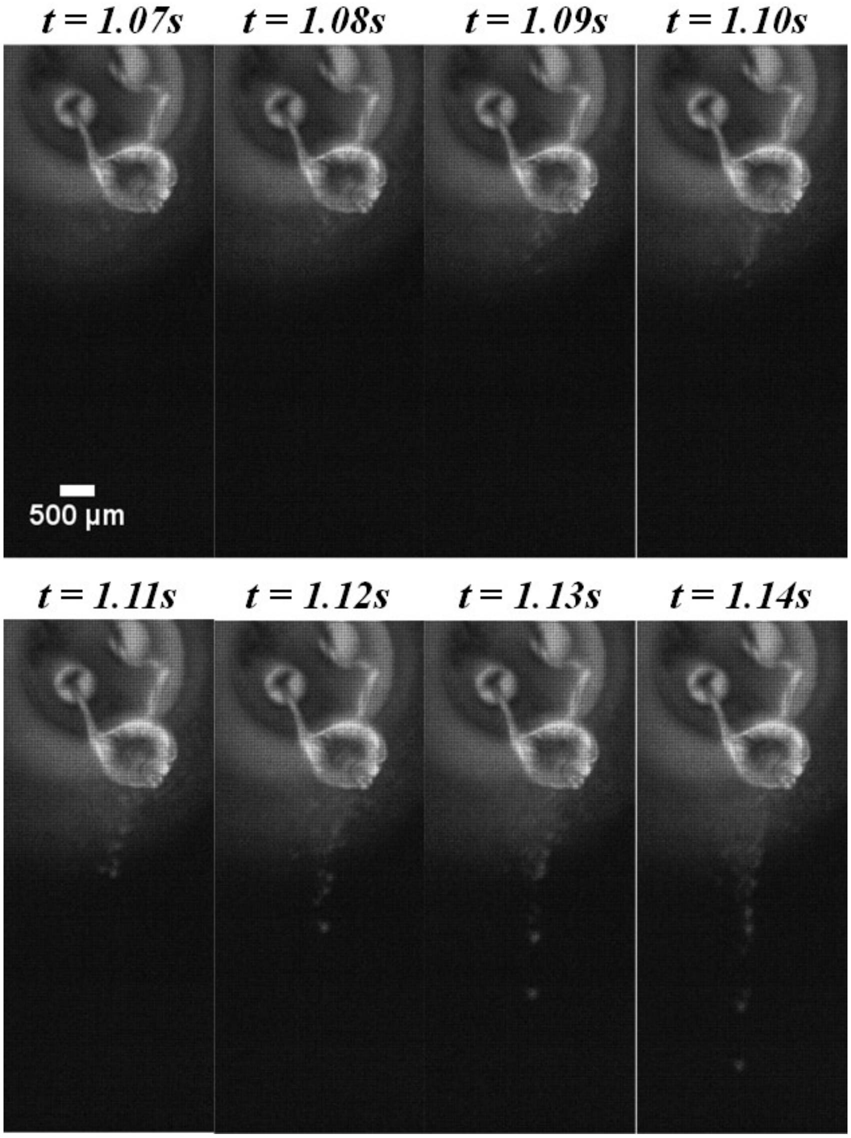

Figure 7-10: Low magnification images of microdroplet attrition behavior in a hexadecane droplet ($d_0$ = 0.88 mm; $t_{res}$ = 1.44s) suspended in low flowrate (5 SCFM) air environment.

### 7.2.6. B100 - Pure Butanol

B100 was a reference alcohol selected for comparison studies with the E-G system. The observations of the behavior of B100 droplets in all the experimental conditions were closely relatable to the E100 droplets. Single bubble formations as seen in Figure 7-2 were followed by the micro-droplet escape behavior with an associated blob behavior (Figure 7-8). As was the case in E100 droplet observations, only DE-1 and DE-4 events could be characterized from the visualizations of B100 droplet. For multiple experimental conditions, no significant changes were observed in terms of droplet behavior events. Figure 7-11 shows the lifetime of a typical B100 droplet suspended inside the IR heater.

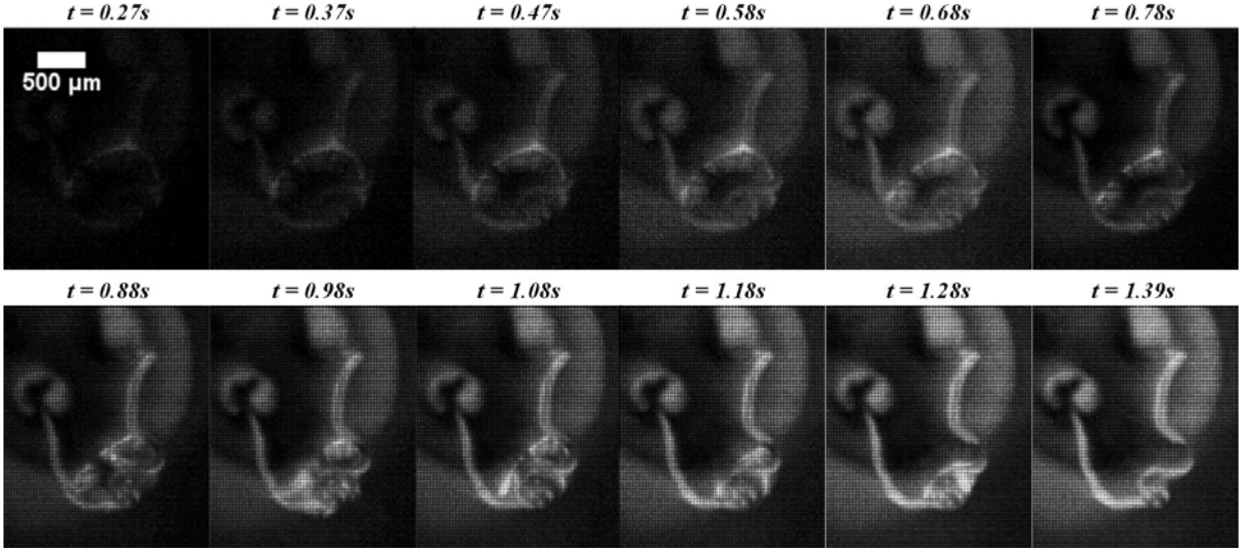

Figure 7-11: Low magnification images of the lifetime of a B100 droplet ($d_0$ = 0.85 mm; $t_{res}$ = 1.24s) suspended in high flowrate (25 SCFM) nitrogen environment.

### 7.2.7. Commercial Engine Oil - BP Turbo Oil 274 (BP Oil)

BP Turbo Oil 274 was selected to be a representative multicomponent liquid for comparison with the E-G system due to our parallel studies with the aviation liquids. From the visualizations, we found the suspended droplets of BP Oil exhibited a collection of the different behavior types discussed with the other liquid types. Followed by the quiescent period, we observed a surface evaporation phase analogous to G100 liquid type with vapors emerging from the droplet surface. This behavior event was followed by the micro-droplet attrition behavior analogous to hexadecane droplets (Figure 7-10), and the multiple bubble formations behavior in low flowrate air or nitrogen environments. We observed only the latter behavior for high flowrate air or nitrogen environments. Following that, droplet microexplosion was observed in all the operating conditions. This microexplosion behavior observed in the BP Oil droplets as shown in Figure 7-12 were found to be different than those observed in the E-G blends (E30G70 and E70G30). In the BP Oil microexplosion events, large cluster of vapor pockets escaped from the droplet surface boundary all at the same instant whereas, in the blend liquids, we observed the pockets of vapor escape from the suspended droplet in an intermittent fashion with a few microseconds apart between such events. Also, in all the operating conditions, residual evaporation behavior lasted for a short period of time as much of the droplet volume was lost in the microexplosion event that occurred earlier.

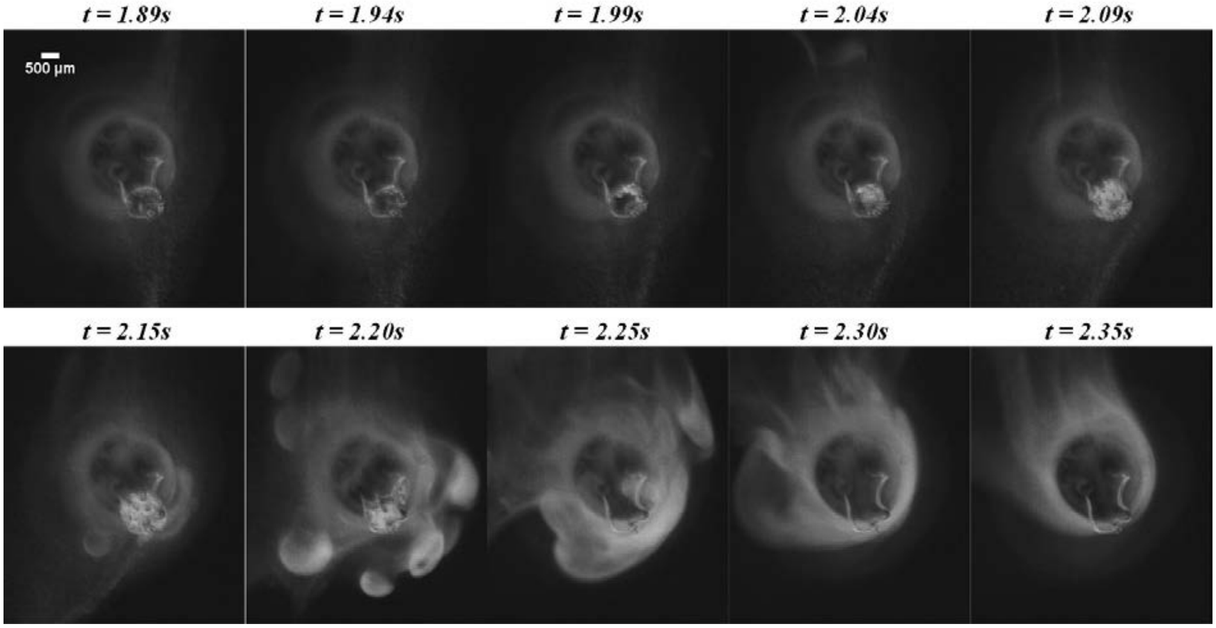

Figure 7-12: Low magnification images of microexplosion behavior in a BP Oil droplet ($d_0$ = 0.95 mm; $t_{res}$ = 2.59s) suspended in low flowrate (5 SCFM) air environment.

Unlike the other liquid types studied, for BP Oil droplet, we observed both vapors in the visualizations and a relatively steep increase in the droplet temperature profile. This evidence might suggest a partial combustion in the BP Oil suspended droplet. However, since the liquid properties of BP Oil are not accessible due to its proprietary nature, we believe it could also be a result of one or many high boiling point low volatile component in the liquid type, and hence we treat the droplet behavior as vaporization.

### 7.2.8. M100 - Pure Methanol

M100 is another pure alcohol type selected for comparative studies with the E-G system. Irrespective of the operating condition (air-low, air-high, nitrogen-low, nitrogen-high) in which the droplet was suspended, all M100 droplets exhibited a volatilizing phenomenon that resembled the residual evaporation behaviors observed earlier with E100, G100, and B100. Figure 7-13 shows the lifetime of a B100 droplet suspended inside the IR heater. No vapors were observed in the visualizations around the droplet surface for the entirety of the droplet lifetime. The visualization image frame marking the first distinct droplet size reduction was considered for the DE-1 event.

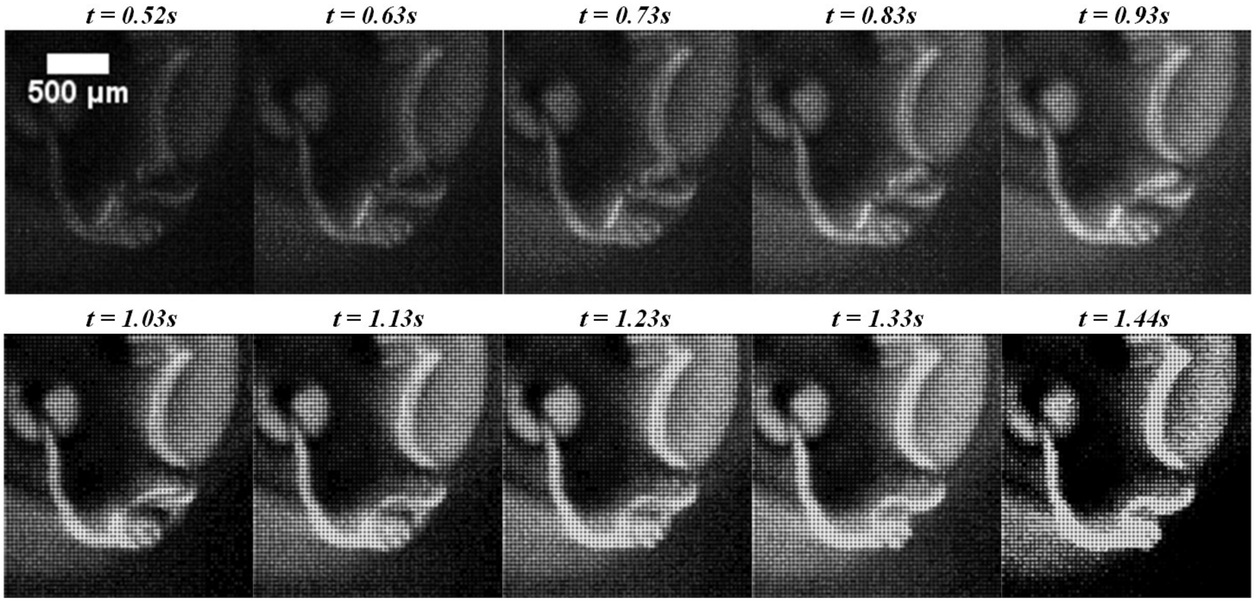

Figure 7-13: Low magnification images of the lifetime of a M100 droplet ($d_0$ = 0.85 mm; $t_{res}$ = 1.44s) suspended in high flowrate (25 SCFM) air environment.

## 7.3. E-G System – Multiple Gas Environment and Gas Flowrate Experiments

Operating conditions which can be controlled inside the IR heater include the type of gas environment, the flowrate at which the gas is pumped into the IR heater, and the heating rate inside the IR heater. In this section, the discussions will focus on the gas environment type and flowrates. The gas environment surrounding the droplet is air (house air) or nitrogen (ultra-high purity grade compressed nitrogen gas cylinder). Rotameters for each gas type on the control system (in SCFM) are adjusted to control the flowrate of the gas into the IR heater droplet experiment tube. The rotameter reading corresponding to 0 SCFM constitutes '*NO FLOW*' (no gas flow - stagnant environment), 5 SCFM constitutes '*LOW*' gas flowrate, 10, 15, and 20 SCFM refers to '*INTERMEDIATE*' gas flowrates, and 25 SCFM refers to '*HIGH*' gas flowrate.

E70G30 (70% Pure Ethanol – 30% Pure Glycerol) liquid type was selected as the test liquid for the gas flow type and flowrate experiments. Droplet experiments for this study were performed on the 125 µm Pt-Rh thermocouple. The IR heater was operated with a RUN ADJUST setting of 10 (maximum heating rate inside IR heater) and TIME ADJUST setting of 10 (IR lamps illuminate for ~9s and then turn off automatically). Droplet behavior videos were recorded with the PCO camera-Nikon 200 mm TF lens (low magnification) visualization setup. As explained before, manual triggering option is used for syncing the IR heater, visualizations and temperature data collection. All the elapsed time reported from here on are adjusted to exclude the offset '$t_{lag}$' of 1.4s that results from the starting delay of the IR heater lamps.

### 7.3.1. Quantitative Low Magnification Visualization Data

Low magnification visualization videos were used to identify distinguishable significant events for each suspended droplet experiment. Such significant events are labelled as DE-1, DE-2, DE-3, and DE-4. DE-1 includes events such as the appearance of a bubble, rippling effect on the droplet surface, swinging behavior of the droplet, appearance of vapors, and first change in the droplet diameter. DE-2 represents the first microexplosion event in a droplet. DE-3 represent the final microexplosion event in a droplet. DE-4 represents the instant at which no droplet is seen on the thermocouple bead. The corresponding elapsed time information for the video frame that marked the start of an event were used for determining the following quantitative data.

*Quiescent time* (QT, ms) – Refers to the elapsed time ($t$) difference between the IR ON and the instant a DE-1 event was observed. This is the time taken for the suspended droplet to respond to the increasing temperature within the droplet under the selected operating condition.

*Behavior time* (BT, ms) – Refers to the elapsed time ($t$) difference between the instants at which the DE-1 and DE-4 events were observed. This is the time taken by the suspended droplet to completely evaporate from the thermocouple bead after its first significant event DE-1 was identified.

*Residence time* (RT, ms) – Refers to the elapsed time ($t$) difference between the IR ON and the instant a DE-4 event was observed. This is the total time the suspended droplet resides on the thermocouple bead, meaning, the instant from which the droplet experiences heating to the instant it completely evaporates from the thermocouple bead.

*Residual evaporation time* (ms) – Refers to the elapsed time difference between the instants at which the DE-3 and DE-4 events were observed. This is the time taken by a *residual droplet* (refers to the droplet volume remaining after a final microexplosion event) to completely evaporate from the thermocouple bead. Quantification of residual evaporation time was relevant only in the droplets of binary and multicomponent mixtures where the microexplosion events were clearly distinguishable.

*First microexplosion time* (ms) – Refers to the elapsed time (*t*) difference between the IR ON and the instant a DE-2 event was observed. This is the total time taken for the suspended droplet to exhibit the first microexplosion event.

### 7.3.2. Effect of Initial Droplet Diameter

To study the effect of operating conditions on droplet evaporation, suspended droplet experiments were carried out at multiple gas flowrates controlled through the rotameter. For every condition, the experiment was repeated for three individual droplets and the corresponding visualizations and temperature data were recorded. Figure 7-14, Figure 7-15 and Figure 7-16 shows the relation of initial droplet diameter ($d_0$) to quiescent, behavior, and residence times.

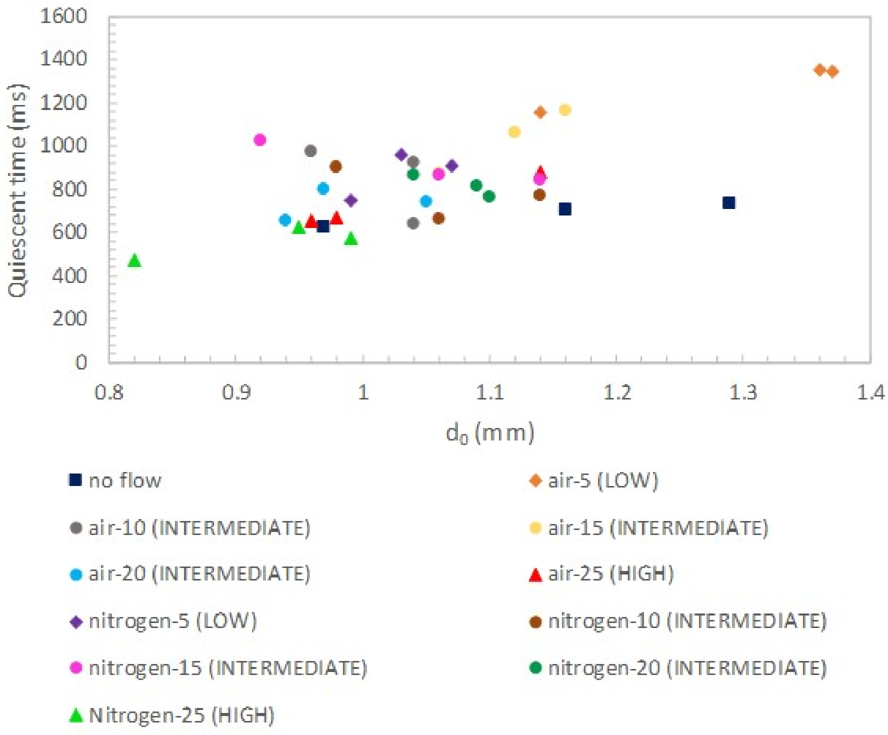

Figure 7-14: Relation between quiescent time and the initial droplet diameter ($d_0$) at multiple flowrates for air and nitrogen environments.

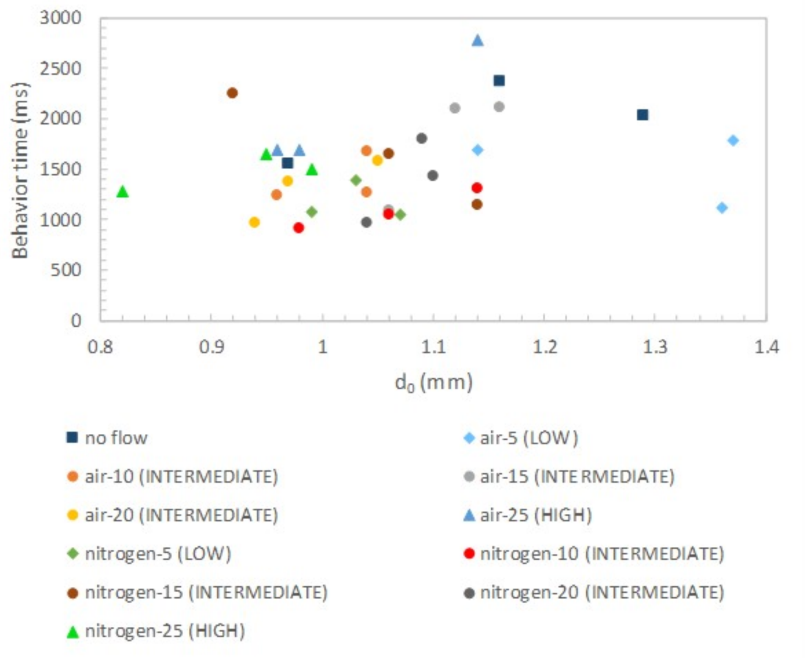

Figure 7-15: Relation between behavior time and the initial droplet diameter ($d_0$) at multiple flowrates for air and nitrogen environments.

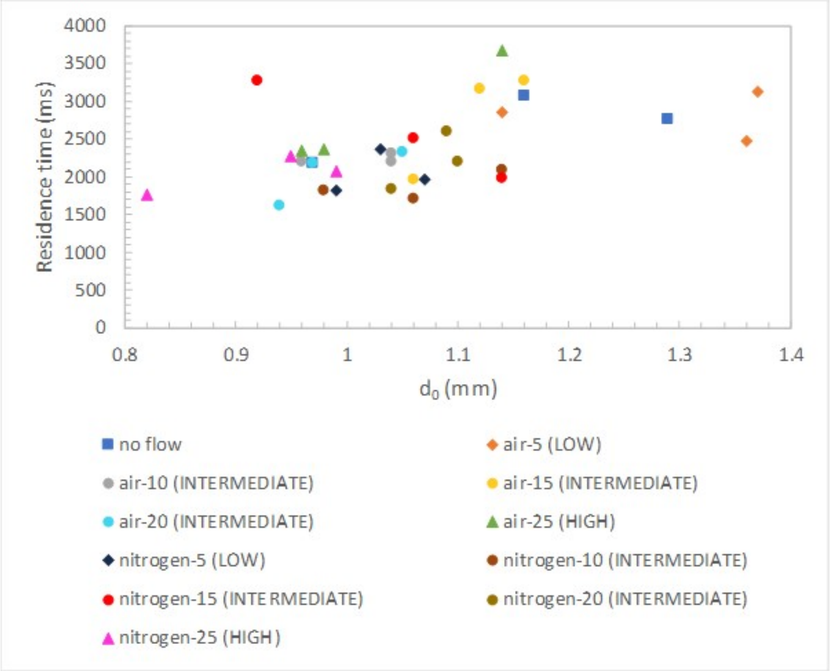

Figure 7-16: Relation between residence time and the initial droplet diameter ($d_0$) at multiple flowrates for air and nitrogen environments.

While the initial droplet size was not deliberately varied, some differences in $d_0$ were inherent in the process. Figure 7-14, Figure 7-15, and Figure 7-16 show that the initial droplet diameter had the same effect on the quiescent, behavior, and residence times. The correlation between each of the three times (quiescent, behavior, and residence) and $d_0$ for all operating conditions are shown in the Figure 7-17 with a linear fit and corresponding $R^2$ values. As we can see from the $R^2$ values, irrespective of the operating condition, the linear fit works reasonably well for the quiescent time but fits poorly for the behavior and residence times. The liquid type E70G30 selected for studying the effect of operating conditions is a binary mixture made up of 70 vol% ethanol and 30 vol% glycerol. Generally, droplets of blends of two or more liquid components with difficulty boiling points exhibit bubbling behavior resulting in microdroplet escape or microexplosion events.

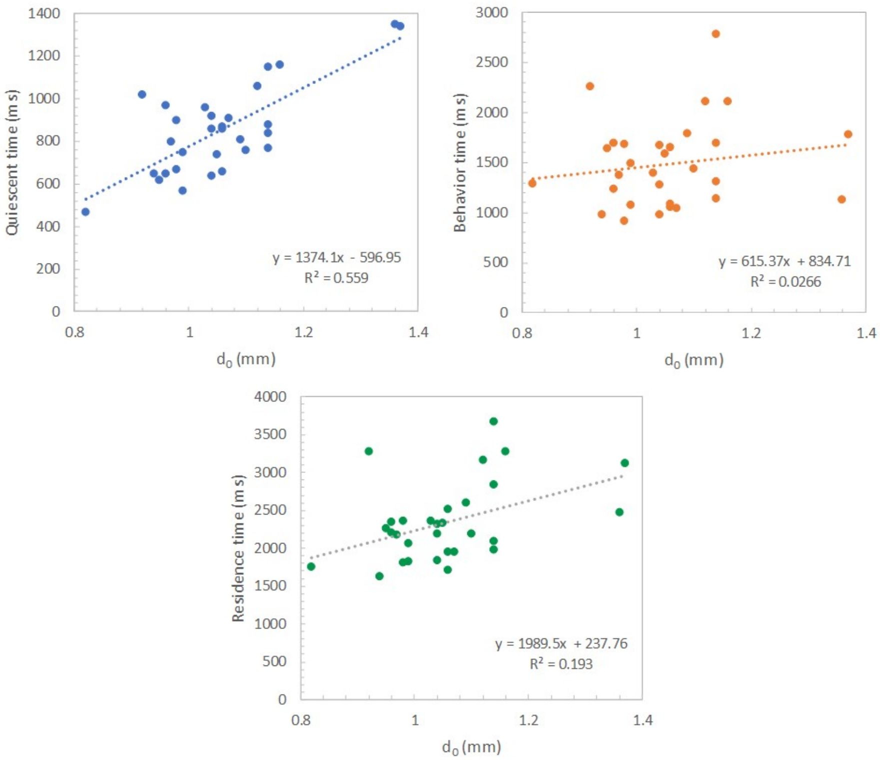

Figure 7-17: Quiescent, behavior, and residence time for E70G30 droplets with the initial droplet diameters ($d_0$) at multiple flowrates for air and nitrogen environments.

The inherently random nature of these events results in the varying behavior time for each droplet irrespective of its $d_0$. Since, the residence times is largely dominated by the value of the behavior time, we see the randomness extending to that as well. This explains the poor fit for the behavior and residence times when plotted against the initial droplet diameter.

### 7.3.3. Effect of Gas Flowrate and Gas Environment

To isolate the effects of gas flowrate and the type of gas environments, droplets of similar $d_0$ were selected for each condition. The average $d_0$ selected for all the gas flowrates (low, intermediate, and high) in air and nitrogen environments is 1.06 mm with a standard deviation of 0.05 mm. Plots from Figure 7-18 shows the effect of operating condition on the quiescent, behavior and residence times.

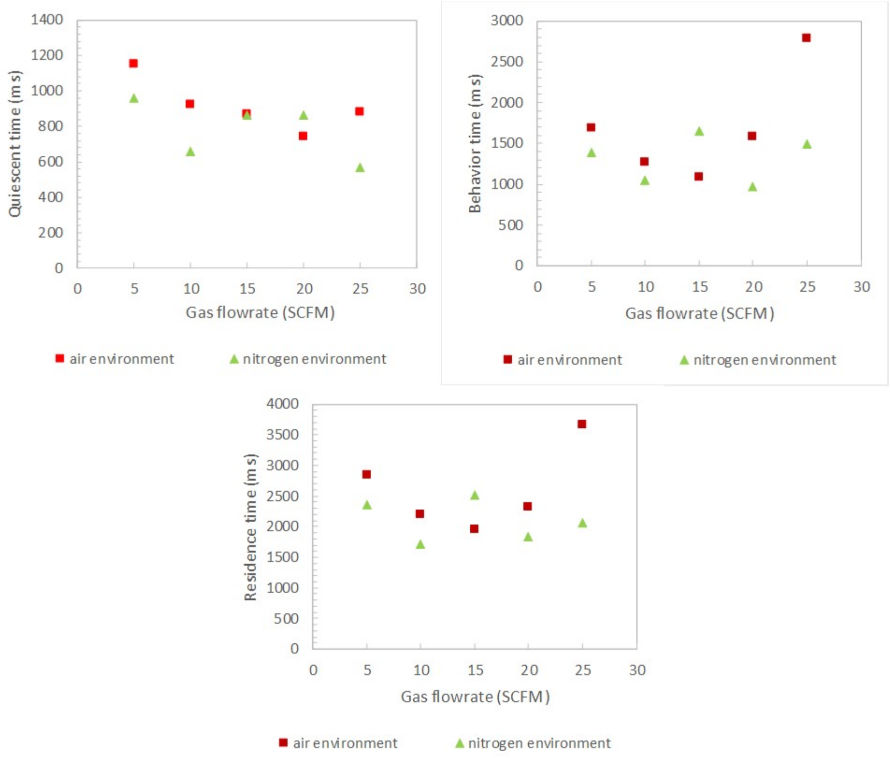

Figure 7-18: Effect of gas flowrate and gas environment type on the quiescent (top left), behavior (top right), and residence (bottom) times for E70G30 droplets of similar $d_0$ (10 SCFM = 1.85 m/s).

The quiescent times for air and nitrogen environments are relatively close with an average difference of 180ms across the different gas flowrate conditions. Figure 7-19 shows the plot of quiescent time to the gas flowrate with a linear fit and corresponding $R^2$ value. From the plot, we see the fit to be poor for the quiescent time with respect to increasing gas flowrate.

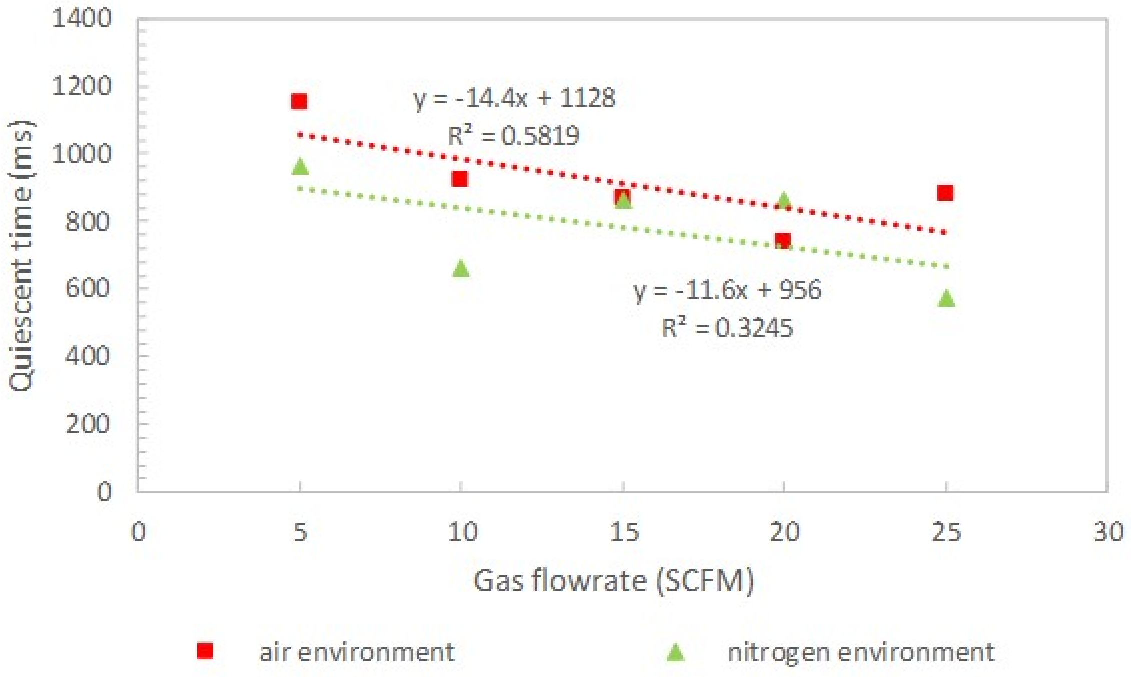

Figure 7-19: Quiescent time of E70G30 droplet with respect to changing gas flowrate in air and nitrogen environment.

From the Figure 7-18, we can see that the behavior and residence times also would fare poorly for a linear fit (fit not shown here). Moreover, we notice longer behavior and residence times at flowrate values near the '*high*' level. As mentioned before, residence time is influenced mainly by the behavior time (usually larger than the quiescent time), and hence the behavior time was investigated to understand this trend. Towards that, the behavior time was characterized into two categories: microexplosion time and residual evaporation time. Figure 7-20 shows the two-part breakdown of the behavior time along with the quiescent time for similar $d_0$ E70G30 droplets in multiple flowrate air and nitrogen environments.

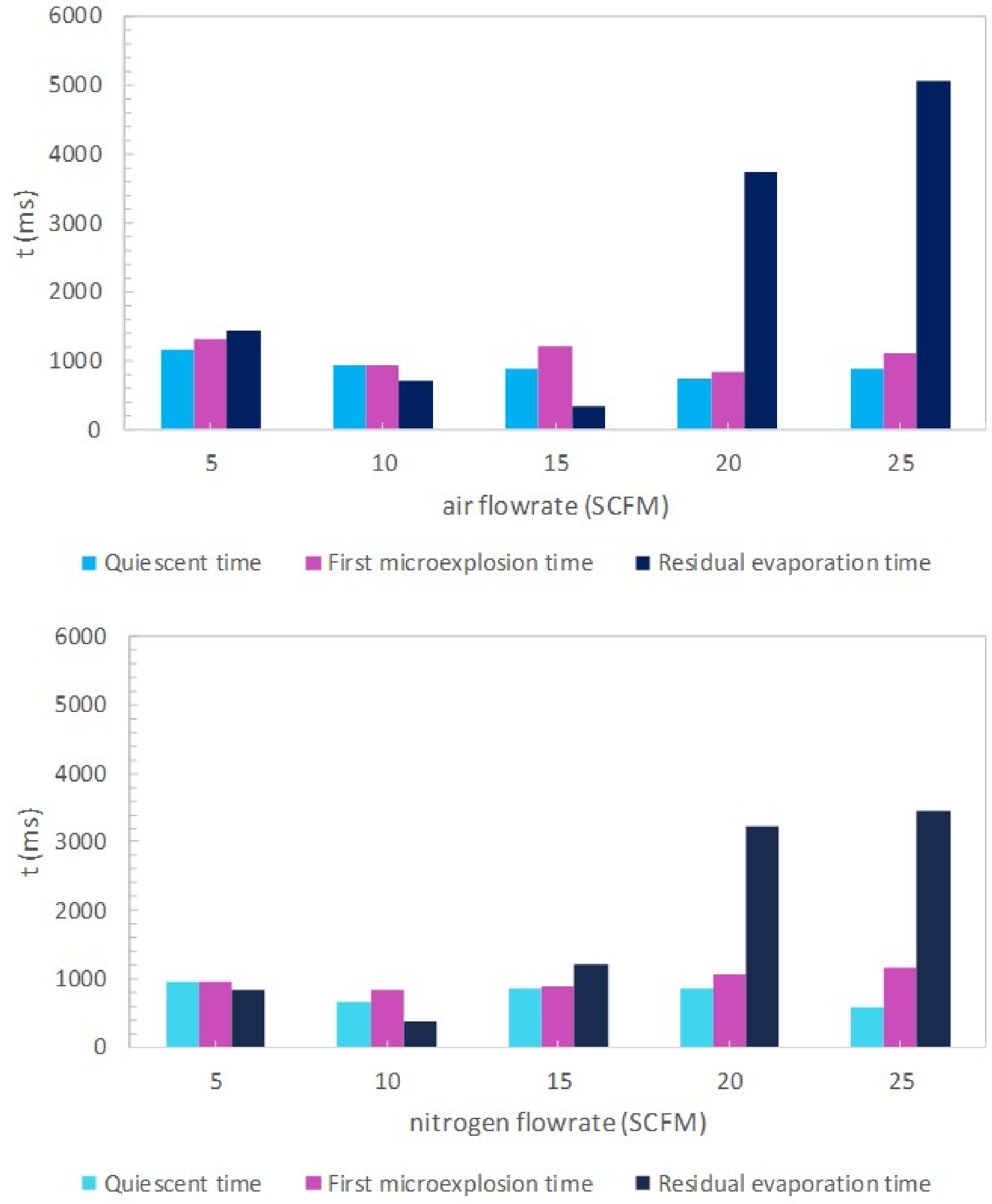

Figure 7-20: E70G30 droplet behavior time breakdown along with the quiescent time for multiple gas flowrate conditions in air and nitrogen environment (10 SCFM = 1.85 m/s).

Observations from the plots show that the first microexplosion time and the quiescent time are very close for majority of gas flowrate conditions. This shows that the first microexplosion time in the E70G30 droplet happens as soon as the quiescent droplet period ends. However, the residual evaporation time of intermediate flowrate (20 SCFM) and the high flowrate (25 SCFM) are very different from the rest of the gas flowrate conditions. The residual evaporation time in 20 and 25 SCFM conditions are more than the double the other flowrate conditions. This shows that the strength of the microexplosion event is not uniform in E70G30 across multiple flowrate conditions. When the microexplosion event in a liquid droplet is strong, it results in an increased loss of liquid volume of the droplet. Subsequently, a smaller volume of the liquid with a larger concentration of the low volatile component (residual droplet) remains on the droplet bead, and it takes a relatively shorter time for that droplet volume to evaporate completely. On the other hand, a weaker microexplosion event results in a large volume of the droplet on the bead and consequently longer times for that residual droplet to evaporate completely.

Low magnification image sequences of the first microexplosion event in a E70G30 droplet are shown in Figure 7-21. From the figure, we see a quiescent droplet at $t$ = 0.967s exhibiting microexplosion for the first time it heats up with the release of satellite droplets starting at $t$ = 0.970s. From the images, we see that the satellite droplets are of varying size with those seen at $t$ = 0.972s (inside circle marker) being larger than that of the satellite droplet seen at $t$ = 0.980s (inside circle marker). Also, we see the droplet return close to its original shape albeit with a lower volume compared to its initial volume ($t$ = 0s) after the microexplosion event as seen at $t$ = 0.984s. This loss of droplet volume during a microexplosion event signifies the strength of the microexplosion. Increased loss of liquid volume during the event generally signifies a strong microexplosion and vice versa in a weaker microexplosion. Figure 7-22 shows the microdroplet escape behavior in a E70G30 droplet. Unlike a microexplosion event, there is minimum fluctuation of the droplet dimeter, and the droplet maintains its original shape from the start of bubbling to the release of satellite droplets as seen from *t* = 1.36s to *t* = 1.344s. From *t* = 1.345s onwards till the end of image sequence, we see the trajectory of the satellite droplets. The droplet shown in the image sequence ($d_0$ = 1.37 µm) is more than 350 µm larger than the average droplets seen in the

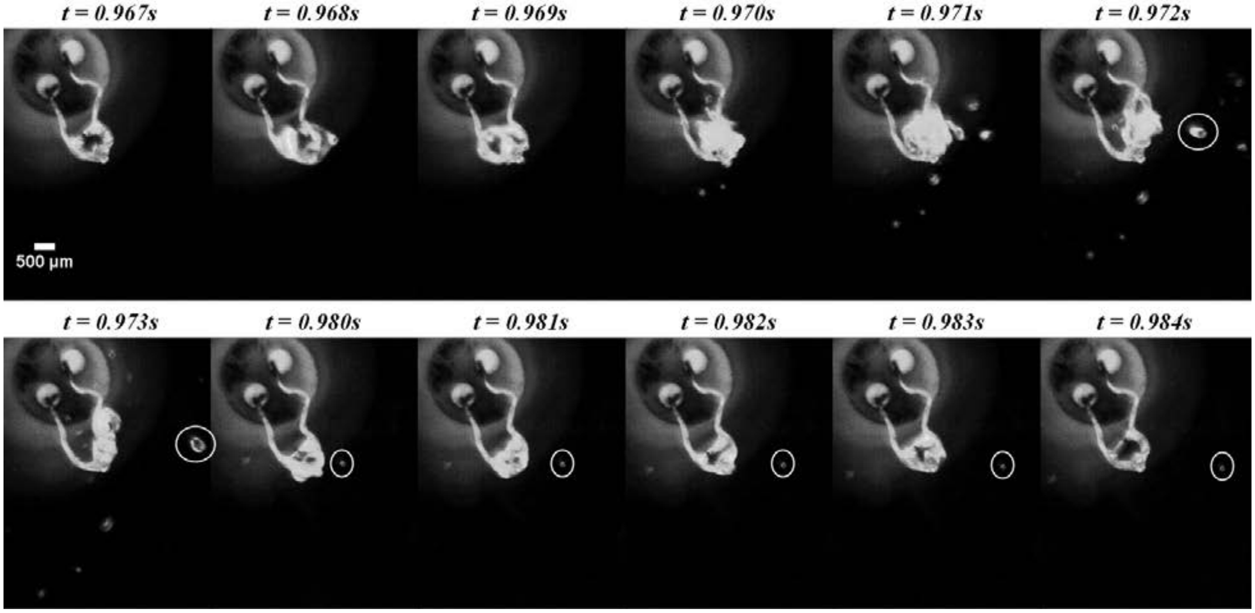

Figure 7-21: Low magnification image sequence of the first microexplosion event in a E70G30 ($d_0$ = 0.96 µm) droplet.

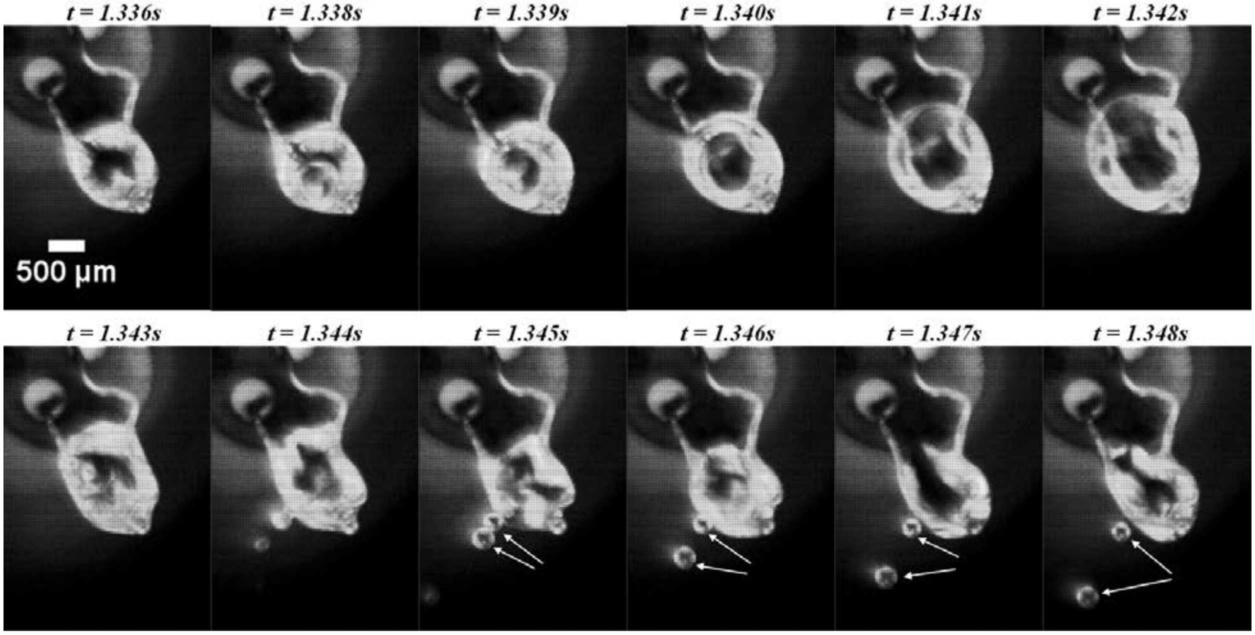

Figure 7-22: Low magnification image sequence of the microdroplet escape behavior in a E70G30 ($d_0$ = 1.37 µm) droplet.

studies. In such droplets, we generally observed the microdroplet escape to precede the first microexplosion event.

The variable strength of the microexplosion events in the E70G30 blend droplets are further emphasized by calculating the quiescent time to behavior time ratio (QT/BT ratio) in all the flowrate conditions of air and nitrogen environments. Figure 7-23 shows the QT/BT ratio and the corresponding correlations with the trendline equations and $R^2$ values. Reasonable good fit from the plots show that the ratio of quiescent to behavior time decreases with increasing gas flowrate for both environments. In other words, the strength of microexplosion event could be inversely proportional to the gas flowrate and that would be true irrespective of the gas environment for the E70G30 liquid type.

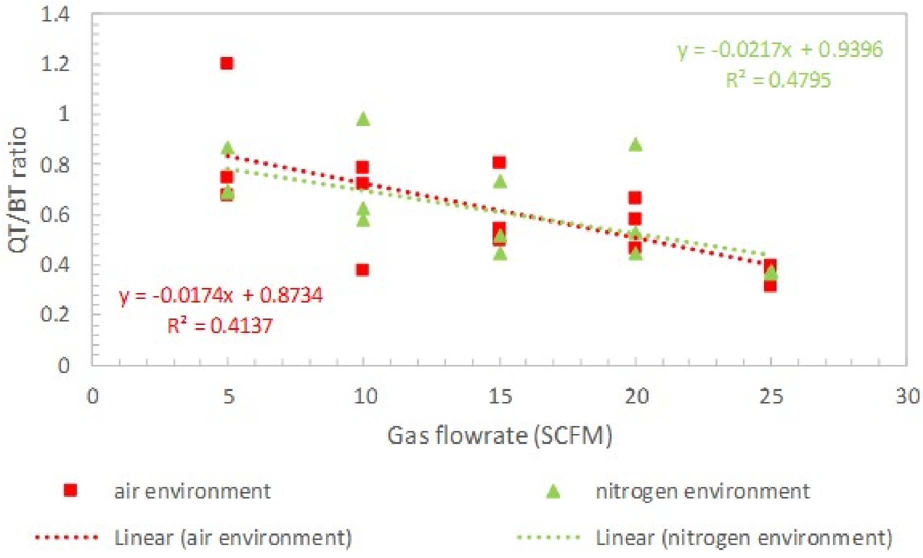

Figure 7-23: E70G30 droplet QT/BT ratio and their respective linear correlations (bottom) for multiple gas flowrate in air and nitrogen environments.

Droplet temperature data were also simultaneously collected with the low magnification visualizations for the evaporating E70G30 droplet in various operating conditions. The temperature data of interest is between the IR ON and the DE-4 droplet event markers. Discussions regarding the typical E70G30 droplet temperature profile are in the following section dealing with multiple liquid types. The droplet temperature profile can be divided into three distinct periods as follows:

*Period-1: Cold droplet heat-up period* (ms) – This refers to the period ranging between the IR ON event and the instant at which the droplet temperature is approximately 12-15°C higher than its starting temperature. The criteria for this period is that the temperature difference between any two readings is around 2-5°C. This temperature difference when expressed as the instantaneous temperature increase $(T_i - T_{i-1}/t_i - t_{i-1})$ comes around 9-17°C/s.

*Period-2: Heating rate period* (ms) - This refers to the period in which the evaporating droplet has the highest heating rate and it generally occurs between the cold droplet heat-up period and a droplet temperature plateau. From the droplet temperature data, this period is identified through the instantaneous temperature increase rate varying between 69-215°C/s. After identification, average temperature increase rate $(T_1 - T_i/t_1 - t_i)$ is calculated. A linear fit for this data provides a slope which is referred to as the maximum heating rate of the droplet (°C/s).

*Period-3: Temperature plateau* (ms) – This refers to the period in which the instantaneous temperature increase is 9-34°C/s but the average temperature increase rate is at its lowest among the three periods.

E70G30 droplet temperature profile comparison across multiple (low, high, and intermediate) gas flowrate conditions between air and nitrogen environments are shown in Figure 7-24, Figure 7-25, and Figure 7-28. The square (■) and triangle (▲) markers in the temperature profile plot provides an estimate of the quiescent time, and residence time respectively for that operating condition. Typical droplet temperature profile trends of a pure ethanol or glycerol liquid type show a linear temperature increase following the cold droplet heat-up period, and end with a temperature plateau as the internal droplet temperature reaches its respective boiling point. However, E70G30 is a blend droplet, and hence the droplet temperature profile analysis does not strictly adhere to behavior trends typical of pure liquids. More on this topic will be discussed in the following section involving multiple liquid types. Any *T* data after the ▲ marker refers to the profile of the thermocouple material with no liquid and are not considered for the analysis. It is important to note that the responsiveness of the thermocouple material to read the temperature data roughly approximates to +0.2s for all the operating conditions and hence the droplet events would be offset by this time when compared with the droplet temperature profile.

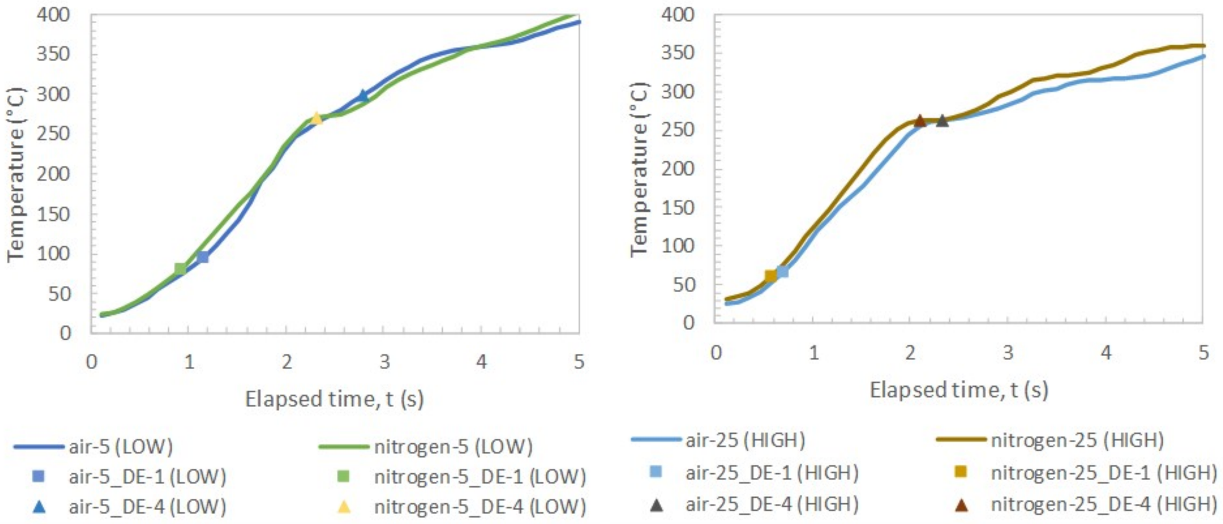

Figure 7-24: Droplet temperature profile comparison between air and nitrogen environments in low (left) and high (right) gas flowrate conditions.

Table 7-1 shows the heating rate values in different temperature periods along with their corresponding time duration and temperature difference for all E70G30 experiments. From the table, we can see that the heating rate period (period-2) is the most dominant in terms of both the temperature increase and the time duration. Figure 7-24 shows that the E70G30 droplet temperature profiles comparisons between air and nitrogen environments in low and high flowrate conditions. From the Figure 7-24 and Table 7-1, we see that the difference in period-2 heating rates between air and nitrogen environments are relatively close for low flowrate (1.6°C/s) over high flowrate (12.1°C/s) conditions.

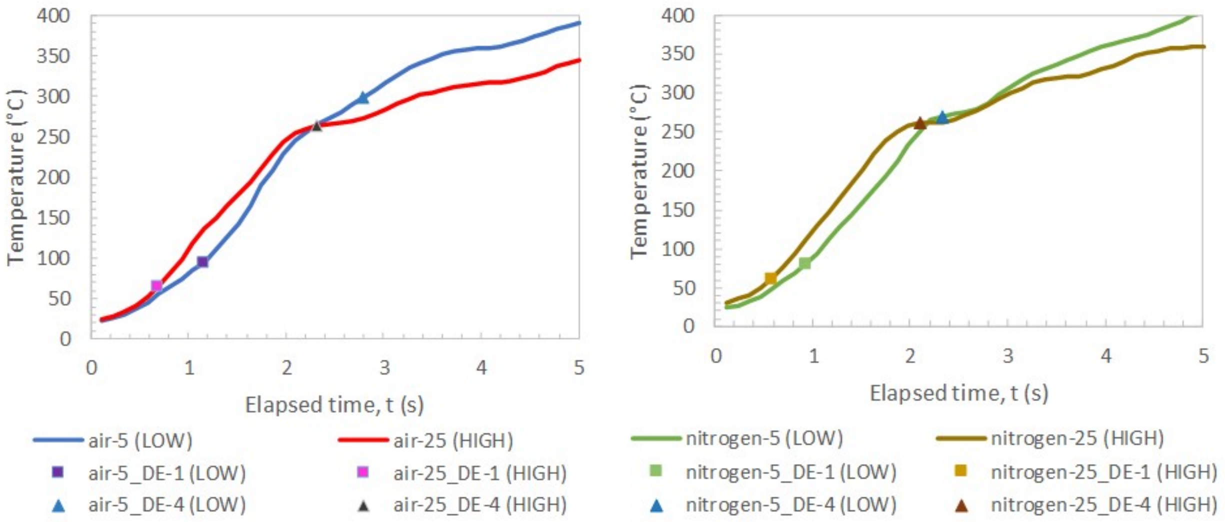

Figure 7-25: Droplet temperature profile comparison between low and high flowrate conditions in air (left) and nitrogen (right) gas environments.

Table 7-1: Heating rate values in different temperature periods along with their corresponding time duration (Δ*t*) and temperature difference (Δ*T*) for all E70G30 experiments.

| Experiment | Period-1: Cold droplet heat-up period | | | Period-2: Heating rate period | | | Period-3: Temperature plateau | | |
|---|---|---|---|---|---|---|---|---|---|
| | Heating rate (°C/s) | Δt (ms) | ΔT (°C) | Heating rate (°C/s) | Δt (ms) | ΔT (°C) | Heating rate (°C/s) | Δt (ms) | ΔT (°C) |
| E70G30-air-5 | 31.5 | 349 | 7 | 128.1 | 1980 | 235 | 0 | 0 | 0 |
| E70G30-air-10 | 32 | 349 | 7 | 138.6 | 1864 | 247 | 37.2 | 233 | 9 |
| E70G30-air-15 | 28.3 | 349 | 7 | 138.8 | 1864 | 232 | 0 | 0 | 0 |
| E70G30-air-20 | 27.4 | 349 | 6 | 101.6 | 2679 | 265 | 0 | 0 | 0 |
| E70G30-air-25 | 34.7 | 349 | 8 | 132.5 | 1747 | 221 | 31 | 1048 | 36 |
| E70G30-nitrogen-5 | 33.6 | 349 | 8 | 129.7 | 1864 | 233 | 35.8 | 582 | 23 |
| E70G30-nitrogen-10 | 32.4 | 349 | 8 | 145.4 | 1631 | 219 | 18.2 | 932 | 22 |
| E70G30-nitrogen-15 | 29.4 | 349 | 7 | 129.8 | 2097 | 245 | 37.3 | 582 | 23 |
| E70G30-nitrogen-20 | 31 | 349 | 7 | 142.3 | 1631 | 214 | 33.3 | 815 | 29 |
| E70G30-nitrogen-25 | 35.7 | 349 | 8 | 144.6 | 1631 | 218 | 19.5 | 582 | 13 |

Figure 7-25 shows the droplet temperature profiles comparison between low and high flowrates in air and nitrogen environments. From the Figure 7-25 and Table 7-1, we see the differences in the period-2 heating rates of low and high flowrate conditions to be 4.4°C/s and

14.9°C/s for air and nitrogen environments. From our experiments with multiple liquids (discussed in the next section), we found the breakdown of the temperature profile into multiple periods to be less robust in blend liquids than pure liquids for analyzing the change in the heating rate of the droplet. Due to the microexplosion and puffing events in a blend liquid such as E70G30, frequently the droplet looses its spherical shape and does not stay on the thermocouple bead for the entirety of the droplet evaporation. During such events, the droplet fragments and the fragments thus formed attach to the thermocouple wire and continue to evaporate. This behavior is exhibited as irregular instantaneous temperature increase ($T_i$ - $T_{i-1}$/$t_i$ - $t_{i-1}$) values and subsequently the absence of period-3 (zero values) as seen for some conditions in Table 7-1.

Figure 7-26 shows the puffing behavior in a E70G30 droplet. From the figure, we see that the droplet size in terms of droplet diameter (*d*) increases and decreases from *t = 1.190s* to *t = 1.214s* without the release of satellite droplets typical of a puffing behavior. At *t = 1.196s* we see how a puffing behavior results in the attachment of the droplet surface to not just the bead, but also to the thermocouple wire. Figure 7-27 shows the fragmentation behavior in E70G30 droplet explained above. As it can be seen in the image at *t = 1.307s*, a weak microexplosion event causes the droplet to fragment. Consequently, we see a portion of the droplet volume on the bead (represented by circle marker) and a portion of the droplet volume on the thermocouple wire (represented by arrow marker). The events described in both the figures results in irregular temperature increase values.

E70G30 droplet temperature profiles for the three intermediate flowrate conditions (10, 15, and 20) are shown in Figure 7-28. The period-2 heating rates for the intermediate flowrates as it can be seen in Table 7-1 do not necessarily increase with the increasing gas flowrates. This follows the earlier trends described for quiescent, behavior and residence times where we showed a lack

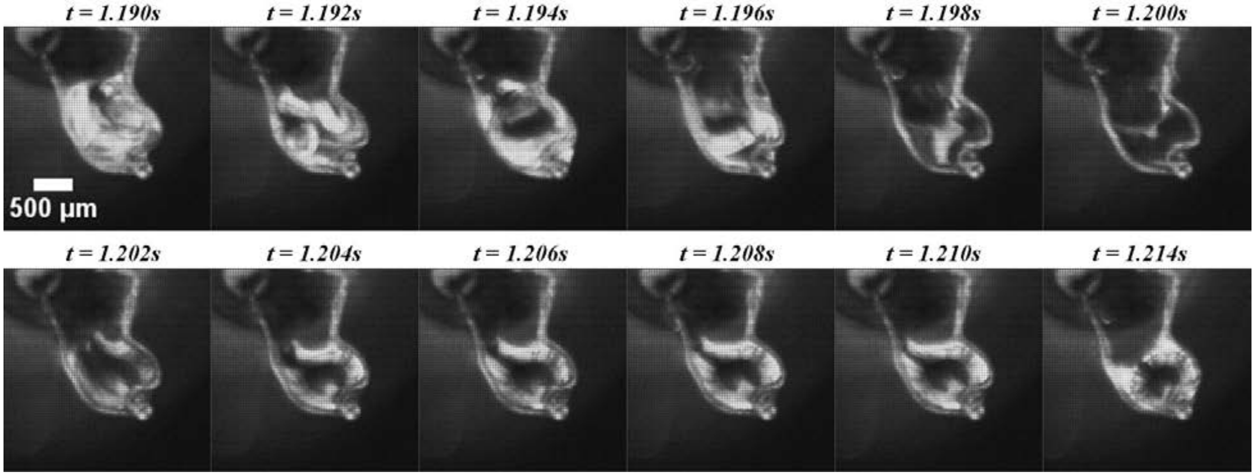

Figure 7-26: Low magnification image sequence of the puffing behavior in a E70G30 ($d_0$ = 1.14 μm) droplet.

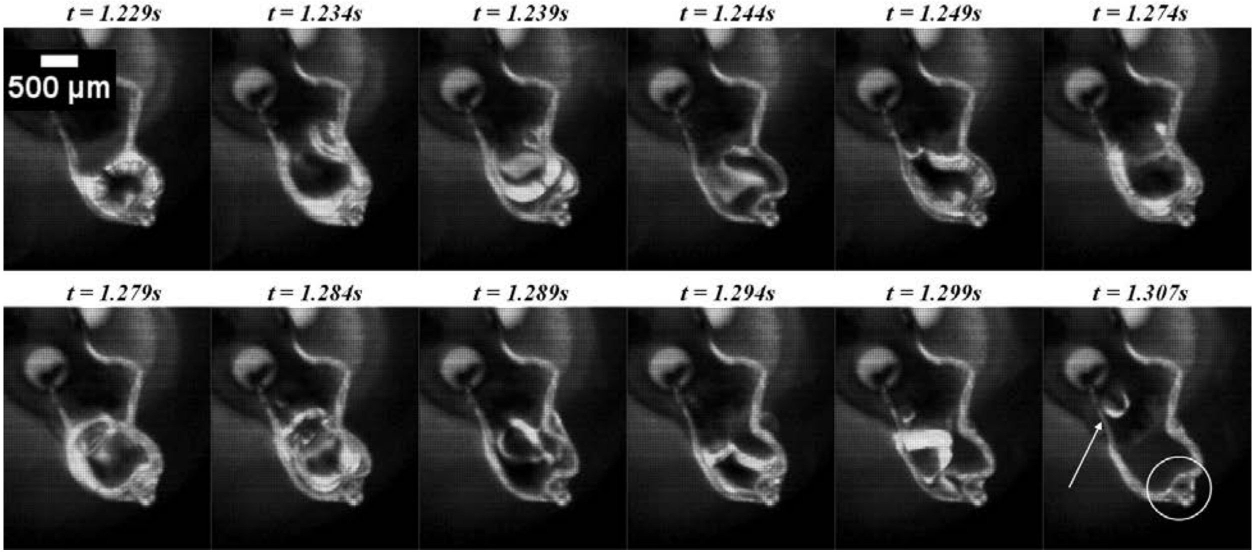

Figure 7-27: Low magnification image sequence showing the fragmentation of a E70G30 ($d_0$ = 1.14 μm) droplet and the subsequent attachment of the fragment to the thermocouple wire.

of correlation between droplet behavior and increasing flowrates in the intermediate flowrate region. As the gas flowrate changes, the convective heat transfer rate around the droplet also changes. From the work of Harada et al. (2011), we find the heat inflow to the droplet through conduction from the thermocouple to the droplet to be constant throughout for a droplet evaporating in the temperature range of 300-500K. In their work, they also found the heat inflow through convection to be at its maximum during the initial heat up period of the droplet, and

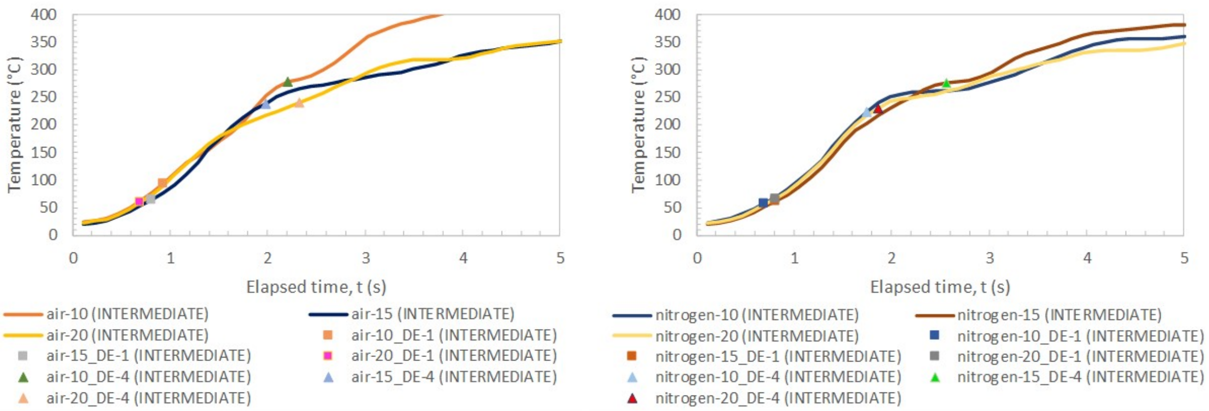

Figure 7-28: Droplet temperature profile comparison at intermediate flowrate conditions in air (left) and nitrogen (right) gas environments.

decrease continuously as the evaporation proceeds. From our experiments, we understand the heat inflow from convection to be different and more influenced by the gas flowrate relative to gas type. Unlike the electric furnace mentioned in their work, we use an infrared heater for our suspended droplet studies. According to the principles of IR heating, only the specimen is heated but not the medium around the specimen. Hence, we believe the conduction to be the dominant factor for the heat inflow during the early period of droplet evaporation. However, as the evaporation proceeds, the convection heat inflow to the droplet becomes more influential as the environment surrounding the droplet increase in temperature. Meanwhile, the conduction heat transfer rate remains constant. Therefore, as the gas flowrate is increased, only the convection heat transfer effects become more prevalent in terms of heat transfer to the droplet. However, after a certain threshold flowrate, we believe the gas flow might affect the droplet evaporation by removing heat from the thermocouple wire and the droplet surface boundary. With the experimental results obtained thus far with E70G30, the gas flowrate condition that adversely affects the droplet evaporation process is unclear.

### 7.3.4. Summary

Low magnification visualizations of E70G30 liquid in multiple gas type and gas flowrate conditions were shown. Significant droplet behavior events such as puffing, microdroplet escape behavior, microexplosion (primary and secondary), and residual evaporation behavior were identified. From the linear fit data, the initial droplet diameter ($d_0$) was observed to have more influence on the quiescent time over the behavior and residence time durations. However, the correlations between the low magnification quantitative data (QT, BT, RT) and the values of $d_0$ in our experiments was weak. For droplets of similar $d_0$, we observed longer BT and RT durations at higher flowrate conditions irrespective of the gas environment type. The behavior time breakdown showed the first microexplosion to happen immediately following the end of quiescent period for most test conditions, while the residual evaporation times were larger for high flowrate conditions (20 and 25 SCFM). The strength of the significant behavior events, mainly microdroplet escape and microexplosion behaviors, of the binary mixture (E70G30) during the behavior time was suggested to plays a vital role. We also observed low QT/BT ratios for higher flowrate conditions. However, linear fit data for the available sample set shows the general correlation between the QT/BT ratio and the different flowrate conditions to be weak for both gas environment types ($R^2 < 0.5$). The droplet temperature data was classified into multiple periods depending on the instantaneous temperature increase rates to understand the heating profile of the droplet. Puffing and weaker microdroplet escape behavior events were shown to result in droplet fragments attaching to the thermocouple wire. This behavior affects the classification of temperature periods for the E70G30 liquid. Overall, we did not observe any trend for the heating rates (period-2) of the E70G30 droplet with respect to different flowrate conditions for both gas environment types.

## 7.4. E-G System – Multiple Liquid Type Experiments

The objective of this systematic study was to understand the similarities and differences in evaporation behavior among several liquid types through the low magnification visualization and droplet temperature information. The droplet behavior of the E-G system of liquids (pure ethanol (E100), 30 vol% ethanol – 70 vol% glycerol (E30G70), 70 vol% ethanol – 30 vol% glycerol (E70G30), and pure glycerol (G100)) were studied alongside pure single component alcohols (pure methanol (M100) and pure butanol (B100)), standard fuel (Hexadecane), and multicomponent aviation liquid (BP Oil). Detailed information on the source and preparation of each liquid types were discussed in the E-G system introduction chapter (section 7.1). Table 7-2 shows properties of all the liquid types discussed in this section.

Droplet experiments were conducted on several liquid types. The IR heater settings were held constant at RA-10 and TA-10 for all experiments. The term operating conditions refers to the gas flowrate and the gas environment type used. Gas flowrate conditions include low (5 SCFM) and high (25 SCFM) settings. Gas environment types include air and nitrogen. For each selected operating condition and liquid type, the experiment was performed on one to three droplets. One droplet from the sample was selected for analysis based on the initial droplet diameter ($d_0$) for each operating condition and liquid type. The sample of data thus selected has an average $d_0$ of 1 mm, and a standard deviation of 0.11 mm.

Table 7-2: Physical and chemical properties of the liquid types.

| Liquid Type | Molecular Weight (g/mol) | Density (kg/m$^3$ at 20°C) | Boiling Point (°C) | Flash Point (Closed Cup, °C) | Auto Ignition Temperature (°C) | Heat of Vaporization (kJ/mol at 25°C) | Heat of Combustion (kJ/mol) | Viscosity (mPa.s) at 25°C | Surface Tension (mN/m) at 25°C |
|---|---|---|---|---|---|---|---|---|---|
| Methanol ($CH_3OH$) | 32.042 | 791.4 | 64.7 | 11 | 464 | 37.34 | 726.1 | 0.544 | 22.07 |
| Ethanol ($CH_3CH_2OH$) | 46.069 | 789 | 78.29 | 17 (97 vol%) | 363 | 42.32 | 1336.8 | 1.074 (at 20°C) | 21.97 |
| 1-butanol ($CH_3CH_2CH_2CH_2OH$) | 74.123 | 809.5 | 117.6 | 37 | 343 | 52.35 | 2676.7 | 2.544 | 24.93 |
| Glycerol ($CH_2OH$-$CHOH$-$CH_2OH$) | 92.094 | 1261.08 | 290 | 160 | 393 | 85.8 | 1654 | 1412 (at 20°C) | 64 (at 20°C) |
| Hexadecane ($C_{16}H_{34}$) | 226.448 | 769.89 (at 25°C) | 286.9 | 135 | 202 | 81.35 | 10699.1 | 3.0248 | 27.47 |
| BP Turbo Oil 274 (Proprietary multicomponent liquid) | NA | 950 | NA | 235 (Open Cup) | NA | NA | NA | 31.7 (at 40°C) | NA |

Linstrom, P. J., & Mallard, W. G. (2001). NIST Chemistry webbook; NIST standard reference database No. 69.
PubChem (2017). [online] Available at: https://pubchem.ncbi.nlm.nih.gov [Accessed December 21, 2017].
Segur, J. B., & Oberstar, H. E. (1951). Viscosity of glycerol and its aqueous solutions. Industrial & Engineering Chemistry, 43(9), 2117-2120. (Glycerol viscosity)
Segur, J. B. (1953). Physical properties of glycerol and its solutions. Glycerol, 2, 347-348. (Glycerol density)
Doll, K. M., & Erhan, S. Z. (2006). Synthesis and performance of surfactants based on epoxidized methyl oleate and glycerol. Journal of surfactants and detergents, 9(4), 377-383. (Glycerol surface tension)
Ross, G. R., & Heideger, W. J. (1962). Vapor Pressure of Glycerol. Journal of Chemical and Engineering Data, 7(4), 505-507. (Glycerol heat of vaporization)
Mehra, R. (2005). Ultrasonic, volumetric and viscometric studies of molecular interactions in binary liquid mixtures of hexadecane with 1-pentanol, 1-hexanol, and 1-heptanol at (298, 308 and 318) (Hexadecane viscosity)
Aralaguppi M.I.; Aminabhavi T.M.; Balundgi R.H.; Joshi S.S.: Thermodynamic Interactions in Mixtures of Bromoform with Hydrocarbons. J.Phys.Chem. 95 (1991) 5299-5308 (Hexadecane density)
Grinchak M.; Elvelt A.; Kiryanen E.: Exzessviskosität und -volumina von binären 1-Butanol-Tetrachlormethan-Mischungen. Eesti Tead.Akad.Toim.Keem 39 (1990) 155-160 (Ethanol density)
Engineering ToolBox, (2001). [online] Available at: https://www.engineeringtoolbox.com/standard-heat-of-combustion-energy-content-d_1987.html [Accessed Jan 4, 2018]. (heat of combustion)
Fraser, F. M., & Prosen, E. J. (1955). Heats of combustion of liquid n-hexadecane, 1-hexadecene, n-decylbenzene, n-decylcyclohexane, n-decylcyclopentane, and the variation of heat of combustion with chain length. J. Res. NBS, 55, 329-333. De (Hexadecane viscosity)
Lorenzi, L., Fermeglia, M., & Torriano, G. (1994). Densities and viscosities of 1, 1, 1-trichloroethane+ paraffins and+ cycloparaffins at 298.15 K. Journal of Chemical and Engineering Data, 39(3), 483-487. (Hexadecane heat of combustion)
BP Turbo Oil 274 MSDS provided by BP (BP Oil properties)

### 7.4.1. Quantitative Low Magnification Visualization Data

Low magnification visualization videos from the PCO camera and Nikon 200mm telephoto lens setup were analyzed to obtain quantitative droplet observations and event data. The quantitative data reported for this study include quiescent time (QT), behavior time (BT), and residence time (RT). Identification and calculation of the elapsed times for the quantitative data were discussed in section 7.3. Figure 7-29 shows the average quiescent, behavior, and residence times of multiple liquid types at all four test conditions along with their calculated ± error. For all liquids, the averaged values shown were calculated from their respective quantitative data determined for the four operating conditions (air-low, air-high, nitrogen-low, and nitrogen-high).

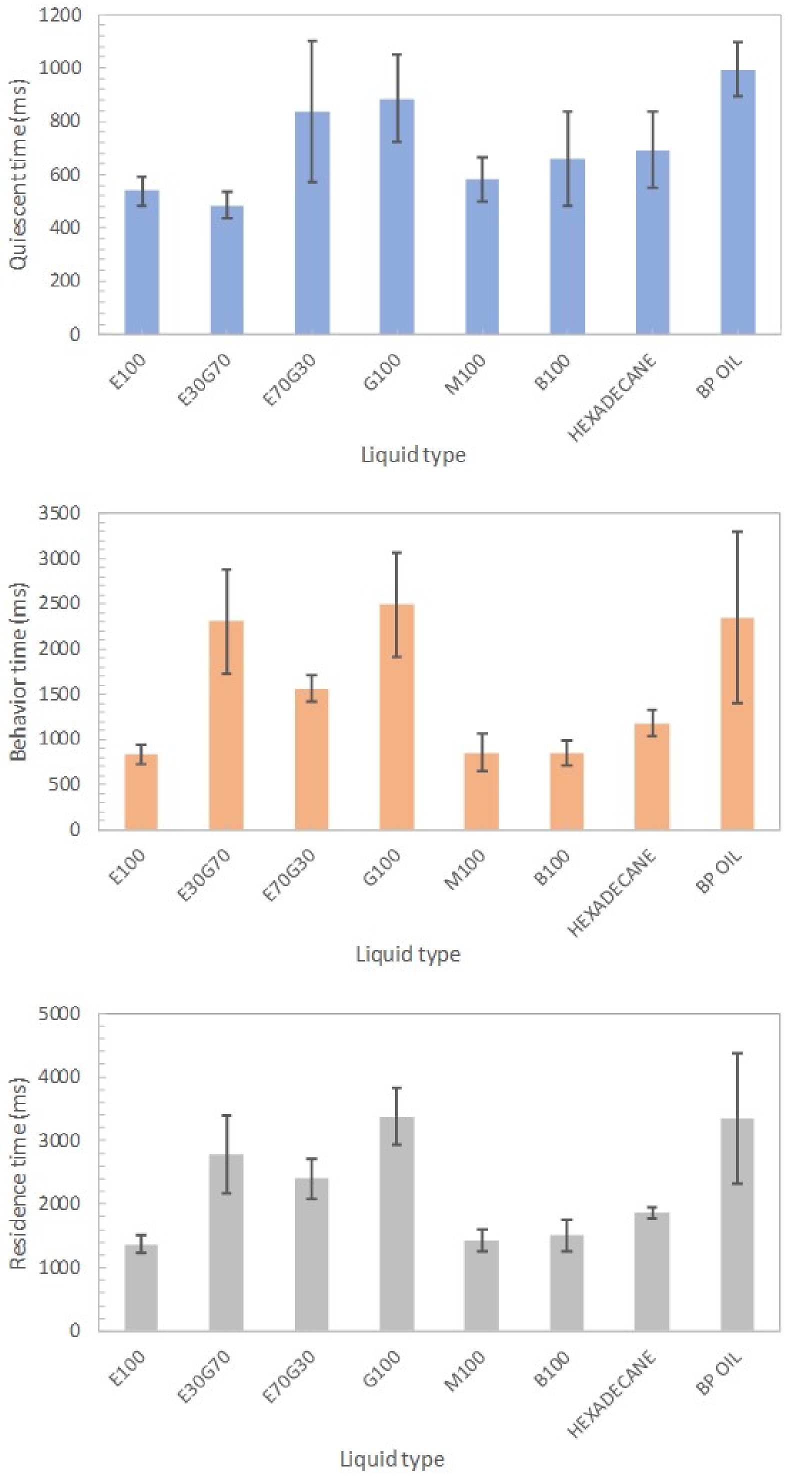

Figure 7-29: Quiescent (top), behavior (middle), and residence (bottom) times average data obtained from four test conditions for multiple liquid types.

In Figure 7-29, for any liquid type, we observe that the average behavior time (BT) and quiescent time (QT) are different. Average residence time (RT) being the sum of the average QT and BT are understandably larger than their respective individual values for all liquid types. For any liquid, the average BT is higher than the average QT. In some liquids, the BT values are several times higher than QT. Hence, we can say that the residence time of the droplet on the thermocouple is heavily influenced by the behavior time over the quiescent time. The average values of QT, BT, and RT shown in the plots are also tabulated in Table 7-3 along with their ±error for all liquids. From the plots of Figure 7-29 we can see that the three alcohols (E100, M100, and B100) and the hexadecane have similar quantitative low magnification values. We also see the average quantitative data of the two binary mixtures (E30G70 and E70G30) ranging between their respective pure components E100 and G100. The multicomponent liquid mixture (BP Oil) has high average values of QT, BT, and RT that are closer to those of G100 liquid type. The quantified data (QT, BT, and RT) averages calculated for M100 and B100 and the E100 liquid of the E-G system are similar. This is understandable considering all the three alcohols have similar liquid properties as shown in Table 7-2. The averaged data for hexadecane (Table 7-3) has values being closer to E100 than G100 than to the E-G blends. Despite the heat of vaporization values of hexadecane and G100 being closer (Table 7-2), the quiescent and behavior time periods are found to be very different between the two liquids. G100, also a single component pure liquid like the other alcohols and standard fuel, has larger average QT, BT, and RT values. This is probably due to the liquid properties, viscosity and density, which are much higher than the other liquid types as shown in Table 7-2.

Figure 7-29 also shows the elapsed time of BP Oil liquid type was closer to that of G100 than any other liquid type. However, BP Oil is a multicomponent liquid unlike G100, and the liquid properties of it are unavailable (proprietary) to understand this behavior. The binary mixtures E30G70 and E70G30 were observed (Figure 7-29, Table 7-3) to have average quantitative low magnification data between corresponding pure liquids types E100 and G100 as expected. Overall, the averaged QT, BT, and RT values of Figure 7-29 and Table 7-3 from the four operating conditions were influenced by respective liquid properties as anticipated.

Numerous literature studies of the behavior of suspended droplets as shown in chapter-5 use visualization methods (low and high magnification) for identifying ignition delay or ignition lag in droplets undergoing combustion. However, the quantitative low magnification data shown here is the first to allow calculation of the quiescent period of a droplet undergoing vaporization. Obtaining high magnification data is challenging and time consuming. Hence, our objective as described before and in the following, is to use the low magnification videos qualitatively and quantitatively (calculation of QT, BT, and RT) to understand droplet behavior, and to supplement this by performing high magnification experiments.

Table 7-3: Average and error for quantitative low magnification data (QT, BT, and RT) of the four operating conditions for multiple liquids.

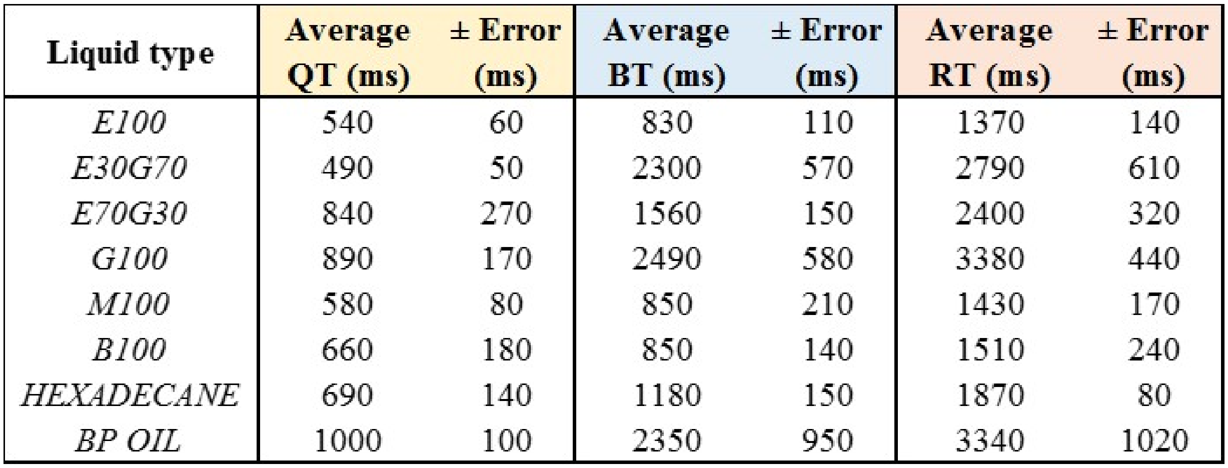

| **Liquid type** | **Average QT (ms)** | **± Error (ms)** | **Average BT (ms)** | **± Error (ms)** | **Average RT (ms)** | **± Error (ms)** |
|---|---|---|---|---|---|---|
| *E100* | 540 | 60 | 830 | 110 | 1370 | 140 |
| *E30G70* | 490 | 50 | 2300 | 570 | 2790 | 610 |
| *E70G30* | 840 | 270 | 1560 | 150 | 2400 | 320 |
| *G100* | 890 | 170 | 2490 | 580 | 3380 | 440 |
| *M100* | 580 | 80 | 850 | 210 | 1430 | 170 |
| *B100* | 660 | 180 | 850 | 140 | 1510 | 240 |
| *HEXADECANE* | 690 | 140 | 1180 | 150 | 1870 | 80 |
| *BP OIL* | 1000 | 100 | 2350 | 950 | 3340 | 1020 |

The differences in the quiescent, behavior, and residence times between the two types of gas environments (air and nitrogen) or the two types of gas flowrate (low and high) were studied for all liquid types. Figure 7-30 and Figure 7-31 shows the QT, BT, and RT comparison for all liquids between different gas environments and different gas flowrates respectively. The primary objective of this study was to investigate the influence of the operating condition (air-low, air-high, nitrogen-low, and nitrogen-high) on the quantitative data obtained from the low magnification visualizations. The differences between any two operating conditions compared were calculated (i.e. $\Delta QT = QT_{\text{condition 1}} - QT_{\text{condition 2}}$) for all liquids to determine the magnitude of the differences. The differences for all liquids for the four operating conditions amount to 32 in total. We separated the differences into 4 categories of 8 differences to assess the role operating conditions play in the QT, BT, and RT values obtained.

Figure 7-32 and Figure 7-33 show the influence of the gas environment and gas flowrate conditions respectively. The tabulated values of the all the differences calculated are shown in Table 7-4 and Table 7-5. The average and error for the four operating conditions are tabulated in Table 7-6. From Table 7-6, we see the ±error of ΔQT, ΔBT, and ΔRT values for several operating conditions are higher than the average. This would suggest a 'non-relation' between the selected operating condition (compared, constant) and quantitative data (ΔQT, ΔBT, and ΔRT) for all liquids. On the contrary, a smaller ±error value associated with the average would suggest a 'relation' between the two for all liquids. However, it is important to note that the sample size of the droplet experiments performed in each operating condition for any liquid type is too small (one to three) to confirm with statistical significance.

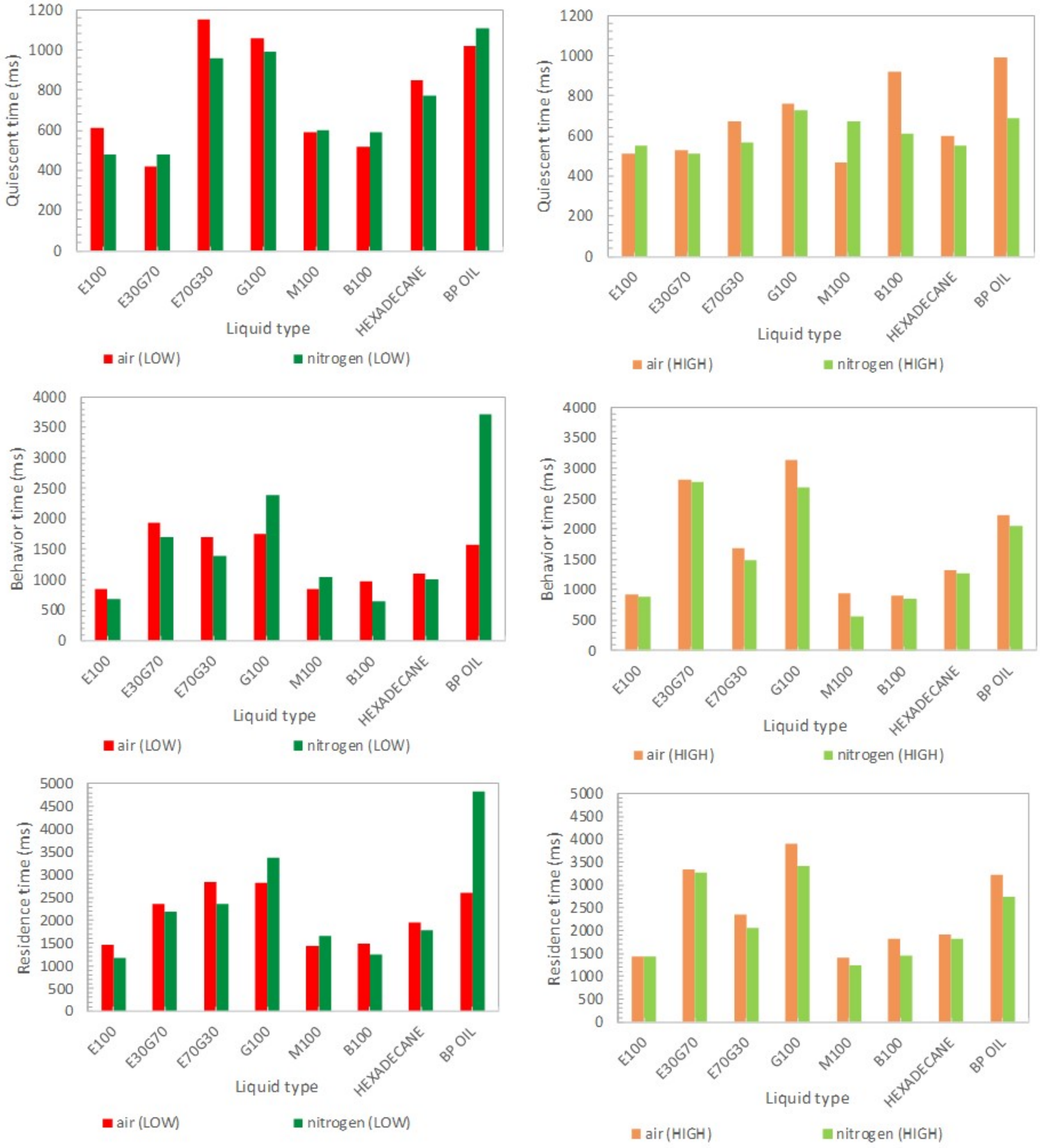

Figure 7-30: Comparison of quiescent (top), behavior (middle), and residence (bottom) times between air and nitrogen environments in low (left) and high (right) flowrates conditions for multiple liquid types.

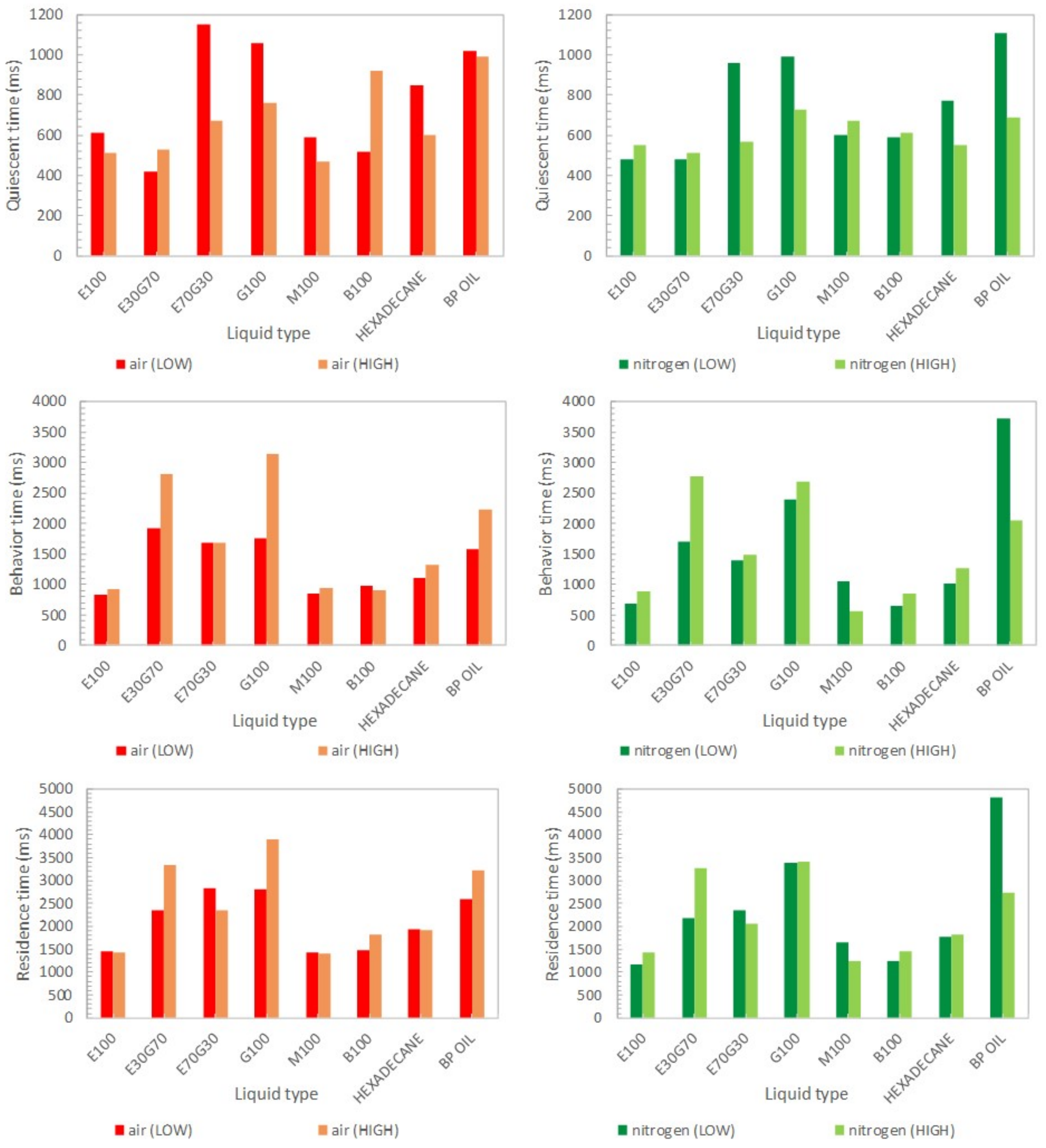

Figure 7-31: Comparison of quiescent (top), behavior (middle), and residence (bottom) times between low and high flowrate in air (left) and nitrogen (right) environments for multiple liquid types.

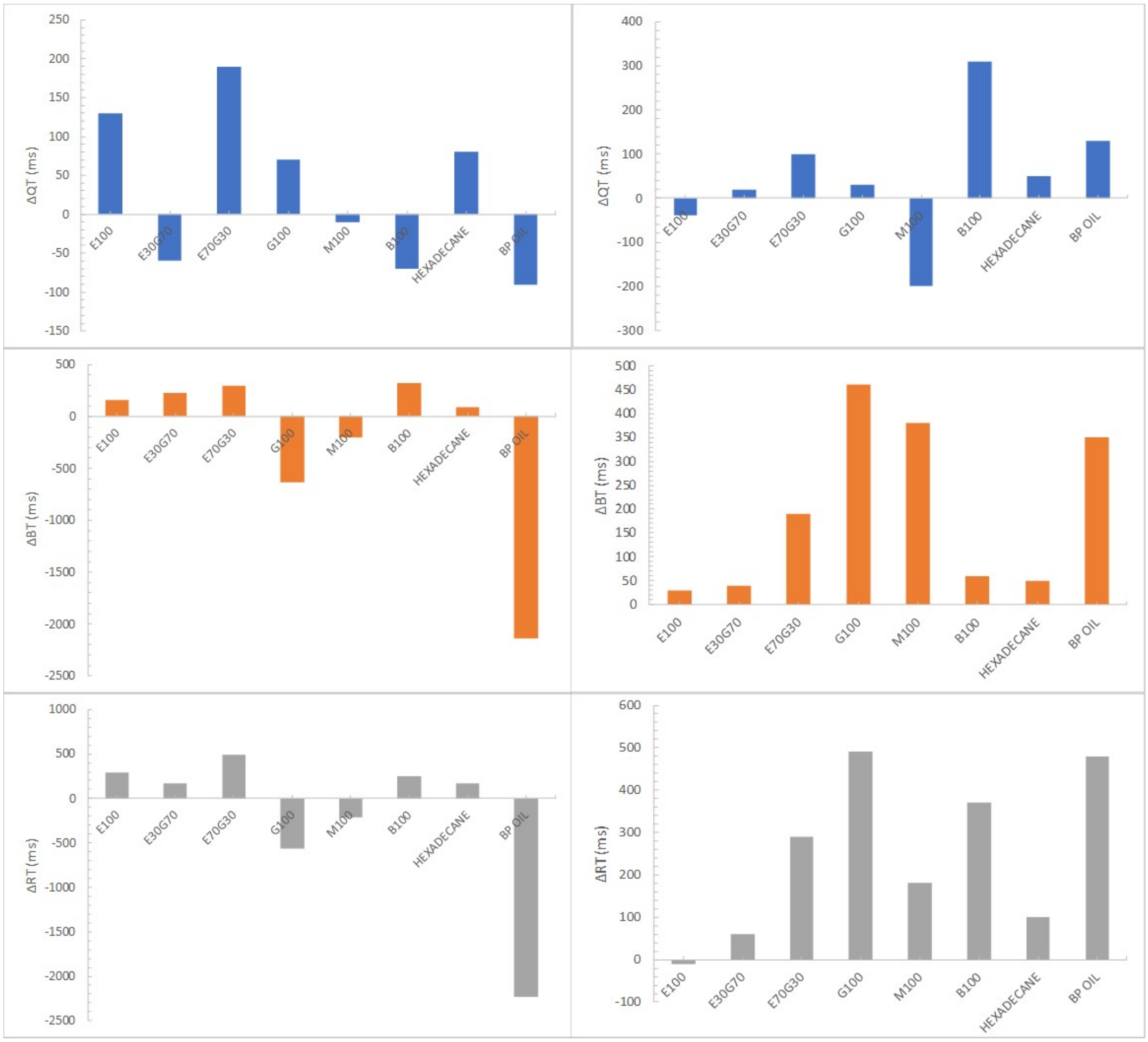

Figure 7-32: Difference of QT (top), BT (middle), and RT (bottom) when compared for air and nitrogen gas environment in low (left) and high (right) gas flowrate condition for all liquids.

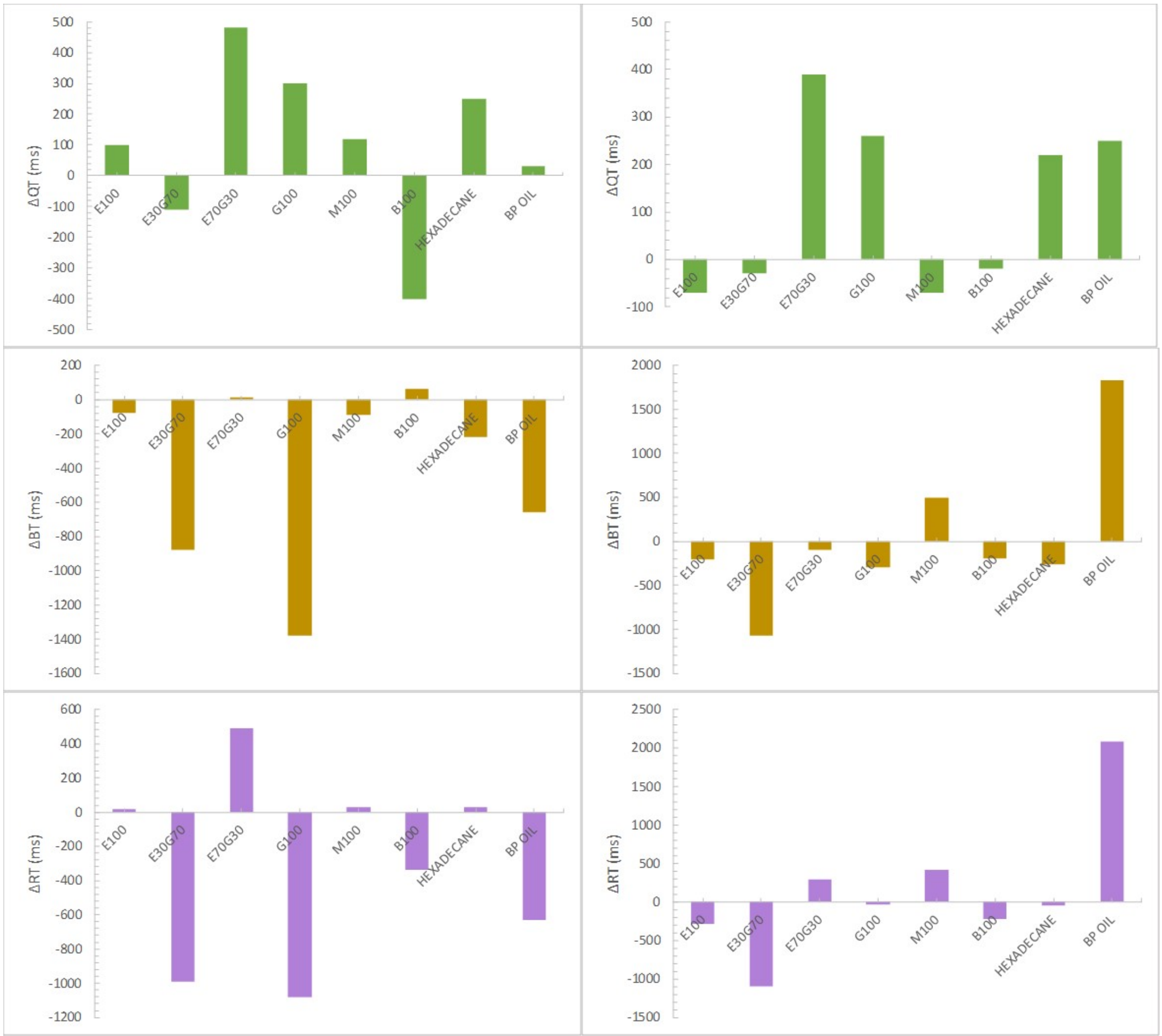

Figure 7-33: Difference of QT (top), BT (middle), and RT (bottom) when compared for low and high gas flowrate conditions in air (left) and nitrogen (right) gas environments for all liquids.

Table 7-4: Difference of QT, BT, and RT for air and nitrogen gas environments in low (top) and high (bottom) gas flowrate conditions for all liquids.

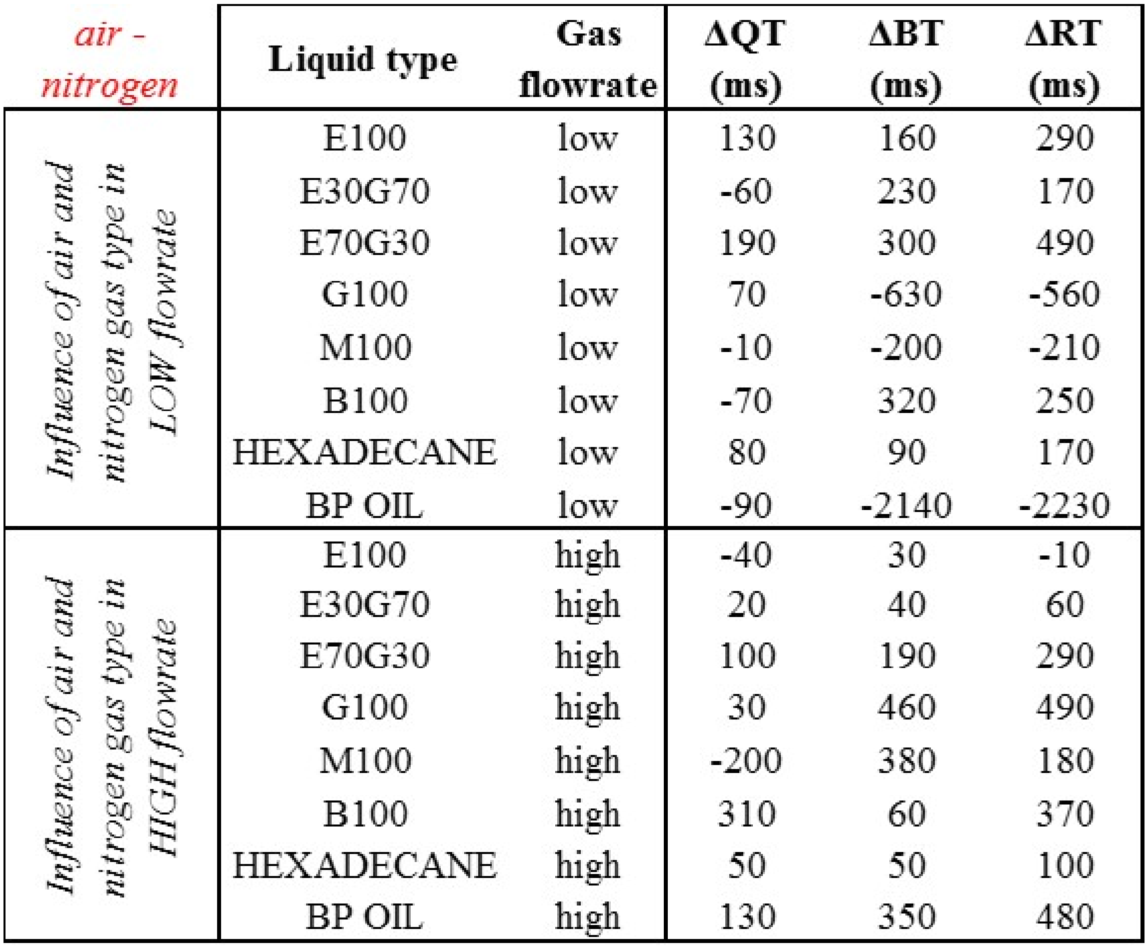

| *air - nitrogen* | **Liquid type** | **Gas flowrate** | **ΔQT (ms)** | **ΔBT (ms)** | **ΔRT (ms)** |
|---|---|---|---|---|---|
| *Influence of air and nitrogen gas type in LOW flowrate* | E100 | low | 130 | 160 | 290 |
| | E30G70 | low | -60 | 230 | 170 |
| | E70G30 | low | 190 | 300 | 490 |
| | G100 | low | 70 | -630 | -560 |
| | M100 | low | -10 | -200 | -210 |
| | B100 | low | -70 | 320 | 250 |
| | HEXADECANE | low | 80 | 90 | 170 |
| | BP OIL | low | -90 | -2140 | -2230 |
| *Influence of air and nitrogen gas type in HIGH flowrate* | E100 | high | -40 | 30 | -10 |
| | E30G70 | high | 20 | 40 | 60 |
| | E70G30 | high | 100 | 190 | 290 |
| | G100 | high | 30 | 460 | 490 |
| | M100 | high | -200 | 380 | 180 |
| | B100 | high | 310 | 60 | 370 |
| | HEXADECANE | high | 50 | 50 | 100 |
| | BP OIL | high | 130 | 350 | 480 |

Table 7-5: Difference of QT, BT, and RT calculated for low and high gas flowrate condition in air (top) and nitrogen (bottom) gas environments for all liquids.

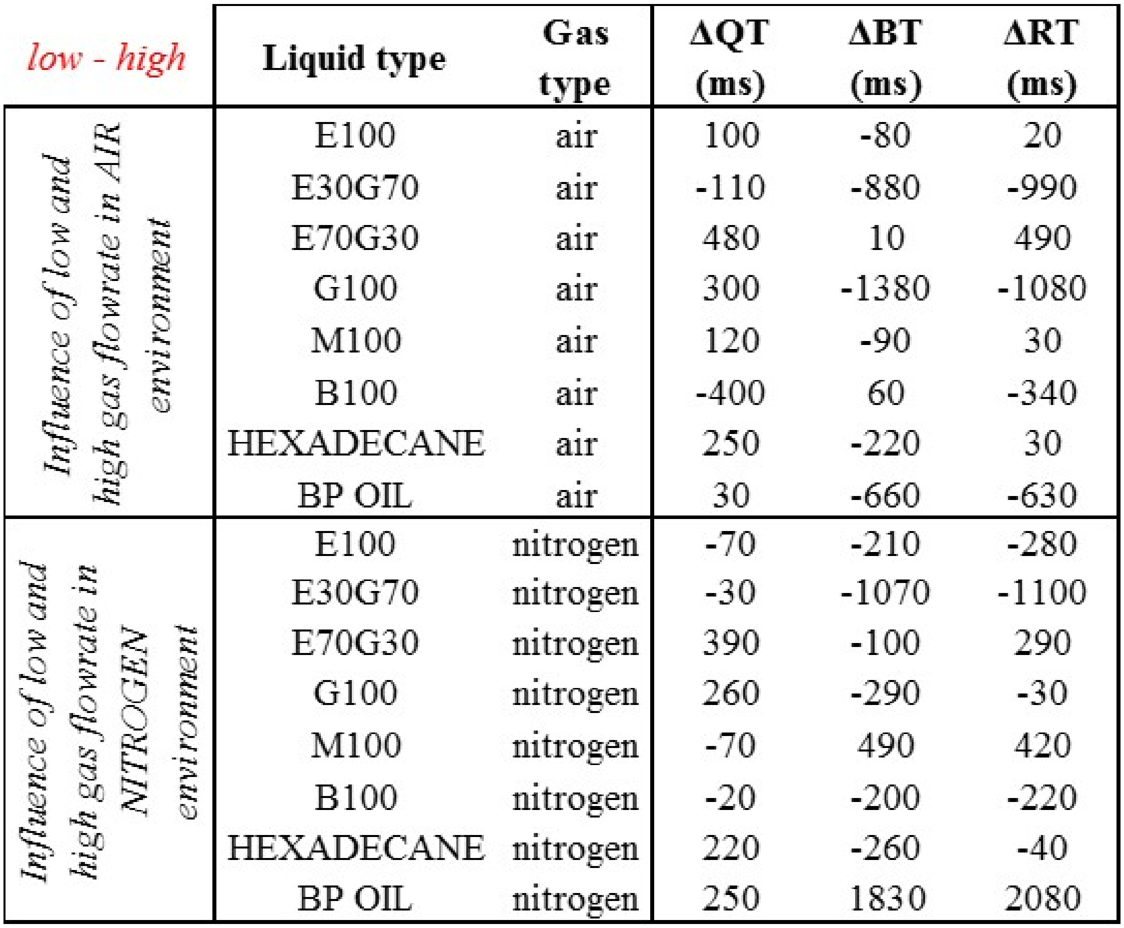

| low - high | Liquid type | Gas type | ΔQT (ms) | ΔBT (ms) | ΔRT (ms) |
|---|---|---|---|---|---|
| *Influence of low and high gas flowrate in AIR environment* | E100 | air | 100 | -80 | 20 |
| | E30G70 | air | -110 | -880 | -990 |
| | E70G30 | air | 480 | 10 | 490 |
| | G100 | air | 300 | -1380 | -1080 |
| | M100 | air | 120 | -90 | 30 |
| | B100 | air | -400 | 60 | -340 |
| | HEXADECANE | air | 250 | -220 | 30 |
| | BP OIL | air | 30 | -660 | -630 |
| *Influence of low and high gas flowrate in NITROGEN environment* | E100 | nitrogen | -70 | -210 | -280 |
| | E30G70 | nitrogen | -30 | -1070 | -1100 |
| | E70G30 | nitrogen | 390 | -100 | 290 |
| | G100 | nitrogen | 260 | -290 | -30 |
| | M100 | nitrogen | -70 | 490 | 420 |
| | B100 | nitrogen | -20 | -200 | -220 |
| | HEXADECANE | nitrogen | 220 | -260 | -40 |
| | BP OIL | nitrogen | 250 | 1830 | 2080 |

Table 7-6: Average and ±error calculated for the differences of QT, BT, and RT in multiple operating conditions.

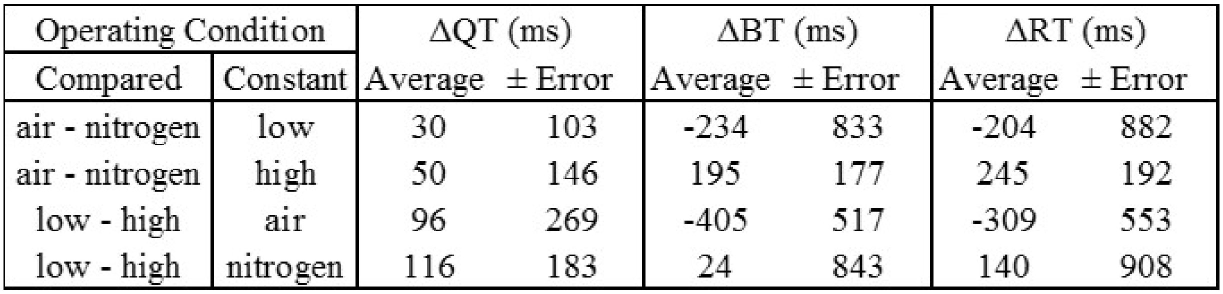

| Operating Condition | | ΔQT (ms) | | ΔBT (ms) | | ΔRT (ms) | |
|---|---|---|---|---|---|---|---|
| Compared | Constant | Average | ± Error | Average | ± Error | Average | ± Error |
| air - nitrogen | low | 30 | 103 | -234 | 833 | -204 | 882 |
| air - nitrogen | high | 50 | 146 | 195 | 177 | 245 | 192 |
| low - high | air | 96 | 269 | -405 | 517 | -309 | 553 |
| low - high | nitrogen | 116 | 183 | 24 | 843 | 140 | 908 |

Due the smaller sample size of the experiments mentioned previously for the four operating conditions, we did not perform any statistical significance tests to determine the magnitude of the differences calculated. However, we investigated the liquid types for which the ΔQT, ΔBT, and ΔRT values were found to be outside the average ± error limit when compared between two operating conditions. This average ± error value used to determine the limit was separately calculated for ΔQT, ΔBT, and ΔRT by separating the pool of differences (32 in total) into two categories of 16. The two categories represent the differences due to gas environment and gas flowrate. The objective was to understand the liquid types for which the quantitative data are potentially influenced by the gas environment or gas flowrate.

#### 7.4.1.1. Influence of Gas Environment Type

For ΔQT, average ± error when compared between two gas environments was calculated to be 270ms. From Figure 7-32 and Table 7-4, we see that only the B100 liquid type compared at a high flowrate condition between air and nitrogen environment fell outside the limit. We did not expect single-component liquids to have ΔQT values outside the limit when gas environments were compared due to the experimental conditions selected for our studies. The droplet studies in the IR heater were in the evaporation region of the droplet and not in the combustion region due to the heating rates achieved and the auto-ignition temperature of the liquid types (Table 7-2). Our understanding is that the QT is influenced by the rate of heating of a droplet. Hence, we expected negligible influence of the gas environment with respect to the heating rate and subsequently the QT values. Therefore, this difference observed in B100 liquid type when compared for the two gas environments is probably an outlier.

For the identification of the significant events (DE-1) in B100 liquid types, elapsed time corresponding to the starting instant of the single bubble formation observed within the droplet was used. Single bubble formations when observed in the droplets of similar liquid types (E100, G100, and M100) were attributed to hot spots on the suspending material (in our case the thermocouple) or due to an existing micro air bubble that was formed during the suspension of the droplet. Normally, both these events that led up to the formation of the bubble were not expected to be affected by the gas environment type irrespective of its flowrate. This lack of correlation between the selected experimental condition and the observed behavior provides further support to consider the B100 as an outlier.

For ΔBT and ΔRT, the average ± error limit was calculated to be 940ms and 980ms respectively. From Figure 7-32 and Table 7-4, only the BP Oil liquid type exceeds the limit with values of -2140ms and -2230ms for ΔBT and ΔRT when compared between air and nitrogen environments in low flowrate condition. Outlier differences of BP Oil are probably due to the differential strength in the microexplosion behavior. Generally, droplet evaporation unlike combustion is not expected to change drastically with different types of gas environment. In section 7.3, we observed the strength of microexplosion in E70G30 liquid type contributing to the different behaviors observed for low and high flowrates. Hence, we suggest that the strength of the microexplosion between the gas environments (air and nitrogen) could contribute to the large differences seen here in BT and RT of the BP Oil. Overall, we can say that the effect of gas environment on QT, BT, and RT is minimal irrespective of the gas flowrate (low or high) in which the droplet was suspended.

#### 7.4.1.2. Influence of the Gas Flowrate Condition

Differences of quiescent (ΔQT), behavior (ΔBT), and residence time (ΔRT) data for all liquids were also compared for the two gas flowrate (low and high) conditions in both air and nitrogen environments. From Figure 7-33 and Table 7-5 we find the liquid types for which the

ΔQT is found to be outliers (outside the average ± error limit) are E70G30 in air (480ms) and nitrogen (390ms), B100 in air (-400ms), and G100 in air (300ms) when compared for the different gas flowrates. E70G30 liquid type as explained in the droplet behavior section (section 7.2) exhibits microdroplet explosion behavior in low flowrate, and microdroplet escape behavior in high flowrate conditions, irrespective of the gas environment. Generally, the QT values are relatively low in E70G30 droplets that exhibit microdroplet escape behavior over the droplets that exhibit microexplosion behavior as explained in section 7.2. This could possibly be the reason behind the ΔQT outlier values of E70G30 liquid type when compared for low and high flowrates. Outlier values of B100 liquid needs further investigation for the same reasons as explained in section 7.4.1.1.

In the case of G100 droplets, to identify the significant event DE-1, the droplet swing behavior or, in some cases, the emergence of vapors around the droplet were used as identifiers. Observation of both instances in the visualizations are influenced by the increased gas flow around the droplet. High gas flows (more than 10 SCFM) cause turbulent conditions to develop around the droplet resulting in a swing behavior (Figure 7-9) or an increased convection flow at high flowrates resulting in an early observation of the droplet vapors in the visualizations. Both these events could result in erroneous QT values at high flowrates and subsequently a larger ΔQT.

For ΔBT and ΔRT, the liquid types outside the average ± error limit are same as observed for ΔQT. They are as seen in Figure 7-33 and Table 7-5: E30G70 in air (-880ms, -900ms) and nitrogen (-1070ms, -1100ms), BP Oil in nitrogen (1830ms, 2080ms), and G100 in air (-1380ms, -1080ms). The outlier values of E30G70 and BP Oil are attributed to their multi-component nature, and the strength of microexplosion. However, in G100 droplet type, due to its single component nature, the outlier value of ΔQT found earlier was expected to be the reason behind the outlier values of ΔBT and ΔRT. But, the differences of behavior and residence times were the exact opposite. In other words, the ΔQT outlier observed earlier was primarily due to the large QT of G100 in the low air flowrate condition (positive difference). Whereas, the large differences observed in the BT and RT were found to be due to their respective values of high air flowrate condition (negative difference). Also, no outliers of ΔBT and ΔRT were observed for G100 droplet evaporating in nitrogen. During the discussions about the G100 liquid type in the droplet behavior section (7.2.4), we mentioned the observations of random bubble formation behavior in some droplets inconsistent with the expected droplet behavior of G100 liquid type. This behavior we believe could be a result of the micro-bubble formations during the suspension of the droplet, since bubble formation due to hot spots is less commonly observed in a liquid type like G100. Because, the G100 droplet heating rates and thermocouple heating rates are similar, there is a low probability for a differential temperature to arise between the two that could result in a hot spot. We believe these micro-bubble formations of the G100 droplet could be contributing to the ΔBT and ΔRT outliers, or could be an anomalous behavior as observed in B100 liquid types. Overall, we understand that the influence of gas flowrate (low and high) conditions resulting in outlier ΔQT, ΔBT and ΔRT values are more prevalent in liquid types made up of two or more components irrespective of the gas environment.

### 7.4.2. Droplet Temperature Data

Droplet temperature data were collected for the same operating condition and liquid types mentioned in 7.4.1. All the plots reported in this section are for droplets of similar $d_0$ and the elapsed times shown are after adjusting them for the IR starting lag (*t'*). As mentioned in 7.3.3, the square (■) and triangle (▲) markers in the temperature profile plots provide an estimate of the quiescent (QT) and residence time (RT) for the selected operating condition. Figure 7-34 shows the droplet temperature profiles for the E-G system of liquids (E100, E30G70, E70G30, and G100) and other liquids (M100, B100, Hexadecane, and BP Oil) selected for comparative studies. The plots in the Figure 7-34 represents the four test conditions (air-low, air-high, nitrogen-low, and nitrogen-high) in which the droplet evaporation was studied. The thermocouple profile without the liquid is denoted as reference profile and it is shown as dotted lines.

Evident from the plots of Figure 7-34, we see that the temperature increase rate of multiple liquid types was distinctly different from the temperature profile of the thermocouple material (reference profile) obtained without the liquid. This shows that the temperature data recorded until the ▲ marker for each liquid is measuring internal droplet temperature. Temperatures recorded after this marker refer only to the thermocouple material. However, it is important to consider the delay (~0.2s or 200ms) that occurs with our experimental setup due to the responsiveness of the thermocouple for the temperature change. As mentioned in the previous section (7.3), droplet temperature profile analysis involves the breakdown of the data into several periods (cold droplet heat-up period, heating rate period, and temperature plateau period). The averaged values (from the four test conditions) of the three periods obtained for each liquid type are shown in Table 7-7. Tabulated data with respect to each liquid type are distinct, and show that the breakdown of the droplet temperature profiles into clearly defined periods is a reasonable way to identify and analyze the differences in the droplet evaporation behavior.

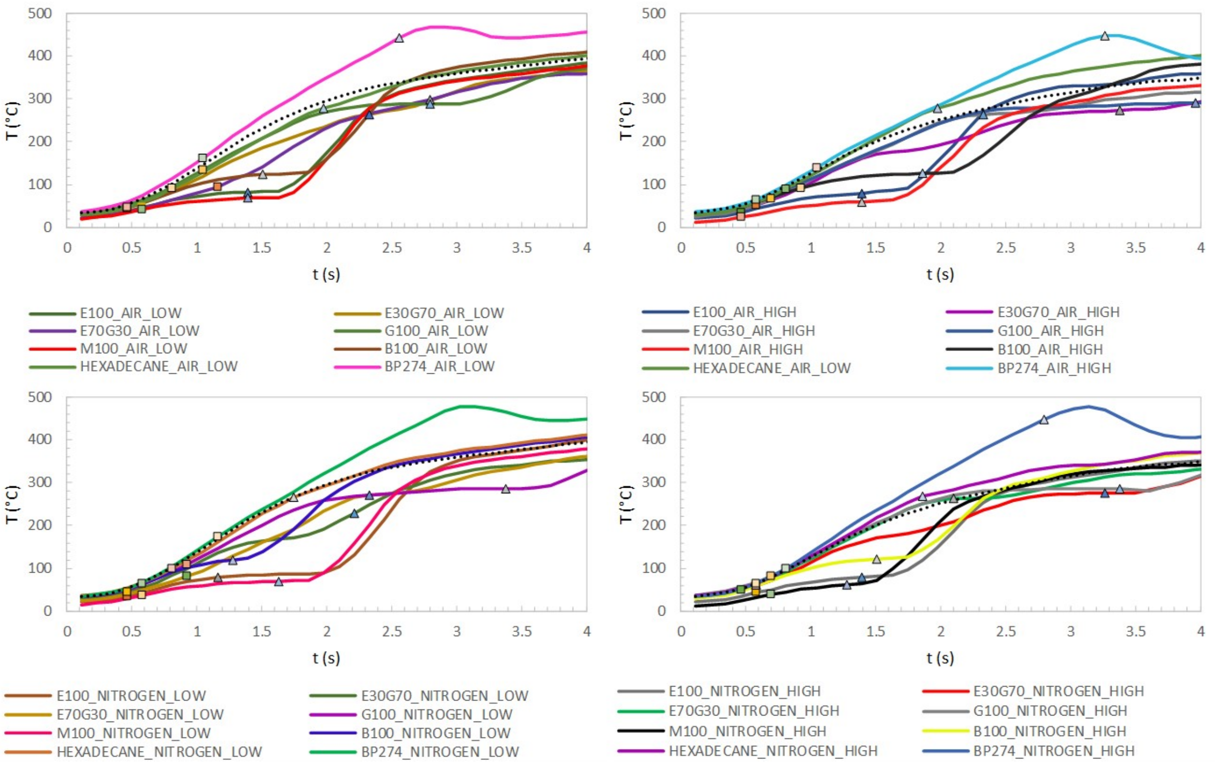

Figure 7-34: Internal droplet temperature profiles of test liquids in comparison with the reference profile for air-low (top left), air-high (top right), nitrogen-low (bottom left), and nitrogen-high (bottom right) operating conditions. ■ and ▲ markers represent DE-1 and DE-4 event respectively.

Table 7-7: Averaged temperature period values obtained from the four operating conditions for multiple liquids.

| *RA-10; TA-10; 125μm TC* | *All numbers represent averages of the individual values of the 4 test conditions (air-low, air-high, nitrogen-low, and nitrogen-high) are for liquid types of similar $d_0$; Δt - calculated from the start to end time of the period defined; ΔT - calculated from the temperature at the start and end of the defined period.* | | | | | | | | |
|---|---|---|---|---|---|---|---|---|---|
| **Droplet temperature period** | **Period-1 Cold droplet heat-up** | | | **Period-2 Heating rate** | | | **Period-3 Temperature plateau** | | |
| **Liquid Type** | **°C/s** | **Δt (ms)** | **ΔT (°C)** | **°C/s** | **Δt (ms)** | **ΔT (°C)** | **°C/s** | **Δt (ms)** | **ΔT (°C)** |
| E100 | 230 | 7 | 30 | 610 | 39 | 64 | 520 | 9 | 18 |
| E30G70 | 230 | 7 | 29 | 2040 | 216 | 105 | 580 | 9 | 23 |
| E70G30 | 230 | 8 | 34 | 1840 | 229 | 135 | 350 | 7 | 17 |
| G100 | 230 | 8 | 35 | 1660 | 217 | 140 | 1370 | 14 | 9 |
| M100 | 230 | 7 | 29 | 500 | 27 | 55 | 550 | 9 | 17 |
| B100 | 230 | 8 | 35 | 700 | 63 | 94 | 500 | 10 | 21 |
| HEXADECANE | 230 | 9 | 37 | 1630 | 237 | 157 | NA | NA | NA |
| BP OIL | 230 | 9 | 38 | 2560 | 411 | 169 | NA | NA | NA |

#### 7.4.2.1. E100 (Pure Ethanol) and G100 (Pure Glycerol)

Ethanol and glycerol constitute the two pure liquids in the E-G system selected to comparatively study with the ethanol-glycerol blends. Figure 7-35 and Figure 7-36 show the E100 and G100 droplet temperature profiles in a low flowrate air environment. The temperature profiles of the thermocouple with and without the liquid are clearly distinguishable from the two plots. For a pure liquid type, the typical droplet profile involves a relatively short cold droplet heat-up period (period-1) followed by the heating rate period (period-2), and a brief temperature plateau (period-3) near the end of droplet evaporation. Detailed information regarding the classification and determination of each period are in 7.3.3. The term 'heating rate' hereafter for any period refers to the average temperature increase per second over the duration of that period. All heating rate values were obtained from the slope values of the linear fit of the data in their respective periods.

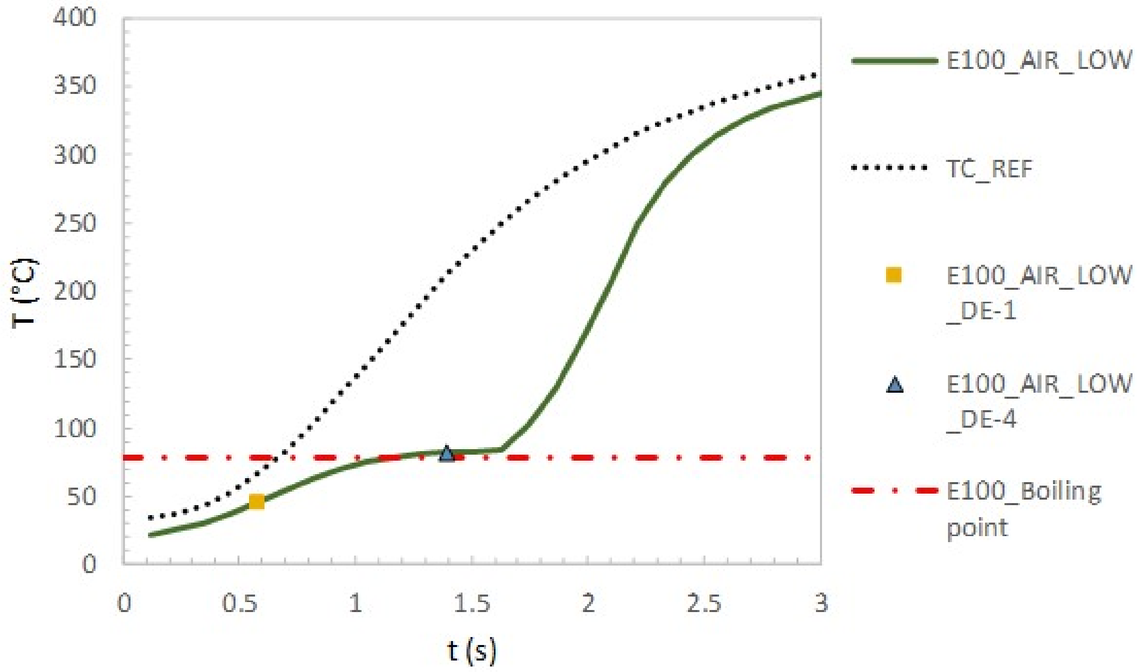

Figure 7-35: Droplet temperature profile of E100 droplet in low (5 SCFM) air flowrate condition.

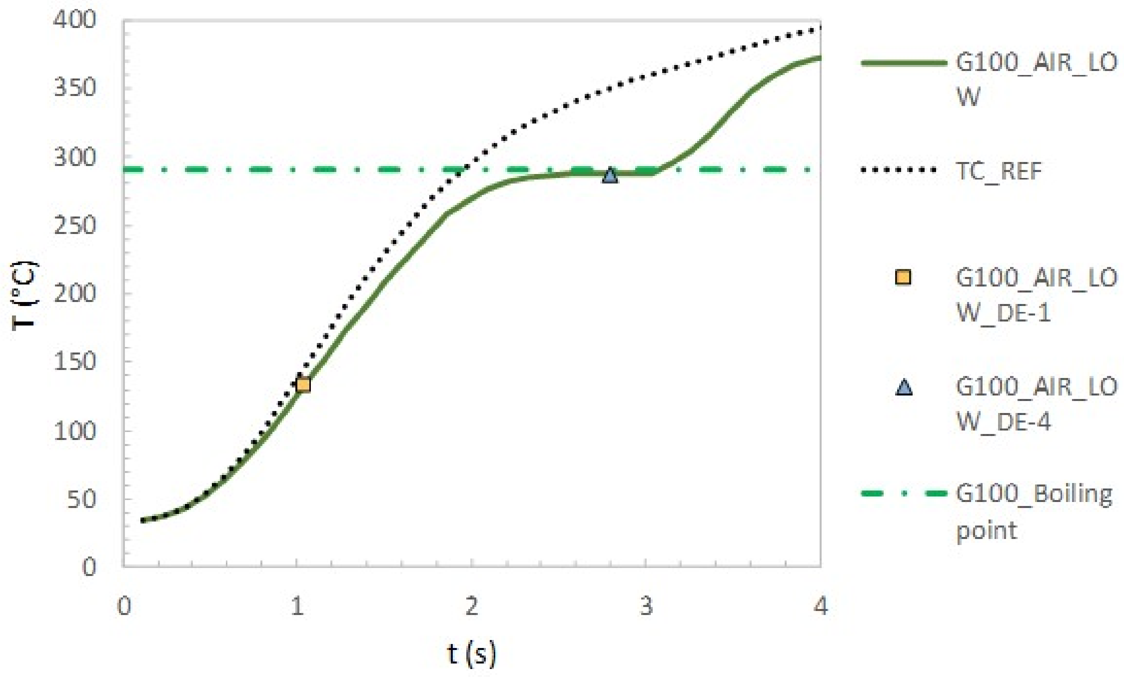

Figure 7-36: Droplet temperature profile of G100 droplet in low (5 SCFM) air flowrate condition.

Under the operating conditions shown (air-low) in Figure 7-35, the cold droplet heat-up period lasts for about 230ms and has a heating rate of 34°C/s. The heating rate period (period-2) lasts for about 610ms and the heating rate is at 66°C/s. As the droplet temperature reaches close to the boiling point of ethanol (78.29°C, Table 7-2), the droplet temperature profile flattens almost becoming horizontal to x-axis, and this is referred to as the temperature plateau (period-3). This period-3 lasts for about 580ms and the droplet heating rate is at its lowest at 15 °C/s. The temperature data shown after the period-3 in the plot corresponds to that of the thermocouple material after the droplet has evaporated completely. This region is usually excluded and not of our interest in droplet evaporation studies.

The breakdown of the G100 profile is followed up in a similar fashion and the three periods have time durations of 230, 1630, and 820ms, respectively. The corresponding heating rate in those three periods are 37, 148, and 6°C/s, respectively. From Figure 7-35 and Figure 7-36 both E100 and G100 show three well established periods. However, the temperature in the y-axis of G100 is relatively higher. Also, the heating rates calculated in period-2 are very different with G100 (148°C/s) being more than the double that of E100 (66°C/s) for the same low air flowrate operating condition. This trend is also observed in the average heating rate values of E100 and G100 irrespective of the operating condition as shown in Table 7-7. With the heat of vaporization values of G100 higher than E100 (Table 7-8Table 7-8), we can understand the former's longer time durations for the droplet to vaporize over the latter. Figure 7-37 shows the droplet temperature profile of E100 (left) and G100 (right) liquid types in all four test conditions. The temperature periods values and the quantitative low magnification data for the two liquid types E100 and G100 are shown in Table 7-8. From the observations of the plot and the tabulated values, we see that the droplet temperature profile for both types of gas environments are similar. The heating rates of period-2 for both the liquid types are relatively lower at the high flowrate conditions. The lower period-2 heating rates of G100 at the high flowrate conditions could also have contributed for the observation of large ΔRT observed in the previous section (7.4.1.2).

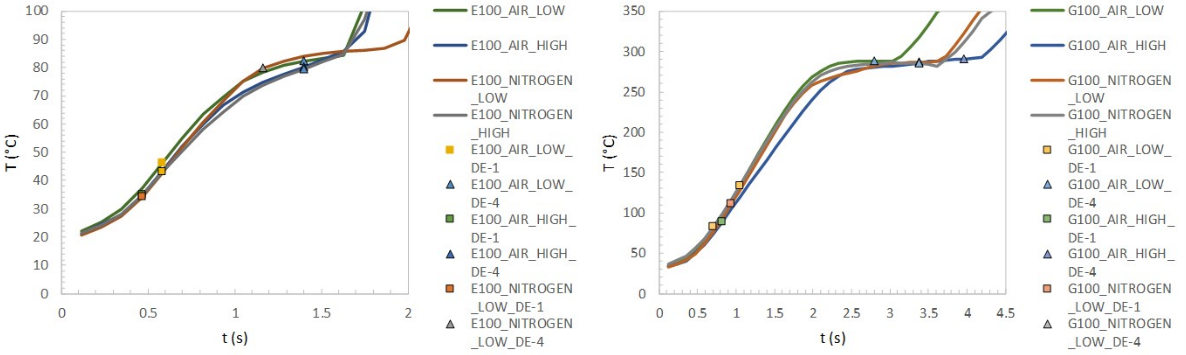

Figure 7-37: Droplet temperature profiles of E100 (left) and G100 (right) liquid type shown for the four test conditions.

Table 7-8: Temperature period (top) and quantitative low magnification data (bottom) for E100 and G100 droplets in all four test conditions.

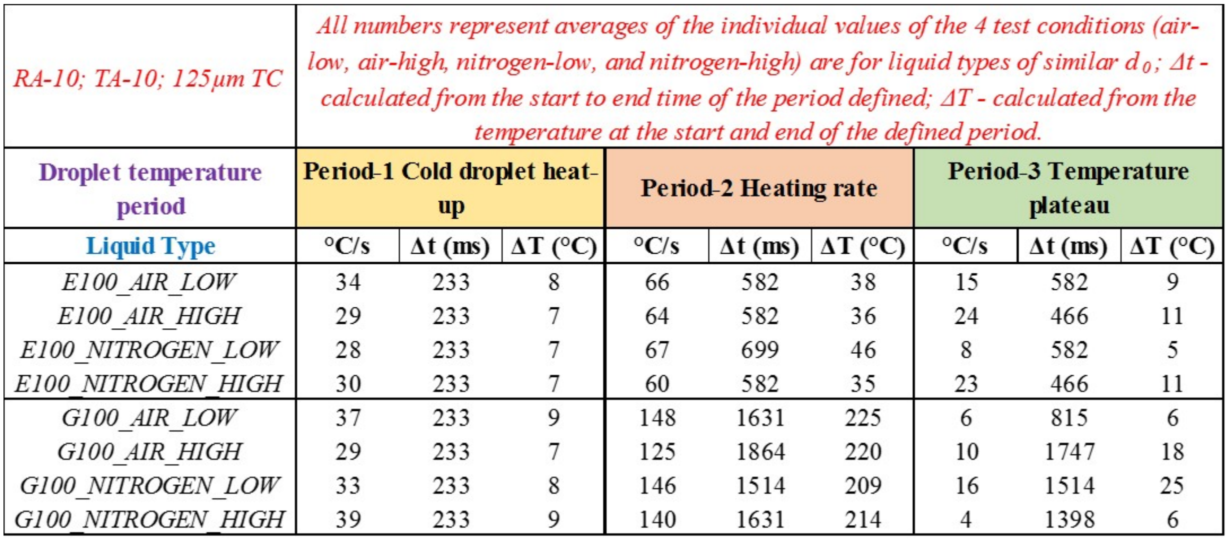

| *RA-10; TA-10; 125μm TC* | *All numbers represent averages of the individual values of the 4 test conditions (air-low, air-high, nitrogen-low, and nitrogen-high) are for liquid types of similar $d_0$; Δt - calculated from the start to end time of the period defined; ΔT - calculated from the temperature at the start and end of the defined period.* | | | | | | | | |
|---|---|---|---|---|---|---|---|---|---|
| **Droplet temperature period** | **Period-1 Cold droplet heat-up** | | | **Period-2 Heating rate** | | | **Period-3 Temperature plateau** | | |
| **Liquid Type** | **°C/s** | **Δt (ms)** | **ΔT (°C)** | **°C/s** | **Δt (ms)** | **ΔT (°C)** | **°C/s** | **Δt (ms)** | **ΔT (°C)** |
| *E100_AIR_LOW* | 34 | 233 | 8 | 66 | 582 | 38 | 15 | 582 | 9 |
| *E100_AIR_HIGH* | 29 | 233 | 7 | 64 | 582 | 36 | 24 | 466 | 11 |
| *E100_NITROGEN_LOW* | 28 | 233 | 7 | 67 | 699 | 46 | 8 | 582 | 5 |
| *E100_NITROGEN_HIGH* | 30 | 233 | 7 | 60 | 582 | 35 | 23 | 466 | 11 |
| *G100_AIR_LOW* | 37 | 233 | 9 | 148 | 1631 | 225 | 6 | 815 | 6 |
| *G100_AIR_HIGH* | 29 | 233 | 7 | 125 | 1864 | 220 | 10 | 1747 | 18 |
| *G100_NITROGEN_LOW* | 33 | 233 | 8 | 146 | 1514 | 209 | 16 | 1514 | 25 |
| *G100_NITROGEN_HIGH* | 39 | 233 | 9 | 140 | 1631 | 214 | 4 | 1398 | 6 |

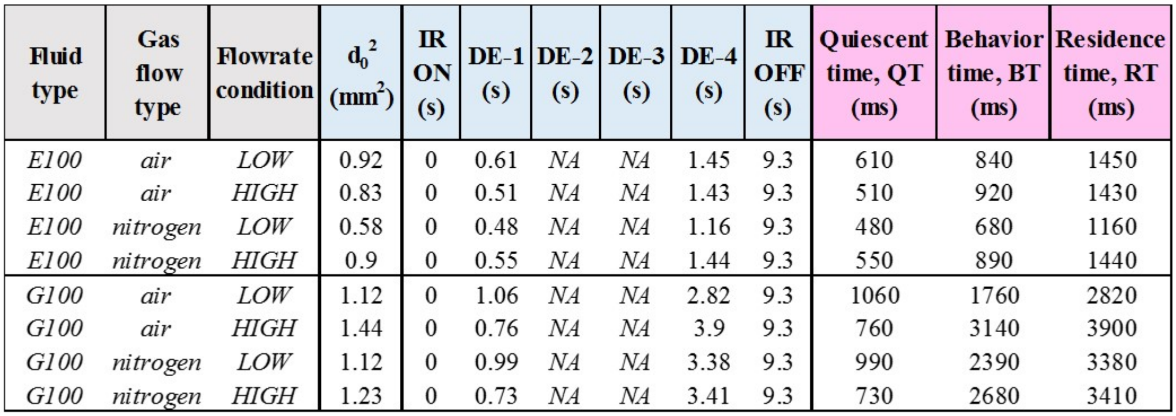

| **Fluid type** | **Gas flow type** | **Flowrate condition** | **$d_0^2$ ($mm^2$)** | **IR ON (s)** | **DE-1 (s)** | **DE-2 (s)** | **DE-3 (s)** | **DE-4 (s)** | **IR OFF (s)** | **Quiescent time, QT (ms)** | **Behavior time, BT (ms)** | **Residence time, RT (ms)** |
|---|---|---|---|---|---|---|---|---|---|---|---|---|
| *E100* | *air* | *LOW* | 0.92 | 0 | 0.61 | *NA* | *NA* | 1.45 | 9.3 | 610 | 840 | 1450 |
| *E100* | *air* | *HIGH* | 0.83 | 0 | 0.51 | *NA* | *NA* | 1.43 | 9.3 | 510 | 920 | 1430 |
| *E100* | *nitrogen* | *LOW* | 0.58 | 0 | 0.48 | *NA* | *NA* | 1.16 | 9.3 | 480 | 680 | 1160 |
| *E100* | *nitrogen* | *HIGH* | 0.9 | 0 | 0.55 | *NA* | *NA* | 1.44 | 9.3 | 550 | 890 | 1440 |
| *G100* | *air* | *LOW* | 1.12 | 0 | 1.06 | *NA* | *NA* | 2.82 | 9.3 | 1060 | 1760 | 2820 |
| *G100* | *air* | *HIGH* | 1.44 | 0 | 0.76 | *NA* | *NA* | 3.9 | 9.3 | 760 | 3140 | 3900 |
| *G100* | *nitrogen* | *LOW* | 1.12 | 0 | 0.99 | *NA* | *NA* | 3.38 | 9.3 | 990 | 2390 | 3380 |
| *G100* | *nitrogen* | *HIGH* | 1.23 | 0 | 0.73 | *NA* | *NA* | 3.41 | 9.3 | 730 | 2680 | 3410 |

#### 7.4.2.2. E30G70 (30% Ethanol-70% Glycerol) and E70G30 (70% Ethanol-30% Glycerol) blends

E30G70 and E70G30 are binary component liquid blends prepared to simulate and study the evaporation behavior of ethanol-glycerol blends used for sustainable energy applications. Figure 7-38 shows the droplet temperature profiles of the two blends in comparison with the two pure liquids E100 and G100. From the four plots shown in Figure 7-38, we see that the temperature profiles of the two E-G blends lie somewhere in between that of the pure liquids. This behavior is understandable considering the blends are 30-70 mixtures of the two liquid types.

The droplet temperature profiles of the blends do not entirely conform to the droplet temperature profiles observed for E100 and G100, where we see a breakdown of the profile into three distinct periods. Table 7-9 shows the heating rate, time duration, and the droplet temperature change in each period for the two blends in all four operating conditions. The first periods involving the cold droplet heat up are similar for both the blends in all four test conditions. The temperature plateau in the profile occurs near the boiling point of glycerol (290°C). Droplets where the plateau is not clearly distinguishable are referred to as *'NA'* in the table. The temperature plateau is not well defined in the blend droplets unlike the pure liquids. In other words, looking at the values in Table 7-9, we see that the time duration of the blend droplets in period-3 are either relatively low or non-existent when compared to E100 and G100. In terms of the averaged values of period-2 heating rates (Table 7-7), E70G30 blend has a higher rate in period-2 than E30G70.

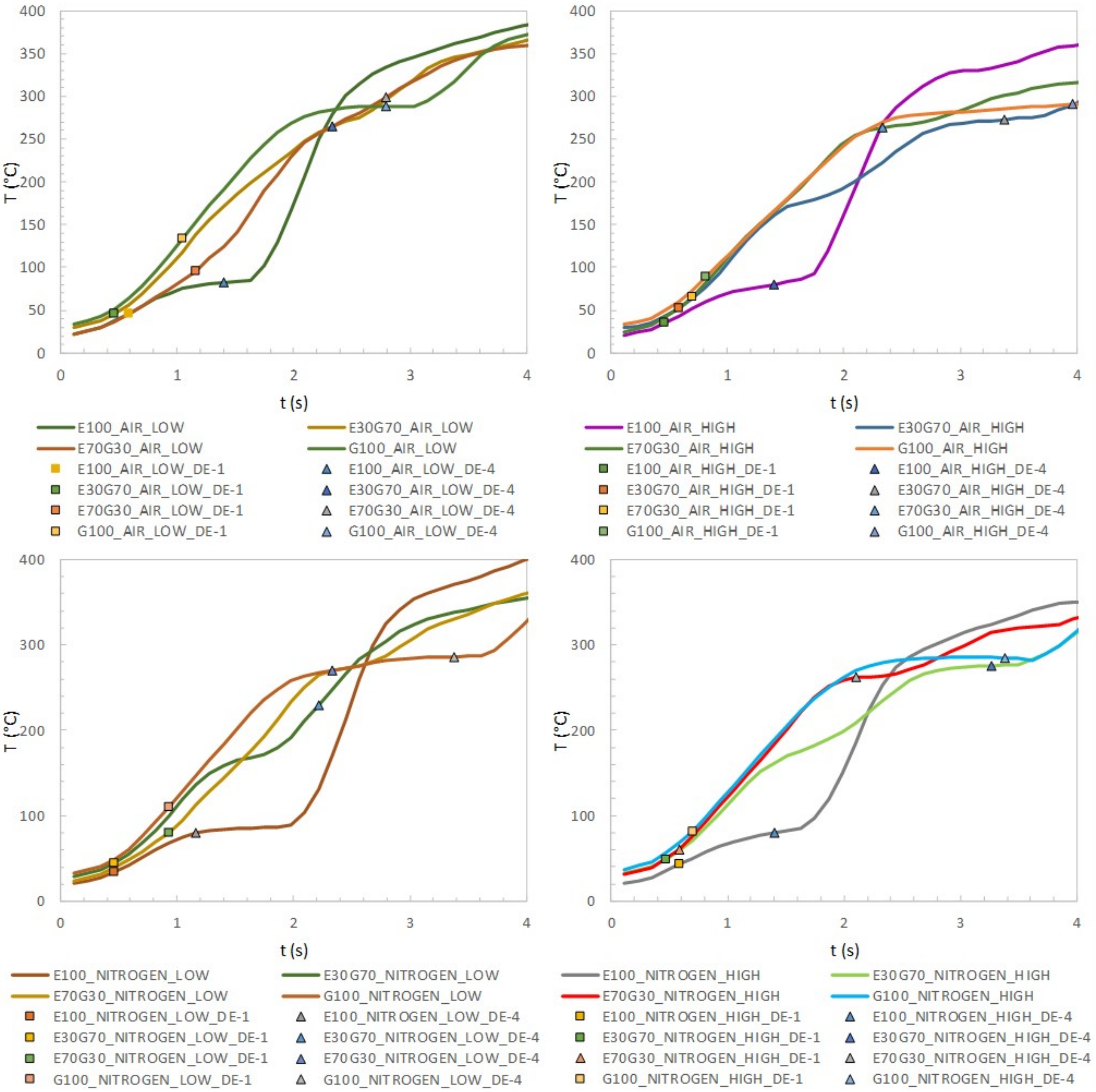

Figure 7-38: Droplet temperature profiles of E30G70 and E70G30 blends shown in comparison with E100 and G100 for air-low (top left), air-high (top right), nitrogen-low (bottom left), and nitrogen-high (bottom right) operating conditions.

Table 7-9: Temperature periods (top) and quantitative low magnification data (bottom) of E30G70 and E70G30 in all four test conditions.

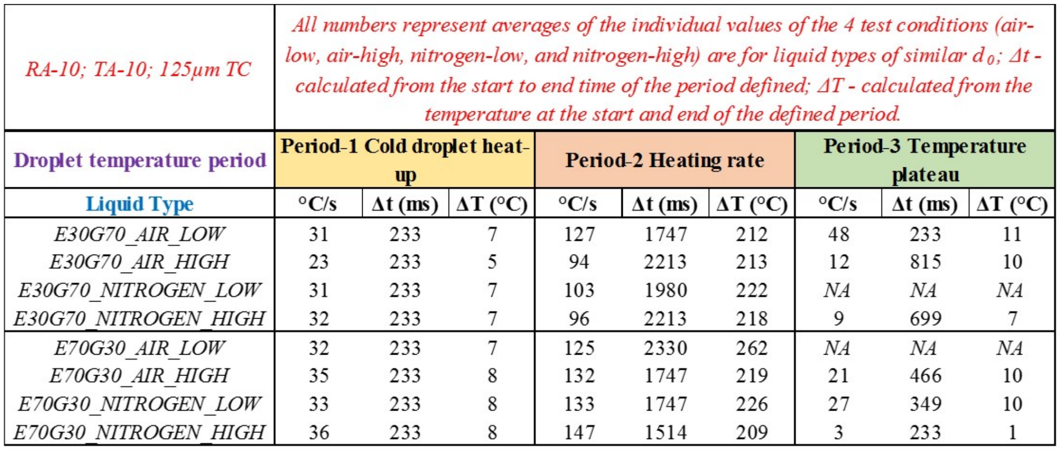

| *RA-10; TA-10; 125µm TC* | *All numbers represent averages of the individual values of the 4 test conditions (air-low, air-high, nitrogen-low, and nitrogen-high) are for liquid types of similar $d_0$; Δt - calculated from the start to end time of the period defined; ΔT - calculated from the temperature at the start and end of the defined period.* | | | | | | | | |
|---|---|---|---|---|---|---|---|---|---|
| **Droplet temperature period** | **Period-1 Cold droplet heat-up** | | | **Period-2 Heating rate** | | | **Period-3 Temperature plateau** | | |
| **Liquid Type** | **°C/s** | **Δt (ms)** | **ΔT (°C)** | **°C/s** | **Δt (ms)** | **ΔT (°C)** | **°C/s** | **Δt (ms)** | **ΔT (°C)** |
| *E30G70_AIR_LOW* | 31 | 233 | 7 | 127 | 1747 | 212 | 48 | 233 | 11 |
| *E30G70_AIR_HIGH* | 23 | 233 | 5 | 94 | 2213 | 213 | 12 | 815 | 10 |
| *E30G70_NITROGEN_LOW* | 31 | 233 | 7 | 103 | 1980 | 222 | *NA* | *NA* | *NA* |
| *E30G70_NITROGEN_HIGH* | 32 | 233 | 7 | 96 | 2213 | 218 | 9 | 699 | 7 |
| *E70G30_AIR_LOW* | 32 | 233 | 7 | 125 | 2330 | 262 | *NA* | *NA* | *NA* |
| *E70G30_AIR_HIGH* | 35 | 233 | 8 | 132 | 1747 | 219 | 21 | 466 | 10 |
| *E70G30_NITROGEN_LOW* | 33 | 233 | 8 | 133 | 1747 | 226 | 27 | 349 | 10 |
| *E70G30_NITROGEN_HIGH* | 36 | 233 | 8 | 147 | 1514 | 209 | 3 | 233 | 1 |

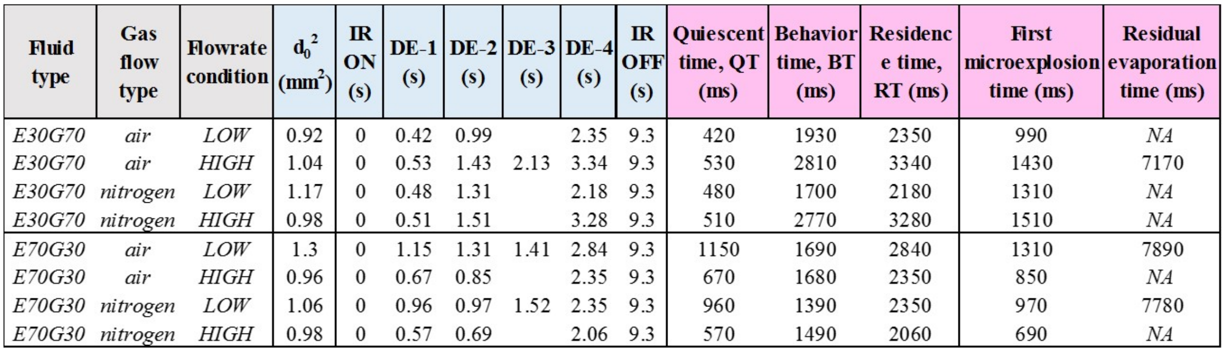

| **Fluid type** | **Gas flow type** | **Flowrate condition** | **$d_0^2$ (mm$^2$)** | **IR ON (s)** | **DE-1 (s)** | **DE-2 (s)** | **DE-3 (s)** | **DE-4 (s)** | **IR OFF (s)** | **Quiescent time, QT (ms)** | **Behavior time, BT (ms)** | **Residence time, RT (ms)** | **First microexplosion time (ms)** | **Residual evaporation time (ms)** |
|---|---|---|---|---|---|---|---|---|---|---|---|---|---|---|
| *E30G70* | *air* | *LOW* | 0.92 | 0 | 0.42 | 0.99 | | 2.35 | 9.3 | 420 | 1930 | 2350 | 990 | *NA* |
| *E30G70* | *air* | *HIGH* | 1.04 | 0 | 0.53 | 1.43 | 2.13 | 3.34 | 9.3 | 530 | 2810 | 3340 | 1430 | 7170 |
| *E30G70* | *nitrogen* | *LOW* | 1.17 | 0 | 0.48 | 1.31 | | 2.18 | 9.3 | 480 | 1700 | 2180 | 1310 | *NA* |
| *E30G70* | *nitrogen* | *HIGH* | 0.98 | 0 | 0.51 | 1.51 | | 3.28 | 9.3 | 510 | 2770 | 3280 | 1510 | *NA* |
| *E70G30* | *air* | *LOW* | 1.3 | 0 | 1.15 | 1.31 | 1.41 | 2.84 | 9.3 | 1150 | 1690 | 2840 | 1310 | 7890 |
| *E70G30* | *air* | *HIGH* | 0.96 | 0 | 0.67 | 0.85 | | 2.35 | 9.3 | 670 | 1680 | 2350 | 850 | *NA* |
| *E70G30* | *nitrogen* | *LOW* | 1.06 | 0 | 0.96 | 0.97 | 1.52 | 2.35 | 9.3 | 960 | 1390 | 2350 | 970 | 7780 |
| *E70G30* | *nitrogen* | *HIGH* | 0.98 | 0 | 0.57 | 0.69 | | 2.06 | 9.3 | 570 | 1490 | 2060 | 690 | *NA* |

Isolated droplet temperature plots of E30G70 and E70G30 for varying flowrate conditions in air and nitrogen environments are shown in Figure 7-39 and Figure 7-40. General behavior of E30G70 droplet as understood from the visualizations is that the droplet initially heats up followed by a bubbling behavior. This behavior transforms into a microdroplet escape/microexplosion behavior (Figure 7-7, Figure 7-3) followed by residual droplet evaporation (Figure 7-5). Both E70G30 and E30G70 droplets exhibit all of these significant behavior events. One of the important differences observed in the quantitative low magnification data is the longer quiescent times of E70G30 over E30G70. We can see from Table 7-7 and Table 7-9 that the average quiescent times of E30G70 are close to E100 whereas the average values of E70G30 are close to that of G100. Similarly, the average maximum heating rates of E70G30 in Table 7-7 are close to that of G100, whereas those of E30G70 are closer to the mean of E100 and G100. The possible explanation for these values lies in the differential behavior types of these blends as is described in the following.

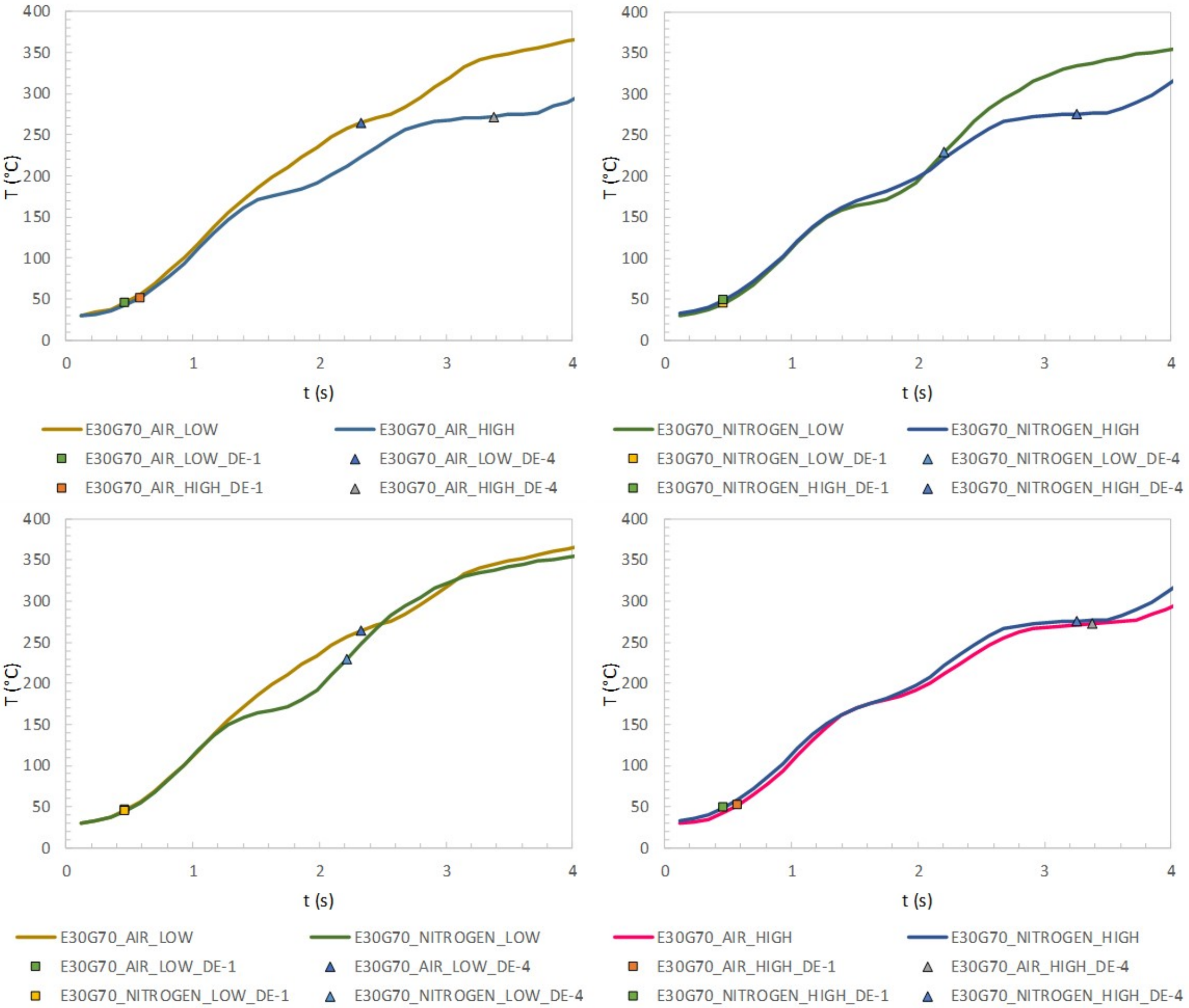

Figure 7-39: E30G70 droplet temperature profile compared at air-low (top left), air-high (top right), nitrogen-low (bottom left), and nitrogen-high (bottom right) operating conditions.

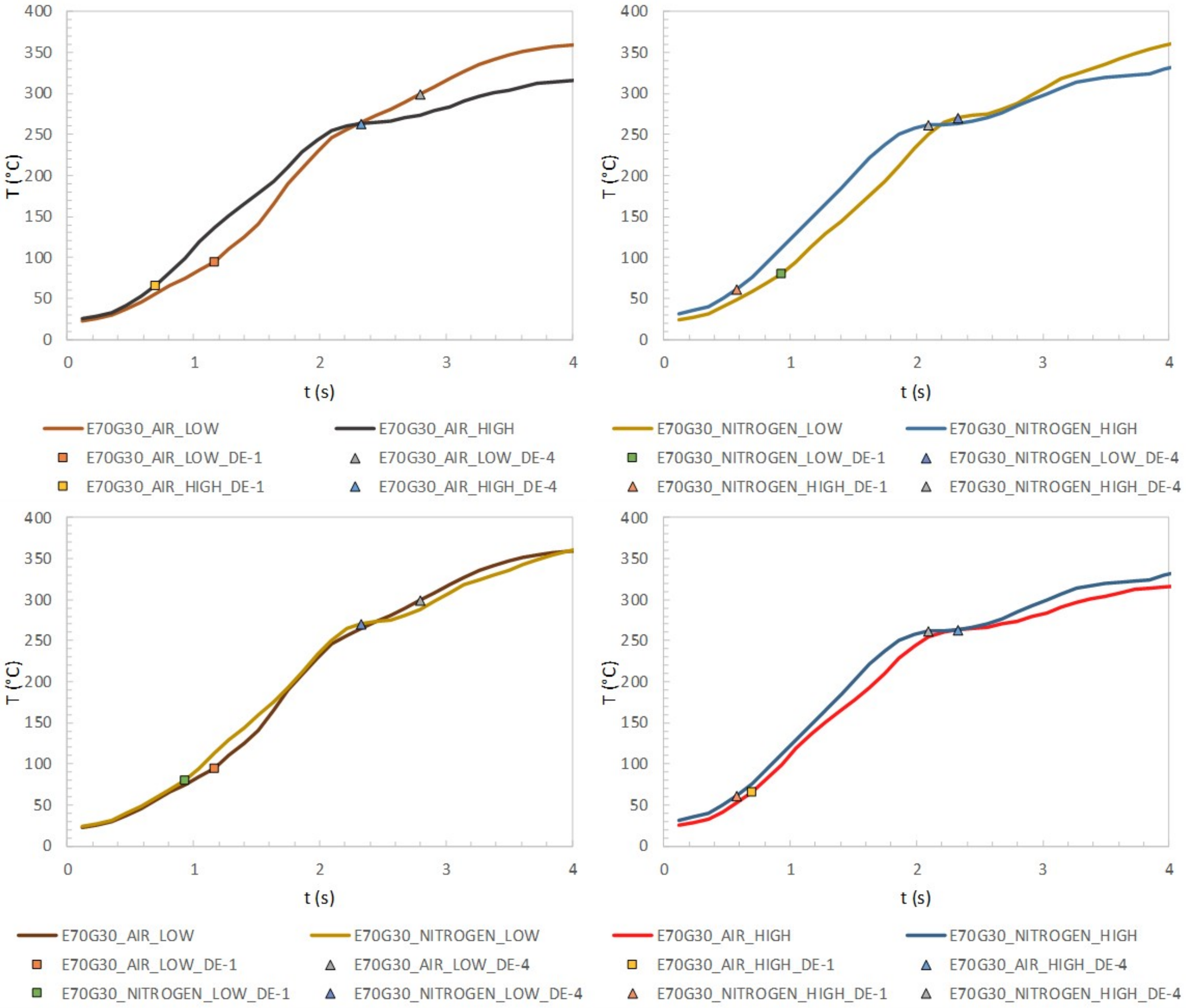

Figure 7-40: E70G30 droplet temperature profile compared at air-low (top left), air-high (top right), nitrogen-low (bottom left), and nitrogen-high (bottom right) operating conditions.

The E70G30 droplet during the initial phases of evaporation behaves like a G100 droplet despite having a lower volume percent of glycerol. The ethanol component of the droplet heats up to its boiling point but remains trapped inside the droplet surface. Due to the larger concentration of the ethanol component, we probably do not see the formation of micro-bubbles that normally occurs during the bubbling behavior and this contributes directly to the larger quiescent time recorded for this liquid type. The vapor pockets trapped as result of the evaporation of the ethanol component increase in pressure, and release from the droplet in the form of a strong microexplosion event with a larger droplet volume loss. The residual droplet remaining after the microexplosion has a higher concentration of glycerol and evaporates like a G100 droplet. This can be confirmed from the temperature plateau behavior of the E70G30 blend occurring near the glycerol boiling point as shown in Figure 7-40.

E30G70 droplets on the other hand have low concentrations of the ethanol component dissolved in a higher concentration of glycerol. As the droplet heats up, the small volume of ethanol reaches its boiling point and transforms into vapor phase. These vapor pockets are the numerous micro bubbles seen inside the droplet during the bubbling behavior. Due to the low concentrations of ethanol, the bubbling behavior is more pronounced in these droplets over E70G30 type and subsequently results in short quiescent times recorded for this droplet type. Also, the quiescent period is followed by a microdroplet escape behavior unlike the direct microexplosion seen in E70G30 droplets. This can be seen in the difference between quiescent time and the first microexplosion time of both the blends as listed in Table 7-9. From Figure 7-39 and Figure 7-40, we also see the temperature profile varying with respect to operating gas flowrate. This can also be observed from the varying period-2 heating rate values of Table 7-9 for both E30G70 and E70G30 with respect to changing flowrates in air and nitrogen environments.

#### 7.4.2.3. M100 (Pure Methanol) and B100 (Pure Butanol)

Figure 7-41 shows the droplet temperature profiles of M100 and B100 in low flowrate air environments. The low magnification visualization of M100 and B100 were shown earlier in Figure 7-13 and Figure 7-11.The droplet temperature profile seen in Figure 7-41 is consistent with the observations discussed earlier with E100 and G100 liquids as both the liquid types exhibit three well defined temperature periods. Temperature period and quantitative low magnification data for the four test conditions are shown in Table 7-10.

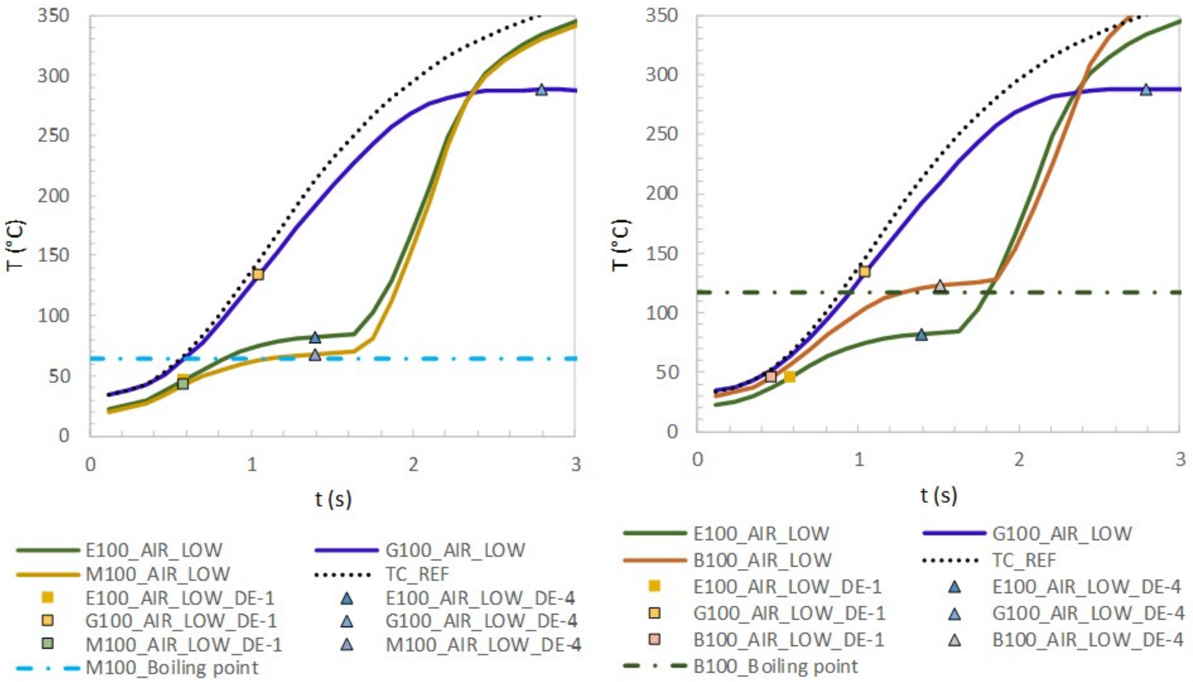

Figure 7-41: Droplet temperature profile of M100 (left) and B100 (right) shown in comparison with the E-G system for a low air flowrate operating condition.

Table 7-10: Temperature period (top) and quantitative low magnification data (bottom) of M100 and B100 liquid types for the four test conditions.

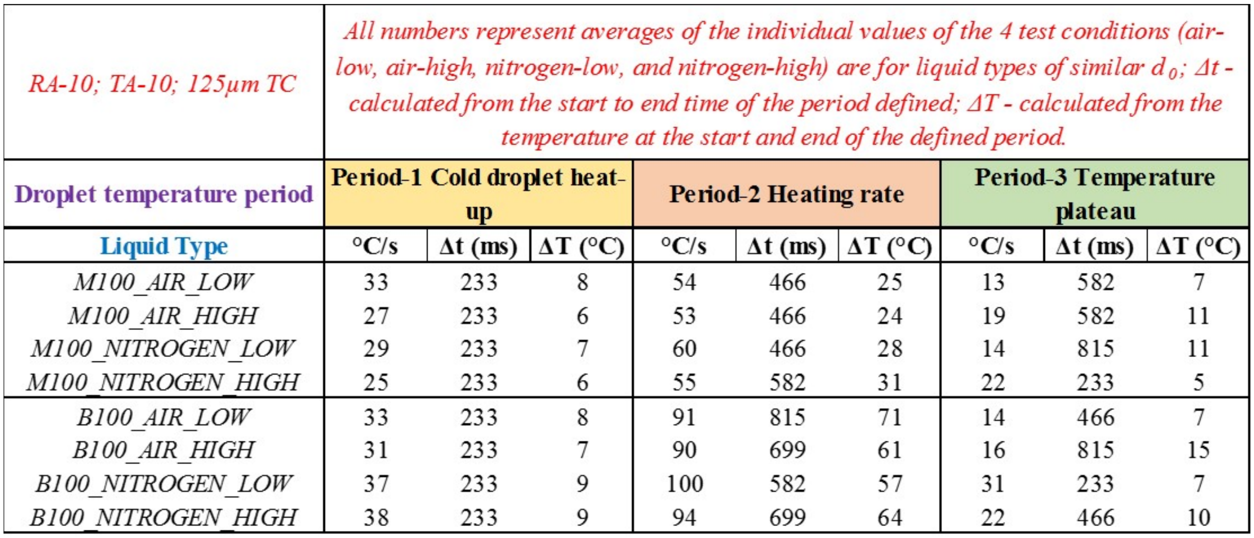

| *RA-10; TA-10; 125μm TC* | *All numbers represent averages of the individual values of the 4 test conditions (air-low, air-high, nitrogen-low, and nitrogen-high) are for liquid types of similar $d_0$; Δt - calculated from the start to end time of the period defined; ΔT - calculated from the temperature at the start and end of the defined period.* | | | | | | | | |
|---|---|---|---|---|---|---|---|---|---|
| **Droplet temperature period** | **Period-1 Cold droplet heat-up** | | | **Period-2 Heating rate** | | | **Period-3 Temperature plateau** | | |
| **Liquid Type** | **°C/s** | **Δt (ms)** | **ΔT (°C)** | **°C/s** | **Δt (ms)** | **ΔT (°C)** | **°C/s** | **Δt (ms)** | **ΔT (°C)** |
| *M100_AIR_LOW* | 33 | 233 | 8 | 54 | 466 | 25 | 13 | 582 | 7 |
| *M100_AIR_HIGH* | 27 | 233 | 6 | 53 | 466 | 24 | 19 | 582 | 11 |
| *M100_NITROGEN_LOW* | 29 | 233 | 7 | 60 | 466 | 28 | 14 | 815 | 11 |
| *M100_NITROGEN_HIGH* | 25 | 233 | 6 | 55 | 582 | 31 | 22 | 233 | 5 |
| *B100_AIR_LOW* | 33 | 233 | 8 | 91 | 815 | 71 | 14 | 466 | 7 |
| *B100_AIR_HIGH* | 31 | 233 | 7 | 90 | 699 | 61 | 16 | 815 | 15 |
| *B100_NITROGEN_LOW* | 37 | 233 | 9 | 100 | 582 | 57 | 31 | 233 | 7 |
| *B100_NITROGEN_HIGH* | 38 | 233 | 9 | 94 | 699 | 64 | 22 | 466 | 10 |

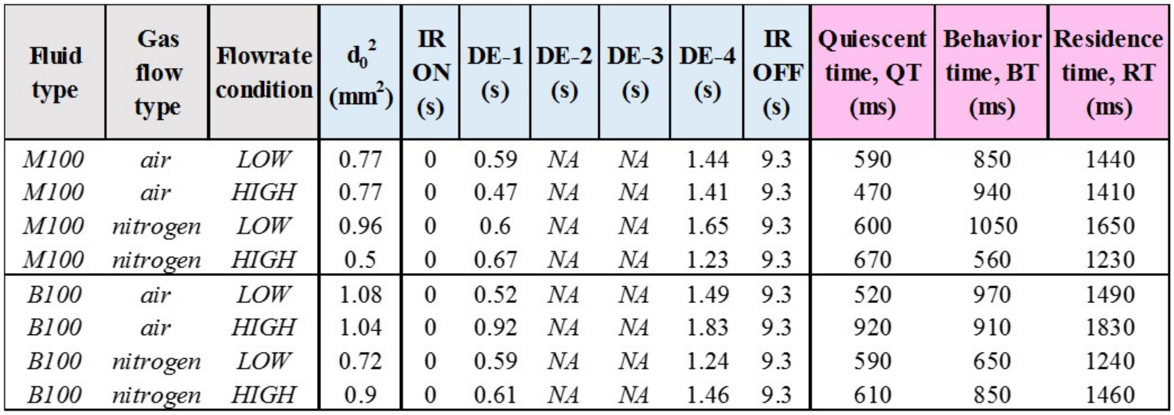

| **Fluid type** | **Gas flow type** | **Flowrate condition** | **$d_0^2$ (mm$^2$)** | **IR ON (s)** | **DE-1 (s)** | **DE-2 (s)** | **DE-3 (s)** | **DE-4 (s)** | **IR OFF (s)** | **Quiescent time, QT (ms)** | **Behavior time, BT (ms)** | **Residence time, RT (ms)** |
|---|---|---|---|---|---|---|---|---|---|---|---|---|
| *M100* | *air* | *LOW* | 0.77 | 0 | 0.59 | *NA* | *NA* | 1.44 | 9.3 | 590 | 850 | 1440 |
| *M100* | *air* | *HIGH* | 0.77 | 0 | 0.47 | *NA* | *NA* | 1.41 | 9.3 | 470 | 940 | 1410 |
| *M100* | *nitrogen* | *LOW* | 0.96 | 0 | 0.6 | *NA* | *NA* | 1.65 | 9.3 | 600 | 1050 | 1650 |
| *M100* | *nitrogen* | *HIGH* | 0.5 | 0 | 0.67 | *NA* | *NA* | 1.23 | 9.3 | 670 | 560 | 1230 |
| *B100* | *air* | *LOW* | 1.08 | 0 | 0.52 | *NA* | *NA* | 1.49 | 9.3 | 520 | 970 | 1490 |
| *B100* | *air* | *HIGH* | 1.04 | 0 | 0.92 | *NA* | *NA* | 1.83 | 9.3 | 920 | 910 | 1830 |
| *B100* | *nitrogen* | *LOW* | 0.72 | 0 | 0.59 | *NA* | *NA* | 1.24 | 9.3 | 590 | 650 | 1240 |
| *B100* | *nitrogen* | *HIGH* | 0.9 | 0 | 0.61 | *NA* | *NA* | 1.46 | 9.3 | 610 | 850 | 1460 |

Table 7-10 values show that the cold heat-up period (period-1) of M100 and B100 are consistent with all the other liquid types discussed before. Peiord-2 heating rates listed for M100 and B100 shows that the changes in gas flowrate or gas type do not affect the droplet heating rate. From Table 7-7, we see that the average heating rate values of M100 are lower than E100 while, B100 heating rates are higher than E100. The boiling point and heat of vaporization of E100 are in-between that of M100 and B100 (Table 7-2). Hence, the observed heating rates of Table 7-7 are understandable and follow the droplet behavior trend described thus far.

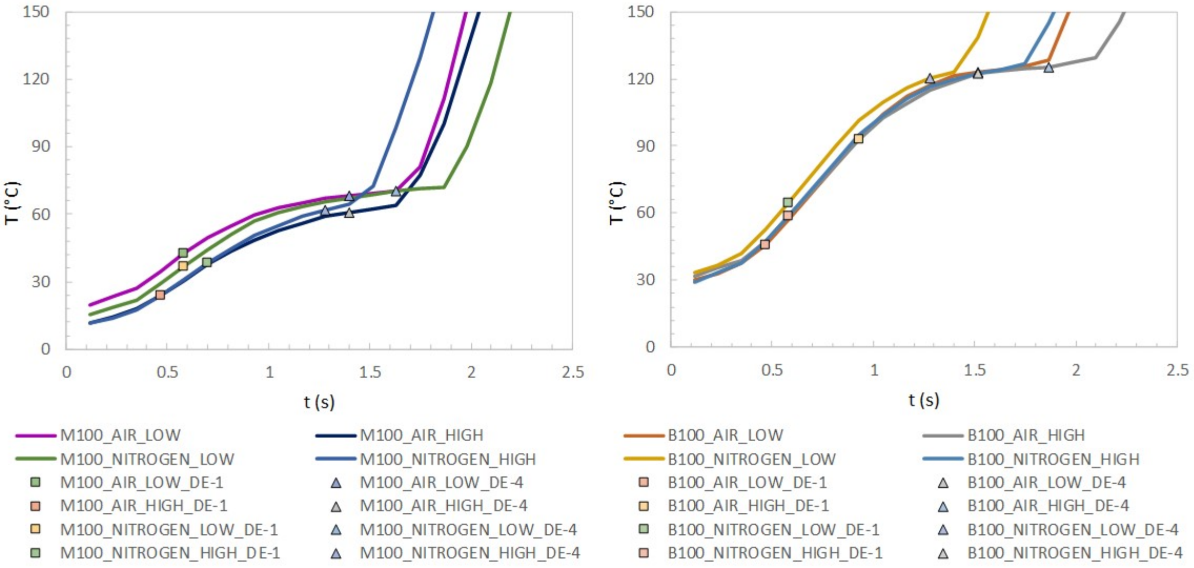

Figure 7-42: Droplet temperature profiles of M100 (left) and B100 (right) liquid types shown for the four test conditions.

Figure 7-42 shows that the droplet temperature profiles of M100 and B100 for the four test conditions. The droplet temperature profile of M100 and B100 observed in Figure 7-42 are similar for all the operating conditions. This behavior trend is consistent with our observations for E100 and G100 as shown earlier in Figure 7-37. Also, from Figure 7-41, we observe the M100 and B100 droplet temperature profiles are in the temperature range resembling E100 more so than G100 of the E-G system. This behavior of the profile is understandable considering all the three (E100, M100, and B100) are closely related alcohols (Table 7-2). Temperature period and quantitative low magnification data of Table 7-10 also confirm the visual observations in the plots. The heating rates were observed to be slightly higher for low flowrates over high flowrate conditions for both M100 and B100 liquid types. This behavior is consistent with the other pure liquids E100 and G100.

### 7.4.2.4. Hexadecane – Standard Fuel

Figure 7-43 shows the droplet temperature profile of a hexadecane droplet alongside E-G system liquids E100 and G100 in low flowrate air environment. This standard fuel was selected for comparison with the E-G system for its high cetane number and the sustainable energy applications of glycerol blends used in this research. The heating rate, time durations, and temperature difference for all conditions along with the quantitative data can be found in Table 7-11.

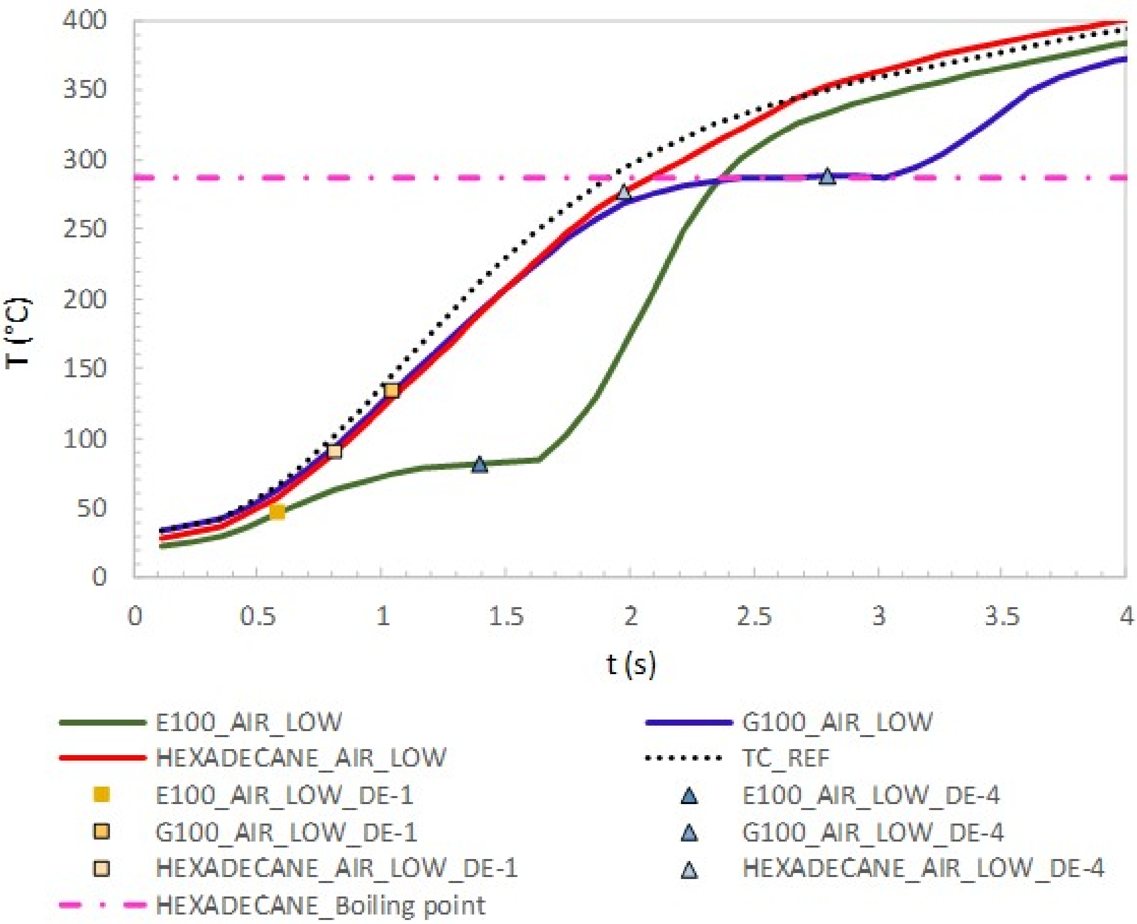

Figure 7-43: Droplet temperature profile of hexadecane liquid type shown alongside the E-G system for a low air flowrate operating condition.

As seen in Table 7-11, the hexadecane droplet temperature profile does not exhibit a plateau formation. Figure 7-44 shows the droplet temperature profiles of hexadecane for multiple operating conditions along with the quantitative data obtained from low magnification visualizations. From this plot, we see that the profile is consistent with the typical profile for multiple operating conditions. Also, we notice that the temperatures corresponding to the residence time for all conditions are below the boiling point of hexadecane (286.9°C). This explains the absence of the temperature plateau (period-3) in this liquid type since the droplet undergoes complete evaporation before it reaches its boiling point. Despite similarities in the physical properties of hexadecane to alcohols in terms of density, viscosity, and surface tension, the maximum heating rate values are closer to glycerol. This can be seen in the plots of Figure 7-43 comparing it to E-G system and the behavior is probably due to hexadecane's heat of vaporization being relatively close to glycerol (Table 7-2).

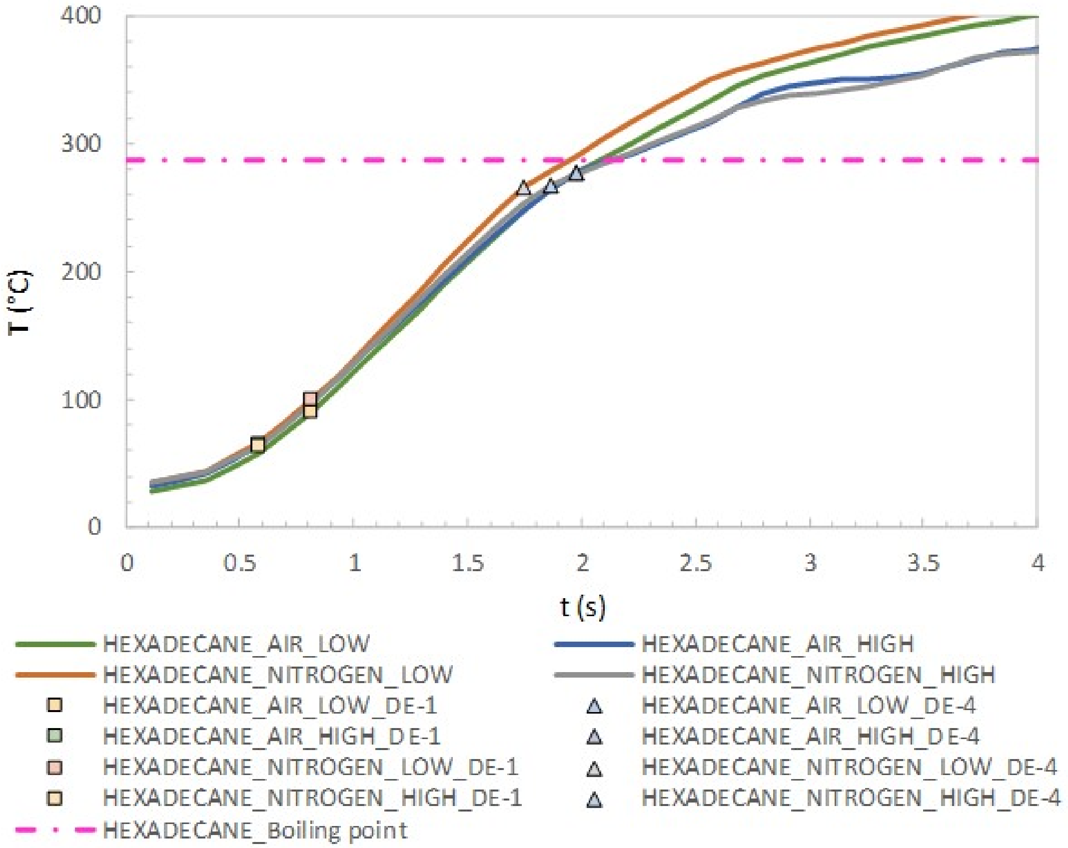

Figure 7-44: Droplet temperature profiles of hexadecane liquid type shown for the four test conditions.

Table 7-11: Temperature period and quantitative low magnification data of hexadecane liquid type for all the test conditions.

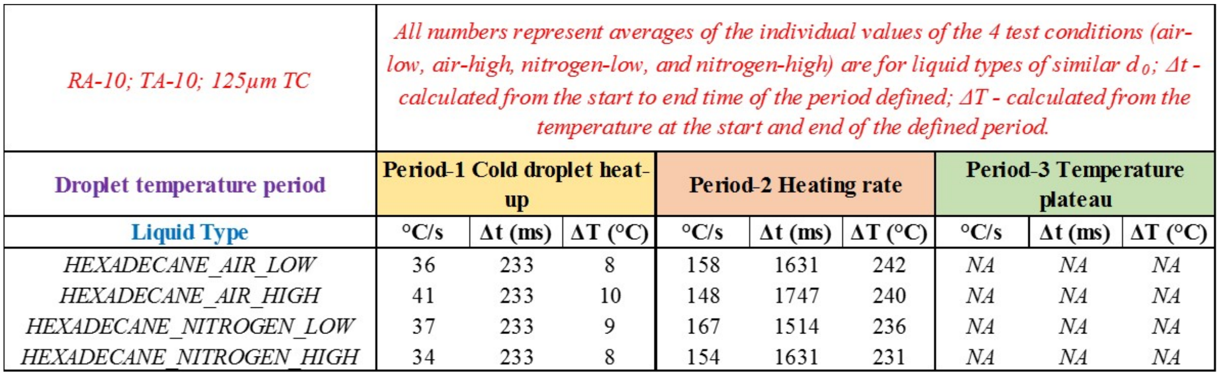

| *RA-10; TA-10; 125μm TC* | *All numbers represent averages of the individual values of the 4 test conditions (air-low, air-high, nitrogen-low, and nitrogen-high) are for liquid types of similar $d_0$; Δt - calculated from the start to end time of the period defined; ΔT - calculated from the temperature at the start and end of the defined period.* | | | | | | | | |
|---|---|---|---|---|---|---|---|---|---|
| **Droplet temperature period** | **Period-1 Cold droplet heat-up** | | | **Period-2 Heating rate** | | | **Period-3 Temperature plateau** | | |
| **Liquid Type** | **°C/s** | **Δt (ms)** | **ΔT (°C)** | **°C/s** | **Δt (ms)** | **ΔT (°C)** | **°C/s** | **Δt (ms)** | **ΔT (°C)** |
| *HEXADECANE_AIR_LOW* | 36 | 233 | 8 | 158 | 1631 | 242 | *NA* | *NA* | *NA* |
| *HEXADECANE_AIR_HIGH* | 41 | 233 | 10 | 148 | 1747 | 240 | *NA* | *NA* | *NA* |
| *HEXADECANE_NITROGEN_LOW* | 37 | 233 | 9 | 167 | 1514 | 236 | *NA* | *NA* | *NA* |
| *HEXADECANE_NITROGEN_HIGH* | 34 | 233 | 8 | 154 | 1631 | 231 | *NA* | *NA* | *NA* |

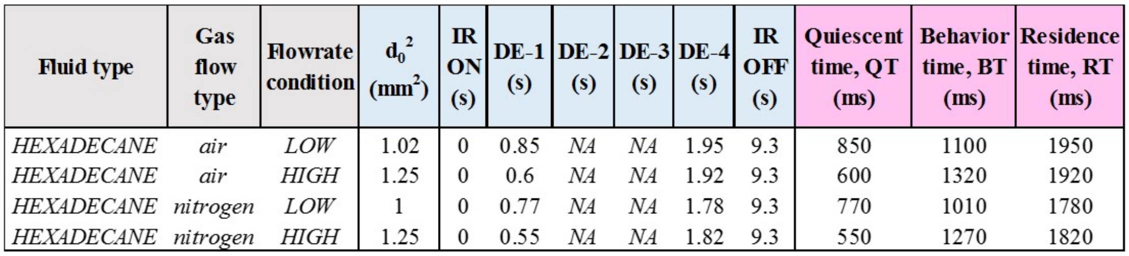

| **Fluid type** | **Gas flow type** | **Flowrate condition** | **$d_0^2$ (mm$^2$)** | **IR ON (s)** | **DE-1 (s)** | **DE-2 (s)** | **DE-3 (s)** | **DE-4 (s)** | **IR OFF (s)** | **Quiescent time, QT (ms)** | **Behavior time, BT (ms)** | **Residence time, RT (ms)** |
|---|---|---|---|---|---|---|---|---|---|---|---|---|
| *HEXADECANE* | *air* | *LOW* | 1.02 | 0 | 0.85 | *NA* | *NA* | 1.95 | 9.3 | 850 | 1100 | 1950 |
| *HEXADECANE* | *air* | *HIGH* | 1.25 | 0 | 0.6 | *NA* | *NA* | 1.92 | 9.3 | 600 | 1320 | 1920 |
| *HEXADECANE* | *nitrogen* | *LOW* | 1 | 0 | 0.77 | *NA* | *NA* | 1.78 | 9.3 | 770 | 1010 | 1780 |
| *HEXADECANE* | *nitrogen* | *HIGH* | 1.25 | 0 | 0.55 | *NA* | *NA* | 1.82 | 9.3 | 550 | 1270 | 1820 |

### 7.4.2.5. BP Oil – Commercial Aviation Engine Oil BP Turbo 274

Commercial BP engine oil used for our aviation fluids research is compared to the E-G system for its multicomponent nature. BP Oil is a proprietary fluid and hence knowledge of its physical and chemical properties is limited. Engine oils are generally made up of numerous additives for applications and hence is comprised of components with a range of volatilities. Figure 7-45 shows the typical temperature profile of a BP Oil droplet undergoing evaporation in comparison with the E-G system. Table 7-12 shows the multiple operating condition droplet temperature and quantitative data obtained through low magnification visualizations.

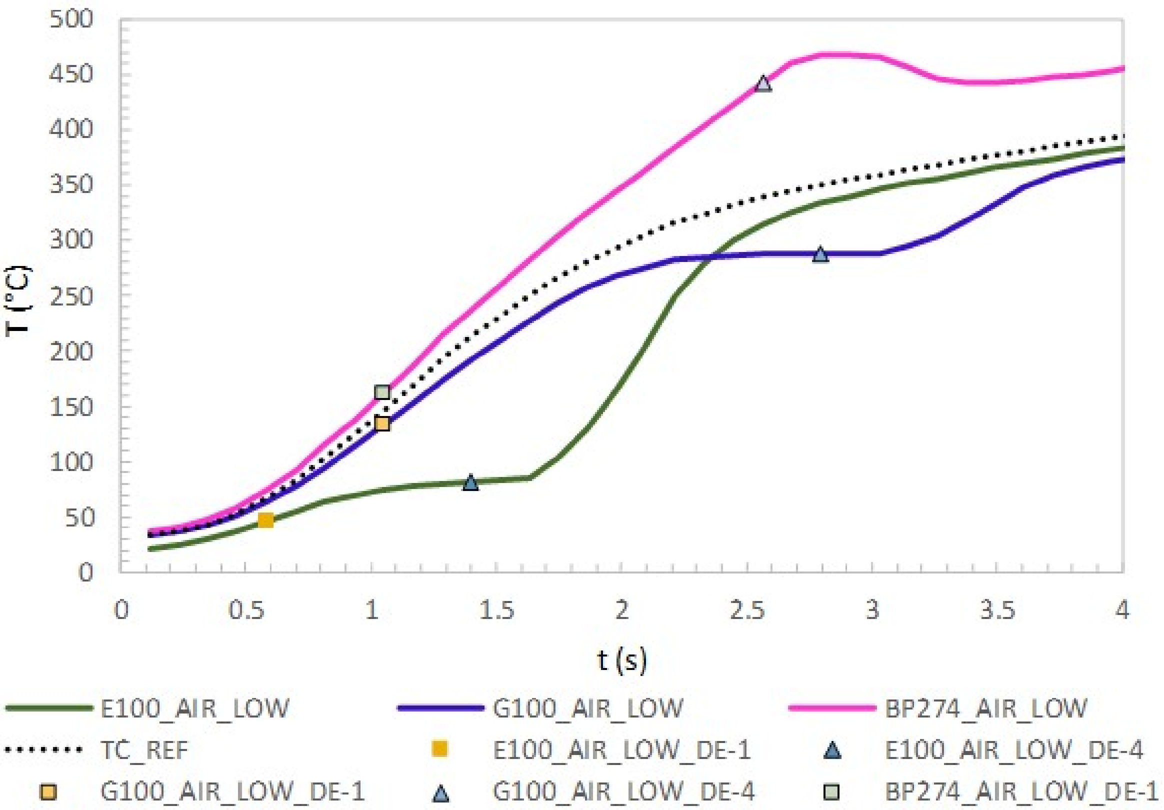

Figure 7-45: Droplet temperature profile of BP Oil liquid type shown alongside the E-G system for a low air flowrate operating condition.

Table 7-12: Temperature period (top) and quantitative low magnification data (bottom) of BP Oil liquid type for all the test conditions.

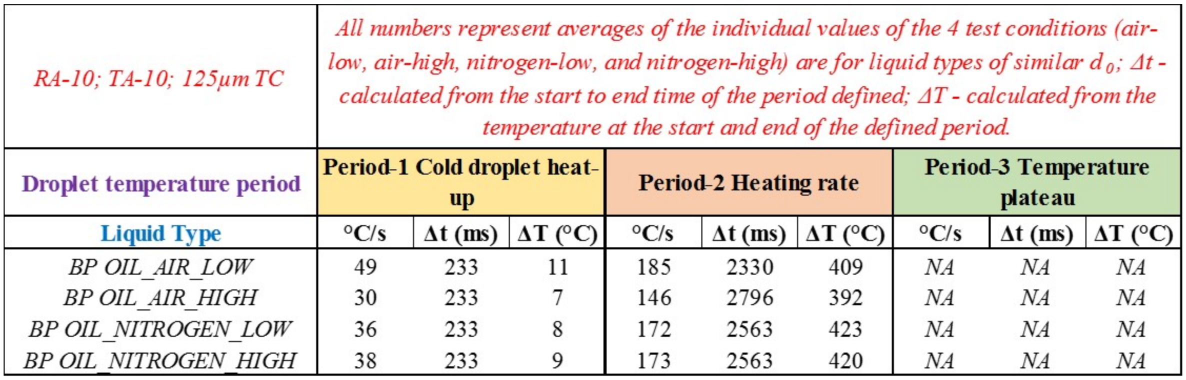

| *RA-10; TA-10; 125µm TC* | *All numbers represent averages of the individual values of the 4 test conditions (air-low, air-high, nitrogen-low, and nitrogen-high) are for liquid types of similar $d_0$; Δt - calculated from the start to end time of the period defined; ΔT - calculated from the temperature at the start and end of the defined period.* | | | | | | | | |
|---|---|---|---|---|---|---|---|---|---|
| **Droplet temperature period** | **Period-1 Cold droplet heat-up** | | | **Period-2 Heating rate** | | | **Period-3 Temperature plateau** | | |
| **Liquid Type** | **°C/s** | **Δt (ms)** | **ΔT (°C)** | **°C/s** | **Δt (ms)** | **ΔT (°C)** | **°C/s** | **Δt (ms)** | **ΔT (°C)** |
| *BP OIL_AIR_LOW* | 49 | 233 | 11 | 185 | 2330 | 409 | *NA* | *NA* | *NA* |
| *BP OIL_AIR_HIGH* | 30 | 233 | 7 | 146 | 2796 | 392 | *NA* | *NA* | *NA* |
| *BP OIL_NITROGEN_LOW* | 36 | 233 | 8 | 172 | 2563 | 423 | *NA* | *NA* | *NA* |
| *BP OIL_NITROGEN_HIGH* | 38 | 233 | 9 | 173 | 2563 | 420 | *NA* | *NA* | *NA* |

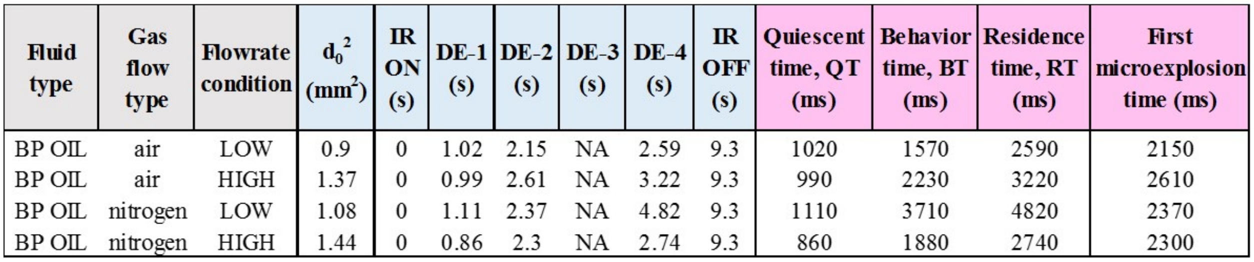

| **Fluid type** | **Gas flow type** | **Flowrate condition** | **$d_0^2$ (mm$^2$)** | **IR ON (s)** | **DE-1 (s)** | **DE-2 (s)** | **DE-3 (s)** | **DE-4 (s)** | **IR OFF (s)** | **Quiescent time, QT (ms)** | **Behavior time, BT (ms)** | **Residence time, RT (ms)** | **First microexplosion time (ms)** |
|---|---|---|---|---|---|---|---|---|---|---|---|---|---|
| BP OIL | air | LOW | 0.9 | 0 | 1.02 | 2.15 | NA | 2.59 | 9.3 | 1020 | 1570 | 2590 | 2150 |
| BP OIL | air | HIGH | 1.37 | 0 | 0.99 | 2.61 | NA | 3.22 | 9.3 | 990 | 2230 | 3220 | 2610 |
| BP OIL | nitrogen | LOW | 1.08 | 0 | 1.11 | 2.37 | NA | 4.82 | 9.3 | 1110 | 3710 | 4820 | 2370 |
| BP OIL | nitrogen | HIGH | 1.44 | 0 | 0.86 | 2.3 | NA | 2.74 | 9.3 | 860 | 1880 | 2740 | 2300 |

From Figure 7-45 and Table 7-12, we see that the heating rate of the BP Oil is the highest of all liquid types studied. As was the case for the hexadecane droplet temperature profile, there is an absence of temperature plateau. The boiling point of the liquid is unknown and the best possible explanation is that the droplet evaporates before it reaches that point. In visualization (Figure 7-12), we see a distinct microexplosion behavior and it is reasonable to expect such behavior in a liquid type made up of multiple components of varying properties. Table 7-12 values show very little variation in BP Oil droplet temperature profile for multiple flowrate conditions. Figure 7-46 shows the BP Oil droplet temperature profile for all the test conditions. Observation from Figure 7-46 and the values in the Table 7-12 shows a large difference in the maximum heating rate of BP Oil between low and high air flow operating conditions. Due to the randomness of the microexplosion behavior of BP Oil droplets, to investigate if the difference observed for heating rates are consistent and significant, larger samples of experimental data are required.

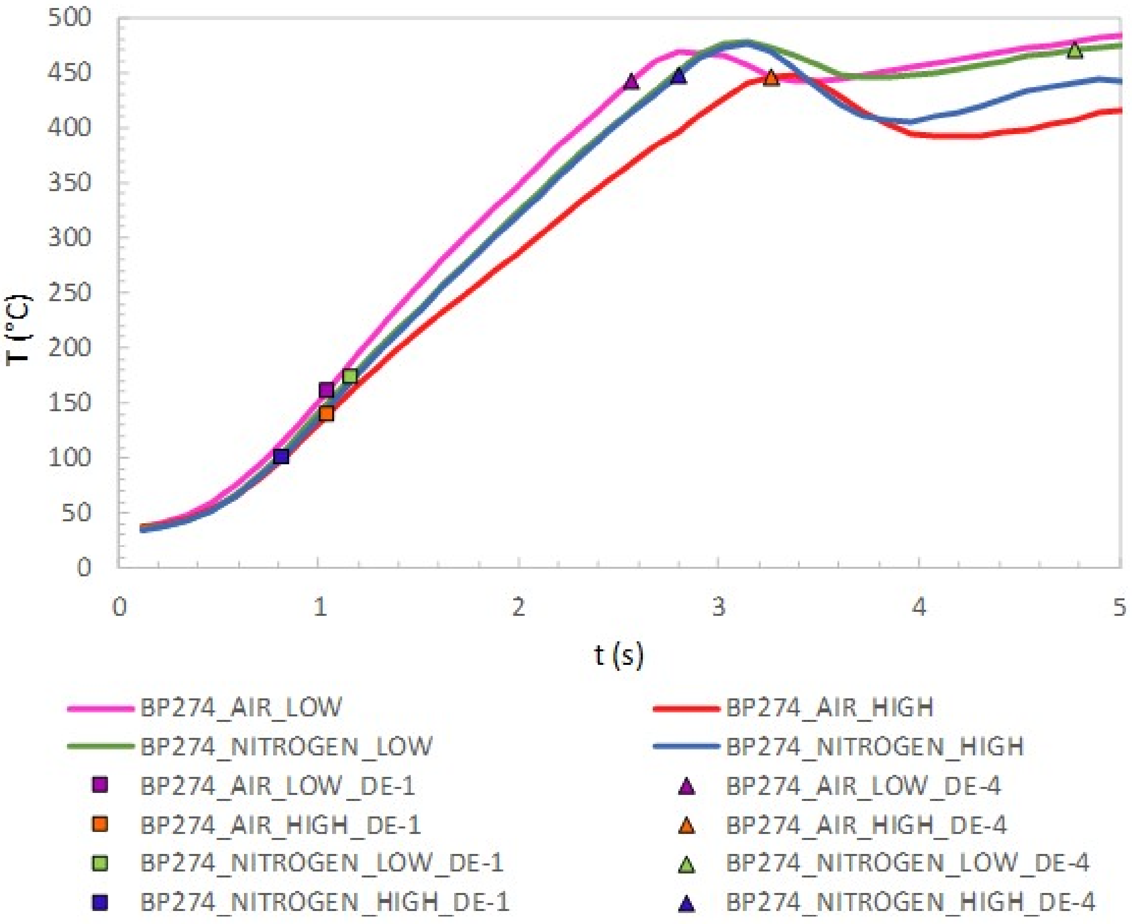

Figure 7-46: Droplet temperature profiles of BP Oil liquid type shown for the four test conditions.

### 7.4.3. Summary

Suspended droplet experiments with different liquid types have been successful in understanding the general behavior of E-G system liquids. Low magnification visualizations of the droplet lifetime for all liquids have been presented along with the identification of significant behavior events such as the droplet attrition behavior in standard fuel (Hexadecane) and distinct microexplosion behavior in aviation liquid (BP Oil). Low magnification quantitative data (QT, BT, RT) were shown for all liquids in four different test conditions (air-low, air-high, nitrogen-low, and nitrogen-high). Averaged values of the low magnification quantitative data (avg QT, avg BT, avg RT) shows the quiescent and behavior periods to be influenced by the liquid properties, specifically the boiling point and heat of vaporization property except for the hexadecane liquid. The hexadecane liquid show QT and BT durations closer to alcohols (E100, M100, B100) rather than G100 despite similar liquid properties to the latter. Overall ±error values associated with the averaged values show the influence of the test condition to be minimum in E100, M100, B100 and hexadecane liquids. Blends (E30G70, E70G30) and liquids with longer residence times (G100, BP Oil) shows increased deviations (±error) in QT, BT, and RT with the four test conditions. Significant behavior events of blend liquids (strength of microexplosion and microdroplet events) and the heat transfer effects (potentially increased role of convective heat transfer) associated with longer residence time were suggested to be responsible for the observed changes in BT with test conditions. Influence of the four test conditions for all liquids was investigated by the calculation of ΔQT, ΔBT, and ΔRT. Overall, the difference values show the gas flowrate to have higher influence over gas type. When averaged, different test condition comparisons showed the deviations of ΔQT, ΔBT, and ΔRT to be larger than their respective average values. Hence, the influence of test condition on the quiescent and behavior time durations warrants further investigation.

The droplet temperature dat for all liquids in the four test conditions were analyzed by classification into three different temperature periods based on their temperature increase rates. Heating rate, time duration ($\Delta t$), and temperature difference ($\Delta T$) of each period was calculated for all liquids and test conditions. Generally, the period-2 heating rates obtained for all liquids were found to be strongly related to their respective liquid properties specifically to the boiling point and heat of vaporization. Blends showed heating rates closer to G100 compared to E100 despite contrasting compositions. Heating rates of hexadecane and G100 were similar except for the absence of temperature plateau (period-3) in the former. BP Oil showed the highest heating rate of all liquids and an absence of temperature plateau. Stronger microexplosion resulting in the absence of residual droplet evaporation were found to be the reason behind the absence of period-3 in the aviation liquid. Investigation of the influence of test condition on heating rates showed E30G70, E70G30, G100, and BP Oil liquids to have a maximum difference of ≥20°C between any two test conditions. The reasoning mentioned earlier for the influence of test condition on QT, BT, and RT holds true for the observed difference in heating rates.

## 7.5. High Magnification Experiments

The main objective of the high magnification experiments was to study the behavior of a droplet using quantitative analysis of the temporal change in the suspended droplet diameter and the droplet temperature. The PCO camera and Questar long-distance microscope lens combination was used to obtain the high magnification visualizations of droplets. Experiments were performed for the four E-G system liquids which include pure ethanol (E100), 30 vol% ethanol – 70 vol% glycerol (E30G70), 70 vol% ethanol – 30 vol% glycerol (E70G30), and pure glycerol (G100). IR controller settings for the experiments are RUN ADJUST at 10 (maximum heating rate) and TIME ADJUST at 10 (lamps illuminate for ~9s). Operating conditions were air environment at a flowrate of 10 SCFM. For all the high magnification experiments, the IR controller settings and the operating conditions were unchanged. For this study, the suspended droplet experiment was performed numerous times until at least six data sets were obtained for each test liquid that contained visualizations suitable to perform droplet diameter calculations. In additions to the visualizations, droplet temperature data were obtained for each experiment.

### 7.5.1. Characteristic Evaporation Phases

Droplet diameter (*d*) for suspended droplets were determined with ImageJ from images selected at periodic intervals. Detailed explanation on the image selection and droplet diameter measurements are explained in the Appendix A. Figure 7-47 shows the temporal droplet diameter for six droplets of each liquid type in the E-G system. From the figure, we observe the droplet diameter decreases with respect to time as the droplet evaporates. For the E100 droplets, we observe *d* reducing with respect to time from its initial droplet diameter ($d_0$). In the case of pure glycerol (G100), during the early period of droplet evaporation, *d* almost remains the same followed by a period of constant reduction with respect to $d_0$. In the blend droplets E30G70 and

E70G30, we observe *d* values fluctuate for a short duration during the droplet evaporation followed by constant reduction in *d* value with respect to $d_0$.

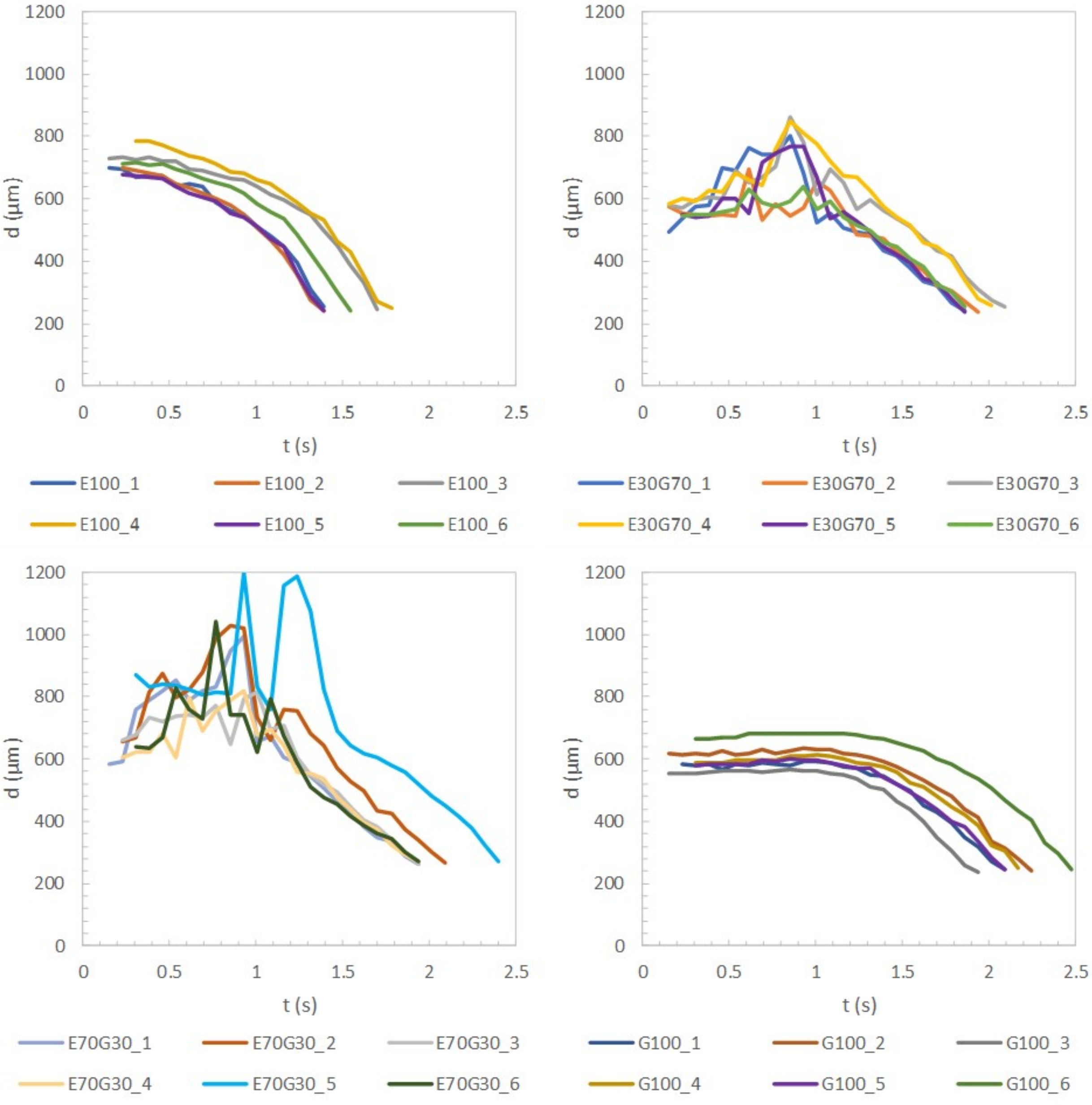

Figure 7-47: Temporal diameter of E100 (top left), E30G70 (top right), E70G30 (bottom left), and G100 (bottom right) for 6 droplets.

The temporal change in the droplet diameter for each test liquid were analyzed into well-defined characteristic evaporation periods as explained in the works Ghassemi et al. (2006) and Ma et al. (2015). The evaporation periods in our experiments are explained as follows.

*Transient Heating Phase* (THP) – It is defined as the phase in which the temporal change in the droplet dimeter ($d$) is minimal and close to the initial droplet diameter ($d_0$). This is the initial phase in droplet evaporation during which the cold droplet heats up. For some liquid types, we also see the occurrence of liquid thermal expansion that reflects in a slight increase of $d$ over $d_0$.

*Fluctuation Evaporation Phase* (FEP) – It is defined as the phase in which the temporal droplet diameter largely fluctuates with respect to $d_0$. Generally, the fluctuations in $d$ values are a result of bubbling, micro droplet escape, or microexplosion behaviors in the droplet and usually occur following the transient heating phase.

*Equilibrium Evaporation Phase* (EEP) – It is defined as the phase in which the temporal change in the droplet diameter is constant with respect to time. During this phase, active droplet evaporation takes place with consistent droplet surface regression. This is usually the final characteristic phase of evaporation and the one in which the $d^2$-law as will be explained later is well established.

In addition to defining characteristic evaporation phases, the droplet residence time ($t_{res}$) is also calculated from the visualization data. It is determined as the elapsed time between the start of the IR heater to the corresponding time of the image in which the droplet surface boundary is undistinguishable from the boundary of the thermocouple bead.

### 7.5.2. Normalized Squared Temporal Droplet Diameter

The temporal droplet diameter change data for each liquid type shown in Figure 7-47 includes droplets of varying $d_0$. It is difficult to suspend a droplet with the same initial droplet diameter on the thermocouple for each experiment. Hence, to reduce the influence of varying $d_0$ on the temporal droplet diameter data change, the values are sometimes reported (Xu et al., 2002) by normalizing with $d_0$ to give normalized droplet diameter ($d/d_0$) that is plotted against the normalized time ($t/d_0$). Figure 7-48 shows the $d/d_0$ data plotted against $t/d_0$ for all the four liquid types. Generally, the basis for the calculation of $d$ versus $t$ in droplet experiments is to understand the change in the surface area of the droplet. Hence, reporting that change in terms of $d^2$ is more meaningful. Therefore, the most widely used method of reporting $d$ in droplet behavior studies is in the form of normalized squared droplet diameter ($d^2/d_0^2$) and the corresponding normalized time ($t/d_0^2$).

Figure 7-49 shows the normalized squared temporal droplet diameter change of the E-G system of liquids (E100, E30G70, E70G30, G100). From the plots, we can see that the $d^2/d_0^2$ vs $t/d_0^2$ profiles for the six droplets are close to each other for E100 and G100 while reasonably close in the case of E30G70 and E70G30 liquid types. The difference in elapsed time of $d^2/d_0^2$ seen towards the end of droplet lifetime when the experiment is repeated for the blend liquids are due to the differing droplet behaviors such as bubbling, microdroplet escape, and microexplosion. Usually, such behaviors lead to differential volumes of the droplet being left on the bead towards latter periods of droplet evaporation which directly relates to the differences seen in the plots. Overall, we can say that the droplet diameter changes seen in the six droplets are consistent for each liquid when repeated for the same IR controller setting and operating condition. Hence, we can say that the normalized droplet diameter data shown for a single droplet is a reasonable representation of the overall normalized droplet diameter change for that liquid type.

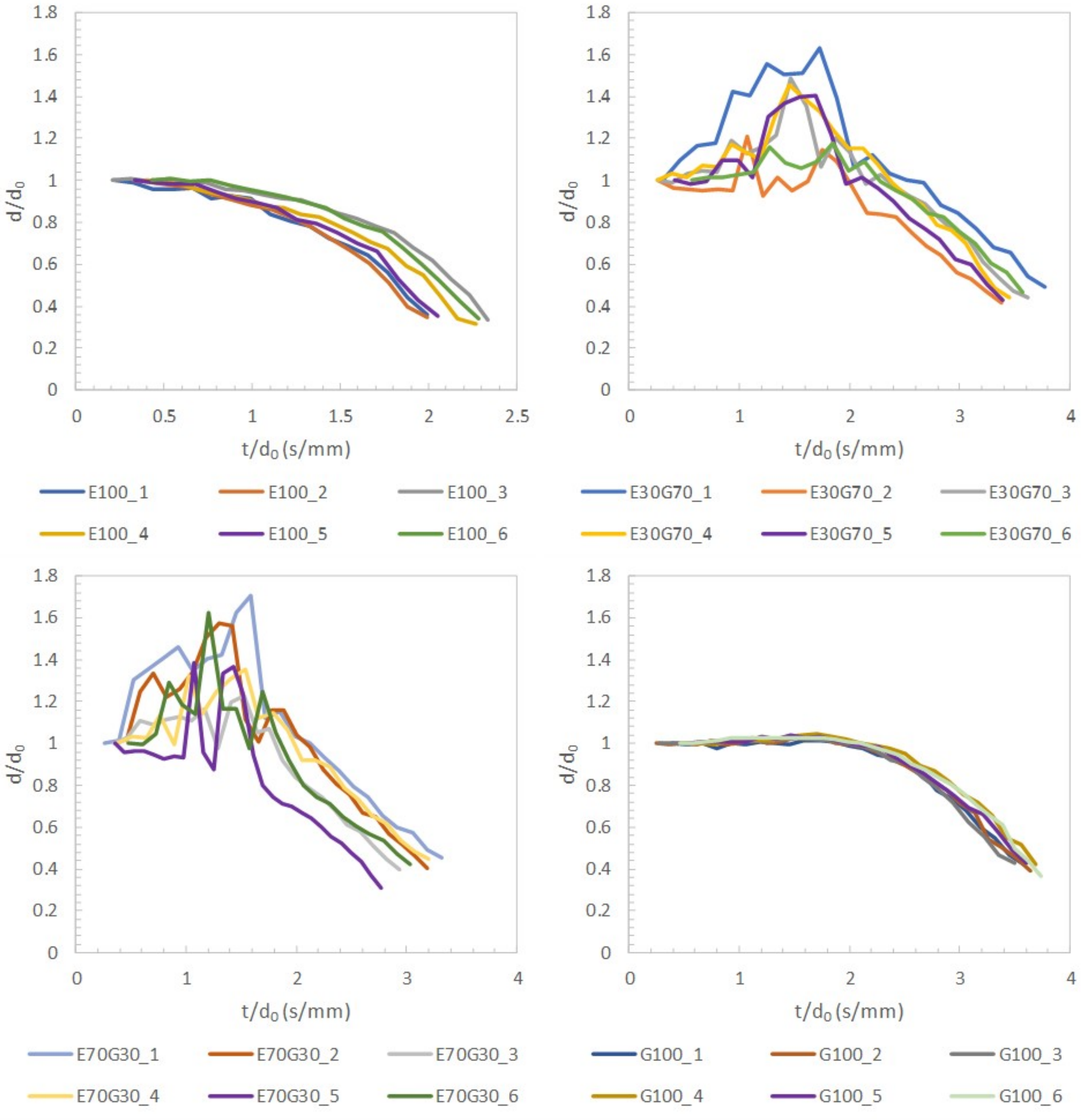

Figure 7-48: Normalized temporal droplet diameter of E100 (top left), E30G70 (top right), E70G30 (bottom left), and G100 (bottom right).

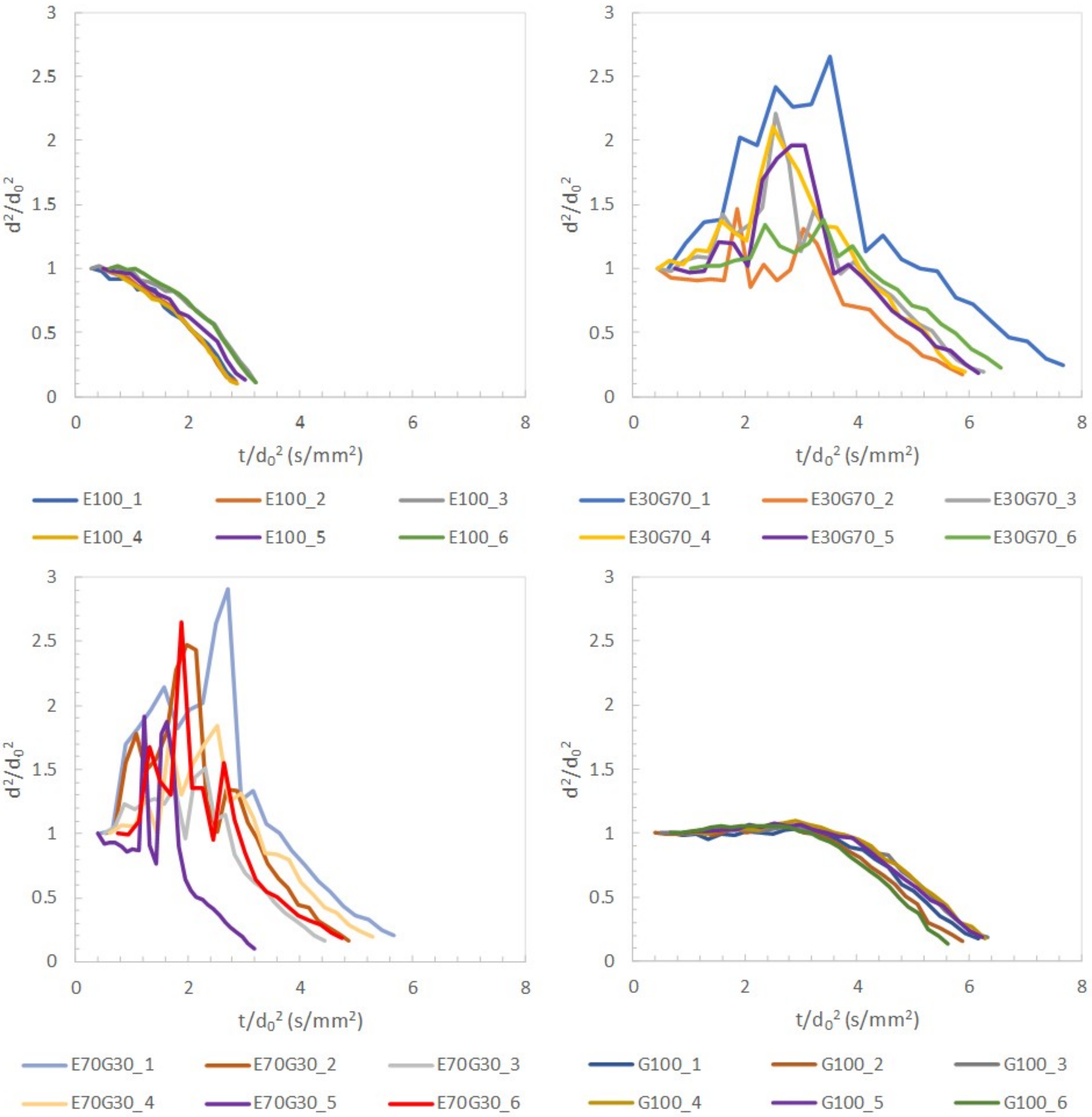

Figure 7-49: Normalized squared temporal droplet diameter change of E100 (top left), E30G70 (top right), E70G30 (bottom left), and G100 (bottom right).

The corresponding $t/d_0^2$ of the lowest values of $d^2/d_0^2$ gives an estimation of the residence time ($t_{res}$) for each liquid type in Figure 7-49. As it can be observed in Figure 7-47 and from Table 7-13, the $t_{res}$ is different for each liquid type. E100 has the shortest average $t_{res}$ at 1.5s while the highest $t_{res}$ is for G100 at 2.2s. The blends E30G70 and E70G30 have a $t_{res}$ of 1.9s and 2.0s respectively.

Table 7-13: Initial droplet diameter and residence time of the E-G system of liquids. The table on the right shows the averaged values of the six droplet experiments for each liquid type.

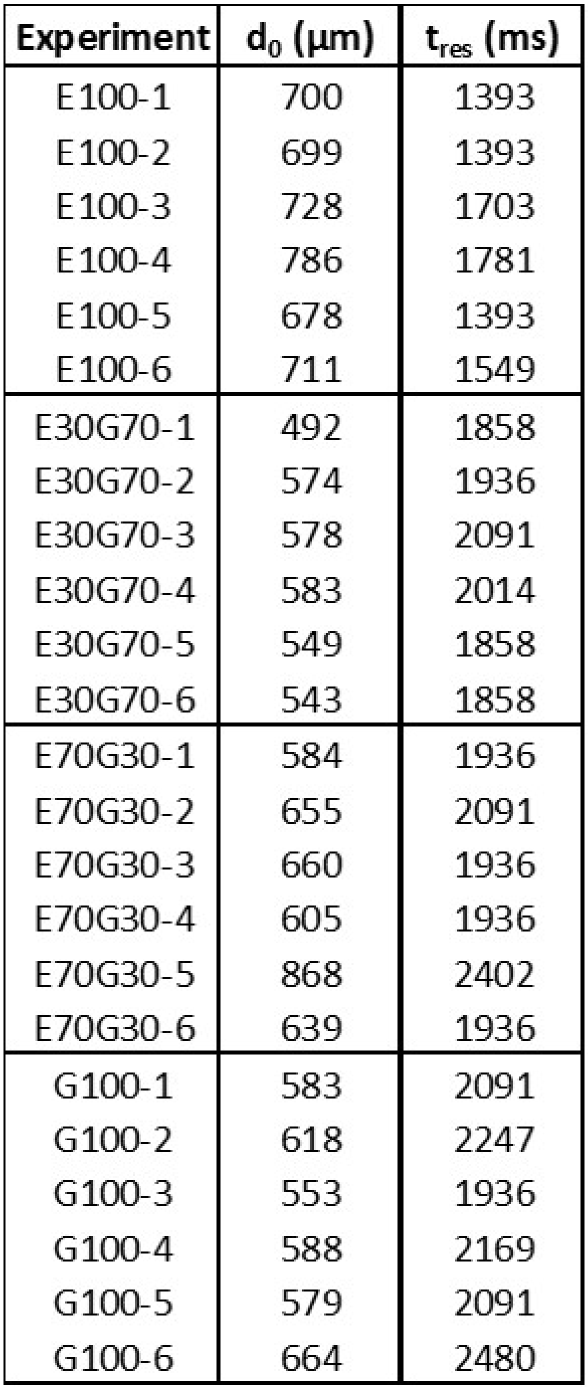

| Experiment | $d_0$ (µm) | $t_{res}$ (ms) |
|---|---|---|
| E100-1 | 700 | 1393 |
| E100-2 | 699 | 1393 |
| E100-3 | 728 | 1703 |
| E100-4 | 786 | 1781 |
| E100-5 | 678 | 1393 |
| E100-6 | 711 | 1549 |
| E30G70-1 | 492 | 1858 |
| E30G70-2 | 574 | 1936 |
| E30G70-3 | 578 | 2091 |
| E30G70-4 | 583 | 2014 |
| E30G70-5 | 549 | 1858 |
| E30G70-6 | 543 | 1858 |
| E70G30-1 | 584 | 1936 |
| E70G30-2 | 655 | 2091 |
| E70G30-3 | 660 | 1936 |
| E70G30-4 | 605 | 1936 |
| E70G30-5 | 868 | 2402 |
| E70G30-6 | 639 | 1936 |
| G100-1 | 583 | 2091 |
| G100-2 | 618 | 2247 |
| G100-3 | 553 | 1936 |
| G100-4 | 588 | 2169 |
| G100-5 | 579 | 2091 |
| G100-6 | 664 | 2480 |

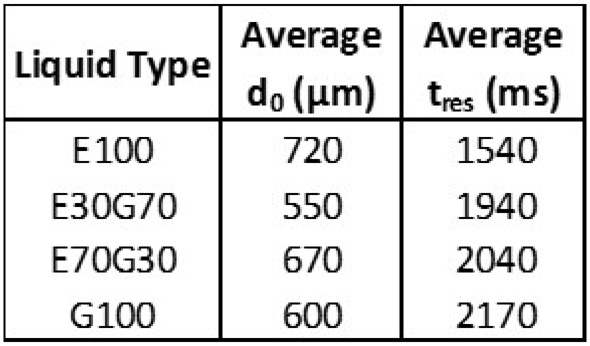

| Liquid Type | Average $d_0$ (µm) | Average $t_{res}$ (ms) |
|---|---|---|
| E100 | 720 | 1540 |
| E30G70 | 550 | 1940 |
| E70G30 | 670 | 2040 |
| G100 | 600 | 2170 |

The different $t_{res}$ values observed for E100 and G100 result from their respective differences in density, boiling point, and heat of vaporization values as listed in Table 7-13. The composition of ethanol-glycerol mixtures and their subsequent droplet behavior events affect the $t_{res}$ in blends.

The temporal droplet diameter change shown in Figure 7-47, Figure 7-48, and Figure 7-49 were classified into different characteristic evaporation phases. Classification and the time duration of each phase for all liquid types are shown with representative droplets in Figure 7-50 and the complete data for all six droplets are shown in Table 7-14. From Figure 7-50 we see that the pure liquids E100 and G100 exhibit two evaporation behavior phases. The E100 droplets show a relatively short duration of the transient heating phase (THP) with an average duration (avg. $\Delta t_{THP}$) of 290ms when compared to G100 liquid type with an avg. $\Delta t_{THP}$ of 1220ms. During the longer THP of the G100 droplet we also see the $d$ to be briefly higher than the $d_0$. This is due to the thermal expansion of the liquid for corresponding increase in the droplet temperature. The THP is followed by a long equilibrium evaporation phase (EEP) for both the E100 and G100 liquid types with average time durations (avg. $\Delta t_{EEP}$) of 1240 and 940ms, respectively.

The blend droplets E30G70 and E70G30 exhibit three evaporation behavior phases as can be seen from Figure 7-50 and Table 7-14. In addition to the THP and EEP, we observed an intermediate fluctuation evaporation phase (FEP). The time duration of the FEP represented as avg. $\Delta t_{FEP}$ are about 750ms and 880ms for E30G70 and E70G30, respectively. The avg. $\Delta t_{THP}$ and avg. $\Delta t_{EEP}$ values for the blends are in between that of the values calculated for E100 and G100 as see in Table 7-14. The bubble formation and subsequent rupture of the droplet by either microdroplet escape or microexplosion results in the expansion and shrinkage of the droplet diameter. These factors affect the duration of FEP in blend liquids. Generally, in multicomponent liquid types, strengthened droplet bubbling and rupture behaviors result in shortened duration of FEP.

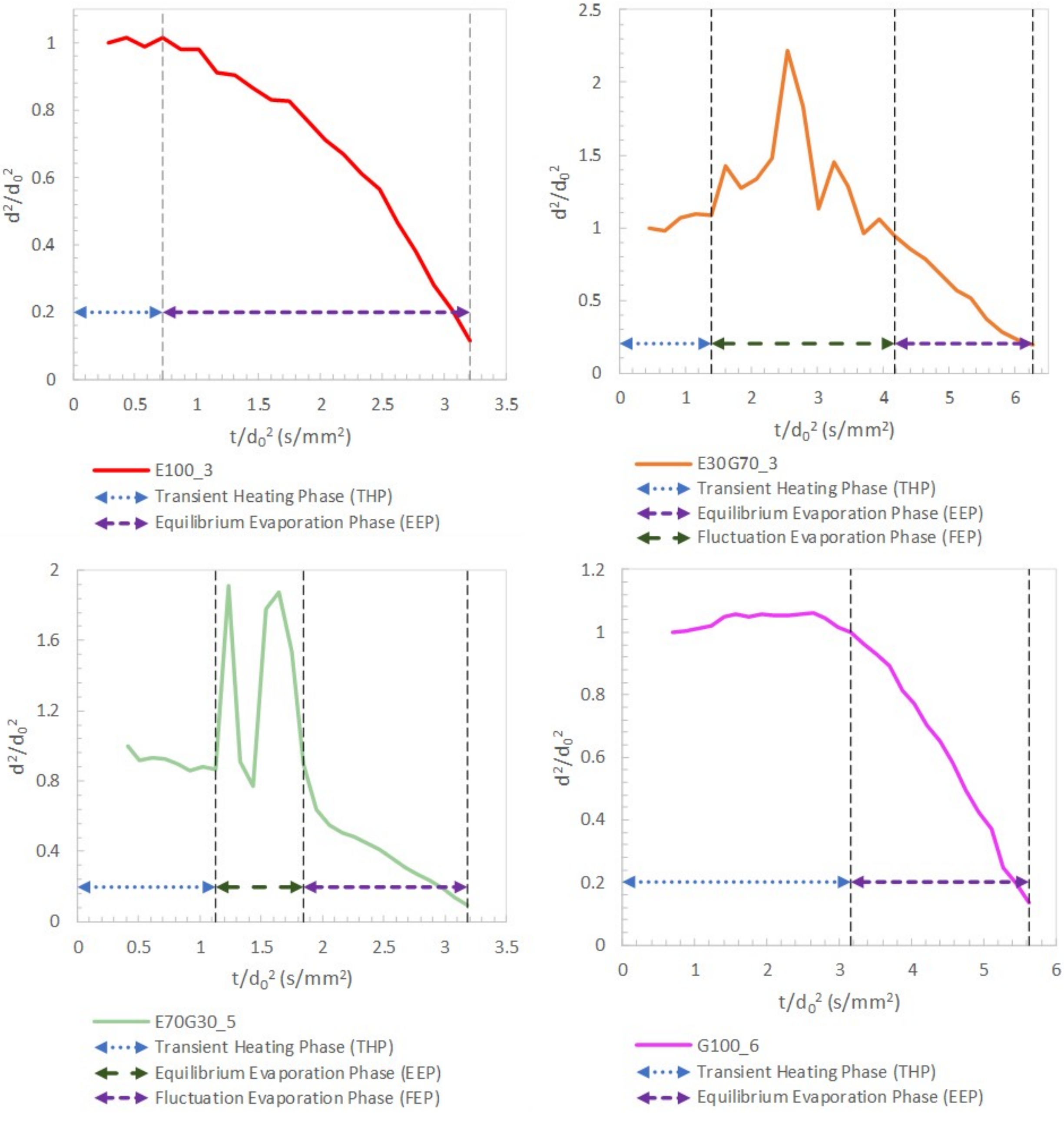

Figure 7-50: Characteristic evaporation phase classification of E100 (top left), E30G70 (top right), E70G30 (bottom left), and G100 (bottom right).

Table 7-14: Duration of characteristic evaporation phases of the E-G system of liquids. The table on the right shows the average values of the six droplet experiments for each liquid type.

| Experiment | $d_0$ (μm) | $\Delta t_{THP}$ (ms) | $\Delta t_{FEP}$ (ms) | $\Delta t_{EEP}$ (ms) |
|---|---|---|---|---|
| E100-1 | 700 | 152 | - | 1240 |
| E100-2 | 699 | 229 | - | 1164 |
| E100-3 | 728 | 385 | - | 1318 |
| E100-4 | 786 | 307 | - | 1474 |
| E100-5 | 678 | 229 | - | 1164 |
| E100-6 | 711 | 462 | - | 1087 |
| E30G70-1 | 492 | 385 | 931 | 542 |
| E30G70-2 | 574 | 540 | 698 | 698 |
| E30G70-3 | 578 | 540 | 853 | 698 |
| E30G70-4 | 583 | 540 | 853 | 621 |
| E30G70-5 | 549 | 695 | 543 | 620 |
| E30G70-6 | 543 | 540 | 620 | 698 |
| E70G30-1 | 584 | 229 | 1087 | 620 |
| E70G30-2 | 655 | 307 | 1086 | 698 |
| E70G30-3 | 660 | 307 | 931 | 698 |
| E70G30-4 | 605 | 385 | 853 | 698 |
| E70G30-5 | 868 | 850 | 542 | 1009 |
| E70G30-6 | 639 | 462 | 776 | 698 |
| G100-1 | 583 | 1160 | - | 931 |
| G100-2 | 618 | 1160 | - | 1087 |
| G100-3 | 553 | 1083 | - | 853 |
| G100-4 | 588 | 1316 | - | 853 |
| G100-5 | 579 | 1238 | - | 853 |
| G100-6 | 664 | 1393 | - | 1087 |

| Liquid Type | Average $d_0$ (μm) | Average $\Delta t_{THP}$ (ms) | Average $\Delta t_{FEP}$ (ms) | Average $\Delta t_{EEP}$ (ms) |
|---|---|---|---|---|
| E100 | 720 | 290 | - | 1240 |
| E30G70 | 550 | 540 | 750 | 650 |
| E70G30 | 670 | 420 | 880 | 740 |
| G100 | 600 | 1220 | - | 940 |

### 7.5.3. $d^2$-Law and Evaporation Rate Constant

The $d^2$-law is the most common and simplest model used in literature to describe droplet vaporization and combustion. Using the $d^2$-law, we can get an estimation of the droplet gasification rate. However, there are major assumptions built into this theory as described in the following adapted from the work of Law (1982). Some of the assumptions that pertain to our droplet vaporization studies include:

(i) *Spherical symmetry:* Forced and natural convection are neglected reducing the analysis to one dimension.

(ii) *No spray effects:* The droplet is an isolated one immersed in an infinite oxidizing environment.

*(iii) Diffusion being rate-controlling*.

*(iv) Isobaric process*.

(v) *Gas-phase quasi-steadiness:* Because of the significant density disparity between liquid and gas, the liquid possesses great inertia such that its properties at the droplet surface, for example the regression rate, species concentrations, and temperature, change at rates much slower than those of the gas-phase transport processes.

(vi) *Single fuel species:* Thus, it is unnecessary to analyze liquid-phase mass transport .

(vii) *Constant and uniform droplet temperature:* This implies that there is no droplet heating. Combined with (vi), we see that liquid-phase heat and mass transport processes are completely neglected. Therefore, the $d^2$-law is essentially a gas-phase model.

(viii) *Saturation vapor pressure at droplet surface:* This assumes that the phase-change process between liquid and vapor occurs at a rate much faster than those for gas-phase transport. Therefore, gasification at the surface is at equilibrium, producing fuel vapor which is at its saturation vapor pressure corresponding to the droplet surface temperature.

*(ix) No Soret, Dufour, and radiation effects.*

Under the above assumptions, the $d^2$-law dictates that the square of the droplet diameter decreases linearly with time. Using this relation, the rate of droplet evaporation can be calculated as,

$$k = - d(d^2)/dt$$

where $k$ represents the evaporation rate constant ($mm^2/s$), $d$ represents the droplet diameter (mm), and $t$ represent the elapsed time (s).

Figure 7-51 shows the determination of the evaporation rate constant for a G100 droplet using the assumption of the $d^2$-law. The evaporation rate constant is generally calculated from the equilibrium evaporation phase of the droplet where the square of the droplet diameter varies approximately linear to the elapsed time. In this phase, the $d^2$ values start at or below the $d_0^2$ and reduces until it is close to the square of the bead diameter ($d_{bead}$ ~ 0.24 mm). As shown in the plot, during this phase, a linear trendline is fit for the $d^2$ vs $t$ curve and the slope of the fit is used to calculate $k$.

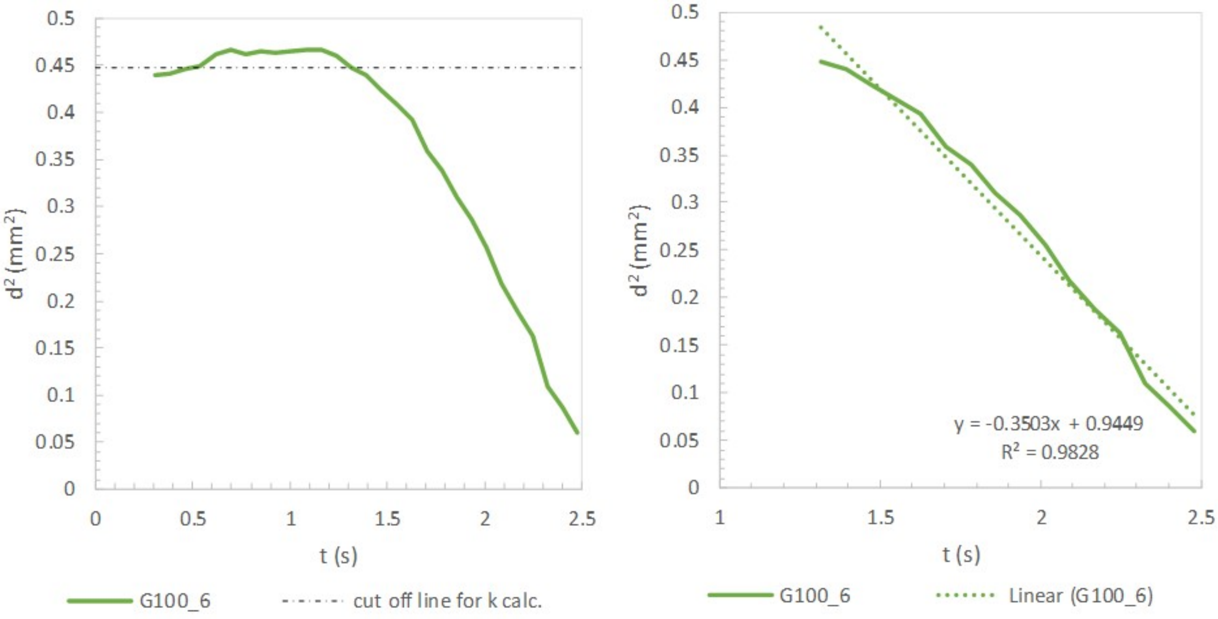

Figure 7-51: Basis of evaporation rate constant calculation using $d^2$-law assumption is shown for a representative G100 droplet.

Figure 7-52 shows the average evaporation constant ($k_{avg}$) for each liquid type along with the respective standard deviation for the six droplets at the selected controller setting and operating condition. From the Figure 7-52, we observe that E100 has a marginally higher evaporation rate than G100 liquid type. This is probably a result of the high volatility and low boiling point property of E100 relative to G100. The $k_{avg}$ of the blends are much closer when we consider their larger standard deviations compared to E100 and G100. The EEP of the blend droplets are preceded by the FEP as shown in Figure 7-49. Our understanding is that the droplet volumes remaining after the significant droplet behavior events of FEP are closer in composition (ethanol-glycerol) than the original composition (30/70 or 70/30 - ethanol/glycerol) of the respective blends when it was suspended.

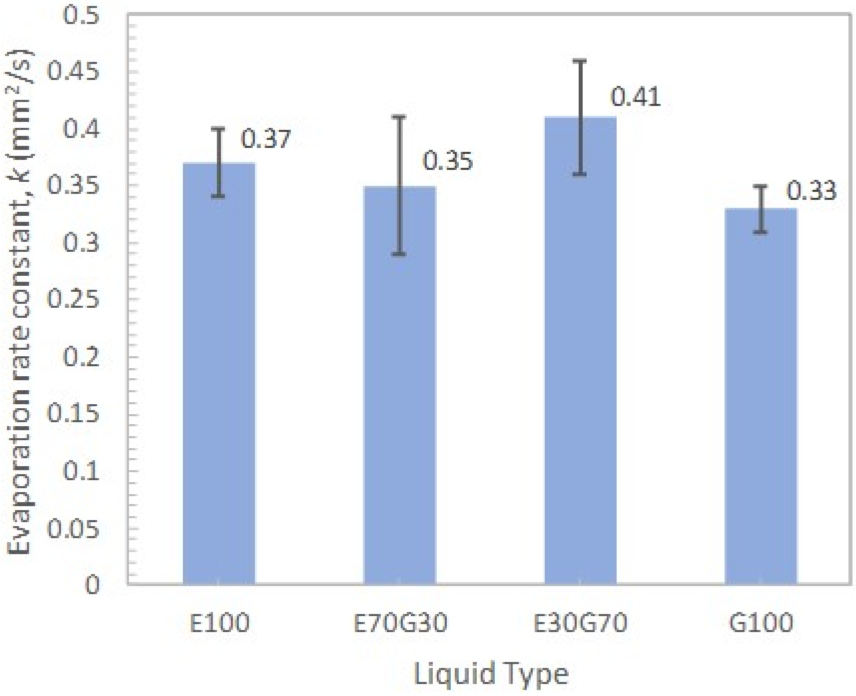

Figure 7-52: Average evaporation rate constant calculated for E-G system of liquids are shown with the error values.

The evaporation rate of a liquid was expected to be independent of the initial droplet diameter ($d_0$). To investigate, the $k$ values were plotted against $d^2$ (Figure 7-53). The linear trendlines and corresponding equations in Figure 7-53 shows that the $k$ values are not a strong function of the droplet surface area confirming the expected. Increase in surface area and the subsequent evaporation rate is counter balanced by the increased heat transfer. As a result, varying $d_0$ does not influence the variations in $k$ values.

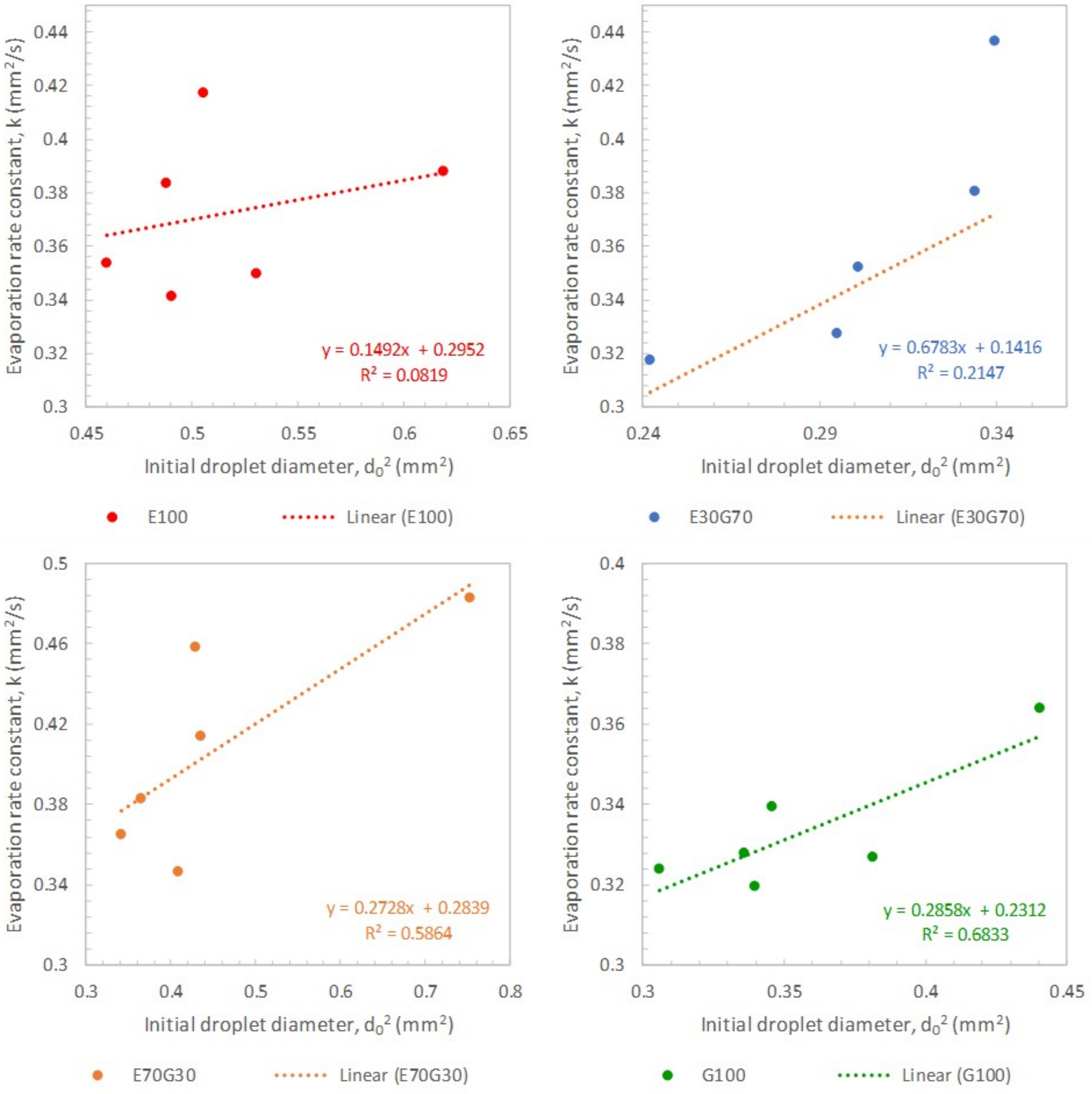

Figure 7-53: Relationship between the evaporation rate constant and squared initial droplet diameter is shown for the E100 (top left), E30G70 (top right), E70G30 (bottom left), and G100 (bottom right).

### 7.5.4. Droplet Temperature – Droplet Diameter Comparisons

Droplet temperature values were measured for all the high magnification droplet experiments. Figure 7-54 shows the droplet temperature in comparison with the corresponding temporal droplet diameter change for all the four liquid types. Representative droplets among the six droplet experiments for each liquid type are selected for these comparisons.

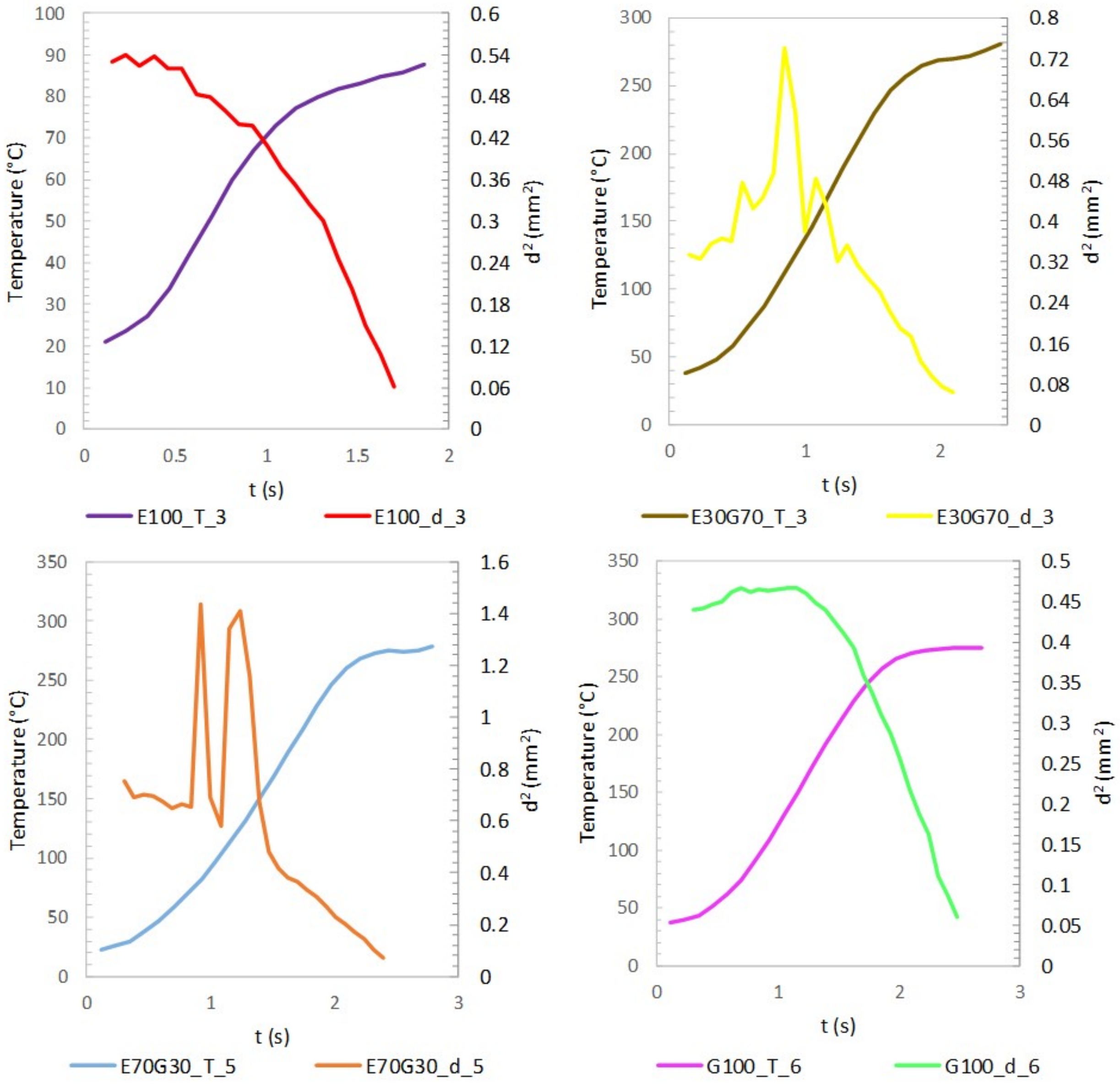

Figure 7-54: Temporal variation of droplet temperature and squared droplet diameter is shown for E100 (top left), E30G70 (top right), E70G30 (bottom left), and G100 (bottom right).

From Figure 7-54 we see that the fluctuations in the droplet diameter due to droplet behavior events do not necessarily result in fluctuation with the droplet temperature profile. This is because the droplet temperature profile shown here and in previous plots are moving averages of the original values. As a result, minor fluctuations in the temperature profile are smoothened to highlight the general droplet temperature profile. We also see that the droplet temperature profile and the squared droplet diameter profile are not synchronous. This is due to the minor time lag (<200ms) that is caused by the responsiveness of the thermocouple to react to temperature changes.

The droplet temperature period classifications and their subsequent heating rates for the four liquid types are shown in Table 7-15. Averaged values of the six droplets for each liquid type are shown in Table 7-16. From Table 7-16, we see that the heating rate of period-2 for E100 is lower than that of the other single component liquid type G100. For E30G70 and the E70G30 the values are much closer to the averaged period-2 heating rate of E30G70 and marginally higher than E70G30. E100 and G100 liquid types have very different boiling points and that reflects in the heating rate and ΔT for both in period-2. However, it is interesting to observe that the two blends have period-2 values closer to G100 than E100 irrespective of their contrasting blend compositions.

The high magnification experiments have been useful to obtain estimates of the evaporation rate constants (*k*) for each liquid type (E100, E30G70, E70G30, G100) through quantitative measurements using the visualization images. We observe that the *k* values of E100 and G100 are close despite their contrasting boiling points. The *k* values of blends are understandably close to the pure component liquid types; however, the blends follow an evaporation behavior with three characteristic phases unlike the former with the addition of fluctuation evaporation phase (FEP). For the selected experimental conditions, we have shown that *k* is a function of liquid type and does not vary with $d_0^2$. Also, the FEP of the blend liquid types have a minor influence on their corresponding droplet temperature profiles.

Table 7-15: Classification of the droplet temperature into characteristic periods is shown for all the experiments with the E-G system of liquids.

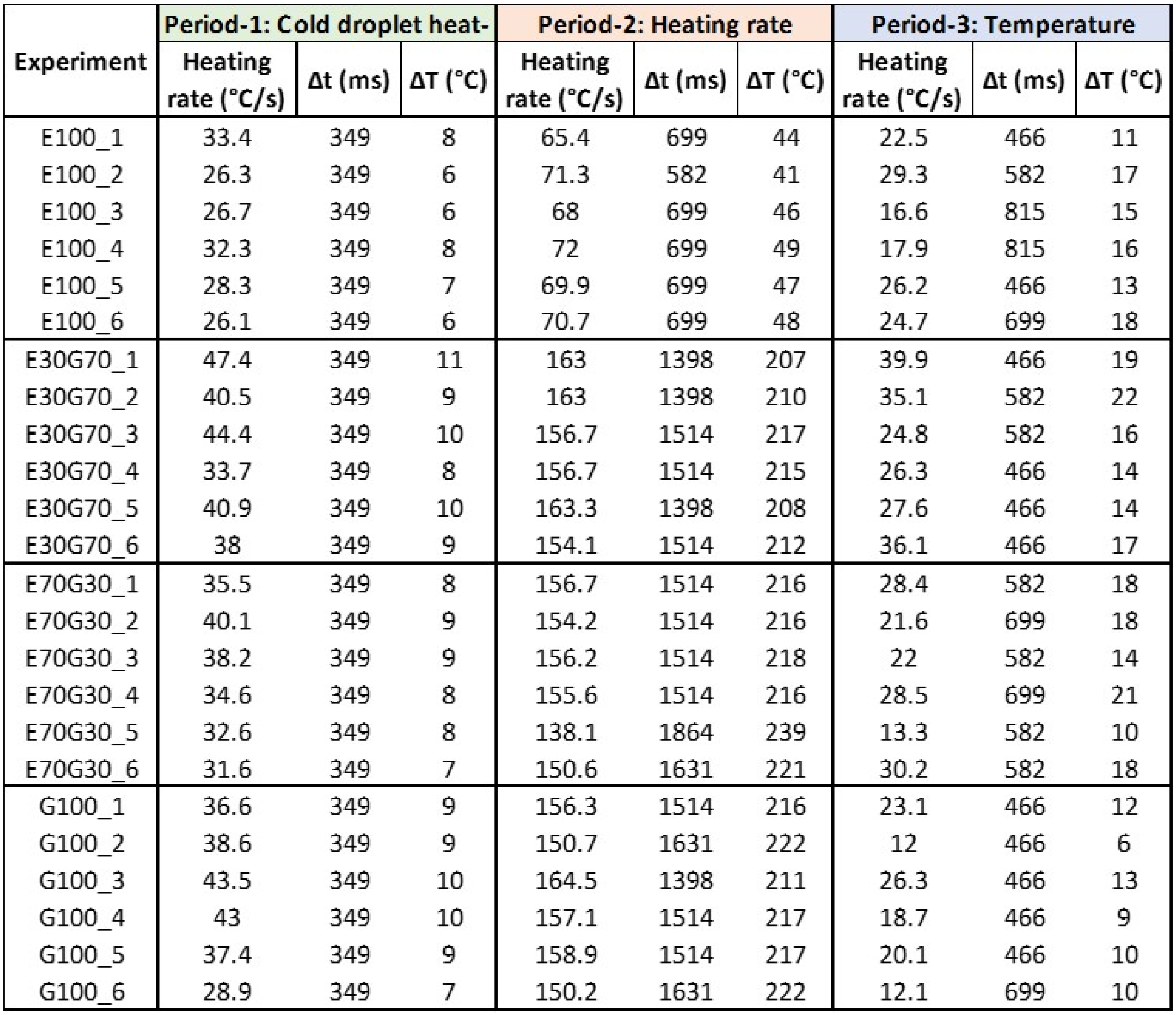

| Experiment | Period-1: Cold droplet heat- | | | Period-2: Heating rate | | | Period-3: Temperature | | |
|---|---|---|---|---|---|---|---|---|---|
| | Heating rate (°C/s) | Δt (ms) | ΔT (°C) | Heating rate (°C/s) | Δt (ms) | ΔT (°C) | Heating rate (°C/s) | Δt (ms) | ΔT (°C) |
| E100_1 | 33.4 | 349 | 8 | 65.4 | 699 | 44 | 22.5 | 466 | 11 |
| E100_2 | 26.3 | 349 | 6 | 71.3 | 582 | 41 | 29.3 | 582 | 17 |
| E100_3 | 26.7 | 349 | 6 | 68 | 699 | 46 | 16.6 | 815 | 15 |
| E100_4 | 32.3 | 349 | 8 | 72 | 699 | 49 | 17.9 | 815 | 16 |
| E100_5 | 28.3 | 349 | 7 | 69.9 | 699 | 47 | 26.2 | 466 | 13 |
| E100_6 | 26.1 | 349 | 6 | 70.7 | 699 | 48 | 24.7 | 699 | 18 |
| E30G70_1 | 47.4 | 349 | 11 | 163 | 1398 | 207 | 39.9 | 466 | 19 |
| E30G70_2 | 40.5 | 349 | 9 | 163 | 1398 | 210 | 35.1 | 582 | 22 |
| E30G70_3 | 44.4 | 349 | 10 | 156.7 | 1514 | 217 | 24.8 | 582 | 16 |
| E30G70_4 | 33.7 | 349 | 8 | 156.7 | 1514 | 215 | 26.3 | 466 | 14 |
| E30G70_5 | 40.9 | 349 | 10 | 163.3 | 1398 | 208 | 27.6 | 466 | 14 |
| E30G70_6 | 38 | 349 | 9 | 154.1 | 1514 | 212 | 36.1 | 466 | 17 |
| E70G30_1 | 35.5 | 349 | 8 | 156.7 | 1514 | 216 | 28.4 | 582 | 18 |
| E70G30_2 | 40.1 | 349 | 9 | 154.2 | 1514 | 216 | 21.6 | 699 | 18 |
| E70G30_3 | 38.2 | 349 | 9 | 156.2 | 1514 | 218 | 22 | 582 | 14 |
| E70G30_4 | 34.6 | 349 | 8 | 155.6 | 1514 | 216 | 28.5 | 699 | 21 |
| E70G30_5 | 32.6 | 349 | 8 | 138.1 | 1864 | 239 | 13.3 | 582 | 10 |
| E70G30_6 | 31.6 | 349 | 7 | 150.6 | 1631 | 221 | 30.2 | 582 | 18 |
| G100_1 | 36.6 | 349 | 9 | 156.3 | 1514 | 216 | 23.1 | 466 | 12 |
| G100_2 | 38.6 | 349 | 9 | 150.7 | 1631 | 222 | 12 | 466 | 6 |
| G100_3 | 43.5 | 349 | 10 | 164.5 | 1398 | 211 | 26.3 | 466 | 13 |
| G100_4 | 43 | 349 | 10 | 157.1 | 1514 | 217 | 18.7 | 466 | 9 |
| G100_5 | 37.4 | 349 | 9 | 158.9 | 1514 | 217 | 20.1 | 466 | 10 |
| G100_6 | 28.9 | 349 | 7 | 150.2 | 1631 | 222 | 12.1 | 699 | 10 |

Table 7-16: Averaged values of droplet temperature periods is shown for the E-G system of liquids.

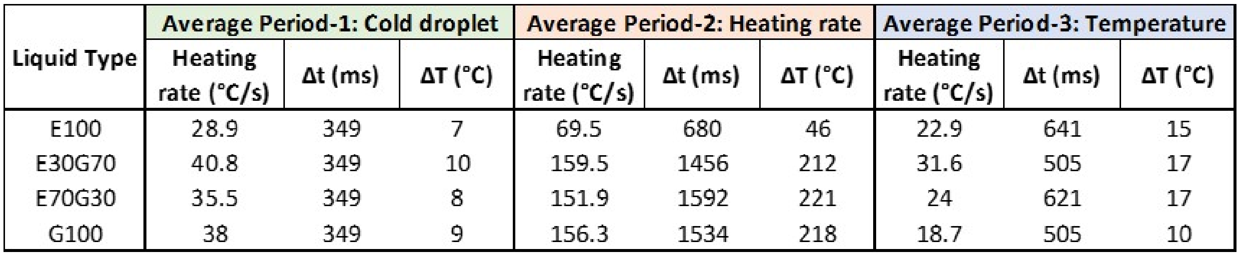

| Liquid Type | Average Period-1: Cold droplet | | | Average Period-2: Heating rate | | | Average Period-3: Temperature | | |
|---|---|---|---|---|---|---|---|---|---|
| | Heating rate (°C/s) | Δt (ms) | ΔT (°C) | Heating rate (°C/s) | Δt (ms) | ΔT (°C) | Heating rate (°C/s) | Δt (ms) | ΔT (°C) |
| E100 | 28.9 | 349 | 7 | 69.5 | 680 | 46 | 22.9 | 641 | 15 |
| E30G70 | 40.8 | 349 | 10 | 159.5 | 1456 | 212 | 31.6 | 505 | 17 |
| E70G30 | 35.5 | 349 | 8 | 151.9 | 1592 | 221 | 24 | 621 | 17 |
| G100 | 38 | 349 | 9 | 156.3 | 1534 | 218 | 18.7 | 505 | 10 |

## 7.6. Discussion

The suspended droplet experiments performed for the E-G system include varying initial droplet diameters ($d_0$) due to the inherent difficulties in controlling the droplet size through our suspension technique. The experiments performed in the low and high magnifications even for the same liquid type differ slightly due to the changes in gas flowrate. Low magnification experiments include data from air and nitrogen gas types in 5 and 25 SCFM flowrates, while the high magnification experiments were all performed for air environment at 10 SCFM. The high-quality visualization videos in *.tiff* format were broken down into a series of low quality *.bmp* images. From this, specific images were selected to be included in an image sequence. The images thus selected were enhanced in brightness and contrast for clarity of display. The term droplet size in this section primarily refers to the droplet diameter calculated from the two-dimensional image of a droplet. The droplets are not perfectly spherical and hence we calculate the area of the irregularly shaped droplet using a polygon tool and related it to an equivalent circle.

### 7.6.1. Pure Ethanol Suspended Droplet Behavior

Visualization images from the high magnification experiments with pure ethanol (E100) are shown in Figure 7-55 along with corresponding elapsed times. The image sequence represents our observation of consistent temporal droplet size reduction characteristic of ethanol droplets. The droplet diameter plots of E100 (Figure 7-47) also confirms this observation. We refer to this behavior of droplets without any fluctuation to the droplet diameter as the volatilizing droplet behavior. Figure 7-56 and Figure 7-57 shows the low magnification E100 droplet behavior in low and high flowrate air environments. The behavior of the E100 droplets are the same irrespective of the gas type and hence only one of the two gas environments were

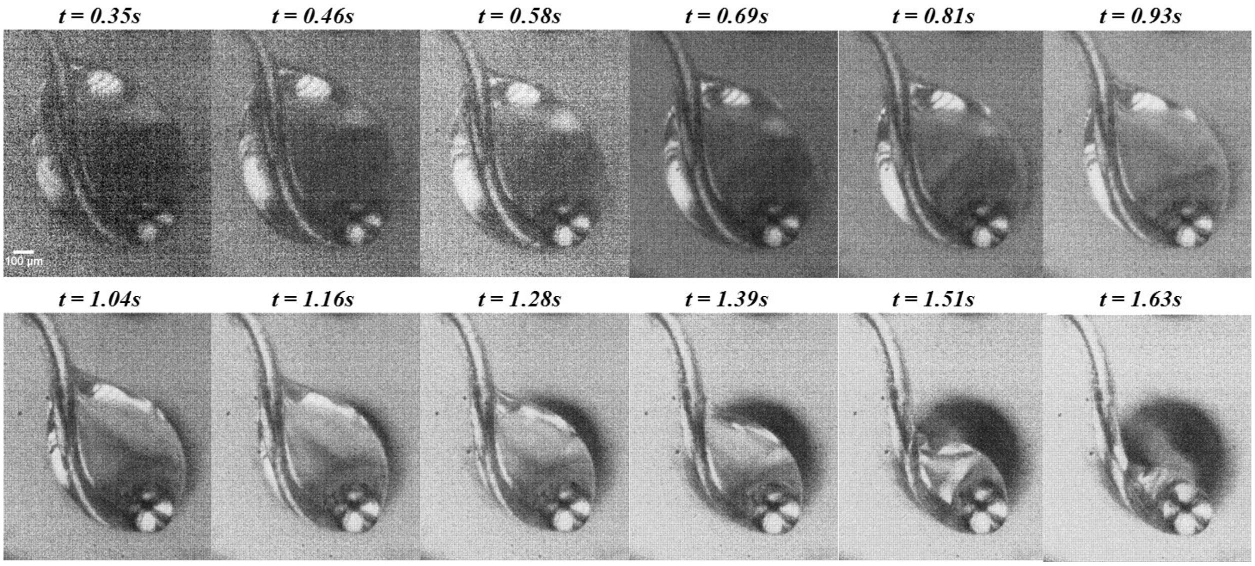

Figure 7-55: High magnification image sequence of E100 ($d_0$ = 786 µm; $t_{res}$ = 1.70s) droplet behavior in intermediate flowrate (10 SCFM) air environment.

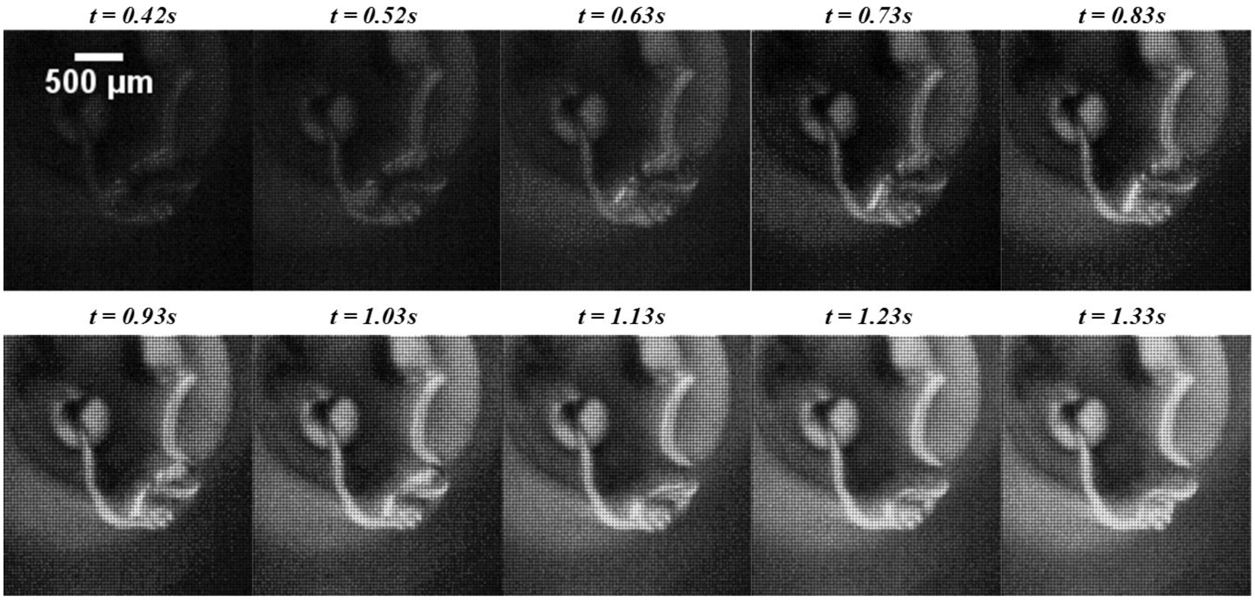

Figure 7-56: Low magnification image sequence of E100 ($d_0$ = 910 µm; $t_{res}$ = 1.43s) droplet behavior in a high flowrate (25 SCFM) air environment.

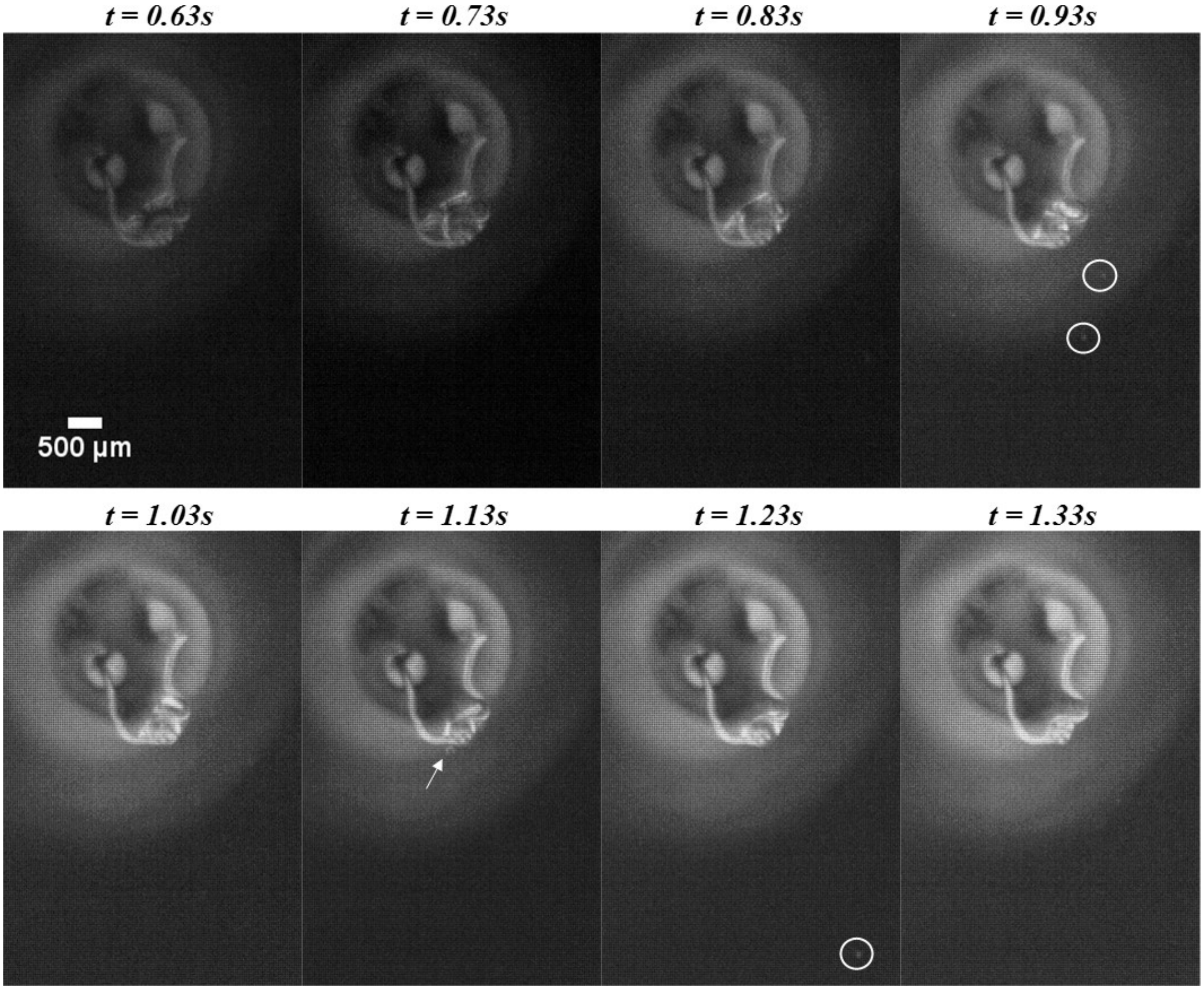

Figure 7-57: Low magnification image sequence of E100 ($d_0$ = 960 µm; $t_{res}$ = 1.45s) droplet behavior in a low flowrate (5 SCFM) air environment.

selected for representation. In Figure 7-56, we see the volatilizing behavior like that of the image sequence in Figure 7-55. However, in Figure 7-57 we observe bubbling behavior inside the droplet. An instance of the droplet bubble originating near the bead can be seen at *t = 0.73s*. We believe the observation of the bubbling behavior is due to the nucleate boiling effect caused by the temperature difference between the droplet and the thermocouple material. The temperature of the thermocouple reaches the saturation temperature of E100 (78.3°C) faster than the liquid droplet and this results in a local vaporization inside the droplet resulting in the forming of an isolated bubble at the thermocouple surface. At *t = 0.83s* we see a bubble that expands until it reaches some critical size, at which point the bubble detaches from the solid surface, escapes from the droplet surface boundary, and sheds into smaller sized satellite droplets (indicated in circles) as shown at *t = 0.93s*. We refer to this phenomenon in the suspended droplet studies as the microdroplet escape behavior. Figure 7-58 shows the image sequence of a bubbling event in an E100 droplet. In this figure we can see how the bubble originates and expands in size until it breaks to release satellite droplets as seen in *t = 0.71s*. Evident from the elapsed times between the first and last image, the bubbling event in the droplet is relatively short lasting for about 100ms. Unlike a bubbling event in a multicomponent droplet discussed later in this section where multiple droplet bubbles are seen within the droplet, we observed only isolated bubble behavior in low flowrate E100 droplets. A single bubble expands in size to escape the droplet boundary and this behavior repeats for a certain elapsed time during the droplet evaporation. This suggests that the bubbling behavior in ethanol droplets is probably due to the formation of hot spots on the thermocouple surface and not due to the differential boiling of the liquid components. This is reasonable considering that the E100 is a single component pure liquid.

Differential heating rates between the droplet and the thermocouple is believed to be the main reason for the nucleate boiling effect if we exclude other factors such as the presence of an existing micro bubble or impurities in the liquid. Temperature increase from the illumination of IR lamps and heat transfer effects (conduction, convection, and radiation) are important factors that influence the heating rate of droplets in our experiments. The E100 droplet heating rate values (calculated from period-2) for both the low and high magnification experiments as reported in Table 7-15 are very close despite the variations in operating conditions in terms of the gas type and flowrate. However, we see the occurrence of bubbling behavior only in the low flowrate conditions of E100 droplet. This suggests that the changes in the heat transfer effects specific to the low flowrate condition might be a reason for the formation of hot spots that leads to the nucleate boiling effect. However, insufficient repetitive experimental data available in low flowrate environments restricts us from the confirmation of such reasoning.

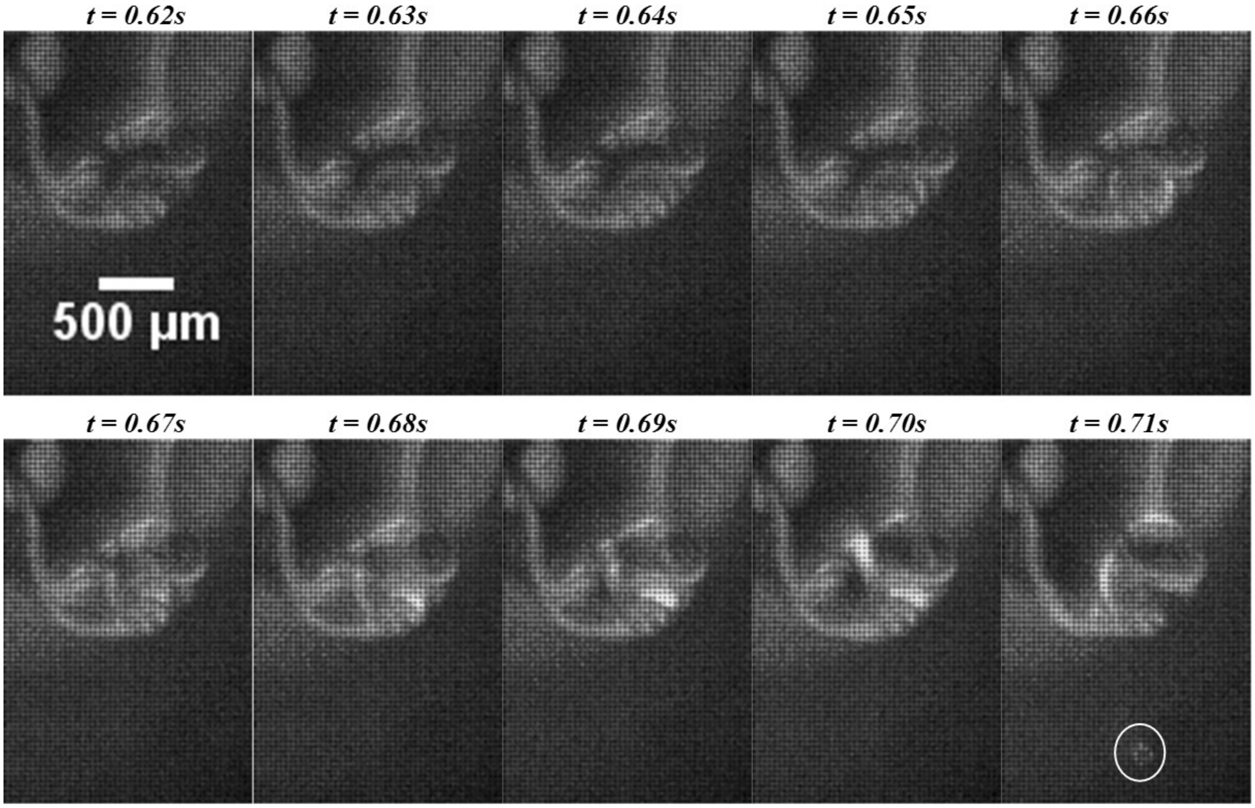

Figure 7-58: Image sequence showing bubbling behavior in E100 ($d_0$ = 960 µm; $t_{res}$ = 1.45s) droplet evaporating in a low flowrate (5 SCFM) air environment.

### 7.6.2. Pure Glycerol Suspended Droplet Behavior

The high magnification visualizations of G100 droplets are shown in Figure 7-59. From the image sequence we see that the G100 droplet exhibits a volatilizing behavior like that of the E100 droplet shown in Figure 7-55. The comparison of elapsed times between the two image sequences shows that the residence time ($t_{res}$) of the G100 droplet is longer. Figure 7-60 and Figure

7-61 shows the low magnification image sequences of the G100 droplet in low and high gas flowrates respectively.

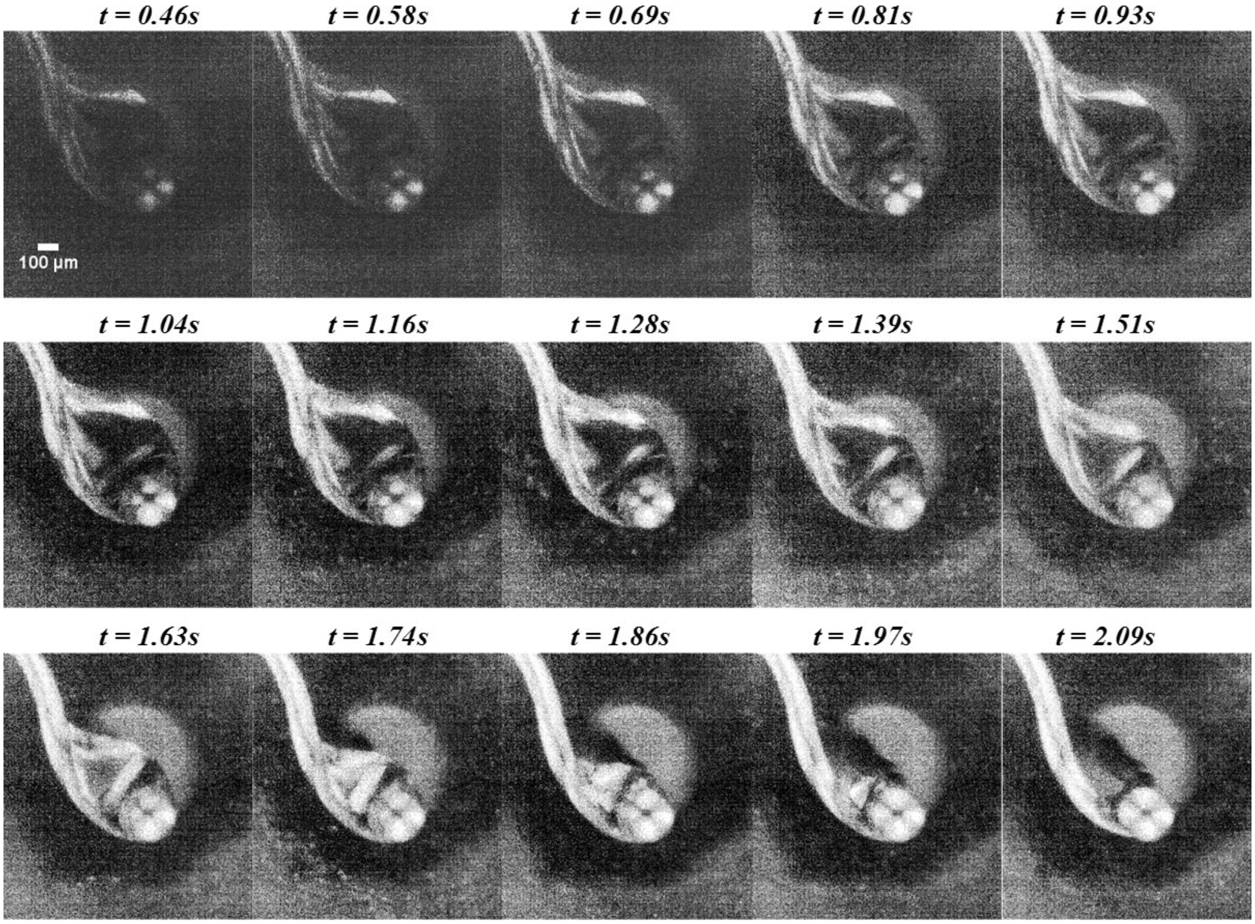

Figure 7-59: High magnification image sequence of G100 ($d_0$ = 588 µm; $t_{res}$ = 2.14s) droplet behavior in intermediate flowrate (10 SCFM) air environment.

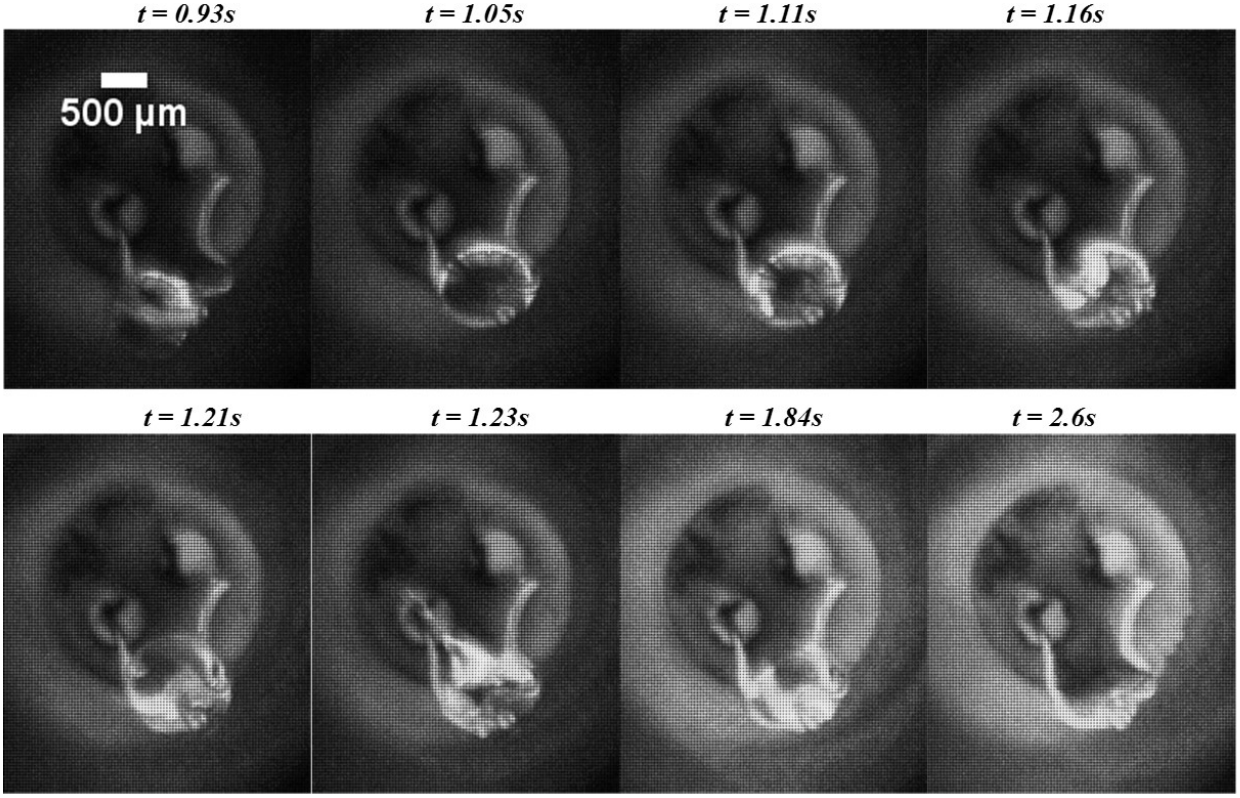

Figure 7-60: Low magnification image sequence of G100 ($d_0$ = 1060 µm; $t_{res}$ = 2.82s) droplet exhibiting bubbling behavior in a low flowrate (5 SCFM) air environment.

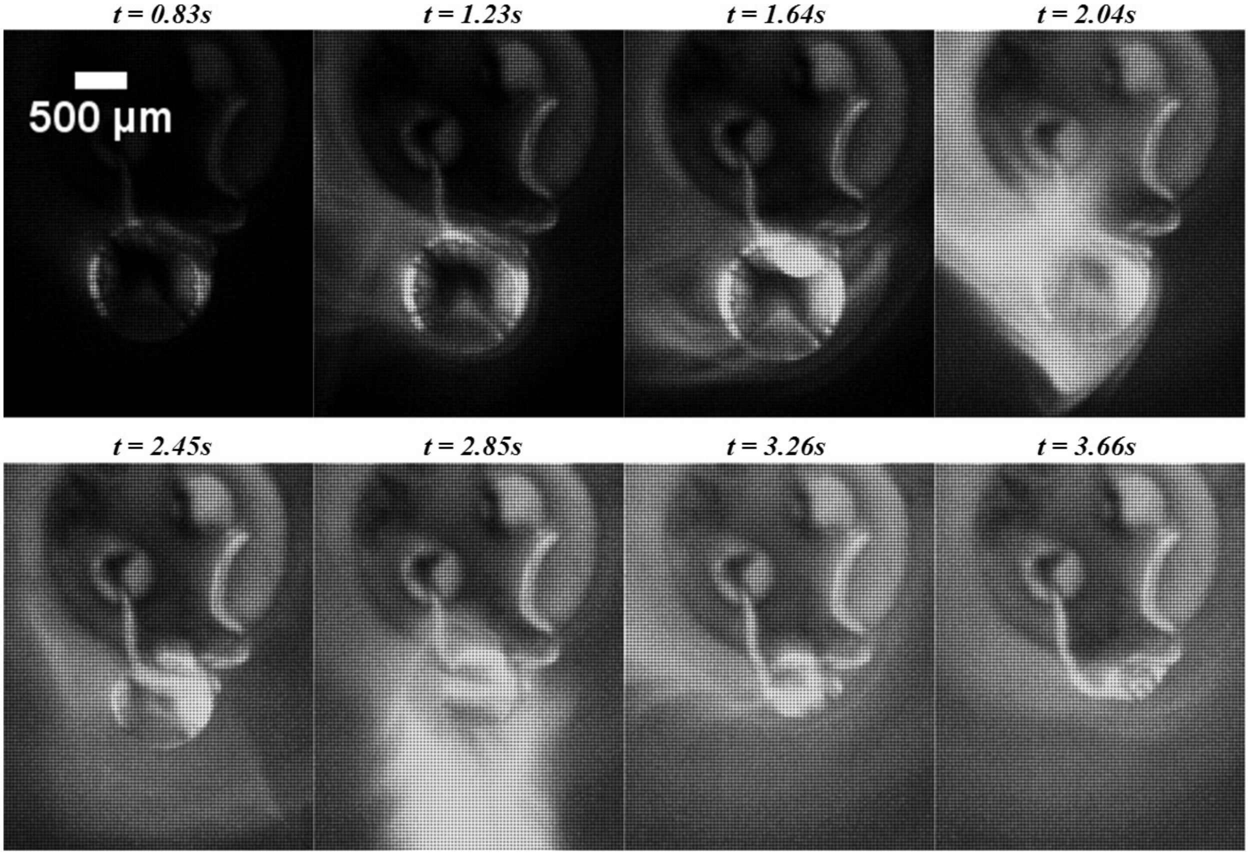

Figure 7-61: Low magnification image sequence of G100 ($d_0$ = 1200 µm; $t_{res}$ = 3.9s) droplet behavior in a high flowrate (25 SCFM) air environment.

In low magnification images of Figure 7-60, we observe bubble formation and expansion at $t = 1.11s$ and $t = 1.16s$, respectively. We also observed the microdroplet escape behavior with the distortion of the droplet surface boundary at $t = 1.23s$. The observations of the droplet behavior in Figure 7-61 and the high magnification images of Figure 7-59 are similar with the droplet evaporating with vapors around the droplet surface. We also see the droplet suspended ($t = 0.83s$) at the thermocouple bead junction with minimal surface contact area. This is due to the high surface tension of the pure glycerol liquid and we also see the droplet orienting ($t = 3.26s$) such that the bead is more at the center of the droplet as it undergoes evaporation due to the changes in viscosity and surface tension of glycerol with increasing temperature.

Observations in the low magnification G100 droplet visualizations were indistinguishable when compared for air and nitrogen environments, and hence only one of the two is shown here in Figure 7-61. The inferences from the G100 visualizations are same as that of E100. Nucleate boiling is believed to be the cause of bubbling behavior in a pure single component liquid type such as G100. Likewise, in E100, we observe bubbling behaviors only in low gas flowrate air and nitrogen environments. The droplet heating rate in period-2 fluctuates a lot more in G100 than the E100 droplets when compared for multiple gas flowrates. Also, the longer residence time of the G100 compared to E100 might suggest a more influential role of heat transfer effects (especially conduction and convection) on the droplet evaporation. However, as mentioned before, the small number of low magnification experiments prevents detailed conclusions.

### 7.6.3. Ethanol-Glycerol Blend Suspended Droplet Behavior

High magnification visualizations from the suspended droplet experiments of E30G70 and E70G30 liquid types are shown in Figure 7-62 and Figure 7-63. The two ethanol-glycerol blends are contrasting in terms of their composition, however, their evaporation behavior as observed in our experiments are very similar. In Figure 7-62 we see a quiescent droplet until t = 0.35s; multiple bubble formation at *t = 0.49s*; coalescence of the bubbles and their subsequent expansion at *t = 0.51s* and *t = 0.57s*; microexplosion events at *t = 0.66s* and *t = 0.76s;* and volatilizing behavior from *t = 1.33s* onwards. Similarly, in Figure 7-63, we see microexplosion at *t = 0.93s* and *t = 1.54s;* bubble expansion at *t = 1.15s* and *t = 1.28s*; and volatilizing behavior from *t = 1.57s* onwards. From the observations of both the figures, we see that blend liquid types show violent microexplosion tendency with an associated microdroplet escape behavior.

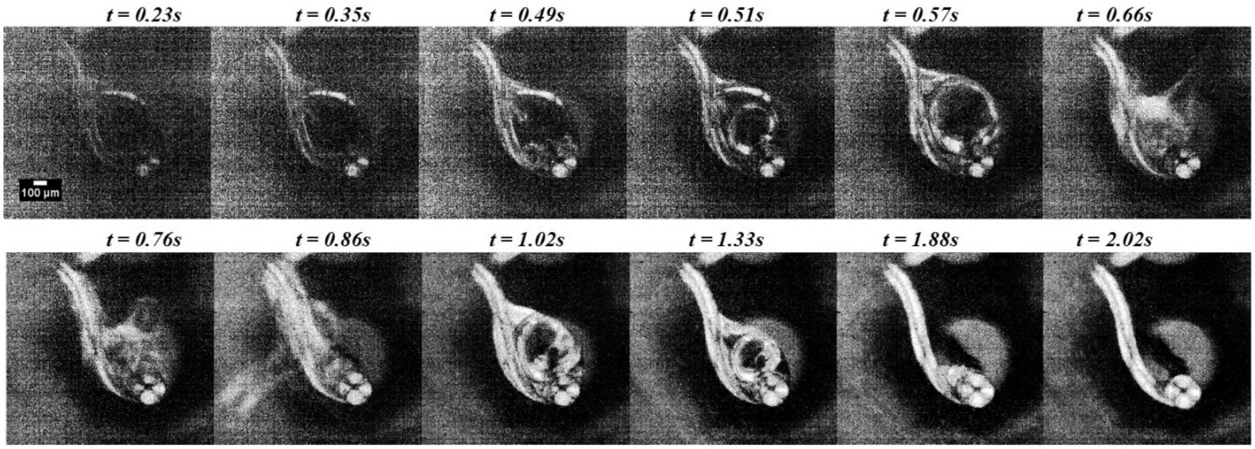

Figure 7-62: High magnification image sequence of E30G70 ($d_0$ = 578 µm; $t_{res}$ = 2.09s) droplet behavior in intermediate flowrate (10 SCFM) air environment.

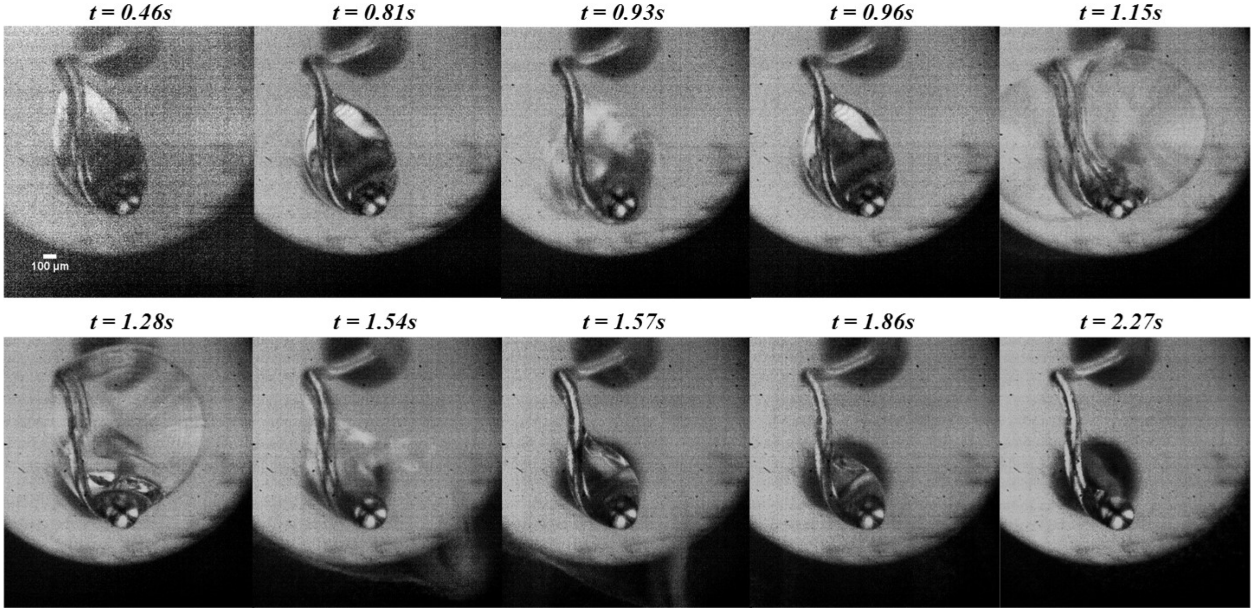

Figure 7-63: High magnification image sequence of E70G30 ($d_0$ = 868 µm; $t_{res}$ = 2.40s) droplet behavior in intermediate flowrate (10 SCFM) air environment.

The microexplosion event is generally preceded by a bubbling/puffing behavior and followed by the microdroplet escape behavior. Figure 7-64 shows a high magnification image sequence of one such microexplosion event in a E70G30 droplet. From the figure, until *t = 1.292s* we see multiple bubble formations within the droplet; at *t = 1.296s* we see the droplet surface is ruptured (indicated by the arrows) without release of satellite droplets (puffing behavior); bubble formation and expansion continues until *t = 1.329s*; at *t = 1.334s* microexplosion occurs distorting the droplet shape (as indicated by the arrow) with the release of micro volumes of the droplet (indicated by the circle); and the droplet assumes its original shape as seen at *t = 1.338s*. It is important to note that in each blend droplet there could be one or more instances of the events described, and not all of them are represented here in these image sequences.

From our understanding, the primary cause for the bubbling behavior in the blend liquids is due to the differential boiling point of the two liquid components (ethanol and glycerol) that make up the blend. As the droplet heats up, under the assumption of a well-mixed mixture, we expect the ethanol and glycerol components to heat up uniformly. However, the ethanol component has a boiling point that is several magnitudes lower than that of the glycerol as seen in Table 7-2. Consequently, the ethanol component of the liquid reaches its saturation temperature relatively quicker and changes into vapor. These vapor pockets that are trapped inside droplet boundary that is relatively concentrated with the low volatile glycerol, increases in pressure and break free, rupturing the droplet surface. This tendency of the droplet to form bubbles that are eventually released from the droplet surface is referred to as microexplosion. The temperature period data obtained for both the pure liquids E100 and G100 (Table 7-15) illustrates this well. From Table 7-15, we observe that the time duration ($\Delta t$) and temperature difference ($\Delta T$) in period-2 of E100 were lower than G100, and hence the early vapor formation of the former followed by the microexplosion behavior. The differences in heating rate of E100 and G100 liquid types as observed in Table 7-15 does not influence the blend under our assumption of uniform heating.

As mentioned in our observations of Figure 7-63, there are instances when the vapor pockets increase in size within the droplet and rupture the droplet surface with minimal distortion to the droplet surface and satellite droplets. Such a droplet behavior event is commonly referred to as puffing. Figure 7-65 and Figure 7-66 shows the puffing behavior events in E30G70 and E70G30 liquid types. In Figure 7-65, we see more than one puffing event, the bubble formed inside the droplet at *t = 1.051s*, *t =1.171s*, and *t = 1.288s,* bubble at its most expansive state is seen at *t =*

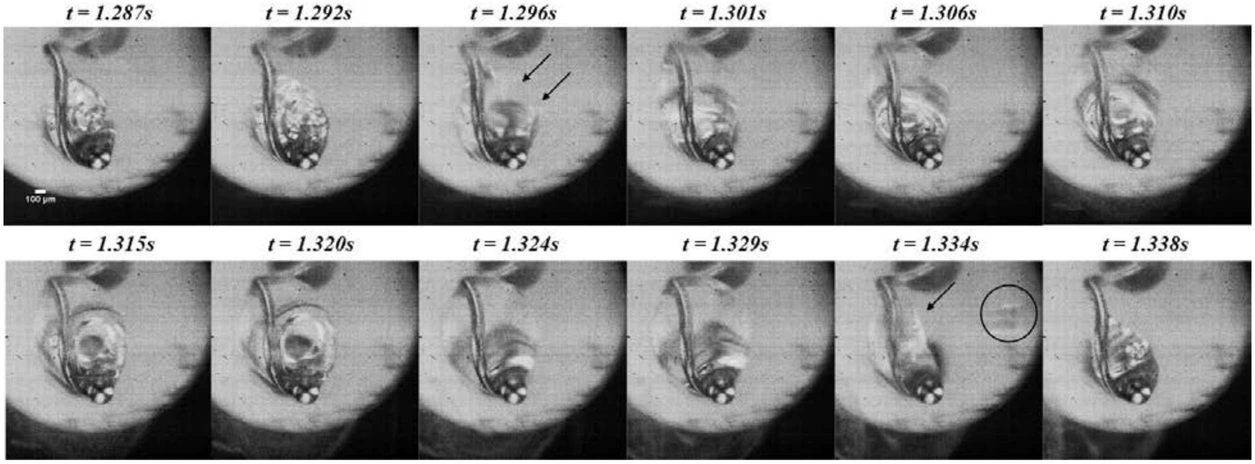

Figure 7-64: High magnification image sequence of E70G30 ($d_0$ = 868 µm; $t_{res}$ = 2.40s) droplet exhibiting microexplosion behavior in intermediate flowrate (10 SCFM) air environment.

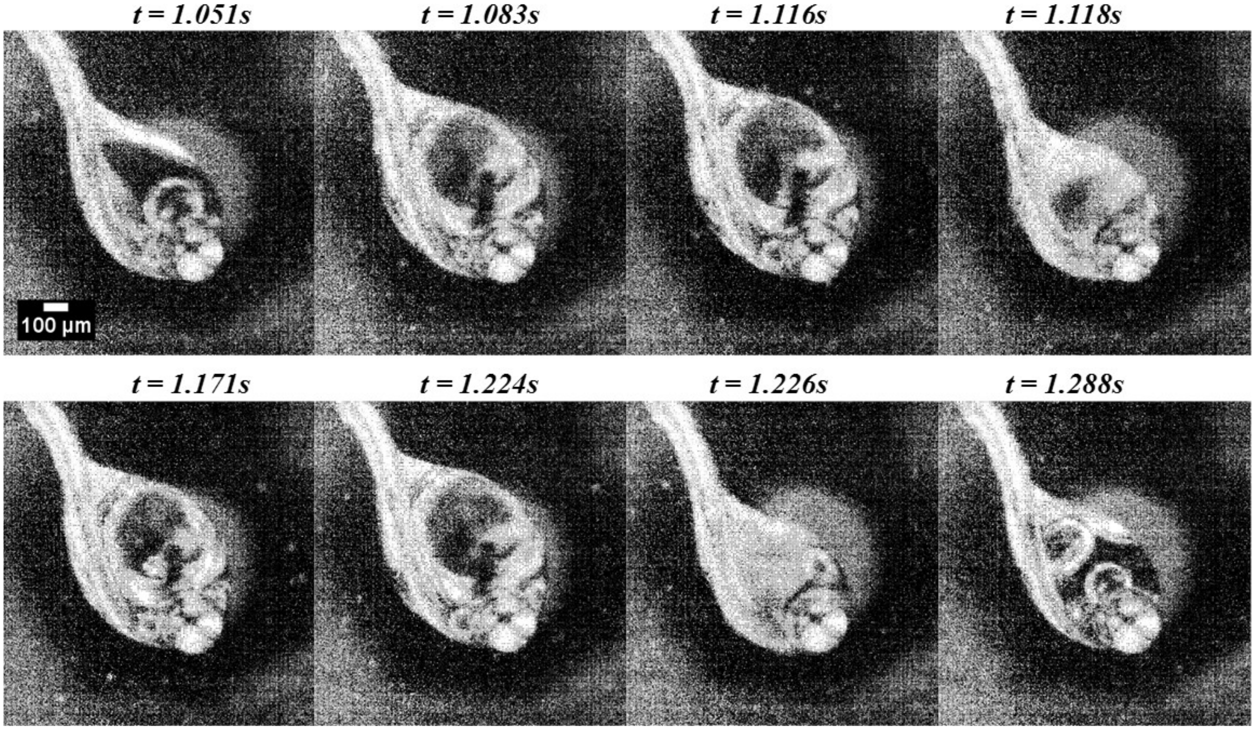

Figure 7-65: High magnification image sequence of E30G70 ($d_0$ = 578 µm; $t_{res}$ = 2.09s) droplet exhibiting puffing behavior in intermediate flowrate (10 SCFM) air environment.

*1.116s* and *t = 1.224s*; and bubble breakage as in a puffing behavior type at *t = 1.118s* and *t = 1.226s*. Similar step-wise puffing behavior can be seen in the E70G30 droplet as shown in Figure 7-66. Notable difference in the E70G30 droplet are the observation of the extremely large bubble expansions seen at *t = 0.981s* and *t = 0.988s*. The larger amount of ethanol in the E70G30 blend is believed to be responsible for the expanded bubble sizes.

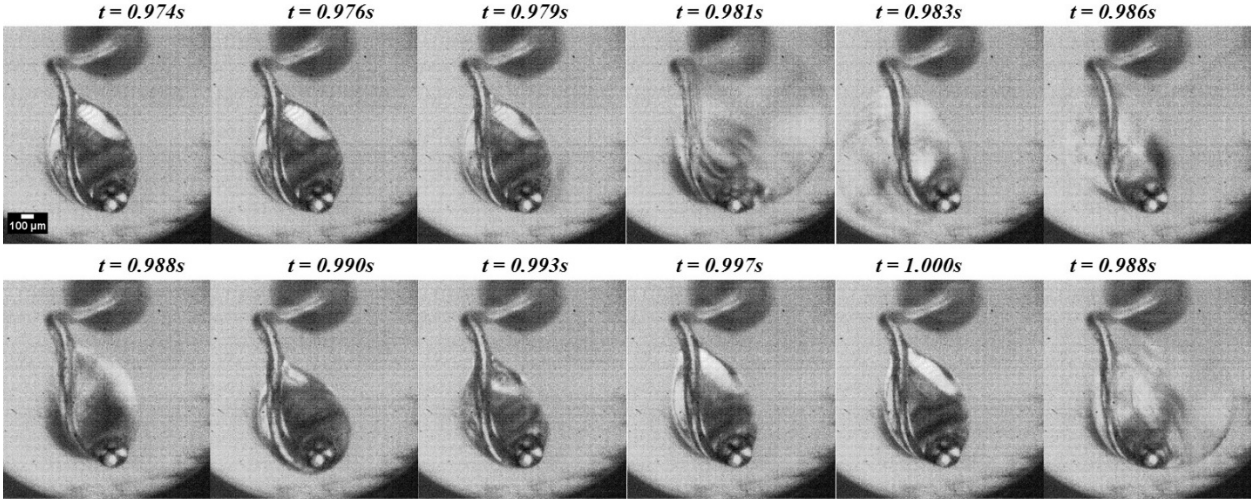

Figure 7-66: High magnification image sequence of E70G30 ($d_0$ = 868 µm; $t_{res}$ = 2.40s) droplet exhibiting puffing behavior in intermediate flowrate (10 SCFM) air environment.

Literature studies on droplet vaporization and combustion of several fuel types show that the bubbling, puffing, and microexplosion behavior in droplet sprays are generally preferred as it facilitates secondary atomization and complete combustion (Kadota and Yamasaki, 2002; Watnabe and Okazaki, 2013; Shinjo et al., 2014). In the blend liquids towards the end of the fluctuation evaporation phase, following the droplet behavior events, relatively low concentration of the ethanol component remains in the droplet. During this phase, the glycerol component of the liquid continues to evaporate in a volatilizing behavior as seen with the E100 and G100 liquid types. In our studies, this phase of droplet evaporation is referred as the equilibrium evaporation phase and sometimes as the residual droplet evaporation. Figure 7-67 shows the duration of the three evaporation phases along with the residence time for the E30G70 and E70G30 blends. Evident from the plots, blend liquid types shows that the time durations for the three characteristic evaporation phases as well as the residence times are similar.

During the low magnification experiments with the blend liquids, we observed a stronger microexplosion tendency in E70G30 droplets over E30G70 droplets. To investigate for any such difference in the strength of microexplosion, fluctuation evaporation phase of similar $d_0$ E30G70 ($d_0$ = 583 μm) and E70G30 ($d_0$ = 584 μm) droplets were analyzed by calculating the temporal droplet variations. Unlike the previous quantitative droplet dimeter ($d$) data reported, more images at closer time intervals (around 70 images at an interval period of 0.1s for each liquid type) were selected for this study. Figure 7-68 shows the temporal droplet diameter change of the two blends during the Fluctuation Evaporation Phase (FEP). Observation of the droplet diameter profiles and the averages droplet diameters during the FEP suggests that the strength of microexplosion are

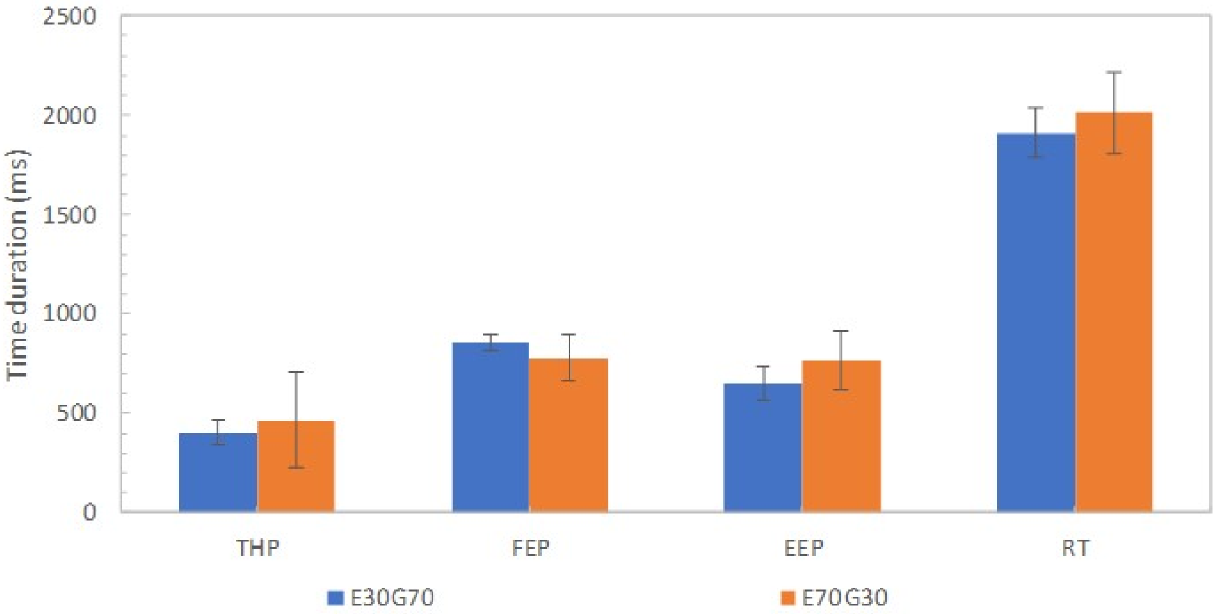

Figure 7-67: Characteristic evaporation phases (THP – Transient Heating Phase; FEP – Fluctuation Evaporation Phase; EEP – Equilibrium Evaporation Phase) and residence time (RT) of ethanol-glycerol blends E30G70 and E70G30.

larger in E70G30 over E30G70. Also, in the E70G30 droplet, the FEP starts and terminates earlier than the E70G30 droplet. In the E70G30 droplet, we see aggressive bubbling behavior early in the FEP with frequent droplet size changes unlike the E30G70 droplet where we observe relatively less fluctuation in *d*. We believe the aggressive bubbling effect seen in E70G30 is primarily due to the higher ethanol composition of the blend liquid. Our understanding is that the pockets of ethanol vapor formed due to differential heating rates have a higher tendency to coalesce because of the increased concentration of ethanol in the droplet. Consequently, larger sized bubbles or vapor pockets are formed, and as they escape the droplet boundary we observe increased distortions in the droplet diameter. Meanwhile, in E30G70 droplets, pockets of ethanol component that have reached the saturation temperature are more isolated among the high concentration of glycerol component. Therefore, a lesser tendency to coalesce and relatively milder distortions are observed in the droplet surface. Among the three characteristic phases for a droplet undergoing evaporation, an extended fluctuation evaporation phase is generally preferred

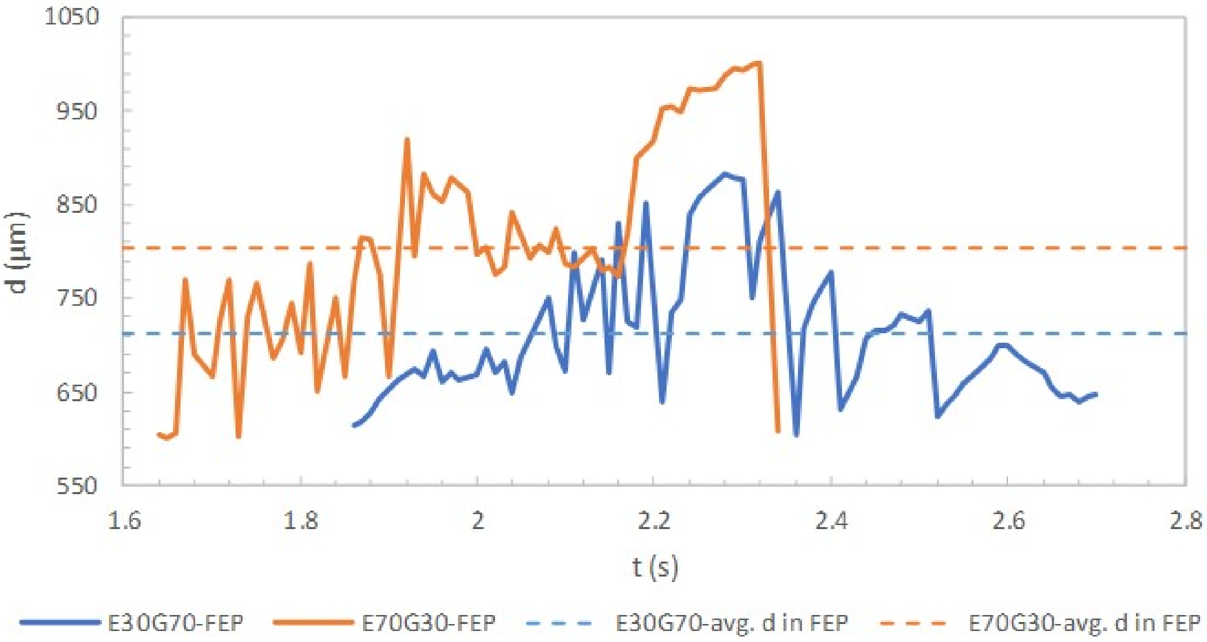

Figure 7-68: Fluctuation evaporation phase analysis of E30G70 ($d_0$ = 583 µm) and E70G30 ($d_0$ = 584 µm) liquid types.

for blend liquids that have fuel applications for the same benefits as mentioned before with the microexplosion phenomenon, as it improves the heat and mass transfer rates during the thermal behavior of the droplet.

### 7.6.4. Other Liquid Types Suspended Droplet Behavior

For the M100 and B100 liquid types, only qualitative analysis was performed using the high magnification visualizations. Figure 7-69 and Figure 7-70 show the image sequences of typical evaporation behavior of M100 and B100 liquid types respectively. As can be seen from the images, no significant droplet behavior events such as bubbling or microexplosion were observed, as both the droplet types exhibit a volatilizing behavior seen earlier in the liquid types E100 and G100.

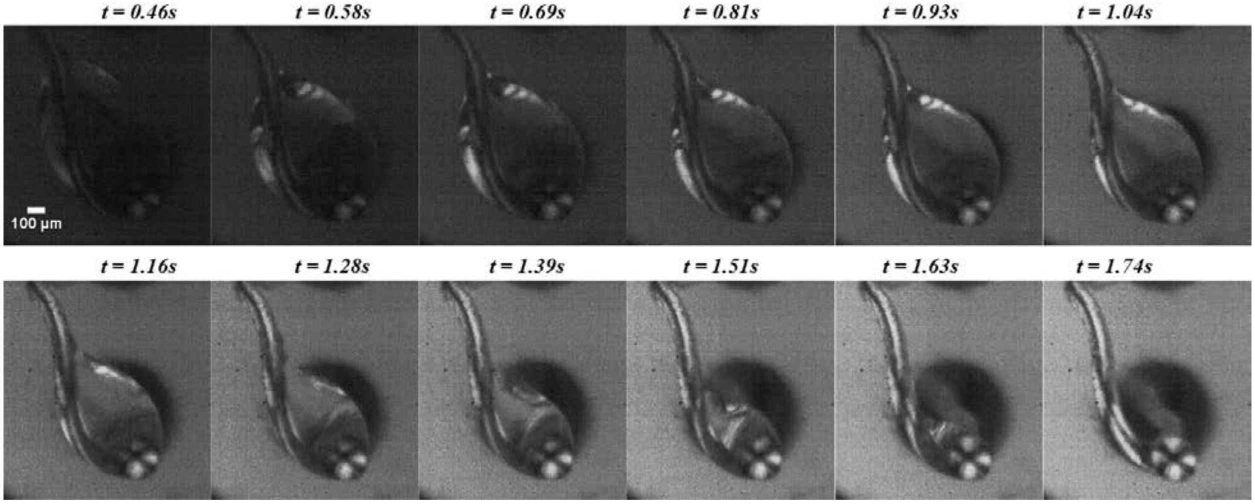

Figure 7-69: High magnification image sequence of M100 ($d_0$ = 842 µm; $t_{res}$ = 1.76s) droplet behavior in intermediate flowrate (10 SCFM) air environment.

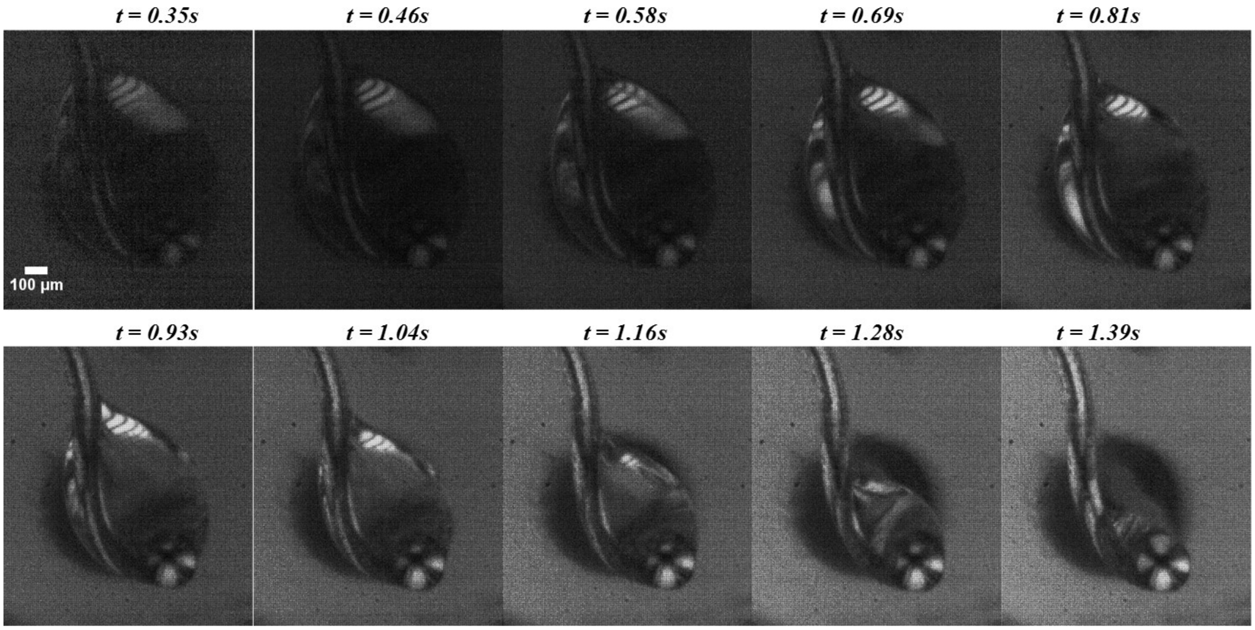

Figure 7-70: High magnification image sequence of B100 ($d_0$ = 869 μm; $t_{res}$ = 1.47s) droplet behavior in intermediate flowrate (10 SCFM) air environment.

The liquid properties of M100 and B100 are relatively close to E100 in terms of their boiling points and heats of vaporization. Also, they are pure single component liquid types like E100 and hence the similarities in their behavior are expected. These high magnification experiments of M100 and B100 confirm our earlier observations from the quantitative low magnification data of these two liquid types having similar quiescent, behavior and residence times to that of E100. Unlike the low magnification experiments, no experimental studies have been performed for the hexadecane liquid type in high magnification. As for the multicomponent liquid mixture BP Oil, the qualitative observations are presented in the aviation liquids section.

# 8. Droplet Studies Involving Aviation Engine Oil (BP Turbo Oil 274)

The studies related to aviation liquid mainly involve the commercially available engine oil BP Turbo Oil 274 (BP Oil). The BP Oil liquid type was studied alongside E-G liquid system (E100, E30G70, E70G30, and G100), standard fuel (Hexadecane), and others (M100, B100). Preliminary observation and results of the free-falling and suspended droplet experiments for the BP Oil liquid type were presented in the proof of method experiments of Chapter 4, 5, and 6. The quiescent and behavior time durations along with heating rates for a BP OIL droplet suspended in an instant heating environment under various gas type and flowrate conditions were shown in Chapter 7. The observations of the individual droplet behavior of the multicomponent BP Oil were presented in comparison with the pure single component liquids and binary mixtures. This chapter discusses the qualitative observations from visualizations and the bulk liquid analysis of BP Oil using thermogravimetric and gas chromatography-mass spectroscopy.

## 8.1. Qualitative Visualization Analysis

The droplet behavior of BP Oil was briefly discussed earlier in section 7.1. We showed the BP Oil liquid type to behave like a blend liquid with disruptive behavior. Figure 8-1, Figure 8-2, Figure 8-3, and Figure 8-4 show the BP Oil droplet lifetime broken into quiescent, attrition, microdroplet escape, and microexplosion behaviors. The multicomponent nature of the aviation liquid is found to exhibit several individual behaviors as observed in other liquid types. The attrition behavior of BP Oil and the hexadecane liquid type are similar. Likewise, the multiple bubbling events of BP Oil and E30G70 liquid type were similar. The gas chromatography mass spectroscopy studies shown in the following section indicate the primary component of the aviation liquid to be the fatty acid ethyl-methyl esters. From general knowledge, we know that a commercial engine oil such as BP Turbo Oil 274 contains numerous additives in addition to the base oil to improve the performance and shelf life of the product. The visualization observations of the BP Oil exhibiting similar behavior as other liquid types used in our study suggest the aviation liquid to contain compounds of similar liquid properties.

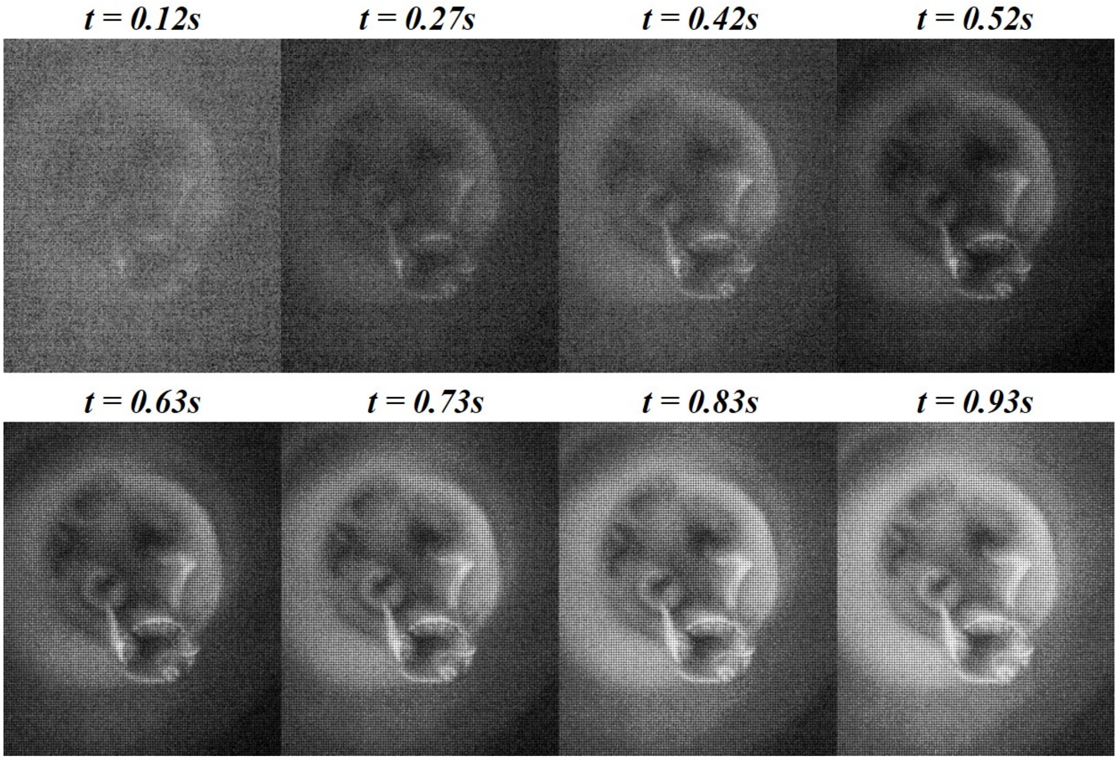

Figure 8-1: Low magnification visualizations of quiescent behavior in BP Oil ($d_0$ = 0.95mm, $t_{res}$ = 2.59s) in low flowrate air environment.

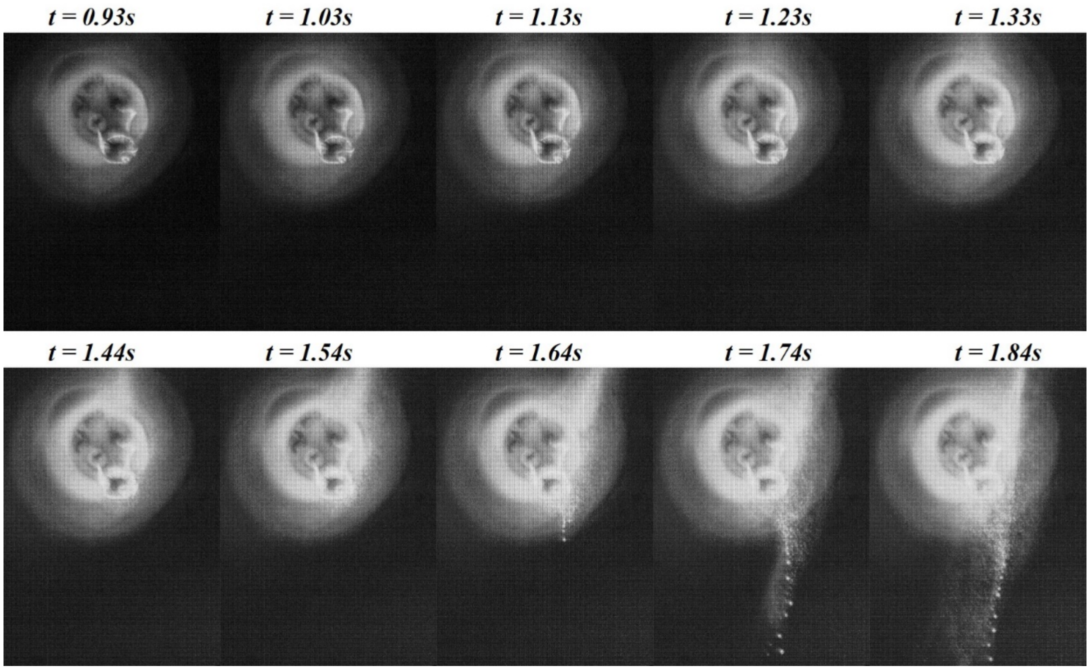

Figure 8-2: Low magnification visualizations of attrition behavior in BP Oil ($d_0$ = 0.95mm, $t_{res}$ = 2.59s) in low flowrate air environment.

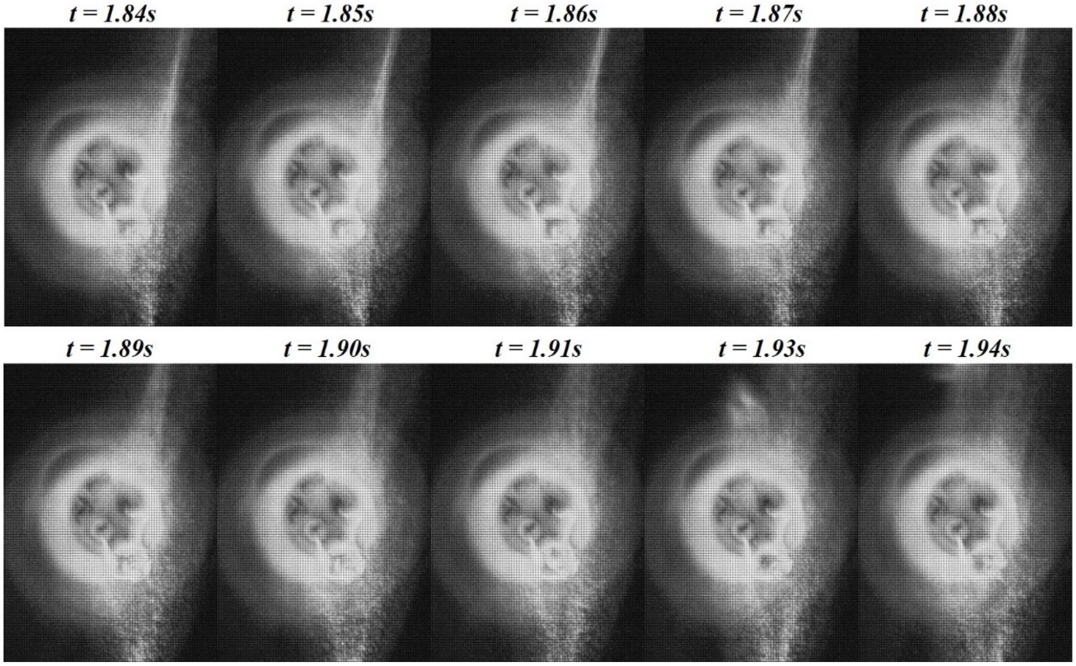

Figure 8-3: Low magnification visualizations of bubbling behavior in BP Oil ($d_0$ = 0.95mm, $t_{res}$ = 2.59s) in low flowrate air environment.

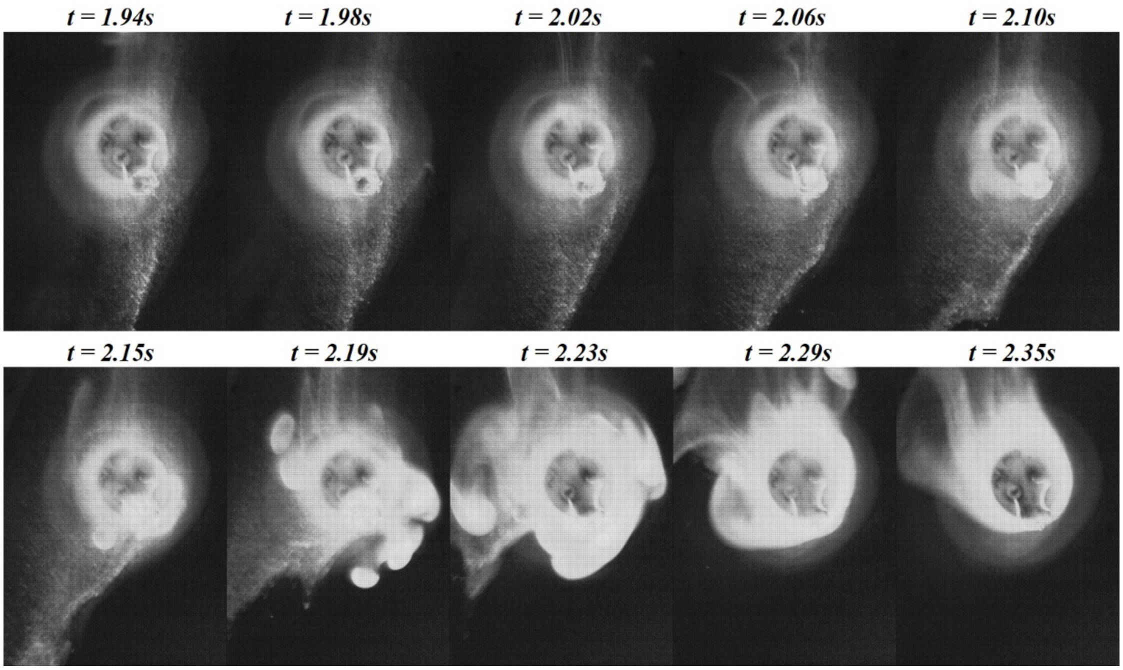

Figure 8-4: Low magnification visualizations of microexplosion behavior in BP Oil ($d_0$ = 0.95mm, $t_{res}$ = 2.59s) in low flowrate air environment.

High magnification visualizations of BP Oil suspended droplets in the IR heater are shown in a similar breakdown in Figure 8-5, Figure 8-6 and Figure 8-7. The quiescent behavior is shown in Figure 8-5, attrition behavior in Figure 8-6, and the microexplosion behavior in Figure 8-7. For scale, the thermocouple wire diameter that is observed in the images sequences is about 125 µm. The microexplosion event (Figure 8-4) is different from those observed in the ethanol-glycerol blends discussed in section 7.6. Unlike the E-G blends, no secondary microexplosion events were observed in BP Oil. The aviation liquid exhibited only a single microexplosion event, and the microexplosion event was much stronger than the blends as can be seen from the low volume of residual droplet on the thermocouple bead. Also, during the microexplosion event of BP Oil, we observe a higher proportion of vapor pockets releasing from the droplet over the blend liquids as is shown in Figure 8-4. One possible reason for such behavior could be the larger difference in the volatility of the compounds that make up the aviation liquid. When the disparity between the boiling points of the mixture are large, the high volatile compound that reaches its saturation temperature and forms vapor pockets requires an increased pressure to break the droplet boundary concentrated with the low volatile liquid component and hence a stronger microexplosion event. Due to the proprietary nature of the aviation liquid, the liquid components responsible for such microexplosion events cannot be addressed any further.

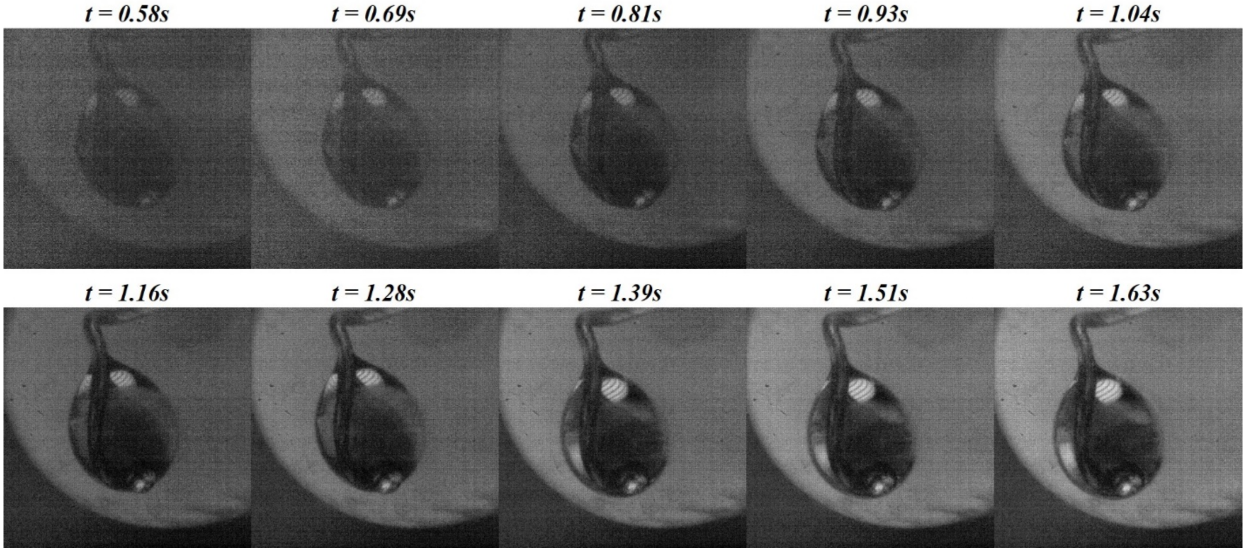

Figure 8-5: High magnification visualizations of quiescent behavior in BP Oil in intermediate flowrate air environment.

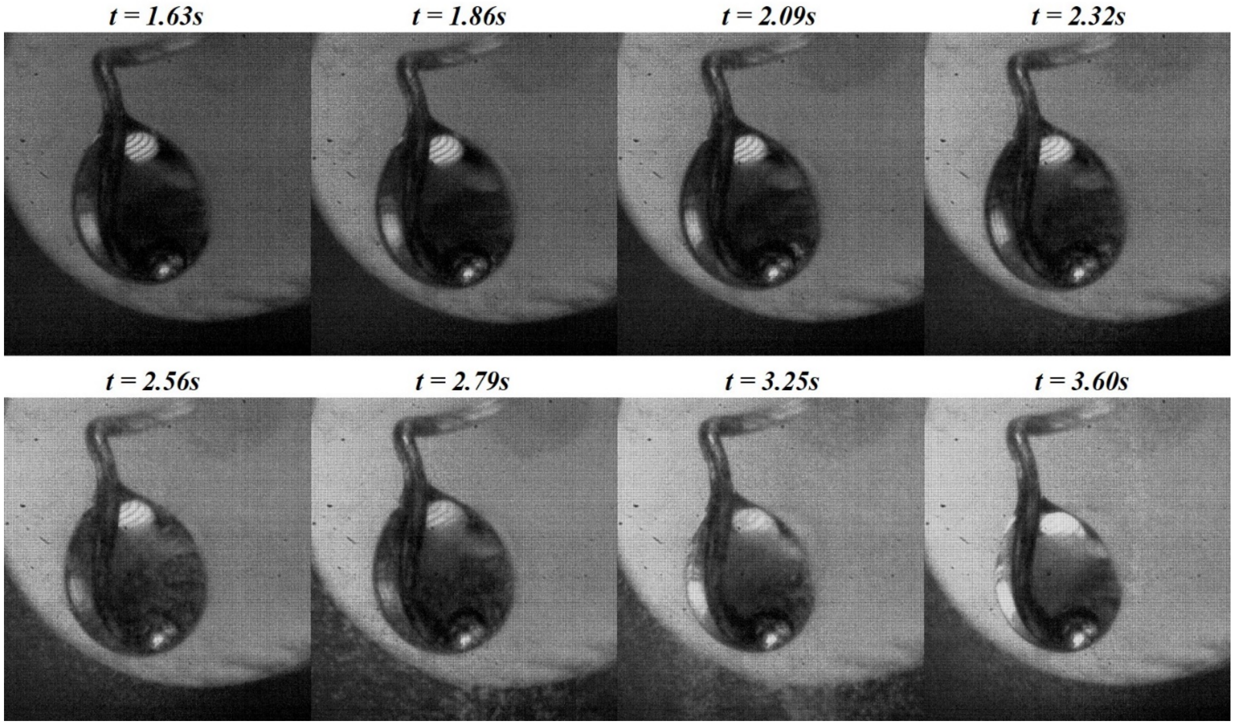

Figure 8-6: High magnification visualizations of attrition behavior in BP Oil liquid in intermediate flowrate air environment.

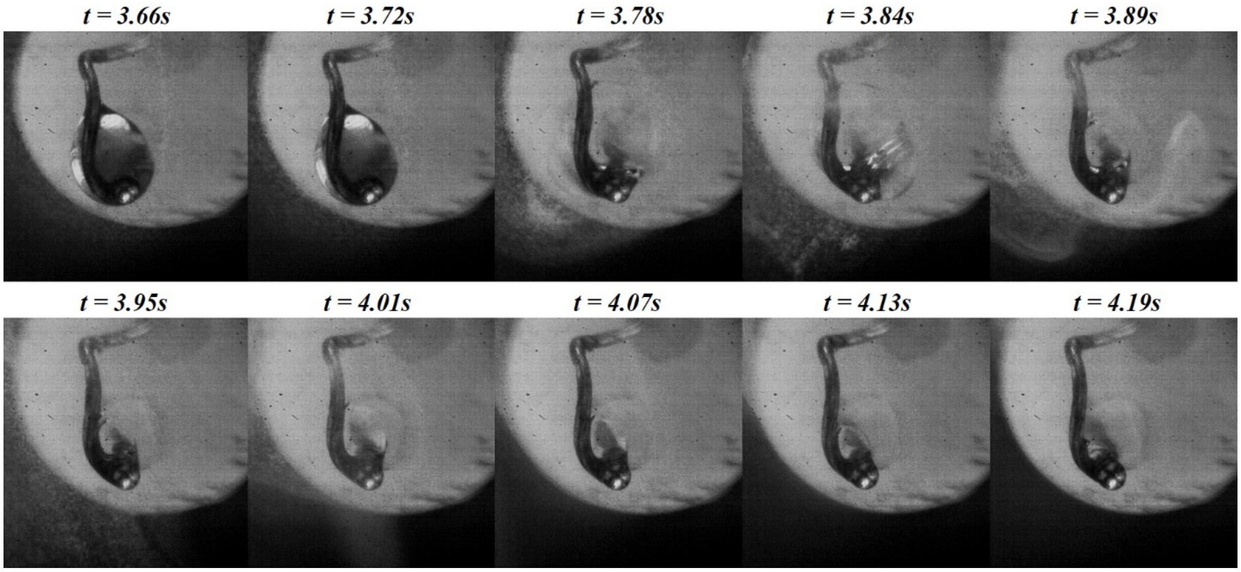

Figure 8-7: High magnification visualizations of microexplosion behavior in BP Oil liquid in intermediate flowrate air environment.

## 8.2. Bulk Liquid Analysis

Thermogravimetric studies on aviation liquid BP Oil have been performed with a TGA 50 Shimadzu Thermogravimetric Analyzer with the help of Dr. Sushil Adhikari's research group (Biosystems Engineering) at Auburn University. Oil samples 5 mg in weight were taken in Alumina crucibles after careful measurement using a high precision balance. The TGA studies were performed for the oil sample at four different heating rates starting from room temperature to 650°C at 10 °C/min, 15 °C/min, 20 °C/min and 30 °C/min. The TGA apparatus was operated in nitrogen atmosphere with 20 ml/min flow rate. The mass loss (TGA) and differential mass loss curves (DrTGA) are shown in Figure 8-8, Figure 8-9, Figure 8-10, and Figure 8-11.

The TGA curves shows a peak mass loss at 309.7 °C for a heating rate of 10 °C/min and the peak temperature progressively increases to 326.2°C, 341.6°C, and 351.7°C as the heating rate was increased to 15, 20, and 30 °C/min respectively. In Figure 8-12 and Table 8-1, the effect of heating rates on the mass loss temperatures are shown. Here, the 'T-start' refers to the temperature at which the mass loss begins in the sample. 'T-peak' refers to the peak temperature and the point where maximum mass loss occurs. It also represents the first mass loss step obtained from the minimum of the DrTGA (Differential TGA) curve. 'T-shoulder' refers to the temperature at which the second maximum mass loss happens. It also represents the second mass loss step and obtained through the maximum of DrDrTGA (Double differential TGA) curve. 'T-end' refers to the temperature at which the rate of mass loss flattens out and residual mass was obtained.

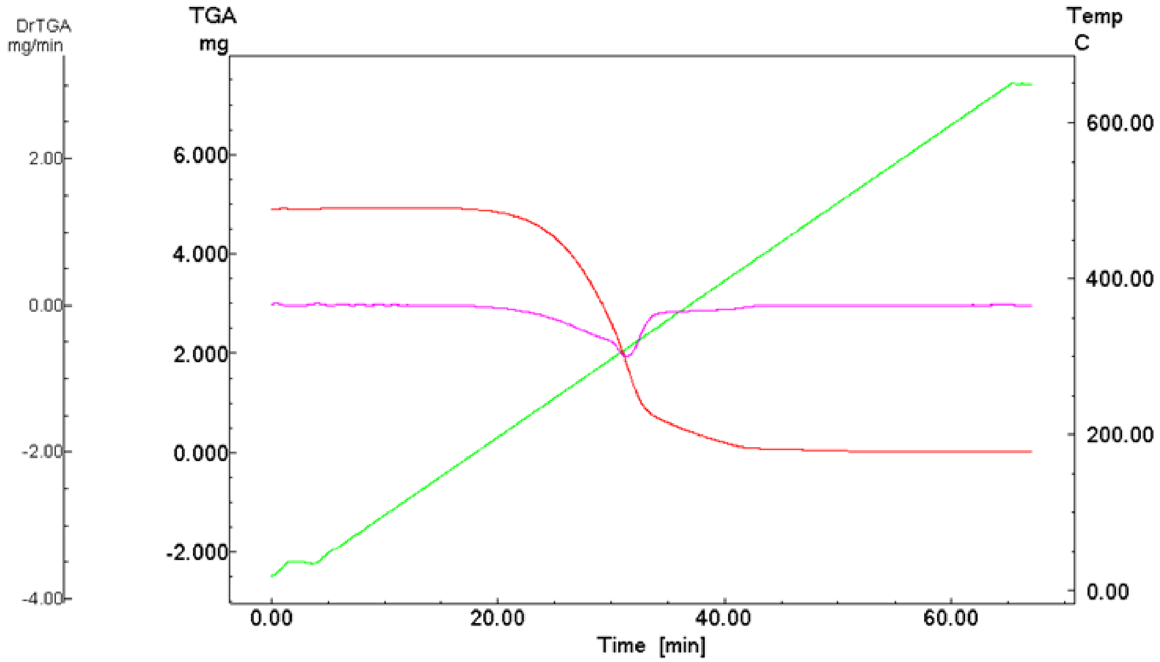

Figure 8-8: TG and DTG curves for BP Oil at a heating rate of 10 °C/min.

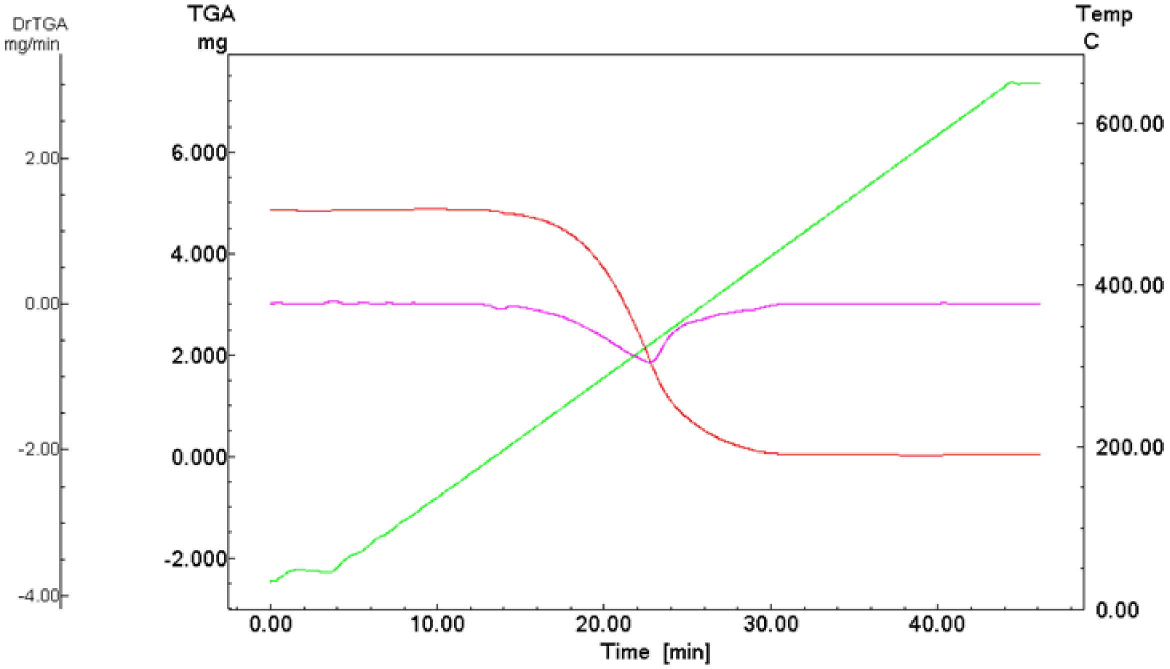

Figure 8-9: TG (red) and DTG (purple) curves for BP Oil at a heating rate of 15 °C/min (green).

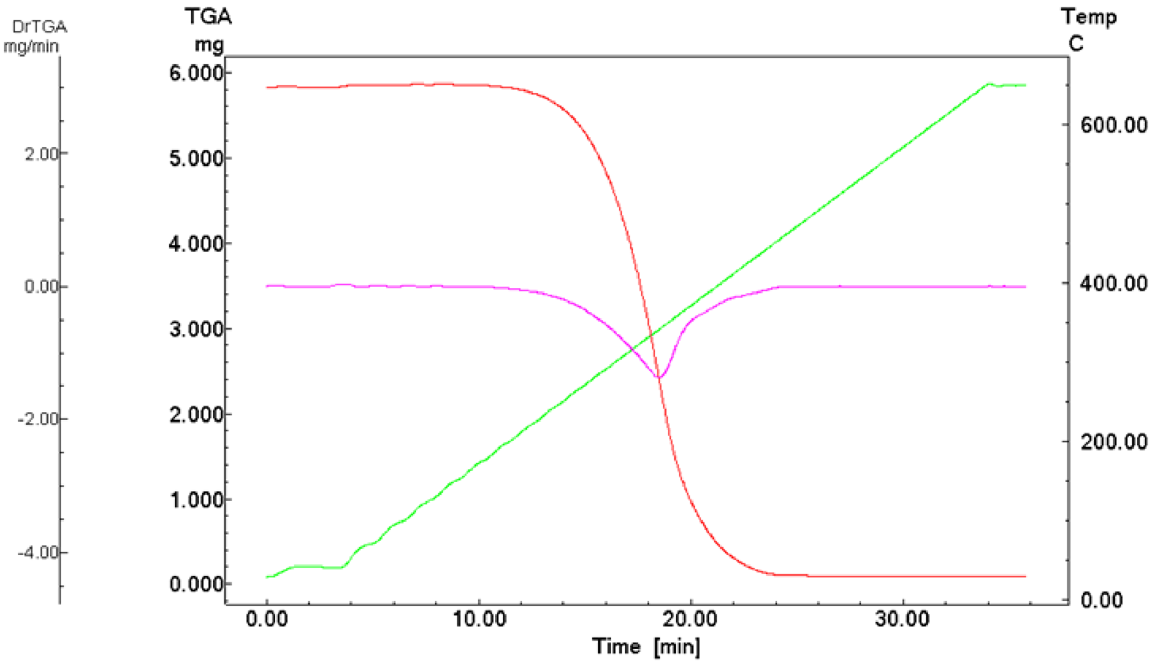

Figure 8-10: TG (red) and DTG (purple) curves for BP Oil at a heating rate of 20 °C/min (green).

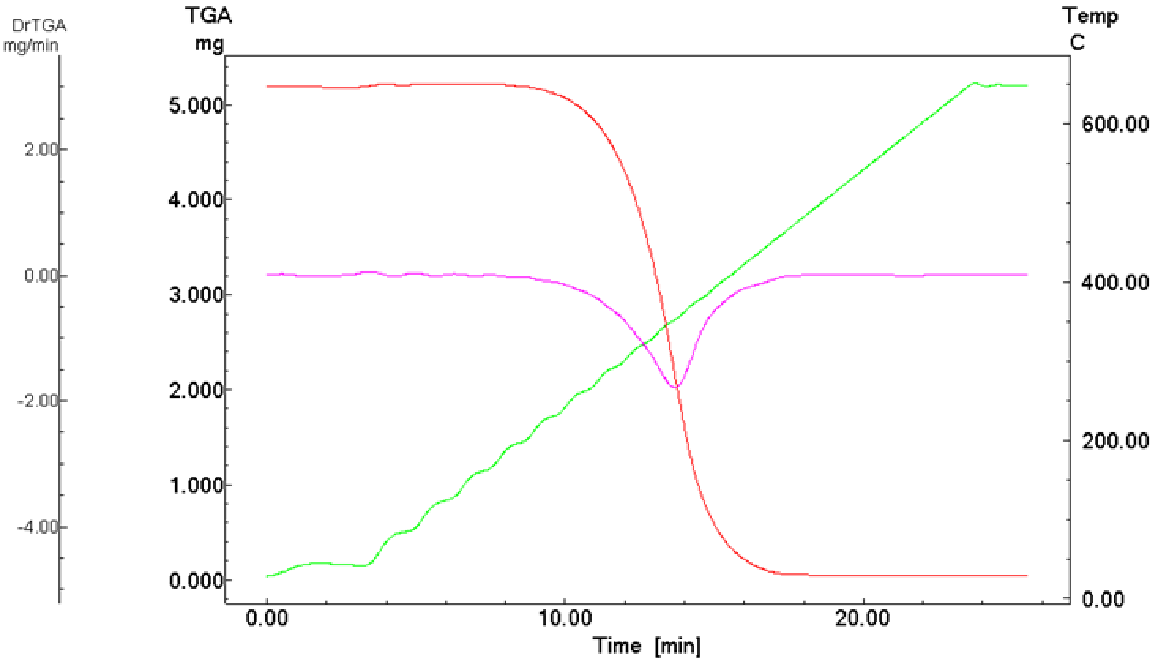

Figure 8-11: TG (red) and DTG (purple) curves for BP Oil at a heating rate of 30 °C/min (green).

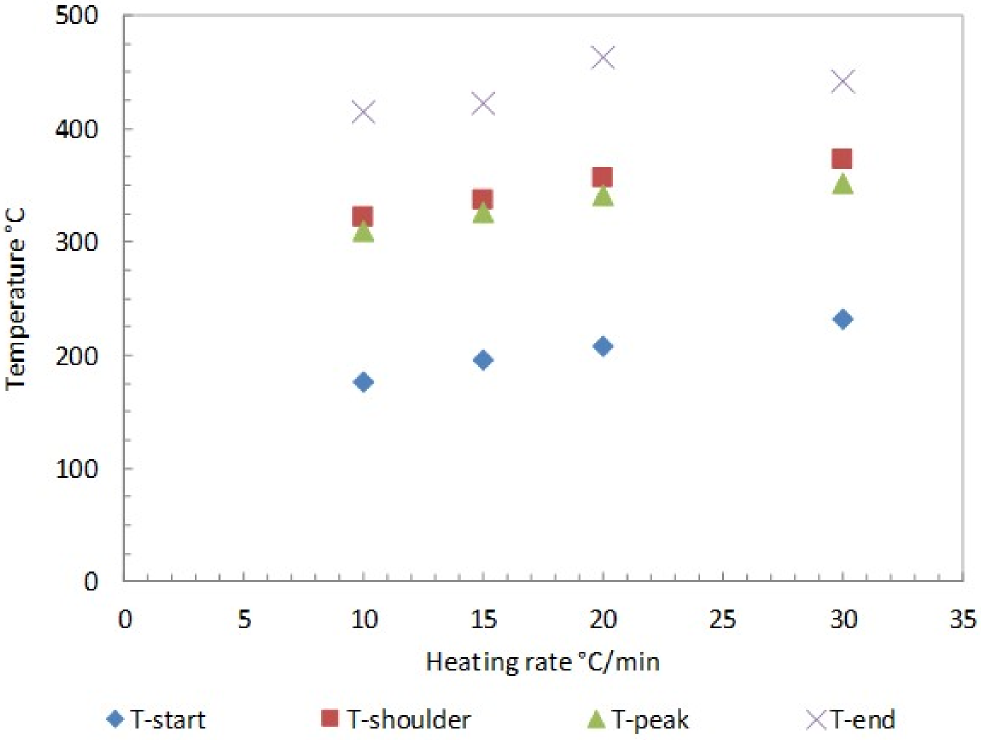

Figure 8-12: Effect of heating rate on mass loss temperature in BP Oil.

Table 8-1: Effect of heating rates on mass loss temperatures, residual sample weight, and %mass loss for BP Oil.

| Heating rate (°C/min) | Parameters | Sample weight (mg) | t (s) | T (°C) | TGA (mg/s) | Δ(T-end - T-start) (°C) | % mass loss |
|---|---|---|---|---|---|---|---|
| 10 | *T-start* | 4.89 | 1076 | 176 | 4.89 | 239 | 95 |
| | *T-shoulder* | | 1953 | 322 | 1.05 | | |
| | *T-peak* | | 1879 | 310 | 1.8 | | |
| | *T-end* | 0.02 | 2510 | 415 | 0.1 | | |
| 15 | *T-start* | 4.85 | 836 | 195 | 4.8 | 227 | 95 |
| | *T-shoulder* | | 1404 | 337 | 1.4 | | |
| | *T-peak* | | 1362 | 326 | 1.93 | | |
| | *T-end* | 0.03 | 1746 | 422 | 0.1 | | |
| 20 | *T-start* | 5.83 | 712 | 208 | 5.8 | 254 | 94 |
| | *T-shoulder* | | 1156 | 356 | 1.48 | | |
| | *T-peak* | | 1111 | 342 | 2.38 | | |
| | *T-end* | 0.09 | 1474 | 462 | 0.1 | | |
| 30 | *T-start* | 5.18 | 585 | 232 | 5.1 | 210 | 95 |
| | *T-shoulder* | | 858 | 372 | 1.18 | | |
| | *T-peak* | | 821 | 352 | 2.16 | | |
| | *T-end* | 0.04 | 1001 | 442 | 0.1 | | |

GC/MS studies were also performed with a pyroprobe for bulk oil samples. The list of compounds identified in GC/MS studies are shown in Table 8-2 and Table 8-3. Preliminary analysis of the GC/MS results shows the aviation liquid composition is based on fatty acid methyl-ethyl esters. No significant evidence of organophosphates and polyaromatic hydrocarbons (PAH's) in the oil composition were found.

Table 8-2: GC/MS results for tests with pyroprobe for BP Oil.

| RT | Area Pct | Library/ID | Ref | CAS | Qual |
|---|---|---|---|---|---|
| 8.0248 | 0.1503 | 1-Heptanol, 6-methyl- | 13240 | 001653-40-3 | 80 |
| 9.3294 | 2.4235 | Nonyl chloroformate | 60932 | 057045-82-6 | 87 |
| 10.7256 | 0.1948 | 1-Octene, 2,6-dimethyl- | 17383 | 006874-29-9 | 90 |
| 10.9488 | 0.3821 | 2-Decene, 8-methyl-, (Z)- | 25947 | 074630-25-4 | 86 |
| 11.1376 | 0.0425 | 2-Undecanethiol, 2-methyl- | 58386 | 010059-13-9 | 80 |
| 11.664 | 0.0977 | 4-Undecene, (E)- | 25923 | 000693-62-9 | 87 |
| 11.9558 | 0.0982 | 2-Decene, (Z)- | 17333 | 020348-51-0 | 83 |
| 12.671 | 0.0491 | Pentafluoropropionic acid, dodecyl ester | 143323 | 006222-04-4 | 86 |
| 16.911 | 0.0797 | Benzene, 1-methyl-4-(1-methylethenyl)- | 13649 | 001195-32-0 | 95 |
| 19.7205 | 1.2996 | Cyclooctane | 6448 | 000292-64-8 | 81 |
| 19.8063 | 0.0833 | 3-Eicosene, (E)- | 112107 | 074685-33-9 | 86 |
| 21.5172 | 0.084 | 4-Trifluoroacetoxytridecane | 121959 | 1000245-47-3 | 80 |
| 22.284 | 0.0411 | Cyclopropane, 1-(2-methylbutyl)-1-(1-methylpropyl)- | 35091 | 064723-36-0 | 86 |
| 23.2224 | 1.0585 | 7-Octenoic acid | 18921 | 018719-24-9 | 95 |
| 23.4684 | 0.1663 | dl-2-Ethylhexyl chloroformate | 51670 | 024468-13-1 | 81 |
| 25.2937 | 1.5592 | Nonanoic acid | 28885 | 000112-05-0 | 90 |
| 28.6182 | 0.2503 | Bacchotricuneatin c | 148777 | 066563-30-2 | 83 |
| 29.1561 | 0.1592 | Phenol, 2-methoxy-4-(1-propenyl)-, (Z)- | 31881 | 005912-86-7 | 98 |
| 29.7111 | 0.1764 | Vanillin | 24745 | 000121-33-5 | 90 |
| 31.3247 | 0.0971 | Hydroquinone mono-trimethylsilyl ether | 45161 | 017881-87-7 | 86 |
| 31.6737 | 0.1531 | Ethanone, 1-(4-hydroxy-3-methoxyphenyl)- | 34048 | 000498-02-2 | 92 |
| 35.5303 | 0.2846 | N-(4-Methoxyphenyl)-2-hydroxyimino-acetamide | 53297 | 1000143-61-3 | 95 |
| 36.1769 | 0.0572 | Benzaldehyde, 4-hydroxy-3,5-dimethoxy- | 45077 | 000134-96-3 | 86 |
| 36.3486 | 0.0167 | 1-Decanol, 2-hexyl- | 86865 | 002425-77-6 | 87 |
| 36.772 | 0.0329 | Cyclotetracosane | 145923 | 000297-03-0 | 93 |
| 36.9436 | 0.0124 | 2-Tetradecene, (E)- | 54521 | 035953-53-8 | 87 |
| 38.0251 | 0.0743 | Phthalic acid, decyl isobutyl ester | 158087 | 1000308-94-2 | 90 |
| 38.1968 | 0.018 | Hexadecanoic acid, ethyl ester | 114847 | 000628-97-7 | 92 |
| 39.5185 | 0.0245 | Cyclohexane, 1,1',1''-(1-propanyl-2-ylidene)tris- | 118758 | 055682-89-8 | 90 |
| 39.633 | 0.0764 | n-Hexadecanoic acid | 96234 | 000057-10-3 | 93 |
| 41.012 | 0.0051 | 1-Octadecene | 93544 | 000112-88-9 | 91 |
| 41.5613 | 0.0077 | Linoleic acid ethyl ester | 129812 | 000544-35-4 | 94 |
| 42.0992 | 0.0138 | Cyclotetradecane | 54513 | 000295-17-0 | 86 |
| 44.1877 | 0.207 | Phenothiazine | 56510 | 000092-84-2 | 95 |
| 44.4166 | 0.0977 | Phenothiazine | 56510 | 000092-84-2 | 96 |
| 44.7656 | 0.0283 | Phenothiazine | 56510 | 000092-84-2 | 86 |
| 45.3034 | 0.0567 | Phenothiazine | 56509 | 000092-84-2 | 80 |
| 45.4866 | 0.1587 | Diisooctyl adipate | 161407 | 001330-86-5 | 83 |
| 45.5838 | 0.3518 | Diisooctyl adipate | 161407 | 001330-86-5 | 93 |
| 46.1446 | 0.1392 | Hexanedioic acid, dioctyl ester | 161409 | 000123-79-5 | 86 |
| 46.2476 | 0.5399 | Hexanedioic acid, bis(2-ethylhexyl) ester | 161421 | 000103-23-1 | 91 |
| 46.5279 | 1.3614 | Diisooctyl adipate | 161407 | 001330-86-5 | 83 |
| 46.6596 | 0.4746 | Hexanedioic acid, bis(2-ethylhexyl) ester | 161421 | 000103-23-1 | 83 |
| 46.9514 | 0.5171 | Hexanedioic acid, bis(2-ethylhexyl) ester | 161421 | 000103-23-1 | 83 |
| 47.2317 | 1.158 | Hexanedioic acid, bis(2-ethylhexyl) ester | 161421 | 000103-23-1 | 86 |
| 47.9642 | 0.1942 | Diisooctyl adipate | 161407 | 001330-86-5 | 91 |
| 48.1644 | 0.5411 | Diisooctyl adipate | 161407 | 001330-86-5 | 90 |
| 48.3418 | 0.1947 | Hexanedioic acid, bis(2-ethylhexyl) ester | 161421 | 000103-23-1 | 86 |
| 53.0624 | 0.4797 | 2,6,10,14,18,22-Tetracosahexaene, 2,6,10,15,19,23-hexamethyl-, (all-E)- | 173571 | 000111-02-4 | 99 |

Table 8-3: GC/MS results for tests bulk oil sample of BP Oil.

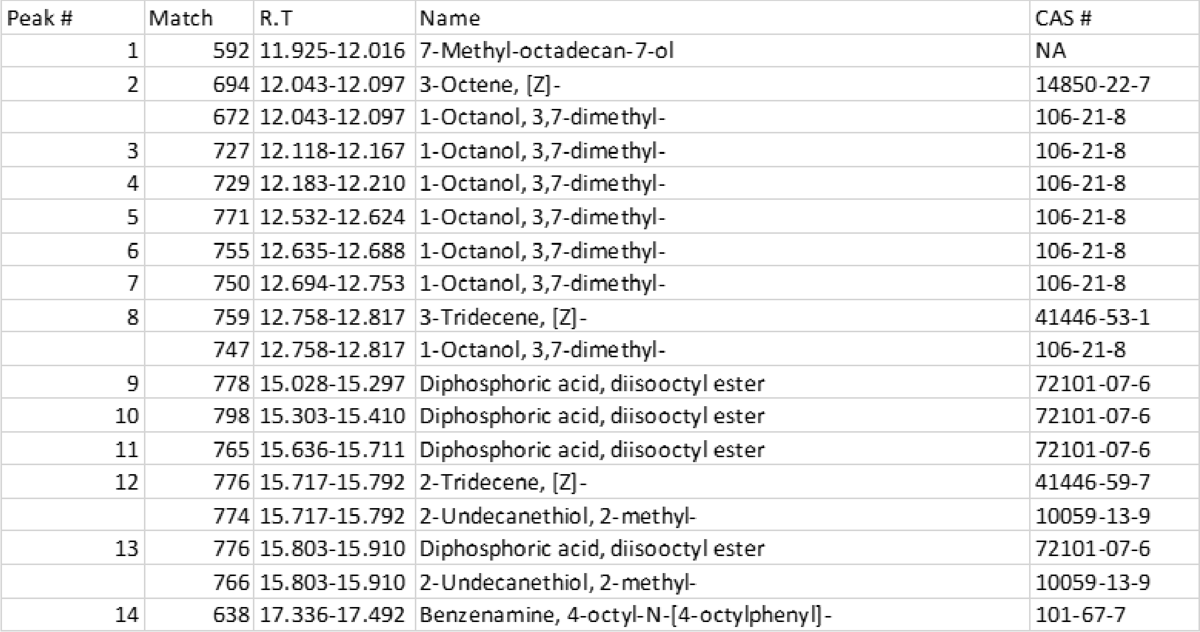

| Peak # | Match | R.T | Name | CAS # |
|---|---|---|---|---|
| 1 | 592 | 11.925-12.016 | 7-Methyl-octadecan-7-ol | NA |
| 2 | 694 | 12.043-12.097 | 3-Octene, [Z]- | 14850-22-7 |
|  | 672 | 12.043-12.097 | 1-Octanol, 3,7-dimethyl- | 106-21-8 |
| 3 | 727 | 12.118-12.167 | 1-Octanol, 3,7-dimethyl- | 106-21-8 |
| 4 | 729 | 12.183-12.210 | 1-Octanol, 3,7-dimethyl- | 106-21-8 |
| 5 | 771 | 12.532-12.624 | 1-Octanol, 3,7-dimethyl- | 106-21-8 |
| 6 | 755 | 12.635-12.688 | 1-Octanol, 3,7-dimethyl- | 106-21-8 |
| 7 | 750 | 12.694-12.753 | 1-Octanol, 3,7-dimethyl- | 106-21-8 |
| 8 | 759 | 12.758-12.817 | 3-Tridecene, [Z]- | 41446-53-1 |
|  | 747 | 12.758-12.817 | 1-Octanol, 3,7-dimethyl- | 106-21-8 |
| 9 | 778 | 15.028-15.297 | Diphosphoric acid, diisooctyl ester | 72101-07-6 |
| 10 | 798 | 15.303-15.410 | Diphosphoric acid, diisooctyl ester | 72101-07-6 |
| 11 | 765 | 15.636-15.711 | Diphosphoric acid, diisooctyl ester | 72101-07-6 |
| 12 | 776 | 15.717-15.792 | 2-Tridecene, [Z]- | 41446-59-7 |
|  | 774 | 15.717-15.792 | 2-Undecanethiol, 2-methyl- | 10059-13-9 |
| 13 | 776 | 15.803-15.910 | Diphosphoric acid, diisooctyl ester | 72101-07-6 |
|  | 766 | 15.803-15.910 | 2-Undecanethiol, 2-methyl- | 10059-13-9 |
| 14 | 638 | 17.336-17.492 | Benzenamine, 4-octyl-N-[4-octylphenyl]- | 101-67-7 |

# 9. Conclusions and Future Directions

Droplet behavior studies of alternative fuels and aviation liquids were performed in drop tube furnace and IR heater in controlled environments. Two techniques, namely, the free-falling and the suspended droplet techniques were demonstrated to study moving and stationary droplet behaviors. Our primary objective to observe and record the droplet behavior in various thermal environments was successful. Three different experimental setups were designed, constructed, and shown to be effective tools to study droplet behavior in high temperature environments. A piezo-electric droplet generator was constructed for microdroplet generation and used successfully in free-falling droplet studies. Droplet generation experiments displayed the ability of our droplet generator to produce microdroplets with the diameter range of 350 to 700 µm, consistent center-to-center spacing, and near-vertical trajectories. Optimum parameters in terms of drive voltage, drive frequency and liquid flowrate were determined from experiments. Drive voltage was shown to influence droplet diameter.

Systematic suspended droplet studies were performed in the IR heater to study the behavior of ethanol-glycerol (E-G) blends. Influence of gas environment and gas flowrate conditions were studied with the E70G30 liquid. From these experiments, the strength of microexplosion was shown to have a potential role in the differences observed for behavior time durations in higher gas flowrate conditions. Comparative studies of the E-G system with similar pure single component liquids (M100 and B100), standard fuel (hexadecane), and multicomponent liquid (BP Oil) were performed for four different test conditions (air-low, air-high, nitrogen-low, and nitrogen-high). Overall, the gas environment type and gas flowrate condition were shown to have minimal influence on the behavior time durations (QT, BT, RT) and heating rates of E100, M100, B100 and hexadecane liquids. For blends and liquids with long residence times, we observed the gas flowrate having relatively more influence over gas type with respect to behavior time durations and heating rates. Significant behavior events of blend liquids (strength of microexplosion and microdroplet events) and the heat transfer effects (potentially increased role of convective heat transfer) associated with longer residence time were suggested to be responsible for such behavior. Liquid properties, specifically the boiling point and heat of vaporization, influenced behavior time durations (BT, RT) for all liquids as excepted, except hexadecane. The heating rates of different liquids also showed a similar trend of varying proportional to their boiling points. Gas type and flowrate were shown to affect the heating rate in blends, G100, and BP Oil. The same reasons as stated before with behavior time duration were suggested to be responsible for the heating rates observed in different test conditions.

High magnification experiments in fixed operating conditions for E-G system liquids were performed and visualization results were presented. Quantitative analysis of the high magnification images provided quantification of temporal droplet diameter and vaporization rate constants for the four liquids of E-G system. Characteristic evaporation phases (transient heating phase, fluctuation evaporation phase, and equilibrium evaporation phase) were identified using normalized temporal droplet diameter plots ($d^2/d_0^2$ vs $t/d_0^2$). The single component liquid types E100 and G100 show two characteristic evaporation phases (THP and EEP) while the blends E30G70 and E70G30 showed an additional FEP. Droplet temperature period classifications (cold droplet heat-up period, heating rate period, and temperature plateau period) were obtained for all four E-G system liquids. From the droplet temperature profiles, we observed the heating rates of both the ethanol-glycerol blends to be closer to G100 than to E100. The amount of ethanol in the blends has minimal influence in terms of the heating rates obtained for the selected operating conditions. The $d^2$-law was evaluated for all four liquids and used in the calculation of evaporation rate constants ($k$). The average evaporation rate constant ($k_{avg}$) of E100 was found to be higher than G100. The two blends shower higher $k_{avg}$ values when compared to G100, and among the two blends the $k_{avg}$ was higher for the blend E70G30 with higher concentration of ethanol. Quantitative data obtained from the high magnification visualizations were also used to compare the fluctuation evaporation phase behavior of E30G70 and E70G30 blends. The results showed aggressive puffing behavior during the early vaporization phase, and stronger puffing, microdroplet escape, and microexplosion events in the blend with higher ethanol composition (E70G30).

Overall, the experiments with IR heater demonstrated a novel method to study suspended droplet behavior using a radiant heating source. Results from our experiments show quantitative analysis of the visualization data corresponding to convection and resistance heating sources can also be performed with IR heater to understand individual droplet behavior. Repetitive suspended droplet experiments, preferably in high magnification, would be useful to understand the role of operating conditions on droplet vaporization and combustion. Also, extending the experiments to understand the behavior of other multicomponent liquids such as crude glycerol, waste oil, bio oil, and commercially available engine oils would be valuable for the real-world applications. Further development of the method to collect and analyze vapors generated from suspended droplet experiments would be useful to obtain a thorough understanding of the degradation behavior of liquid droplets in heated environments.

# References

Akkapeddi, S. (2008). Alternative solid fuels for the production of portland cement. Master's Thesis, Auburn University.

Astbury, G. R. (2008). A review of the properties and hazards of some alternative fuels. Process Safety and Environmental Protection, 86(6), 397-414.

BAe Systems (2000). BAe 146 manufacturer's operations manual: notice to aircrew, operational notice: No. OP 16 and 43 (Issue 1). British Aerospace Systems, Hatfield, UK.

Bartl, P., Völkl, C., & Kaiser, M. (2008). Chemical characterization of polyol ester aviation lubricant residues. Lubrication Science, 25(1), 1-16.

Bohon, M. D., Metzger, B. A., Linak, W. P., King, C. J., & Roberts, W. L. (2011). Glycerol combustion and emissions. Proceedings of the Combustion Institute, 33(2), 2717-2724.

Bolt, J. A., & Saad, M. A. (1955). Burning of individual fuel drops in a furnace.

Brooks, B. (2015). Transport modeling and response characteristics of commercial catalytic bead sensors. Master's Thesis, Auburn University.

Buck, A. (2014). Steady state and transient response characteristics of commercial carbon monoxide sensors. Master's Thesis, Auburn University.

Calabria, R., Chiariello, F., & Massoli, P. (2007). Combustion fundamentals of pyrolysis oil based fuels. Experimental Thermal and Fluid Science, 31(5), 413-420.

Chigier, N. A. (1979). The atomization and burning of liquid fuel sprays. Energy and Combustion Science (pp. 183-200).

Chinyama, M. P. (2011). Alternative fuels in cement manufacturing. Alternative Fuel. InTech.

Chung, S. S., & Kawaguchi, O. (1990). An experimental study on the evaporation of freely falling droplet under high temperature and high pressure gas stream. KSME Journal, 4(2), 172-177.

D'Alessio, J., Lazzaro, M., Massoli, P., & Moccia, V. (1998, January). Thermo-optical investigation of burning biomass pyrolysis oil droplets. In Symposium (International) on Combustion (Vol. 27, No. 2, pp. 1915-1922). Elsevier.

Dee, V., & Shaw, B. D. (2004). Combustion of propanol–glycerol mixture droplets in reduced gravity. International Journal of Heat and Mass Transfer, 47(22), 4857-4867.

Duan, J., Venkatasubramanian, V., Norris, B., Duke, S. R., & Schindler, A., (2011). Visualization and temperature analysis of alternative fuel particle combustion in a drop tube furnace. In 2011 AICHE Annual Meeting. American Institute of Chemical Engineers.

Faeth, G. M. (1996). Spray combustion phenomena. Symposium (International) on Combustion (Vol. 26, No. 1, pp. 1593-1612). Elsevier.

Federal Aviation Administration. Forecast Highlights 2010-2030. FAA Aerospace Forecast Fiscal Years 2010-2030, Retrieved: November 3, 2010 from http://www.faa.gov/data_research/aviation/aerospace_forecasts/2010-2030

Folta, A. (2010). Alternative fuels and their effects on portland cement. Master's Thesis, Auburn University.

Trading Economics (2014). Fossil fuel energy consumption (% of total) in the United States. Retrieved: August 20, 2014, from http://www.tradingeconomics.com/united-states/fossil-fuel-energy-consumption-percent-of-total-wb-data.html

Fox, R. B. (2000). Air quality and comfort measurement aboard a commuter aircraft and solutions to improve perceived occupant comfort levels. Air Quality and Comfort in Airliner Cabins. ASTM International.

Garcia-Perez, M., Lappas, P., Hughes, P., Dell, L., Chaala, A., Kretschmer, D., & Roy, C. (2006). Evaporation and combustion characteristics of biomass vacuum pyrolysis oils. IFRF Combustion Journal, 200601, 1-27.

Ghassemi, H., Baek, S. W., & Khan, Q. S. (2006). Experimental study on binary droplet evaporation at elevated pressures and temperatures. Combustion Science and Technology, 178(6), 1031-1053.

Giddings, D., Eastwick, C. N., Pickering, S. J., & Simmons, K. (2000). Computational fluid dynamics applied to a cement precalciner. Proceedings of the Institution of Mechanical Engineers, Part A: Journal of Power and Energy, 214(3), 269-280.

Giles, S., Venkatasubramanian, V., Duan, J., & Duke, S. R. (2013). Generation of liquid fuel microdroplets for combustion imaging. AUJUS, 59.

Greco, C., Picciotti, G., Greco, R. B., & Ferreira, G. M. (2004). Fuel selection and use. Innovations in portland cement manufacturing. Portland Cement Association, Skokie, 1404.

Gülder, Ö. L., Smallwood, G. J., & Snelling, D. R. (1992). Diesel spray structure investigation by laser diffraction and sheet illumination (No. 920577). SAE Technical Paper.

Hallett, W. L. H., & Clark, N. A. (2006). A model for the evaporation of biomass pyrolysis oil droplets. Fuel, 85(4), 532-544.

Haney, R., Neer, A., Siddiqui, N., Fergus, J., Overfelt, R., & Prorok, B. Monitoring of potential bleed air gas contaminants with FTIR spectroscopy. 41st International Conference on Environmental Systems (p. 5109).

Hanle, L. J., Jayaraman, K. R., & Smith, J. S. (2004). $CO_2$ emissions profile of the US cement industry. Washington DC: Environmental Protection Agency.

Harada, T., Watanabe, H., Suzuki, Y., Kamata, H., Matsushita, Y., Aoki, H., & Miura, T. (2011). A numerical investigation of evaporation characteristics of a fuel droplet suspended from a thermocouple. International Journal of Heat and Mass Transfer, 54(1-3), 649-655.

Harrison, R., Murawski, J., & Guerriero, J. (2009). Exposure to aircraft bleed air contaminants among airline workers a guide for healthcare providers.

Haverikommission, S. (2001). Incident onboard aircraft SE-DRE during flight between Stockholm and Malmo, M County, Sweden, on 12 November 1999. Case L-102/99. Report RL 2001: 41e.

Huang, F. (2010). Development of a drop tube furnace for visualization of combustion of fuel particles. Master's Thesis, Auburn University.

Hunt, E. H., Reid, D. H., Space, D. R., & Tilton, F. E. (1995, May). Commercial airliner environmental control system: Engineering aspects of cabin air quality. Aerospace Medical Association Annual Meeting.

Ikegami, M., Xu, G., Ikeda, K., Honma, S., Nagaishi, H., Dietrich, D. L., & Takeshita, Y. (2003). Distinctive combustion stages of single heavy oil droplet under microgravity. Fuel, 82(3), 293-304.

Johnson, D. T., & Taconi, K. A. (2007). The glycerin glut: Options for the value-added conversion of crude glycerol resulting from biodiesel production. Environmental Progress & Sustainable Energy, 26(4), 338-348.

Kadota, T., & Yamasaki, H. (2002). Recent advances in the combustion of water fuel emulsion. Progress in Energy and Combustion Science, 28(5), 385-404.

Kuniyoshi, H., Tanabe, H., Sato, G. T., & Fujimoto, H. (1980). Investigation on the characteristics of diesel fuel spray (No. 800968). SAE Technical Paper.

Law, C. K. (1982). Recent advances in droplet vaporization and combustion. Progress in Energy and Combustion Science, 8(3), 171-201.

Law, C. K. (2010). Combustion physics. Cambridge University Press.

Lefebvre, A. H. (1998). Gas turbine combustion. CRC Press.

Lippmann, M., Burge, H. A., Jones, B. W., Macher, J. M., Morgan, M. S., Nazaroff, W. W., ... & Weiss, B. (2002). The airliner cabin environment and the health of passengers and crew. Committee on Air Quality in Passenger Cabins of Commercial Aircraft. Board on environmental studies and toxicology. National Academy Press.

Livingston, S. (2010), Visualization and analysis of the combustion of alternative fuels for the replacement of coal in energy production. Undergraduate Honors Thesis, Auburn University.

Ma, X., Zhang, F., Han, K., Yang, B., & Song, G. (2015). Evaporation characteristics of acetone–butanol–ethanol and diesel blends droplets at high ambient temperatures. Fuel, 160, 43-49.

Mackerer, C. R., Barth, M. L., Krueger, A. J., Chawla, B., & Roy, T. A. (1999). Comparison of neurotoxic effects and potential risks from oral administration or ingestion of tricresyl phosphate and jet engine oil containing tricresyl phosphate. Journal of Toxicology and Environmental Health Part A, 57(5), 293-328.

Mascolo, G., Rausa, R., Bagnuolo, G., Mininni, G., & Tinucci, L. (2006). Thermal degradation of synthetic lubricants under oxidative pyrolytic conditions. Journal of Analytical and Applied Pyrolysis, 75(2), 167-173.

Mascolo, G., Rausa, R., Mininni, G., & Tinucci, L. (2004). The gas phase decomposition of synthetic lubricants under pyrolytic conditions. Journal of Analytical and Applied Pyrolysis, 71(1), 165-178.

Metz, B., Davidson, O., De Coninck, H. C., Loos, M., & Meyer, L. A. (2005). IPCC, 2005: IPCC special report on carbon dioxide capture and storage. Prepared by Working Group III of the Intergovernmental Panel on Climate Change. Cambridge, United Kingdom and New York, NY, USA, 442.

Muir, H., Walton, C., & McKeown, R. (2008). Cabin air sampling study functionality test. Report prepared for the Department of Transport. Cranfield University, UK.

National Ready Mixed Concrete Association (2012). Retrieved from http://www.nrmca.org/sustainability/Concrete $CO_2$ fact sheet Feb 2012.pdf

Norris, B., Duke, S. R., & Schindler, A., (2011). Visualization and temperature analysis of alternative fuel particle combustion in a drop tube furnace. AICHE Annual Meeting. American Institute of Chemical Engineers.

Nye Lubricants (2013). https://www.nyelubricants.com/faq#3568. Retrieved on 20 March.

Patzer, R., Norris, M., Doering, A., Jorgenson, R., Neece, C., & Zimmerli, B. (2007). Stack emissions evaluation: Combustion of crude glycerin and yellow grease in an industrial fire tube boiler. Agricultural Utilization Research Institute, Marshall, MN, USA.

Portland Cement Association (2007), “Senate Hansard” Parliament of the Commonwealth of Australia, presented by Senator K. O’Brien, 20 Sept 2007, 10:22am, p.15.

Portland Cement Association (2009). Retrieved from http://www.cement.org/index.asp

Prevention, I. P. (2001). Control (IPPC) – Reference document on best available techniques in the cement and lime manufacturing industries. European Commission.

Rahmat, N., Abdullah, A. Z., & Mohamed, A. R. (2010). Recent progress on innovative and potential technologies for glycerol transformation into fuel additives: A critical review. Renewable and Sustainable Energy Reviews, 14(3), 987-1000.

Roberts, M. (2014). Steady state and transient response characteristics of commercial non-dispersive infrared carbon dioxide sensors. Master's Thesis, Auburn University.

Segawa, D., Yamasaki, H., Kadota, T., Tanaka, H., Enomoto, H., & Tsue, M. (2000). Water-coalescence in an oil-in-water emulsion droplet burning under microgravity. Proceedings of the Combustion Institute, 28(1), 985-990.

Setyawan, H. Y., Zhu, M., Zhang, Z., & Zhang, D. (2016). Ignition and combustion characteristics of single droplets of a crude glycerol in comparison with pure glycerol, petroleum diesel, biodiesel and ethanol. Energy, 113, 153-159.

Shinjo, J., Xia, J., Ganippa, L. C., & Megaritis, A. (2014). Physics of puffing and microexplosion of emulsion fuel droplets. Physics of Fluids, 26(10), 103302.

ASHRAE Standard (2007). 161: Air quality within commercial aircraft. American Society of Heating, Refrigerating and Air-Conditioning Engineers.

Taylor, H. F. (1997). Cement chemistry. 2$^{nd}$ Edition. Thomas Telford.

van Gerpen, J. (2005). Biodiesel processing and production. Fuel Processing Technology, 86(10), 1097-1107.

van Netten, C. (2005). Aircraft air quality incidents, symptoms, exposures and possible solutions. In Air Quality in Airplane Cabins and Similar Enclosed Spaces (pp. 193-210). Springer, Berlin, Heidelberg.

van Netten, C. (2002). Analysis and implications of aircraft disinsectants. Science of the Total Environment, 293(1-3), 257-262.

van Netten, C. (2000). Analysis of two jet engine lubricating oils and a hydraulic fluid: their pyrolytic breakdown products and their implication on aircraft air quality. In Air Quality and Comfort in Airliner Cabins. ASTM International.

van Netten, C. (1999). Multi-elemental analysis of jet engine lubricating oils and hydraulic fluids and their implication in aircraft air quality incidents. Science of the Total Environment, 229(1-2), 125-129.

van Netten, C. (1998). Air quality and health effects associated with the operation of BAe 146-200 aircraft. Applied Occupational and Environmental Hygiene, 13(10), 733-739.

van Netten, C., & Leung, V. (2001). Hydraulic fluids and jet engine oil: pyrolysis and aircraft air quality. Archives of Environmental Health: An International Journal, 56(2), 181-186.

van Netten, C., & Leung, V. (2000). Comparison of the constituents of two jet engine lubricating oils and their volatile pyrolytic degradation products. Applied Occupational and Environmental Hygiene, 15(3), 277-283.

Vedantham, A. (1999). Aviation and the global atmosphere: A Special Report of IPCC Working Groups I and III.

Wakuri, Y., Fujii, M., Amitani, T., & Tsuneya, R. (1960). Studies on the penetration of fuel spray in a diesel engine. Bulletin of JSME, 3(9), 123-130.

Wang, C. H., Liu, X. Q., & Law, C. K. (1984). Combustion and microexplosion of freely falling multicomponent droplets. Combustion and Flame, 56(2), 175-197.

Wardana, I. N. G. (2010). Combustion characteristics of jatropha oil droplet at various oil temperatures. Fuel, 89(3), 659-664.

Watanabe, H., & Okazaki, K. (2013). Visualization of secondary atomization in emulsified-fuel spray flow by shadow imaging. Proceedings of the Combustion Institute, 34(1), 1651-1658.

Watanabe, H., Harada, T., Matsushita, Y., Aoki, H., & Miura, T. (2009). The characteristics of puffing of the carbonated emulsified fuel. International Journal of Heat and Mass Transfer, 52(15-16), 3676-3684.

Winder, C., & Balouet, J. C. (2002). The toxicity of commercial jet oils. Environmental Research, 89(2), 146-164.

Wornat, M. J., Porter, B. G., & Yang, N. Y. (1994). Single droplet combustion of biomass pyrolysis oils. Energy & Fuels, 8(5), 1131-1142.

Worrell, E., Price, L., Martin, N., Hendriks, C., & Meida, L. O. (2001). Carbon dioxide emissions from the global cement industry. Annual Review of Energy and the Environment, 26(1), 303-329.

Xu, G., Ikegami, M., Honma, S., Ikeda, K., Nagaishi, H., Dietrich, D. L., & Takeshita, Y. (2002). Burning droplets composed of light cycle oil and diesel light oil. Energy & fuels, 16(2), 366-378.

# Appendix A. Data Measurement and Analysis

## A.1. Elapsed Time and Moving Average Calculation

The experiments with IR heater involving the E-G system use a manual triggering method as explained in chapter 7. Using this method, the IR heater, visualization system (high speed camera and high magnification lens) and the temperature data logger was started simultaneously. The frames per second (fps) was preset in the high-speed camera using the 'camera control' function in the PCO 1200hs as shown in Figure A-1. The exposure, delay, and sensor size settings shown in figure 1 determine the fps of each recording. In the event of a fps rate set by the user being higher than the maximum fps recording rate limit of the camera, the Camware dialog box (Figure 1) shows the actual fps with which the visualization video was recorded. The frequency at which the temperature data logger collects data was specified using the software program (C program code) that controls the operation of the data logger. The IR heater operating voltage and time duration were manually set using the RA and TA knobs respectively, as shown in figure 2. For our experiments, commonly used settings are RA-10 (maximum output voltage to lamps) and TA-10 (IR heater operation for approximately 20s).

The timestamp data embedded in each image provides the precise timescale for each image. Also, from the analysis of over 5000 temperature data points obtained from the data logger over the period of this research, we found the device to record the temperature data every 0.1165s when in operation. From the temperature data obtained during each droplet experiment, we observed the first temperature change at the thermocouple to be at 1.4s (minimum of 1°C change) from the time the IR heater was switched ON. This period between the application of voltage to lamps to the observed temperature change in the thermocouple data is referred to as $t_{lag}$ in chapter 7. Generally, the $t_{lag}$ period is excluded from representation in the temperature data plots and in the calculation of DE - 1, 2, 3, 4 events.

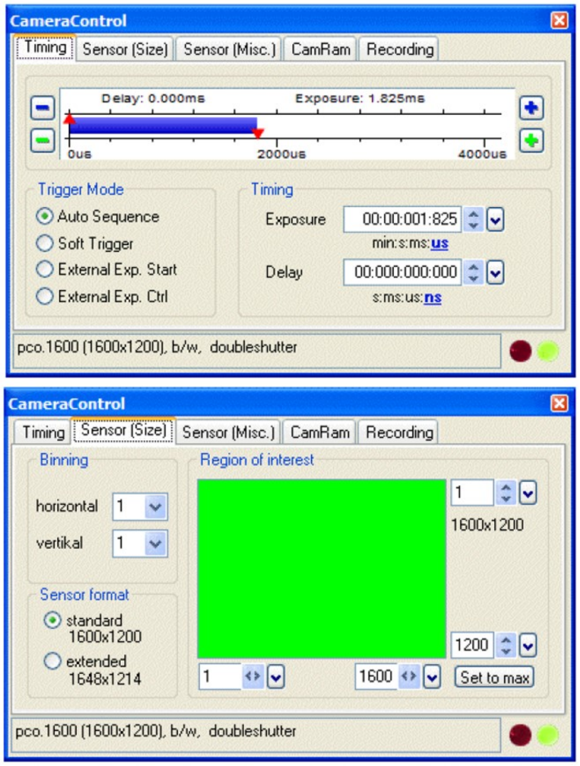

Trigger Mode
● Auto Sequence
○ Soft Trigger
○ External Exp. Start
○ External Exp. Ctrl

Timing
Exposure 00:00:001:825 min:s:ms:us
Delay 00:000:000:000 s:ms:us:ns

pco.1600 (1600x1200), b/w, doubleshutter

Binning
horizontal 1
vertikal 1

Sensor format
● standard 1600x1200
○ extended 1648x1214

Region of interest
1
1600x1200
1200
1
1600

pco.1600 (1600x1200), b/w, doubleshutter

Figure A-1: Camera control dialog boxes in Camware software used for setting fps of visualization recordings.

The objective of the temperature data plots of the E-G system studies were to obtain the general heating profile trend of various liquids in different test conditions. Therefore, the experimental data were all presented as moving average data for clarity in comparison plots. Moving average interval 5 was used for representing all the temperature data of E-G system studies. This moving average procedure results in four empty kernels at the beginning of each data set. To be in sync with the raw temperature profile, the whole data set obtained after moving average calculation was shifted 2 cells back. Also, the remaining two empty kernels were calculated to be the average of first 3 and first 4 data points, respectively. Figure 3 shows the plot obtained after moving average calculations shown in comparison with the raw data. As it can be seen from figure 3, the moving average plot is a good representation of the general trend of the original temperature profile obtained from the thermocouple.

Figure A-2: Photograph of IR heater controller showing RUN ADJUST (RA) and TIME ADJUST (TA) settings.

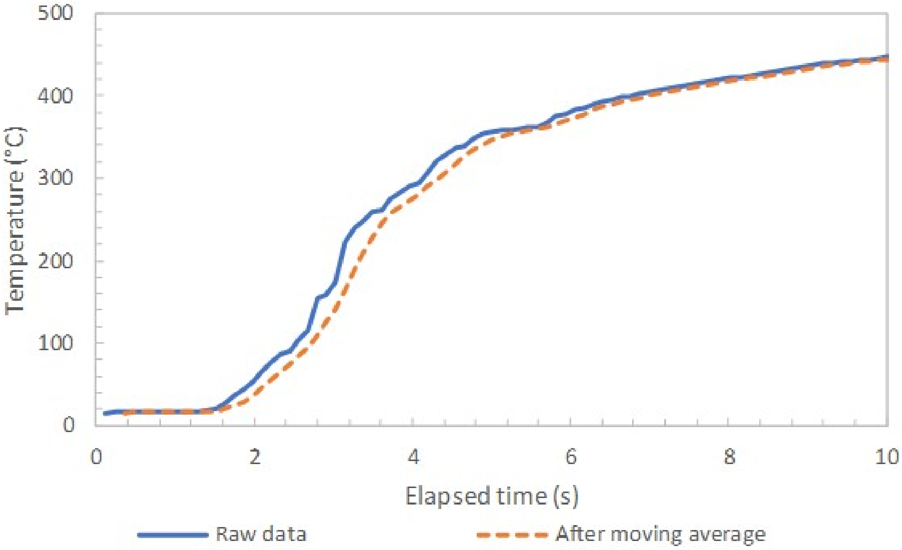

Figure A-3: Thermocouple temperature data shown before and after moving average calculations

## A.2. Droplet Diameter Calculation

Quantitative image analysis was performed for both low and high magnification visualizations. In low magnification visualization only $d_0$ was obtained. For high magnification visualizations temporal change in $d$ was obtained by making measurements throughout the droplet lifetime period. For all these measurements, the known outer diameter of the thermocouple wire (125µm) was used as a scale. The droplet diameter is calculated by obtaining the area of the droplet using ImageJ and equating the area to an equivalent circle. This equivalent circle's diameter is represented as the diameter of the droplet. Figure 4 shows the calculation of the area of a droplet using the polygon selection tool in ImageJ.

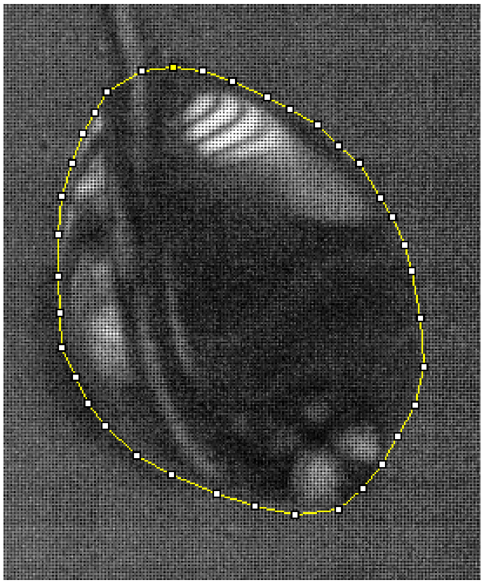

Figure A-4: Droplet diameter calculation using polygon selection tool in ImageJ.

# Appendix B. BP Turbo Oil 274 Appearance Tests

BP Turbo Oil 274 (BP Oil) samples were investigated for the observed change in coloration during prolonged exposure to lab atmosphere.

## B.1. Experiment

For this experiment, 2 ml samples of oil were tested in three different conditions that include an open glass dish, an open plastic dish, and a covered plastic dish. The three oil samples in dish were undisturbed throughout this experiment. Images were recorded at periodic intervals to observe for possible changes in the external appearance of the oil. During early periods of the experiment, the images were taken for every hour, and gradually the intervals were increased 24-hour periods.

## B.2. Observation

The photographs of the three samples collected throughout the duration of the experiment were shown in Figure B-1. Visual observations showed color change in the open glass dish and in the open plastic dish. No color change was noticed in covered plastic dish. For the samples showing color change, the first observation of change was after 5 hours. The color change became very clearly noticeable after the first 24 hours. The pattern of color change was from light yellow to dark brown over a period of 20 days. The liquid in the covered plastic dish stayed light yellow, same as the initial coloration, during the entire period of the experiment.

## B.3. Inference

Commercial aviation engine oil such as the BP Turbo Oil 274 experimented here contains small amounts of additives that have the tendency to darken with exposure to sunlight, UV light, temperature, or when in contact with air (Nye Lubricants, 2013). The change in coloration commonly observed in oil is from a brown to orange tint. The color change observed is generally a result of the oxidation of the additives, which make up a relatively small portion of the oil when compared to the base compound. For most cases, the change in coloration does not result in the functional change of the oil. Hence, the change observed with the BP Oil color is suggested to not affect the vaporization or combustion behavior at elevated temperatures.

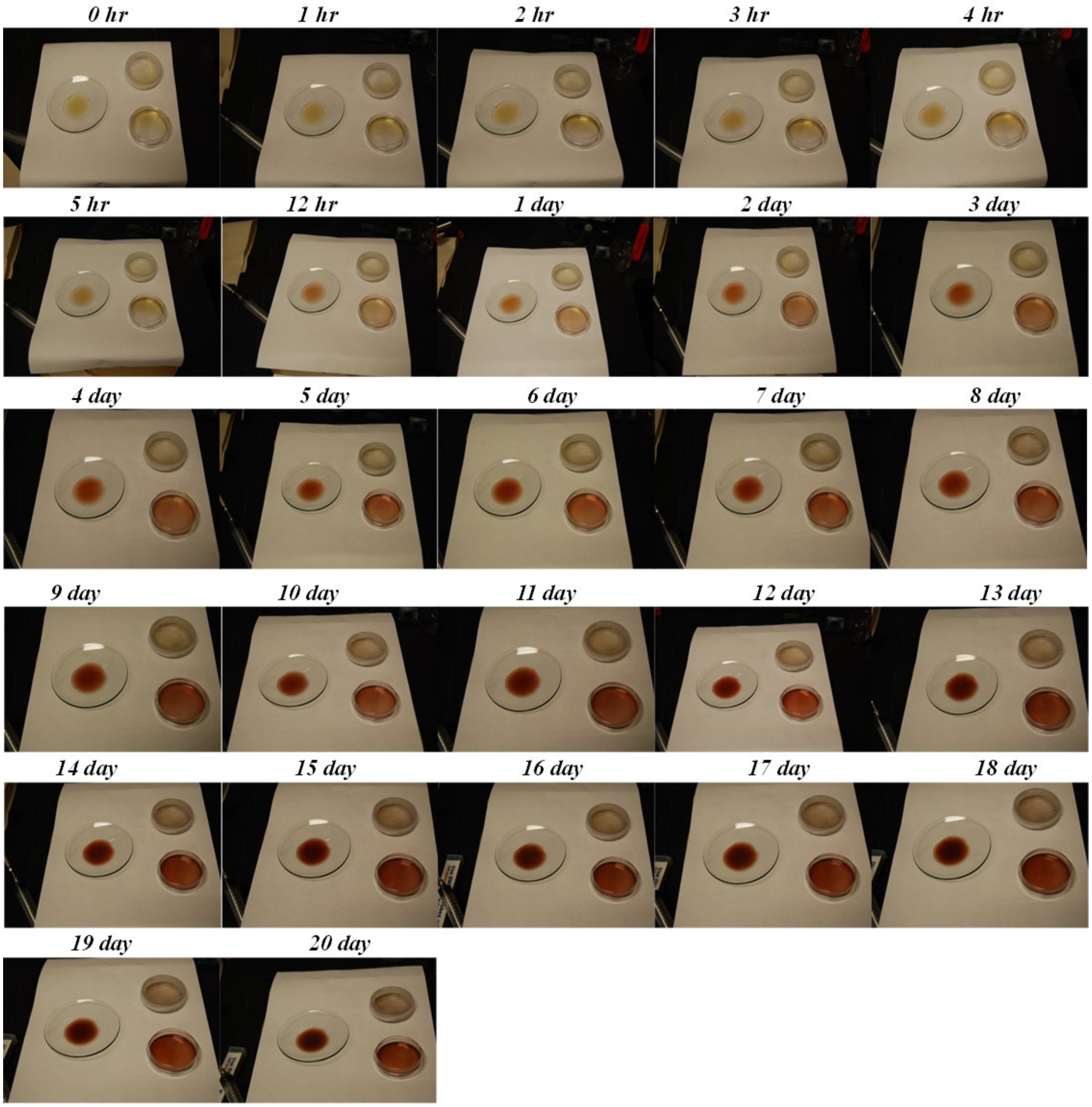

Figure B-1: Photograph of BP Oil color change experiments.